Linking structure and dynamics of integrin $\alpha_{IIb}\beta_3$ to its biological function via molecular dynamics simulations and free energy calculations

Inaugural-Dissertation

zur Erlangung des Doktorgrades

der Mathematisch-Naturwissenschaftlichen Fakultät

der Heinrich-Heine-Universität Düsseldorf

vorgelegt von

Giulia Pagani

aus Mailand

Düsseldorf, Februar 2018

Aus dem Institut für Medizinische Chemie und Pharmazie

der Heinrich-Heine-Universität Düsseldorf

Gedruckt mit der Genehmigung der

Mathematisch-Naturwissenschaftlichen Fakultät der

Heinrich-Heine-Universität Düsseldorf

Referent: Prof. Dr. Holger Gohlke

Korreferent: Jun. Prof. Dr. Birgit Strodel

Tag der mündlichen Prüfung:

22.03.2018

Eidesstattliche Erklärung

lch versichere an Eides Statt, dass die Dissertation von mir selbständig und ohne unzulässige fremde Hilfe unter Beachtung der „Grundsätze zur Sicherung guter wissenschaftlicher Praxis an der Heinrich-Heine-Universität Düsseldorf“ erstellt worden ist.

Diese Dissertation wurde in der vorgelegten oder einer ähnlichen Form noch bei keiner anderen Institution eingereicht und es wurden bisher keine erfolglosen Promotionsversuche von mir unternommen.

Düsseldorf, den 23 Februar 2018

To my family

“...Nell'anno '18 di nostra vita io Giulia, eterna studentessa,

perché la materia di studio sarebbe infinita e soprattutto perché so di non sapere niente...”

F. Guccini

TABLE OF CONTENTS

LIST OF PUBLICATIONS

This thesis is based on the following publications:

I. Donner, L., Fälker, K., Gremer, L., Klinker, S., **Pagani**, **G**. **(10%)**, Ljungberg, L. U., Lothmann, K., Rizzi, F., Schaller, M., Gohlke, H., Willbold, D., Grenegard, M., Elvers, M.

Blood platelets contribute to the formation of amyloid deposits in cerebral vessels via integrin $\alpha_{IIb}\beta_3$ induced outside-in signaling and clusterin release. **Sci. Signal. 2016**, 9, RA52.
Impact factor reported in 2016: 6.494

II. **Pagani**, **G**. **(40%)**, Pereira, J. P. V., Stoldt, V. R., Beck, A., Scharf, R. E., Gohlke, H.

The human platelet antigen-1b variant of $\alpha_{IIb}\beta_3$ allosterically shifts the dynamic conformational equilibrium of the integrin toward the active state.
J. Biol. Chem. 2018, DOI: 10.1074/jbc.RA118.002149
Impact factor reported in 2016: 4.125

III. **Pagani**, **G**. **(70%)**, Gohlke, H.

On the contributing role of the transmembrane domain for subunit-specific sensitivity of integrin activation.
Sci. Rep. 2018, DOI: 10.1038/s41598-018-23778-5

ABBREVIATIONS

ΔG	change in Gibbs free energy
Aβ	amyloid beta
AD	Alzheimer's disease
ADMIDAS	site adjacent to MIDAS
APP	amyloid precursor protein
βTD	β-tail domain
CAA	cerebral amyloid angiopathy
CG-MD	coarse-grained molecular dynamics
CNA	Constraint Network Analysis
COM	center of mass
CT	cytoplasmic tail
DPPC	dipalmitoylphosphatidylcholine
DMPC	dimyristoylphosphatidylcholine
ECM	extracellular matrix
EGF	epidermal growth factor
EM	electron microscopy
FDA	US Food and Drug Administration
FRET	fluorescence resonance energy transfer
Fn	fibronectin
FF	force field
GB	generalized Born
HPA	human platelet antigen
IMC	inner membrane clasp
K_B	Boltzmann factor
K_D	dissociation costant
KLD	Kullback-Leibler divergence

LIMBS	ligand-associated metal-binding-site
MD	molecular dynamics
MIDAS	metal-ion-dependent adhesive site
NMR	nuclear magnetic resonance
OMC	outer membrane clasp
OPM	orientations of proteins in membranes
PDB	Protein Data Bank
PME	particle mesh Ewald
PMF	potential mean force
PSI	plexins-semaphorins and integrins
RAC	RMS average correlation
RGD	arginine-glycine-aspartate
RHD	arginine-histidine-aspartate
RMSD	root mean square deviation
RMSF	root mean square fluctuation
Rg	radius of gyration
SAXS	X-ray scattering
SEM	standard error of mean
SMD	steered molecular dynamics
SyMBS	synergistic metal ion binding site
TMD	transmembrane domain
US	umbrella sampling
vWF	von Willebrand factor
WHAM	Weighted Histogram Analysis Method

ABSTRACT

Integrins are a large family of adhesion receptors that can be grouped into several subgroups or subfamilies based on differences in their sequence, function and patterns of expression. Integrins, partly by way of their originally recognized role of structural connectors between the intracellular and extracellular environment, are considered to regulate a plethora of developmental processes, including cell proliferation, migration and differentiation. Additionally, integrins are important signaling molecules involved in transmission of mechanical forces and biochemical data across the plasma membrane. By contrast, when inappropriately expressed, integrins contribute to the pathogenesis of many human diseases.

During the last decade, there has been an increasing interest in characterizing integrins on a molecular level. Research efforts were driven by the need to comprehend the exact regulatory mechanism of integrins on the atomic level to be able to understand their influence on many cellular functions and the molecular origin of diverse pathological states.

However, many questions regarding the relationship between integrin structure and function, especially in many integrin-related diseases are still open, and integrins remain an important area of research.

The goal of this thesis was to obtain atomic-level insights into the integrin structure on its own and in complex with ligands, and the mechanisms of allostery transmission by means of molecular dynamics (MD) simulations and free energy calculations, in the attempt to gain a better focus on how cellular functions are regulated by integrins.

First, the event of binding of $A\beta_{40}$ to the integrin isoform $\alpha_{IIb}\beta_3$ is linked to the pathogenesis of Alzheimer's disease. As part of multidisciplinary project, a computational investigation of the integrin $\alpha_{IIb}\beta_3$ bound to $A\beta_{40}$ was performed, and this allowed the characterization of the binding mode at an atomistic level followed by a description of the ligand-induced conformational changes undergone by integrin $\alpha_{IIb}\beta_3$. **Second**, the molecular mechanism through which the human platelet antigen (HPA) alloimmune system shifts the conformational equilibrium of integrin $\alpha_{IIb}\beta_3$ towards the active state was elucidated. These findings, in creating a link to the clinical and experimental data, provide an atomic level explanation of this specific phenotype. **Third**, a strategy based on the combination of long time scale MD simulations with free energy calculations was applied to perform a comparative analysis of the transmembrane domain (TMD) of three integrin isoforms ($\alpha_{IIb}\beta_3$, $\alpha_v\beta_3$, and $\alpha_5\beta_1$), to gain a deeper understanding of the origin of the subunit-specific sensitivity to activation.

ZUSAMMENFASSUNG

Integrine sind eine große Familie von Adhäsionsrezeptoren die, basierend auf Unterschieden in Sequenz, Funktion und Expressionsmuster, in verschiedene Untergruppen oder -familien unterteilt werden kann. Integrine sind, zum Teil wegen ihrer ursprünglich erkannten Rolle als strukturelle Verbindungen zwischen der intra- und extrazellulären Umgebung, für eine Reihe von Entwicklungsprozessen, einschließlich Zellprofileration, Migration und Differenzierung, verantwortlich. Zusätzlich sind Integrine wichtige Signalmoleküle, die an der Transmission mechanischer Kräfte und biochemischer Informationen durch die Plasmamembran beteiligt sind.

Wenn fehlerhaft exprimiert, tragen Integrine jedoch zur Pathogenese von menschlichen Krankheiten bei.

Im letzten Jahrzehnt wuchs das Interesse, Integrine auf molekularer Ebene zu beschreiben/untersuchen. Forschungsarbeiten wurden durch die Notwendigkeit angetrieben, die exakten Regulationsmechanismen von Integrinen auf atomarer Ebene nachvollziehen zu können, um ihren Einfluss auf viele Zellfunktionen und den molekularen Ursprung verschiedener pathologischer Zustände einzuschätzen.

Allerdings stehen viele Fragen zur Beziehung zwischen Integrinstruktur und Funktion – vor allem hinsichtlich vieler Integrin-bezogener Krankheiten - noch offen, und so bleiben Integrine ein wichtiges Forschungsfeld.

Das Ziel dieser Dissertation war, ein Verständnis auf atomarer Ebene von der Integrinstruktur selbst und Strukturen im Komplex mit Liganden sowie den Mechanismen bei allosterischen Transmissionen mit Hilfe von Moleküldynamiksimulationen (MD) und Berechnungen der freien Energie zu erlangen, um gezielt zu verstehen wie Integrine Zellfunktionen regulieren.

Die Bindung von $A\beta_{40}$ an die Integrinisoform $\alpha_{IIb}\beta_3$ ist mit der Alzheimer-Krankheit verbunden. Als Teil eines multidisziplinären Projekts wurden computergestützte Untersuchungen zur Bindung von $\alpha_{IIb}\beta_3$ FIntegrin an $A\beta_{40}$ durchgeführt. Dies ermöglichte die Charakterisierung des Bindungsmechanismus' auf atomarer Ebene sowie die Beschreibung der durch Liganden verursachten Konformationsänderungen des Integrin $\alpha_{IIb}\beta_3$.

Der molekulare Mechanismus, in dem das menschliche „Thrombozyten-Antigen alloimune System“ das konformationelle Gleichgewicht des Integrins $\alpha_{IIb}\beta_3$ zum aktiven Zustand verschiebt, wurde erklärt. Diese Erkentnisse, die eine Verbindung zwischen klinischen und

experimentellen Daten bilden, bieten eine Erklärung des spezifischen Phänotyps auf atomarer Ebene.

Eine Strategie basierend auf der Kombination von langen MD-Simulationen mit Berechnung der freien Energie wurde angewandt, um eine komparative Analyse der Transmembrandomäne (TMD) von drei Integrinisoformen ($\alpha_{IIb}\beta_3$, $\alpha_v\beta_3$ und $\alpha_5\beta_1$) auszuführen mit dem Ziel, ein tieferes Verständnis der Untereinheit-spezifischen Sensibilität der Aktivierung zu erlangen.

1 INTRODUCTION

It was already in 1965 when Richard Feynman, in his famous speech following the Nobel price in Physics stated that "everything that living things do can be understood in terms of the jigglings and wigglings of atoms" [1]. In light of this, a detailed characterization of the dynamics of a biological system has become essential in the attempt to improve our knowledge of the system itself [2]. However, much more time was required before the idea of the use of theoretical approaches in combination with experiments was accepted also in the field of biology [3]. It was nearly 40 years ago, when the first *molecular dynamics* (MD) simulation was successfully applied to a biological macromolecule. This study, dated 1977 [2], albeit simple, transformed completely the way of approaching and dealing with biological systems. Rather then rigid entities, they are now seen as an ensemble of particles that move in space and time, and whose internal motions govern many biological events [3]. Since then, it became clear that the knowledge of the dynamics is the key to comprehend events and functions on a biological level. In this sense, thanks to their ability to identify the internal motions occurring on the timescale from the femtoseconds to milliseconds [4, 5], MD simulations offer the possibility to overcome the spatiotemporal limitations typical of experimental techniques [4]. Of course, the use of computational methods, such as MD simulations, is not meant to completely replace the use of experiments. They rather offer the possibility to reach a more rigorous and precise description of the investigated system [1]. This way, weaknesses intrinsic to both experimental and computational methods, can be overcome by the tight interplay of these two, complementary, approaches.

In all metazoa, from the simplest sponges to humans, cell adhesion to the extracellular matrix (ECM) as well as cell-cell adhesion interactions represent the key to evolve from simple cells to a multicellular organism formed by different tissues and organs [6]. Integrins are the major metazoan receptors mediating adhesive events and, since their recognition in 1987 [7], great effort has been dedicated to understand the molecular basis of their biological function. Expressed on the cell surface in their inactive state [8], they act as mechanical linkers that provide physical support and enable the adhesion between cells and to the ECM [9-11]. By binding ligands on either side of the cell, integrins become activated and trigger a cascade of signals that initiate many biological events, including cell proliferation, migration, growth and survival [12-14]. Thus, integrins are also fully considered as signaling receptors [15]. Both in cause and in effect of their role in tissue organization, cell development, signaling and pathways

regulation, integrins are also implicated in a number of human diseases [6]: cardiovascular diseases, pathological thrombus formation [16], but also, inflammation [8], immune responses [17] and cerebral dysfunctions [18-20], only to cite a few. As such, integrins represent a pharmaceutically meaningful and attractive target [21]. It is then not surprising that, since the last decade, integrins have been extensively investigated and a number of studies, both experimental and computational, have been carried out [8]. However, the exact mechanism that regulates integrins' activation and response continues to represent a controversial topic [8]. As introduced, integrins are adhesion receptors, but also complex signaling machines [15]. They are involved in a plethora of biological events [22], and this versatility is also reflected in their structure. Integrins are robust entities, as to sustain the pulling forces occurring during adhesion [23]. However, at the same time, they must be highly plastic and dynamic to switch from the inactive to the active state and readapt in response to changes in the extracellular and intracellular environment [24]. As a consequence, unveiling the mechanism that regulates integrins ultimately means to comprehend their energetics and dynamics. A great advance in understanding integrins in their structure and function must be ascribed to the determination of the first crystal structure almost 20 years ago [25, 26]. Since then, studies combining structural data together with experiments have proven to be a successful approach for addressing integrins [27, 28].

In this thesis, I primarily focused on the main platelet integrin receptor, also known as integrin $\alpha_{IIb}\beta_3$ [29, 30]. The main focus of my work has been dedicated to understand the complex regulation of integrin activation in atomic detail. To achieve my goals, I applied different MD techniques and performed free energy calculations. My computational findings together with experimental data resulted in three publications.

In **Publication I**, the consequences of binding to ligands in the extracellular environment constituted the object of study. Here, the main aim was to understand how the amyloid beta 40 ($A\beta_{40}$) binding event relates to the contribution of platelets to cerebral amyloid angiopathy (CAA) in the context of Alzheimer's disease (AD).

In **Publication II**, the impact of the human platelet antigen (HPA)-1 alloimmune system, a clinically relevant variant of integrin $\alpha_{IIb}\beta_3$ was studied. The internal motions undergone by integrin $\alpha_{IIb}\beta_3$ in the presence/absence of this particular mutation constituted a valuable

approach to analyze the allosteric influence of the HPA-1 on the conformational equilibrium between the inactive and active integrin.

In **Publication III**, a computational investigation has been carried out on integrin $\alpha_{IIb}\beta_3$, $\alpha_v\beta_3$ and $\alpha_5\beta_1$ to shed light on how the transmembrane (TM) domain association is disrupted during activation and, with it, to understand how subunit-specific differences relate to a subunit-specific sensitivity to activation of different integrin isoforms.

2 BACKGROUND

2.1 INTEGRIN OVERVIEW

The term “integrin” was chosen to identify an integral membrane protein complex that was first identified in 1986 [13, 31]. This name relates to the intrinsic property of integrins to integrate the extracellular and intracellular environments [32]. This way, integrins mediate cell-matrix and cell-cell adhesion events [7, 14, 33, 34], which constitute a crucial step in tissue generation and cell development [14, 35]. Intracellular, integrins anchor to the cytoskeleton in response of binding of specific intracellular ligands [14, 36, 37], whereas, extracellular, the adhesion to the ECM is mediated by a wide variety of extracellular ligands and soluble proteins [12]. Hence, integrin’s adhesive function relies on the fine-tuned regulation of integrin affinity towards ligands on either side of the cell [38]. This is achieved upon integrin activation, a mechanism by which integrins undergo a rapid and reversible rearrangement of their entire structure [36, 39-41]. The mechanism of activation implies a shift from the inactive and closed form to the active and open form, which allows ligand binding [8, 13]. Additionally, integrins provide a physical link between the cytoskeleton inside the cell and the ECM outside the cell [34, 42], which allows the transmission of mechanical forces and biochemical signals across the plasma membrane [43, 44]. This mechanism occurs bidirectionally, via outside-in and inside-out signaling [13, 32, 45]. Following the classic outside-in signaling pathway, integrins act as environmental sensors able to capture information outside the cell, and transmit them as mechanical signals inside the cell [14, 15, 46]. These signals are then translated into many different cellular responses, including cell survival/apoptosis, motility, proliferation and differentiation [8]. In outside-in signaling, the extracellular portion of integrin is able to expose the binding site to extracellular ligands [36], inducing conformational changes that reach the intracellular portion and initiate the internal cascade of signals [12]. However, integrin affinity for extracellular ligands is spatially and temporally tightly regulated internally through the mechanism of inside-out signaling [12, 43, 47]. Other membrane receptors (e.g. G protein-coupled receptors [32]) transmit signals to the cell to initiate the process of integrin activation [32]. This is achieved through the binding of cytoskeletal elements (e.g. Talin) to

the intracellular portion of integrins, which leads to a structural rearrangement that reaches the extracellular site, driving the opening of the binding site and, thus, modulating the affinity towards the extracellular ligands (Figure 1) [12, 32, 48, 49].

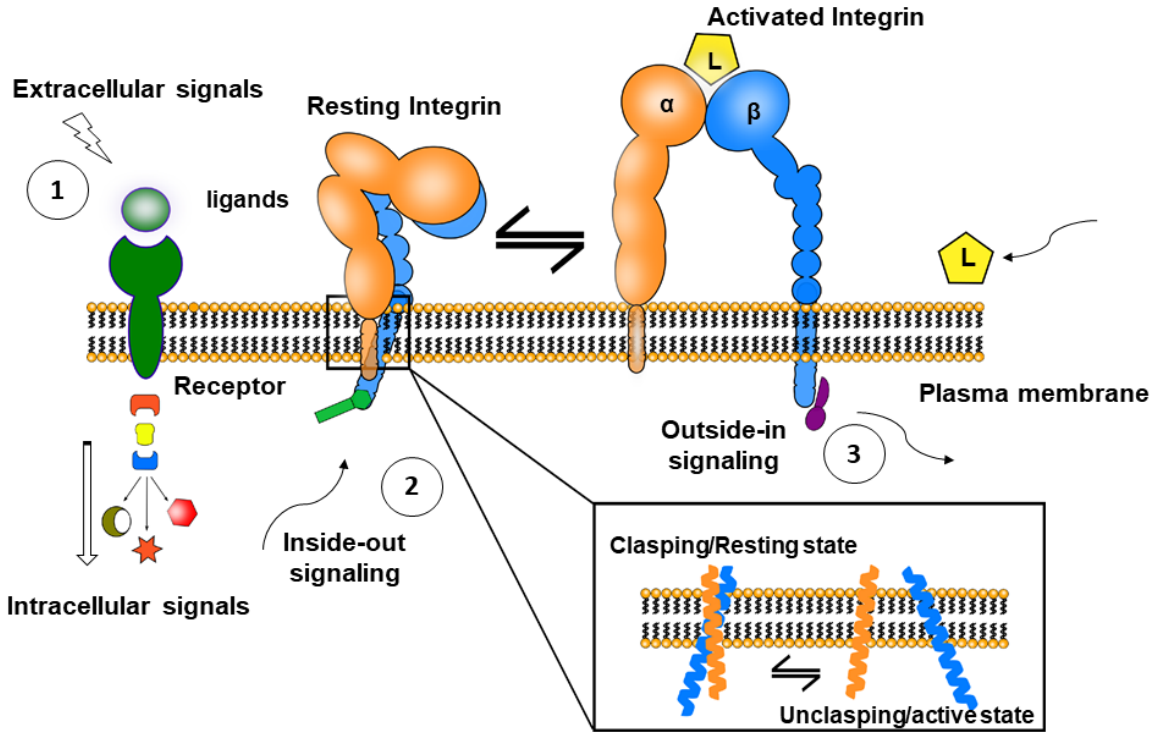

Figure 1 Bidirectional transmission of signaling in integrins. Ligand binding to a non-specified membrane receptor (e.g. G protein-coupled receptor) triggers a signal transduction cascade inside the cell (1). This is rapidly followed by integrin binding to cytoskeletal elements (e.g. Talin), which causes inside-out signaling via the conversion from the inactive to the active state (2). In the active form, the binding site is open and can be accessed by extracellular matrix ligands (L), thus leading to outside-in signaling (3). Figure adapted from reference [50].

A detailed description of all the knowledge about integrins is beyond the scope of this thesis. However, in this section, I will review the main aspects regarding integrin function and structure, with a specific focus on integrin isoform $\alpha_{IIb}\beta_3$, which constituted the main biological target of the studies here presented.

2.1.1 Integrin family

Identified in 1987 [7], integrins are heterodimeric transmembrane adhesion receptors found in all metazoans in a number related to the complexity of the organism [8, 12, 51, 52]. All integrins are expressed as heterodimers of an α and a β subunit [34], whose association is maintained through a series of non-covalent interactions [13]. Their association occurs in the endoplasmic reticulum [35, 53], where the amount of integrins depends on the concentration of the α subunits, which are expressed at a lower level [53]. The two subunits are evolutionary completely unrelated between each other [35]. In contrast, conserved regions are found within the subunits, showing a sequence identity of roughly 30% for the α subunit, and up to 45% for the β subunits [54]. In humans, at least eighteen different α subunits and eight different β subunits were reported [8, 34]. These form a family of 24 known integrins [8]. This disproportion in the number of the two subunits necessarily means that there are integrins, which share the same β subunit while paired to a different α subunit [55]. Accordingly, it is possible to classify the different family members of integrins based on their subunit composition (Figure 2) [56]. The advantage of this classification is that it permits the identification of mainly three large groups in which integrins can be divided. A group containing the β_1 subunit (β_1 integrins), a group carrying the β_2 subunit (β_2 integrins) and a group which binds to the same α_v subunit (α_v containing integrins) [56].

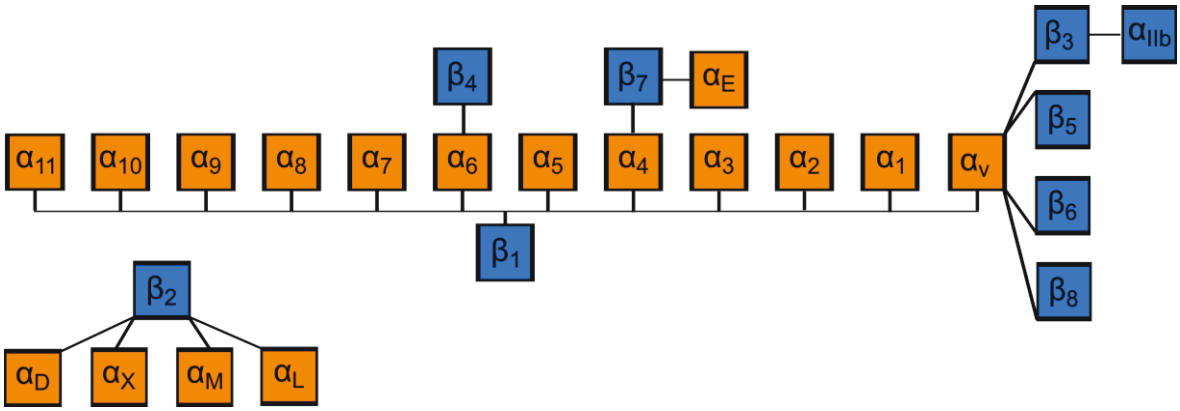

Figure 2 Superfamily of integrin receptors. The eighteen different α subunits (orange) and eight different β subunits (blue) forming the superfamily of human integrin are here schematically represented. Solid lines indicate combinations, resulting in a total of 24 different integrins.

Another way to group integrins is based on their ligand binding specificity (Table 1). Each integrin can bind only a specific set of ECM ligands, so that its biological function is unique and different from the others [11]. Moreover, the same integrin, but expressed on different cell types, also bind to different ligands, thus expanding the definition of specificity [57]. In this complex scenario, it is nevertheless possible to cluster integrins based on their binding specificity into four different categories [56].

Table 1. Integrins family divided into 4 categories based on the ligand binding properties.

Binding specificity	Integrin isoforms
RGD receptors	$\alpha_5\beta_1$, $\alpha_8\beta_1$, $\alpha_{IIb}\beta_3$, $\alpha_v\beta_3$, $\alpha_v\beta_5$, $\alpha_v\beta_6$, $\alpha_v\beta_8$, $\alpha_v\beta_1$
Laminin receptors	$\alpha_3\beta_1$, $\alpha_6\beta_1$, $\alpha_7\beta_1$, $\alpha_6\beta_4$
Leukocyte-specific receptors	$\alpha_L\beta_2$, $\alpha_M\beta_2$, $\alpha_X\beta_2$, $\alpha_D\beta_2$, $\alpha_9\beta_1$, $\alpha_4\beta_1$, $\alpha_4\beta_7$, $\alpha_E\beta_7$
Collagen receptors	$\alpha_1\beta_1$, $\alpha_2\beta_1$, $\alpha_{10}\beta_1$, $\alpha_{11}\beta_1$

In the present work, I focused on the RGD-binding integrins, whose mechanism of binding will be treated in more detail in **paragraph 2.1.4**.

2.1.2 Integrin architecture

Integrin's α and β subunits are type I membrane glycoprotein [58], each of which is formed by a large extracellular domain (ectodomain), a single-span transmembrane domain (TMD) and a short cytoplasmic tail (CT) [59]. Apart from small variations among the different integrin isoforms, each subunit contains in total > 1600 amino acids [8], of which around 1000 are located in the α ectodomain and around 750 in the β ectodomain [8, 13, 58]. In contrast, in the intracellular environment, around 30 more amino acids are counted for the β subunit, with the α cytoplasmic tail being formed by around 20 amino acids [8, 58]. In its totality, an integrin is roughly 280 Å long, with a weight of ~ 150-180 kD for the α subunit

and ~ 90 kD for the β subunit [60]. The two subunits associate together in forming the globular 'head' of integrin [58]. Where the two subunits meet constitutes also the largest area of contact in integrin with a surface of ~ 1600 $Å^2$ [58]. Interestingly, this exceeds in size all other interfaces formed between two contiguous domains across integrin [59]. In addition, the extracellular ligand-binding site is located within the head, at a distance of 150-200 Å above the plasma membrane [61] (**see paragraph 2.1.3**). In fact, the head is found at the top of two C-terminal long legs [62], or also alternatively called stalks [59], which contact at their respective knees of each subunit and terminate into the transmembrane domain and cytoplasmic tail [63]. As such, albeit further divided into different domains, whose number and topologies vary for the α or β subunits [22], integrins can be virtually divided into two major parts, the upper part, or head of the protein, and the lower part, or legs [64] (Figure 3). Through EM images of integrins [63, 65, 66], researchers have known about the global topology of this protein long before the first crystal structures were made public [13, 30, 39, 67, 68].

However, our understanding of the structure and function of integrins has greatly benefited from the availability of high-resolution crystal structures. In particular, these crystallographic structures provided the first glimpse of the large-scale reorientation of the structure affecting the overall structure and the bases on which the models of integrin activation were grounded [69]. Integrin $\alpha_v\beta_3$ ectodomain has been the first one to be resolved by Xiong *et al.* [25], followed by the crystal structure of integrin $\alpha_{IIb}\beta_3$ ectodomain obtained by Xiao *et al.* [70]. Surprisingly, the crystal of integrin $\alpha_v\beta_3$ in the presence of Ca^{2+} exhibited a severe degree of bending of the head over the two parallel legs [29]. In this conformation, the head part is now placed in the proximity of the legs, so that the two parts now interact over an interface of > 4000 $Å^2$ [25, 45, 71, 72]. Accordingly, also the ligand-binding site has changed its position, and it lies now in the vicinity of the plasma membrane [61]. However, when extended, the crystal adopted a conformation similar to that of integrin $\alpha_{IIb}\beta_3$ in the presence of Mn^{2+} as revealed by EM images [45]. Likewise, the crystal of integrin $\alpha_{IIb}\beta_3$ resolved in the extended conformation is consistent with the EM images of integrin $\alpha_v\beta_3$ in the presence of a ligand [73]. When in the inactive form, integrin $\alpha_v\beta_3$ is folded at a ~ 135° obtuse angle [74] with the point of bending located between the thigh and calf-1 domains of the α_v subunit [75]. The ectodomain adopts a V-shaped structure, which drastically differs from the extended one [26]. When extended, EM images revealed that the two subunits are separated with an angle of ~ 62° and a distance of ~70 Å at the bending point [29]. In addition, EM images of rotary-shadowed integrin $\alpha_v\beta_3$ are consistent with the crystal

structure and together indicate that in the extended form, integrin $\alpha_v\beta_3$ is ~160 Å long and ~ 60 Å wide [63, 76-78]. More recently, also the crystal structure of integrin $\alpha_5\beta_1$, that closely resembles those of integrin $\alpha_{IIb}\beta_3$ and $\alpha_v\beta_3$, has become available [79].

Nowadays, there is ample evidence that supports the thesis that the V-shaped conformation of integrin represents the bent, low affinity state of integrin in contraposition to the open, high affinity one [45, 70, 72, 80-84].

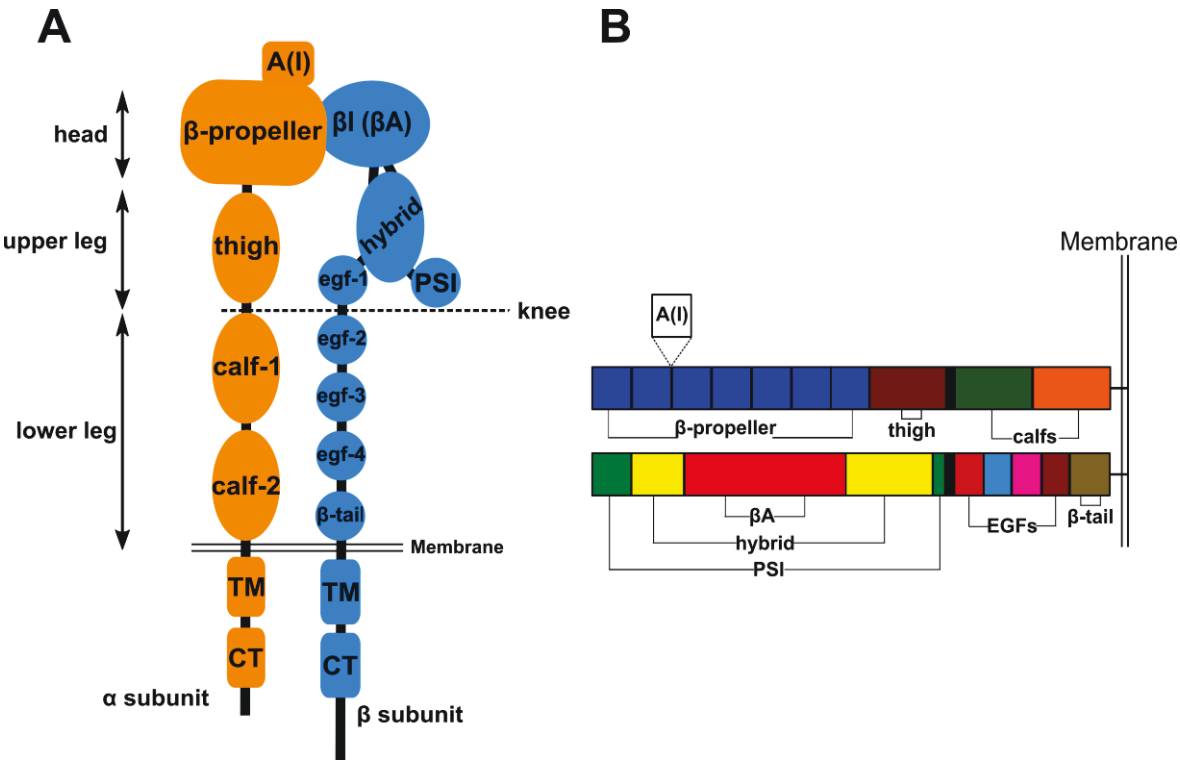

Figure 3 Schematic representation of integrin architecture. **(A)** The α-ectodomain is divided into four different domains (five domains when the A(I) domain is also expressed), while eight domains form the β-ectodomain. The knees of the protein are highlighted by a black dashed line and lie between the thigh and calf-1 domain in the α subunit, and between the PSI and egf-1/egf-2 domain in the β subunit, respectively. A double line is used to indicate the plasma membrane, spanned by the TM domains, in turn followed by the cytoplasmic tail. The N- and C- termini are labeled. **(B)** Domain organization within the ectodomain in accordance with the primary structure. Figure adapted from reference [59].

The head of integrins

The N-terminus of the α subunit consists of seven 60 amino acids long segments [59] folded into a seven-bladed β-propeller domain [25, 70, 85], with a cation-binding sequence located between repeats 4-7 [86]. Seven integrin α subunits (α_1, α_2, α_D, α_E, α_L, α_M, α_X) contain an additional domain inserted between repeats 2-3 [87, 88]. This domain is termed the "I" domain, where I stands for insertion or interaction within the β-propeller domain [54, 59].

However, it is also commonly referred to as the 'A' domain, because of its sequence homology with the A domain of von Willebrand factor (vWF) [89]. In total, this domain is formed by ~ 200 amino acids arranged in five β sheets surrounded by seven α helices [13, 37]. Its main importance is due to the fact that, when it is present, it represents the major ligand-binding site [59]. On the β subunit, the βI domain and the hybrid domain, homologous to a set immunoglobulin (Ig)-like domain, interplay together in forming the head part [90]. The former consists of 240 amino acids that pack against the β-propeller [90] and, together with the hybrid domain, buries a surface area of roughly 600 $Å^2$ [25, 91]. Interestingly, the βI domain expresses a cation ligand-binding site and is homologous to the α-like domain (reason why it is also known as βA domain) [44, 88]. The βI (βA) domain originates from a loop extending from the hybrid domain (BC loop) [44]; the hybrid domain is assembled as β-sandwich and organized in two distinct sections, with the insertion of the βI (βA) domain between them [13] (Figure 4).

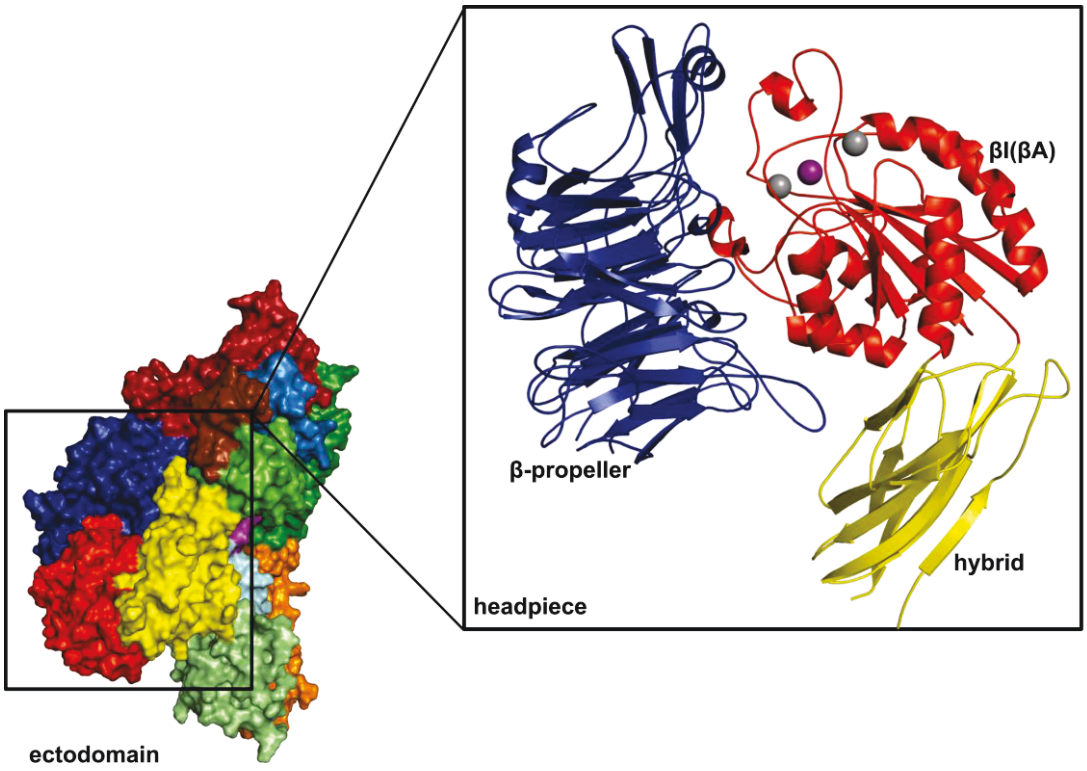

Figure 4 Integrin ectodomain structure; the headpiece. Surface representation of the ectodomain of integrin $\alpha_{IIb}\beta_3$ (PDB ID 3FCS) in the inactive state (bent conformation). The blow-up shows the three domains forming the upper section or headpiece of the protein. Domains are in cartoon representation, labeled and colored as in Figure 3B. The three metal ions forming the cation binding-site are shown as spheres (see **paragraphs 2.1.3** and **2.1.4** for further details).

For consistency with the works presented here, in the following sections I will refer to the βI (βA) domain as βA domain.

The legs of integrins

The head of integrin sits on each subunit leg [67]. These are formed by four or five different domains in the α subunit, and seven domains in the β subunit [13]. In the α subunit, the head is attached by means of a flexible linker to the thigh domain [13], which, in turn, is connected to the calf domains, termed respectively calf-1 and calf-2 domains [25, 85]. Both the thigh and calf domains are similar in structure to the Ig-like domains [25], showing the typical β-sandwich folds [13, 87]. However, integrin domains have, in general, 40-70 additional residues (each domain has usually 140-170 amino acids), thus allowing the formation of more β strands [13]. Usually, a distinction is made between the upper leg, formed by the thigh domain, and the lower leg, that contains both the calf domains [59]. These two segments of the leg are connected by a small Ca^{2+}-binding loop [59], also known as "genu" or knee of the protein [13]. This flexible linker is essential for the extension of the α subunit, as described in more detail in **paragraph 2.2.2**. In contrast, the interface between the two calf domains is large and mainly formed by hydrophobic residues [92], that confer a substantial rigidity to the lower leg section or C-terminus of the α-ectodomain [44]. Instead, the β leg shows a more complex and peculiar organization and is believed to be more flexible than the α leg [13, 25, 70]. According to the amino acids sequence, the PSI domain and not, as one would expect, the βA domain, constitutes the N-terminus of the β subunit [68] (see also figure 3A). PSI stands for plexins-semaphorins and integrins and forms a small domain of 54 amino acids [93]. The βA domain is inserted within the hybrid domain [13], which constitutes the upper leg [59]. In turn, the hybrid domain is embedded within the PSI domain [13, 59], which, accordingly, is formed by two separate segments [70, 94]. In fact, a very short segment (yet considered as PSI domain due to the presence of a well conserved disulphide bridge between this small portion and the first segment of the PSI domain [94-96]) connects the hybrid domain to the epidermal growth factor (EGF)-like domains [13, 59]. The lower β leg is formed by four EGF domains and a β-tail, which represents the C-terminus of the β ectodomain [59, 75] (see also figure 3A). According to the crystal structure of integrin $\alpha_{IIb}\beta_3$ [97], each EGF domain contains eight cysteines connected by disulphide bridges following the C1-C5, C2-C4, C3-C6, C7-C8 pattern (with the only exception of EGF-1, where the C2-C4 connection is missing) [13, 98]. The EGF-1 and EGF-2 domains

are rather disordered and of difficult resolution [44]. This explains also why both the domains were not included in the first crystal structure of integrin $\alpha_v\beta_3$ [25]. In contrast, the EGF-3 and EGF-4 domains are assembled in β-strands and have a rod-shaped like structure [26, 98, 99]. The junction between the hybrid/EGF-1 as well as between EGF-1/EGF-2 is considered flexible, while the interface between EGF-3/EGF-4 is rather stable [100]. The reason for this must be ascribed to the fact the knee, or genu, of the β subunit (geometrically placed next to the knee of the α subunit [68]) lies between the PSI/EGF-1 and EGF-2 domains [59]. Finally, the EGF-4 domain ends through a flexible linker into the β-tail domain, formed by four-stranded β-sheet and placed next to the plasma membrane [70, 92, 94] (Figure 5).

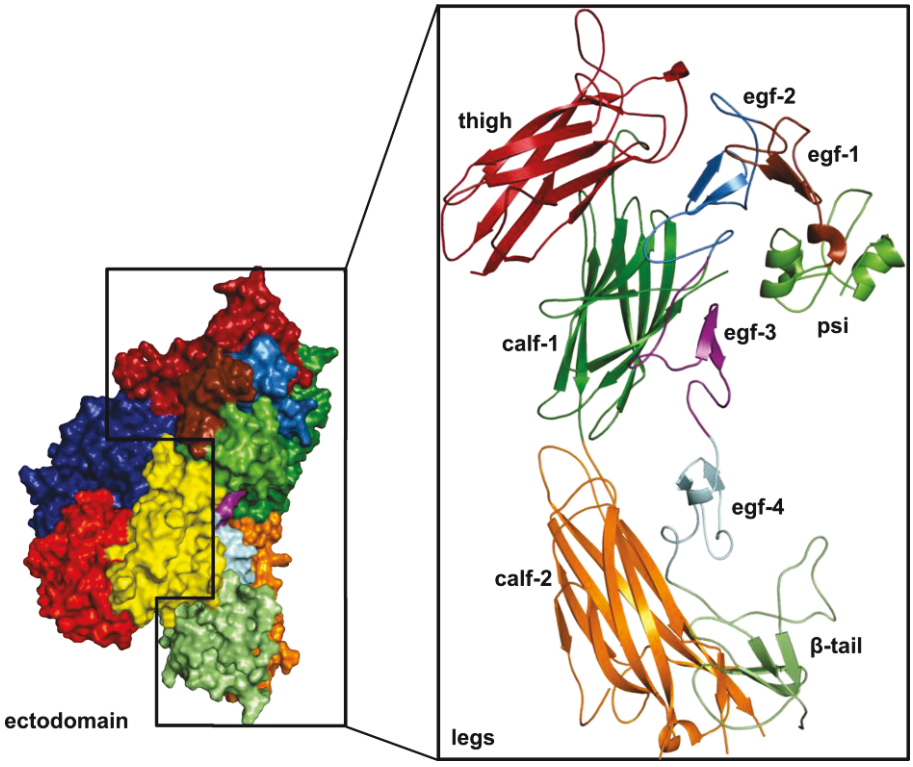

Figure 5 Integrin ectodomain structure; the legs. Surface representation of the complete ectodomain of integrin $\alpha_{IIb}\beta_3$ (PDB ID 3FCS) in the inactive state (bent conformation). The blow-up shows the nine domains forming the legs of the protein. Domains are in cartoon representation, labeled, and colored as in Figure 3B.

Transmembrane domain

With the lack of high-resolution crystal structures available in the Protein Data Bank, the only structural information relative to the transmembrane region derive from NMR experiments [101-104]. Primarily, the TMD, spanning the plasma membrane, serves as

physical linker connecting the extracellular with the intracellular environment [105]. Therefore, while the ectodomain carries the extracellular binding site, and the CT the intracellular binding site [36], the TMD represents the principal protagonist of the mechanical mechanism leading to the switch between the inactive and active state [30, 106]. A more detailed description of the role played by the TMD during activation is given in **paragraph 2.2.2**, whereas the focus here is on its structural features. In 2009, two NMR structures of the integrin α_{IIb} and β_3 TM segments helped revealing the general structure [104, 107] (Figure 6). To start, it is known that each subunit exists as a right-handed coiled coil structure arranged into two transmembrane α-helices [107]. Both helices are rather short, as they count a maximum of 20-30 amino acids each, connected at their N-terminus to the ectodomain through two flexible and unstructured linkers [104, 108]. Although there are also studies showing that the two helices can exist as two separate homomeric TM *in vitro* [109, 110], this is not the most supported view [13]. In fact, according to several different studies, including EM experiments [101], disulfide cross-linking [111], activating mutations [112], computational studies [113], and modeling studies [114-116], the two helices are predicted to associate in the inactive state [13, 107]. In particular, thanks to these studies, it was possible to unveil the specific way of packing of the two helices [13, 106]. According to the NMR structure of integrin $\alpha_{IIb}\beta_3$ TMDs [104], the α_{IIb} TM segment is slightly shorter than the β_3 TM segment; 24 against 30 amino acids [104]. Furthermore, while the α_{IIb} TM segment is oriented straight through the membrane, the β_3 TM segments is tilted inside the membrane [104]. This way, the two segments cross each other, with a measured crossing angle of 25-30° [107, 117]. The NMR structure also revealed the presence of a GXXXG-like motif in the α_{IIb} subunit [6], which represents a highly overexpressed dimerization motif in the TM domains of membrane proteins [118]. Gly residues were also found in the counter part of the β_3 TM segment so that the existence of an interacting interface was first established [6]. A role of primary mediators of the helix packing for these Gly residues was then further confirmed by mutational studies [119], disulphide scanning experiments [41] and a Leu scanning experiment [41]. Mutating Gly on both subunits with different residues, including bulky residues, has been shown to prevent correct helix packing and abolish helix association [6]. To highlight the importance of this interface, it was named the outer membrane clasp (OMC) [104]. Another highly conserved dimerization motif formed by five consecutive Gly-Phe-Phe-Lys-Arg (GFFKR) amino acids was also found in the membrane-proximal region of the α_{IIb} subunit [120]. In particular the two Phe residues are expressed in all the α subunit [6]. The crucial role of these conserved dimerization motifs has been established by

mutational studies, showing that a modification in either of them, with no differences between the two subunits, results in a constitutive activation of integrin [121-123]. This interacting interface at the membrane-proximal region was for consistency termed the inner membrane clasp (IMC) [104]. Interestingly, two charged residues are also present in the immediate proximity of the IMC; the α subunit carries an Arg (Arg^{995} in α_{IIb}), which interacts with an Asp from the β subunit (Asp^{723} in β_3) [121]. The resulting interaction has been extensively investigated, and the majority of the studies consider it of crucial importance in stabilizing the IMC and preventing helix dissociation [36, 124-126].

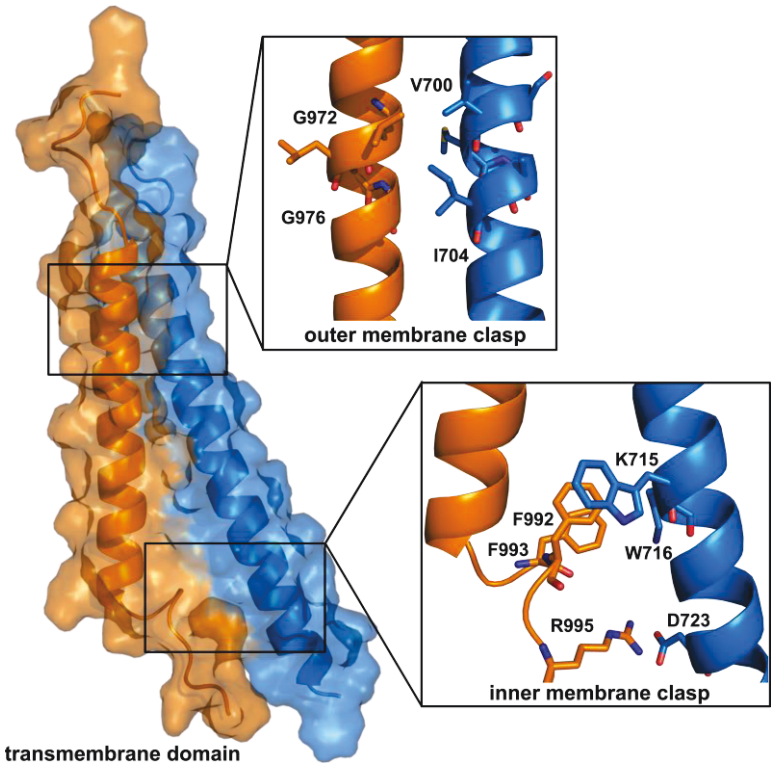

Figure 6 Integrin transmembrane domain. NMR structure of α_{IIb} (orange) and β_3 (blue) TMDs in surface and cartoon drawing (PDB ID 2K9J). Close-up views illustrate the OMC and IMC, whose key residues are labeled and depicted as sticks.

Cytoplasmic domain

A number of amino acids ranging from 10 to 70 forms the short cytoplasmic domain of integrins, more often simply indicated as cytoplasmic tail [127]. Rather flexible, the cytoplasmic tails are mainly unstructured [13], and only NMR data of integrin $\alpha_{IIb}\beta_3$ CT is available [36, 124, 128]. This portion of integrin has not been considered in my studies and

therefore it is not discussed in this thesis. A more detailed description of it can be found elsewhere by others [129-131].

2.1.3 Extracellular ligand binding site

The extracellular ligand-binding site lies at the interface formed between the β-propeller and the βA domain [61], with the α subunit playing the major role in determining the ligand specificity [56]. This is simply evidenced by the fact that there are more α than β subunits, and integrins sharing the same β subunit bind different ligands [55]. The central feature of the ligand-binding site is the presence of three divalent cations [60] (generally a central Mg^{2+} flanked by two Ca^{2+} cations [13]), which enhance the affinity for ligands, discriminate among different ligands and/or block the ligand-binding event itself [132]. It is now well established that, when expressed, the additional α-I domain represents the major binding site [133] with the interplay of the close β-propeller domain [134, 135]. However, since the binding pocket is shared with the βA domain, conformational changes triggered by the ligand-binding event irradiate from the α-I domain to the βA and hybrid domain, down to the entire structure [59] (see also **paragraph 2.2.2**). The structure of the α-I domain has been elucidated by crystallographic and NMR studies [90, 136-139]. It adopts the dinucleotide-binding (Rossmann) fold, with seven helices to surround five central β-sheets [44, 56]. However, this domain is only expressed in few integrins, yet all integrins are able to bind extracellular ligands [44]. In fact, while not all the α subunits express the α-I domain, all the β subunits have the βA domain showing the same dinucleotide-binding (Rossmann) fold [88], with the addition of two segments, which account for ligand specificity and mediate the heterodimer assembly [44, 59]. The core of the mechanism of binding has been unveiled for the first time in 1995 by two distinct studies [90, 140]. In a rather concise description of their major findings, the authors discovered that i) the α-I domain includes a Mg^{2+} coordination site that was named “metal-ion-dependent adhesive site” (MIDAS) [60]; ii) alterations of the MIDAS motif can inhibit the binding event; iii) two crystal structures grown in either the presence of Mg^{2+} or Mn^{2+} differ greatly.

Since in my studies I focused only on integrins lacking the α-I domain, here I discuss the mechanism of binding mediated by the βA domain.

Biochemical [141-144] and EM [77] studies led to the observation that the interface between the β-propeller and βA domain encloses the ligand-binding site pocket [44]. Interesting, a MIDAS motif, all in all equivalent to the one found in the α-I domain [60], is also included

in the βA domain [59]. Broadly speaking, negatively charged residues, projecting from three surface loops, coordinate the divalent Mg^{2+} ion of the MIDAS [70, 97]. The first loop has an Asp-X-Ser-X-Ser motif, the second one a conserved Glu residue, and the third one an Asp residue [44, 145]. In the absence of the ligand, the metal ion is located in the "site adjacent to MIDAS" or ADMIDAS [60]. The most likely explanation for this is that the conserved Glu protrudes its side chain towards the Asp-X-Ser-X-Ser motif, allowing a hydrogen bond interaction with the Asp and thus closing the access to the metal ion [44]. In the ADMIDAS, the coordination occurs through the carbonyl oxygen of the last Ser from the Asp-X-Ser-X-Ser motif, the side chains of Asp^{126} and Asp^{127} from the α1 helix and the carbonyl oxygen of Met^{335} expressed on the top of the α7 helix [44] (numbering in the β_3 subunit). This way, the ADMIDAS metal ion creates a link between these two α helices within the βA domain [75], whose importance in the mechanism of activation is discussed in **paragraph 2.2.2**. In the presence of the ligand, the conserved Glu is now reoriented to free the access of the metal ion into the MIDAS [146], whose coordination is now mediated by the oxygen-containing side chains projecting from the Asp-X-Ser-X-Ser motif and by an Asp as replacement of Met^{335} [44]. The existence of a second metal ion site, the ADMIDAS, represents the major difference between the βA domain and α-I domain, which expresses only the MIDAS, and it is permanently occupied by a metal ion [25, 60].

Besides the MIDAS and ADMIDAS, the crystal structures also revealed the presence, roughly 6 Å away from the MIDAS, of a third metal ion site called the ligand-associated metal-binding-site or LIMBS [44]. Interestingly, all the liganded βA domains across integrins are reported to carry the LIMBS, whose coordination is mediated by the conserved Glu (as described above) implicated in blocking the access to the binding site [75]. In order to complete the picture of the binding site, one should also add that the MIDAS is believed to contain a Mg^{2+} ion, while both the ADMIDAS and LIMBS are loaded with two Ca^{2+} ions [37, 45, 95]. However, Springer *et al.* in resolving the X-ray structure of integrin $\alpha_v\beta_3$ in the absence of ligand, challenged the assumption that also the LIMBS contains a Ca^{2+} ion [60]. A similar result was also obtained in resolving the crystal structure of integrin $\alpha_{IIb}\beta_3$ [97]. Accordingly, the authors proposed to rename it with the alternative name of synergistic metal ion binding site or SyMBS [45].

2.1.4 RGD-containing ligands

Identified for the first time in fibronectin in 1984 by Pierschbacher and Ruoslahti [147], the Arg-Gly-Asp (RGD) sequence was also identified in fibronectin, vibronectin, fibrinogen and many others ECM ligands [57]. Expressed for the majority of ligands within a flexible loop region, this sequence is indicated as the major integrin ligand recognition site [56]. This feature is rather interesting, as one may argue that only one third of integrins effectively bind RGD-containing ligands [148, 149]. Nevertheless, X-ray structures of integrin $\alpha_{IIb}\beta_3$ and $\alpha_v\beta_3$ in complex with cyclic RGD peptides [25, 60, 70] revealed the core of the ligand-binding event and the structure of the ligand-binding site [37]. These structures showed that the three residues fit into a pocket created at the interface between the β-propeller and βA domain [75]. Here, the RGD peptide is oriented such that the first (basic) amino acid points towards the α subunit, whereas the last (acidic) amino acid faces the β subunit. [13]. Arg (R of **R**GD) places its side chain into a crevice created by a loop between blades 2 and 3 (D3A3 loop) and a loop between blades 3 and 4 (D4A4 loop) within the β-propeller domain [44]. Instead, Asp (D of RG**D**) orients its carboxylate group into a groove formed by two loops (A'α1 and C'α3 loops) within the βA domain [44]. Furthermore, it also directly coordinates the MIDAS metal ion. Comparison of the liganded and unliganded head led to the observation that the most remarkable differences occur in the βA domain [59, 150]. RGD binding is initially accompanied by a movement of the β1-α1 and β6-α7 loops, coupled to a subsequent rearrangement of the α1- and α7- helices [59, 70] (Figure 7). In an allosteric manner, ligand binding causes a lateral shift of the β6-α7 loop, such that the coordination of the ADMIDAS by the Met^{335} is lost [44, 151]. Interestingly, in both crystal structures of integrin $\alpha_{IIb}\beta_3$ and $\alpha_v\beta_3$, this event yields to the same consequences; the ADMIDAS metal ion can no longer link the α1 and α7 helices and it is shifted in its position by about ~ 4 Å [25, 60, 70, 151]. In parallel, the β1-α1 loop, which coordinates both the MIDAS and ADMIDAS, is also pushed inwards and its motion has been associated to a complete reorganization of the entire ligand-binding site [146].

In summary, upon binding, the MIDAS, directly interacting with the Asp from the ligand (RG**D**), becomes the major binding site; the ADMIDAS, whose coordination is altered in the presence or absence of the ligand, regulates the ligand-binding event. Finally, the LIMBS or SyMBS plays a role in stabilizing the binding pocket surface [58, 97, 152].

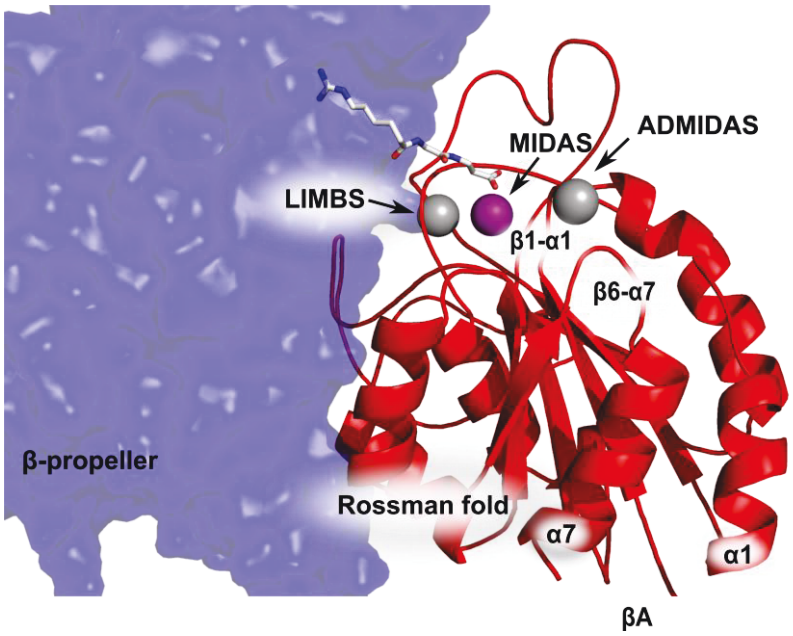

Figure 7 Structure of the βA domain in integrin $\alpha_{IIb}\beta_3$. The head of integrin, formed by the β-propeller domain (in surface representation and colored in blue) together with the βA domains (in cartoon drawing and colored in red), constitutes the ligand-binding pocket for ECM ligands. Three metal ions, which mediate the ligand binding, are located in proximity of the β1-α1 and β6-α7 loops (on the top of the βA domain). Mg^{2+} (MIDAS) and Ca^{2+} (ADMIDAS and LIMBS) are labeled and shown as purple and gray spheres, respectively. Upon binding, changes in metal coordination causes a major shift of the β1-α1, β6-α7 loops and α1/ α7 helices (highlighted in the structure). In order to depict the binding event, a fragment extracted from the antagonist Eptifibatide (in sticks representation) and bound to the head of integrin $\alpha_{IIb}\beta_3$ is used (PDB ID 2VDN).

In the previous paragraphs, I introduced the duality of integrins, as receptors existing in either an open (extended) conformation as well as in a closed (bent) conformation. Furthermore, I described integrin on a structural level in order to provide an understanding of the structural features underlying the mechanical shift between the two conformations. Finally, I discussed in atomic detail the mechanism of extracellular ligand-recognition and ligand-binding. In the following section, I will focus on how the capability of exerting their biological function is achieved by integrins through the mechanism of activation (including the regulation of the ligand-binding affinity and the large-scale structural rearrangement across the entire structure of integrin).

2.2 INTEGRIN ACTIVATION

The process of integrin activation has been described as fast (< 1 s) [75, 153], temperature-dependent [75, 154], and reversible [75, 155, 156]. It is considered to be physiologically

controlled by extracellular ligands (outside-in signaling), intracellular adaptors (inside-out signaling) and mechanical forces [6, 64, 157]. As shown in Figure 1, following the outside-in pathway, other receptors (i.e. G-protein coupled receptors) located on the cell surface send signals to the cell, which reach the cytoplasm to be then conveyed (see **Paragraph 2.2.2**) [32], following the inside-out pathway, across the receptor to the extracellular binding site [13]. Several studies confirmed that integrins in the bent conformation have low affinity for ligands, whereas they show high affinity when in the open conformation [28, 45, 81, 158, 159]. The most recent measurements done at the time of writing this thesis, revealed an increase of the affinity for the ligands of ~ 4000-fold in the extended conformation compared to the closed one [32, 61, 84]. In this sense, the usual paradigm for allostery, according to which an allosteric protein exists only in two mutual exclusive states, an open state where the binding event is possible, and a closed state, where no binding can occur seems to be applicable also to integrin [88]. However, there are also several lines of evidence that speak against the existence of a 1:1 model. To cite a few, these include crystal structures and EM images of integrin $\alpha_v\beta_3$ in complex with ligands despite being bent [60, 74]; fluorescence resonance energy transfer (FRET) experiments [160-162] that failed in detecting an increase corresponding to a full extension of the structure, but rather suggested a partial unbending. In a rather provocative way, Askari *et al.* [39] raised doubts posing the question whether "is bent integrin inactive?" However, up to now, the most supported view remains similar to the model proposed by Mould already in 1996 [88] (Figure 8).

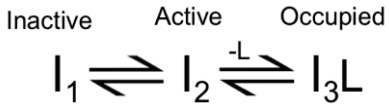

Figure 8 Allosteric model proposed by Mould in 1996 for integrins. According to the model, there are three different states, all in equilibrium between each other (double arrows). From the left to the right, it can be distinguished the "inactive" state (I_1) that prevents any possible ligand binding event, followed by an "active" state (I_2), in which the binding site is open, that precedes the effective binding of the ligand (I_3L). Figure adapted from reference [163].

Accordingly, it is thought that integrins in being allosteric proteins, adopt three conformational states: bent-closed, extended-closed, and extended-open [32, 39, 59, 164]. However, the uncertainty remains, as for the belief that next to these three defined states, integrin is likely to adopt a wide range of unknown, intermediate states, all in equilibrium among each other [92, 157].

2.2.1 Model of activation

Since it has been demonstrated that integrin function depends on the transition between the two states [25, 165], several groups have concentrates their efforts on understanding the pathway of these conformational changes occurring upon activation. As introduced previously, the majority of the crystal structures available today show the integrin ectodomain in a V-shaped conformation [25, 45, 166], in which the head is oriented towards the membrane, thereby blocking the access to the binding site [13]. However, the point of bending lies in the knee region, which is judged as a region of high flexibility [167], and, as such, allows the opening of the structure as if the protein would take a 'breath' [89, 98]. In the attempt to describe the underlying mechanism of integrin activation, two main models have been proposed. The first one is known as the "switchblade" model [98], due to the fact that the process of activation is described as a consequence of a switchblade-like rearrangement of the entire structure [45, 98, 153, 158]. This way, in response to the binding of specific cytoskeletal ligands, the CT and TMDs separate in a scissor-like manner, thus causing a jackknife-like leg separation at their knees [45, 168]. This, in turn, allows the opening up movement of the headpiece with the swing out movement of the hybrid domain and enables the access to the extracellular binding site [25, 70]. The second model, proposed by Arnaout *et al.* [75] provides an alternative explanation of the opening mechanism. The authors called it the "deadbolt" model due to the presence of a loop, projecting from the β-tail domain towards the βA domain, able to lock integrins in the inactive conformation. However, even though it is still a matter of debate to what extent the hybrid domain moves away from the βA domain [70, 80, 169], there is a general agreement in considering this movement as the key step in going from the inactive to the active state [111, 151, 170, 171].

2.2.2 Mechanism of activation

Outside-in signaling

The structural reorganization of the β-propeller/βA interface upon ligand-binding represents only the first of the conformational changes occurring upon activation [92] (Figure 9). EM studies [28] conducted in the presence of ligands [172] or activation epitopes [45, 89] showed the occurrence of large scale structural rearrangements upon activation [23]. In order to give an idea of the magnitude of the movement, the transition between the two states has an extension of more than 130 Å [157]. This is prompted by the change of the angle at the

knees (also termed the hinge angle), which drives the opening of the interface between the head and the upper legs [111, 151, 170, 171]. Even though the amplitude of the hybrid domain swinging out movement is still a matter of debate [70, 80, 169], mutational studies and monoclonal-antibody experiments provided evidences of an increase of the βA/hybrid domain interface during the transition between the two states [170, 171, 173]. Also MD simulations of the β_3 integrin headpiece helped shedding light on the pathway of conformational changes between the two states at the atomistic level [151]. As such, despite some controversial that are still existing, the essential core of the allosteric mechanism of integrin activation has been defined [39, 70, 174]; the outswing movement of the hybrid domain, causing its physical separation from the βA domain, is the central event in going from the bent to the open conformation [39, 45, 70, 169]. As pointed out previously, upon ligand binding, a lateral shift of the β6-α7 loops promotes a movement of both the α1 and α7 helices [70, 119]. This is of particular importance if one considers that the α7 helix serves as a linker connecting the βA domain with the hybrid domain [92]. It has been proposed that a similar movement occurs in both the α-I domain and βA domain; as consequence of the lateral shift of the β6-α7 loop, the α1 helix straightens [175], while the C-terminus of the α7 helix is pushed down by about 7 Å [30, 70, 94]. This movement drives a rearrangement of the interdomain βA/hybrid interface, allowing the outward swing movement of the hybrid and PSI domains from the head of the protein [70]. In this context, both EM images and crystallographic structures agree in showing an increase of 60° of the hinge angle [29].

However, although the β-propeller/βA domain rearrangement following the movements of the β6-α7 loop is incontrovertible [176-178], the authors of the deadbolt model provided an alternative explanation of the underlying causes [75]. They observed that in the unliganded crystal structure of integrin $\alpha_v\beta_3$ [25], the β6-α7 loop contacts the CD loop belonging to the β-tail, thus creating an interacting surface between the βA domain and β-tail. Hence, the authors proposed that the CD loop acts a regulator that, through the proposed deadbolt mechanism, prevents the movement of the β6-α7 loop and *de facto* locks the βA domain in a inactive conformation [75]. However, in both cases, as revealed by EM images of integrin $\alpha_{IIb}\beta_3$ in the active state [70, 73], the direct outward movement of the hybrid domain [100] leads to displacement of the PSI domain, which triggers a 70 Å separation at the knees of the two legs [70].

Interestingly, it has been shown that the addition of disulphide bonds preventing the lower legs separation has a negative impact on the whole activation process [28]. As such, also the PSI domain is believed to be an active protagonist of the process of integrin activation [94].

From a functional perspective, this is due to the fact that a ligand-inducible metal binding site (LIMBS), which serves as binding site for the activation-sensitive monoclonal antibody AP5 [179], is expressed at the N-terminus of the PSI domain [180]. From a structural perspective, the bending region corresponds to the area of contact between the PSI and EGF-1/EGF-2 domains [181]. In light of this, the displacement of the PSI domain following the hybrid domain upon integrin activation has been proposed to be required to convey the conformational changes from the extracellular binding site down to CT [70].

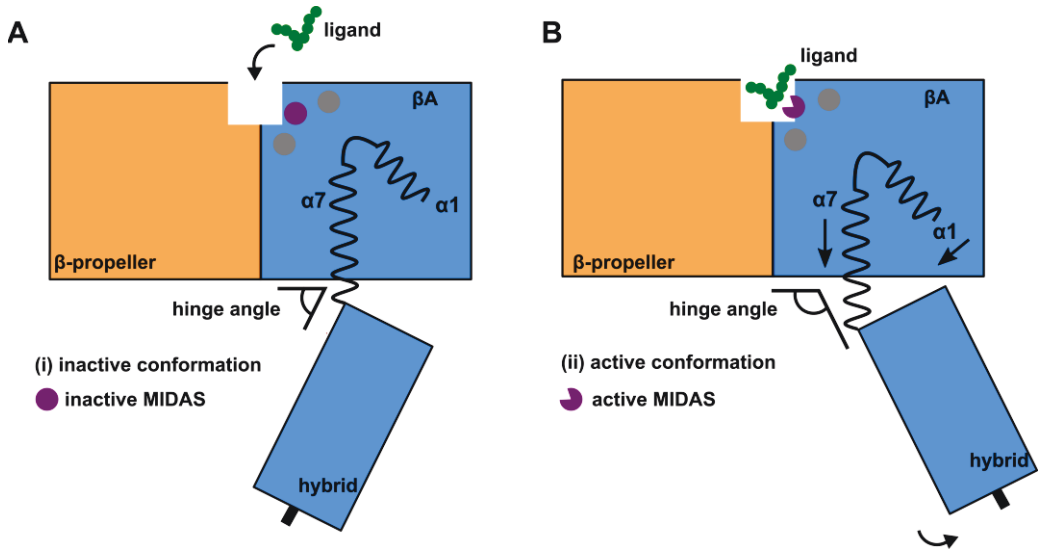

Figure 9 Structural rearrangement of the ectodomain leading to activation. Simplified representation of the headpiece of an integrin receptor lacking the A domain. In the inactive state (**A**), the ligand cannot enter the binding pocket and be coordinated by the MIDAS (highlighted in purple). Upon ligand-binding, the switch to the active state (**B**) is accompanied by movements of the α1 helix and α7 helix, which lead to an increase of the interdomain βA/hybrid hinge angle, thus enabling the outswing movement of the hybrid domain.

An interesting aspect is that the consequences of ligand-binding are (initially) limited to the β subunit [32]. Secondly, that these changes can be quantified in a ~ 2 Å rearrangement within the extracellular binding site, which, nevertheless, result in a ~70 Å separation of the legs at the integrin knee [32] (Figure 10). This is ascribed to the fact that the βA domain is inserted within the hybrid domain, which is, in turn, embedded within the PSI domain in connecting the headpiece with the lower leg. As such, the previously described changes within the βA domain (see **paragraph 2.1.3**), considered to be the fulcra of the allosteric shift from the bent to the open conformation [58], are accompanied and amplified by movement of the hybrid and PSI domains leading to the separation at at the integrin knee.

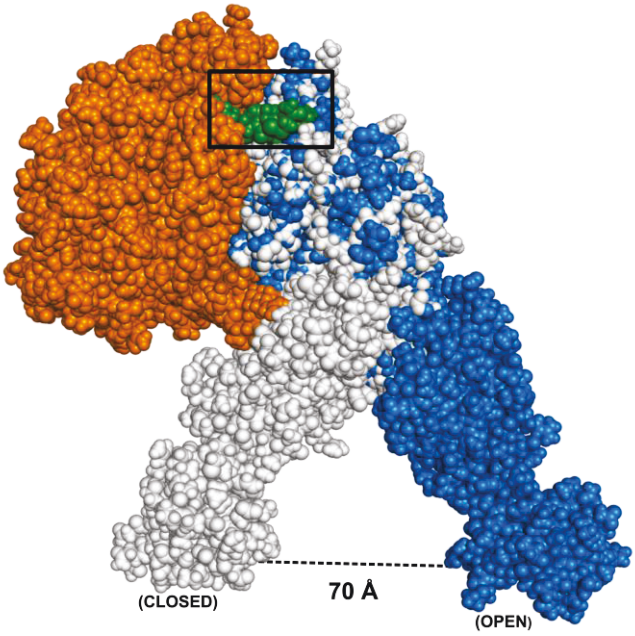

Figure 10 β-leg rearrangement linked to ligand binding. Superimposition of the integrin $\alpha_{IIb}\beta_3$ headpiece in the open conformation (white spheres) and bound to the antagonist Eptifibatide (green spheres) (PDB ID 2VDN) onto the integrin $\alpha_{IIb}\beta_3$ headpiece in the closed conformation (PDB ID 3FCS). A black dashed line highlights the magnitude of separation at the integrin β knee during the transition between the two conformations.

Inside-out signaling

There is a general agreement in considering the two TMD as associated in the inactive state [101, 114], and fully dissociated in the active state [182-184]. As such, the mechanism of integrin activation also implies a reversible clasping/unclasping mechanism of the two TM segments, which controls the shift between the clasped (inactive) and unclasped (active) state [69] (see **Paragraph 2.1.1**). There are two main models describing the way of TMD separation occurs [106]. In the 'scissor-like' model, the separation between TM segments is a consequence of scissor-like movements [40, 109], although the amplitude of this separation is still debated [37, 66, 156]. This is because if one places the hinge point in proximity of the extracellular binding site, the degree of separation is necessarily much larger than placing it within the TMD (Figure 11). Alternatively, it has been proposed that the TMD separation occurs following vertical, or piston-like, movements of the TM segments, which cause a shift of the two legs [74].

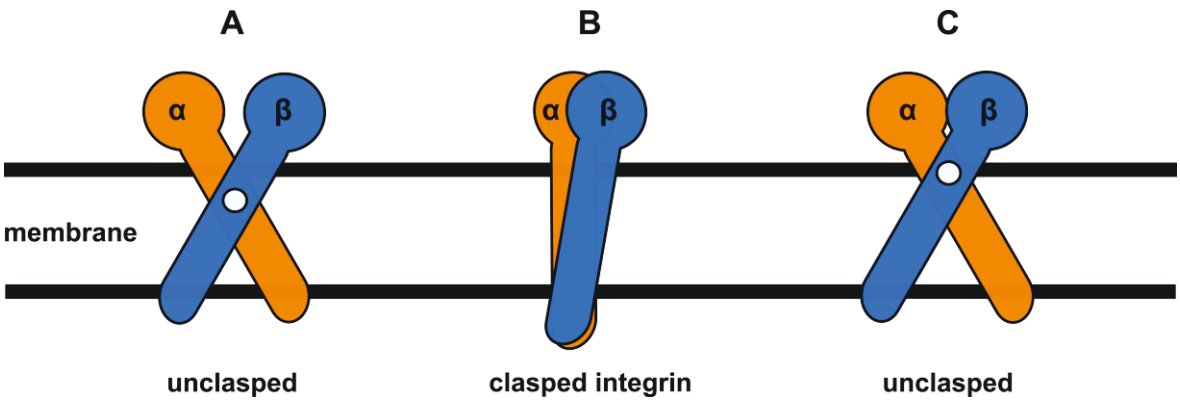

Figure 11 Scissor-like TMD separation. Two different models have been proposed to describe the scissor-like separation of the TMD. In the inactive state, the two TM segments are clasped and the association is preserved (**B**). According to the model in (**A**), the hinge point is found in the TMD region, while according to the model in (**C**), its position is much closer to the head. Figure adapted from reference [185].

2.3 PLATELET INTEGRINS

Integrin $\alpha_{IIb}\beta_3$, together with the isoform $\alpha_v\beta_3$ forms the β_3 subfamily of integrins [30]. The two members share the same β_3 subunit, but only 36% of sequence similarity with respect to the α subunit [186]. Both isoforms are expressed on platelets [141, 187]. However, integrin $\alpha_{IIb}\beta_3$ has been reported to be present only on platelets, megakaryocites [188], mast cells, basophils, and some tumors [92, 189-192], while integrin $\alpha_v\beta_3$ is found in multiple cell types [92, 193-195]. Integrin $\alpha_{IIb}\beta_3$ is usually referred to as the major plasma membrane protein, with approximately 80,000 to 100,000 copies per cell [196]. Alternatively, this means that 3% of the total number of proteins expressed on platelets and 17% of the platelet membrane protein mass is due to integrin $\alpha_{IIb}\beta_3$ [197]. As for the function, while the contribution of integrin $\alpha_v\beta_3$ to platelet's adhesion and aggregation is uncertain [198], integrin $\alpha_{IIb}\beta_3$ represents the principal modulator of platelet aggregation [199, 200]. Upon activation, integrin $\alpha_{IIb}\beta_3$ can bind effectively fibrinogen, von Willebrand factor (vWF), vibronectin, and fibronectin [29, 201, 202]. These are all ligands that, due to their specific capability of cross-bridging platelets together [203], are considered essential in orchestrating the process of platelet aggregation [186]. Besides integrin $\alpha_{IIb}\beta_3$ and $\alpha_v\beta_3$, platelets contain also three isoforms belonging to the β_1 subfamily and being responsible for the adhesion to the ECM proteins, such as collagen, fibronectin, and laminin [29]. Among them, there is the $\alpha_5\beta_1$ isoform, which is primarily known as the receptor for fibronectin (Fn) [80] and, as such, fundamental for cell generation and tissue development [204]. In fact, as a result of binding,

Fn fibril formation and the ECM assembly can take place [205]. Integrin $\alpha_5\beta_1$ binds to Fn through the RGD sequence, and this ligand-binding event is considered to be the prototype of integrin-ligand association [206, 207]. Interestingly, a lack of either integrin $\alpha_5\beta_1$ or Fn has been reported to lead to early embryonic mortality [208-210].

2.3.1 Integrin $\alpha_{IIb}\beta_3$ as therapeutic target

Since its essential role in orchestrating the process of platelet aggregation, a central feature of hemostasis and thrombosis [69], already in the early 1990s, integrin $\alpha_{IIb}\beta_3$ has been proposed as the ideal target for antithrombotic therapy [21]. The physiological hemostatic response of the human body is dependent on platelets that maintain and preserve the vascular integrity in case of uncontrolled bleeding following an injury [211, 212]. In fact, platelet aggregation leads to platelet-induced thrombus formation [21], which creates a physical obstacle to the life-threating loss of blood [92]. In contrast, an alteration of the normal platelet physiology, leads to severe vascular consequences, including cardiovascular diseases (i.e. stroke and myocardial infarction) [211], pathological thrombus formation [213, 214], atherosclerosis [215], but also inflammation [216, 217], immune response [17], and cerebral dysfunction (i.e. Alzheimer's disease (AD) [18]). Due to its role in mediating platelet aggregation and localization in the blood stream [29], integrin $\alpha_{IIb}\beta_3$ are expressed in their inactive state on the surface of platelets [8]. The shift to the active state occurs as culmination of the inside-out signaling process, triggered by the binding of agonists and intracellular ligands to the CT [92], which prompt the transmission of the allostery resulting in the opening of the extracellular binding site [32] (see **paragraph 2.2**). Once in the active form, integrin $\alpha_{IIb}\beta_3$ can bind to fibrinogen and vWF [201, 202], which create intracellular bridges between platelets [29, 69], and lead to thrombus formation [92]. As such, once it became clear that blocking integrin $\alpha_{IIb}\beta_3$ prevents platelet aggregation and thrombus formation, the bases for a successful antithrombotic strategy were laid [21]. Several integrin $\alpha_{IIb}\beta_3$ antagonists were identified and three of them — abciximab, eptifibatide, and tirofiban — were approved by the Food and Drug Administration (FDA) becoming drugs widely applied in the clinical practice [21]. Although the use of these antagonists has then decreased in the mid-2000s, the inhibition of platelet aggregation has remained a hallmark of the antithrombotic strategy [21].

In addition, a connection between vascular diseases and neurodegenerative disorders has started becoming more and more evident, and an involvement of platelets in the development

of Parkinson's disease [19], schizophrenia [20] and AD [18] has been established. As a consequence, the possibility of expanding the use of antiplatelet drugs has started to emerge as an attractive strategy in preventing or treating neurodegenerative disorders [27].

2.3.2 Integrin $\alpha_{IIb}\beta_3$ as new target in the treatment of Alzheimer's disease

Deposits of insoluble amyloid fibrils forming amyloid plaques have been linked to the pathogenesis of Alzheimer's disease [218, 219]. Under physiological conditions, amyloid β (Aβ) peptides are expressed as nontoxic soluble peptides [220]. In Alzheimer's disease, Aβ peptides form aggregates or neurotoxic fibrils [219, 221, 222]. They are difficult to degrade, and pile up to form stable fibers [223]. The Aβ peptide originates from a large amyloid precursor protein (APP) [218], and the process of amyloid formation (also known as amyloidosis) has been quite well characterized: first, APP is cleaved by a β-secretase and released as soluble APP which, in turn, is rapidly cleaved by a γ-secretase and generates the Aβ peptide [224]. Based on the number of residues, Aβ peptides can be distinguished into two forms, the $A\beta_{40}$ peptide (cut at position 40), which is also the most abundant form, and $A\beta_{42}$ peptide (cut at position 42) [219, 224]. Platelets express high levels of APP and are able to convert APP proteins into an Aβ peptide [18, 225]. An alteration occurring during the process of Aβ formation from APP is expected to be the origin of neurotoxic Aβ aggregates [226]. While it is widely accepted that the presence of amyloid fibrils drives the development of AD [224], it is instead not completely clear the factors causing the Aβ deposition [27] (Figure 12).

Interestingly, deposits of Aβ peptide are not just found in brain parenchyma, but also in cerebral blood vessels referring to a pathological condition also known as cerebral amyloid angiopathy (CAA) [227]. CAA is responsible for bleeding in the brain, as a direct consequence of the damage of the walls of the blood vessels [228]. As such, CAA is considered an active protagonist of Alzheimer's disease [227, 228], and different studies support the existence of a link connecting vascular diseases with the progression of neurodegenerative disorders [18-20, 229]. Since platelets contain APP in high concentration, the presence of Aβ peptide in the blood stream directly depends on platelets [230-232]. Likewise, the conversion of soluble Aβ peptide into fibrillary Aβ aggregates is driven by platelets [27]. Aβ peptide is, together with fibrinogen, von Willebrand factor, and vibronectin among the variety of ligands that bind to integrin $\alpha_{IIb}\beta_3$ [233]. Interestingly, Aβ peptide is not an RGD-containing peptide as the aforementioned ligands, but it contains an RHD

sequence [234]. It has been suggested that ligands that contain an RHD sequence can bind to integrin in a way that closely resembles the RGD-dependent motif (see **paragraph 2.1.4**) [234]. To the best of my knowledge, it was still uncertain whether $A\beta_{40}$ peptide binds to integrin $\alpha_{IIb}\beta_3$ in the same manner as fibrinogen does [147]. However, as the involvement of platelets in the progression of AD has been established, interfering with integrin $\alpha_{IIb}\beta_3$ activity through the use of antiplatelet drugs has started emerging as an exciting therapeutic strategy [235]. The importance of understanding the underlying mechanism of $A\beta_{40}$ binding to integrin $\alpha_{IIb}\beta_3$ in atomic detail and, hence, to provide insights into the structural mechanisms of integrin activation laid the basis for the work presented in **section 4**.

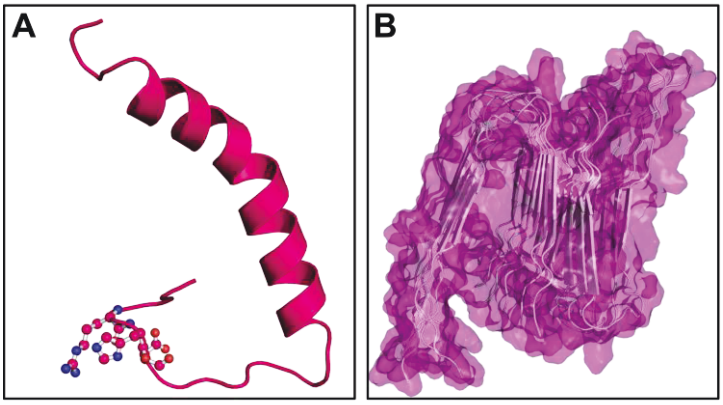

Figure 12 $A\beta_{1\text{-}40}$ peptide. (**A**) NMR structure of a soluble $A\beta_{40}$ peptide resolved in a water-micelle environment (PDB ID 1BA4). The cartoon drawing representation shows the helical nature of the peptide, and the RHD binding sequence is highlighted in ball and sticks representation. (**B**) NMR structure of $A\beta_{40}$ peptide forming neurotoxic aggregates of fibrils with two-fold symmetry, shown in cartoon drawing and surface representation (PDB ID 2LMN).

2.3.3 Integrin $\alpha_{IIb}\beta_3$ is the carrier of the HPA polymorphism

Polymorphisms are genetic alterations of the DNA [196], which do not initiate a pathological condition on their own, but they can affect the physiological functionality when in concert with other risk factors, i.e. age, blood pressure, and cigarette smoking [236]. The human platelet antigen (HPA)-1 or PI^A was found on the β_3 subunit of integrins and is believed to be involved in the syndrome of immune-mediated platelet destruction [94]. The HPA-1 polymorphism arises from a thymidine→cytosine nucleotide substitution at position 1565 in exon 2 of the β_3 gene [237] resulting in a leucine→proline exchange at position 33 of the β_3 leg [196]. Hence, from a structural perspective, it means that this amino acid exchange is located within the PSI domain [94]. As a consequence of this polymorphism, two different genotypes exist; the Leu33 (HPA-1a) platelets, and the Pro33 (HPA-1b) platelets [238]. Interestingly, the presence of Pro33 (HPA-1b) platelets is not rare, as ~ 25% of northern

Europeans are estimated to carry, at least, on allele [196]. However, despite of its high frequency among the population and several studies carried out since the mid-1990s [196], conflicting results have prevented a general agreement on the consequences of this polymorphism on a clinical level. In 1996, Weiss *et al.* [239] reported the first clinical observations suggesting a correlation between the expression of the Pro33 (HPA-1b) allele with an increased occurrence of episodes of myocardial infarction. Later studies also confirmed it, thus supporting the association of Pro33 (HPA-1b) platelets with premature myocardial infarction [240, 241]. Similarly, other clinical studies showed the correlation of this polymorphic allele with an increased risk for coronary artery disease leading to thrombosis [196]. Interestingly, these studies were directly challenged by another study [242], whose conclusions spoke against a correlation between Pro33 (HPA-1b) platelets and vascular disorders. Part of the work is grounded on clinical studies showing the association of HPA-1b platelets with premature myocardial infarction [240] and altered thrombi formation [243]. Evidences that have contributed to the idea of the HPA-1b platelets as a prothrombotic variant [238]. If one looks at this polymorphism from a structural prospective, a leucine amino acid, with its long, hydrophobic side chain is replaced by a conformationally restricted amino acid, such as proline [244]. Moreover, as stated above, this polymorphism is located within the PSI domain, which, together with the EGF-1 and EGF-2 domains, constitutes the β_3-knee (Figure 13) [94]. Activating substitutions have been already identified within the PSI domain [245]. Likewise, an active role played by the PSI-EGF/-EGF/2 domains in restraining integrins has been hypothesized [94]. In light of this, a molecular investigation of the HPA-1 polymorphism has been considered useful in helping our understanding of the phenomenon itself [94]. The aim of the work presented in **section 5** is to investigate whether this amino acid exchange impacts the stability at the β_3-knee and, through a modification of the PSI-EGF/-EGF/2 interface [70, 94], promotes integrin activation and thereby supports the notion of prothrombotic HPA-1b variant.

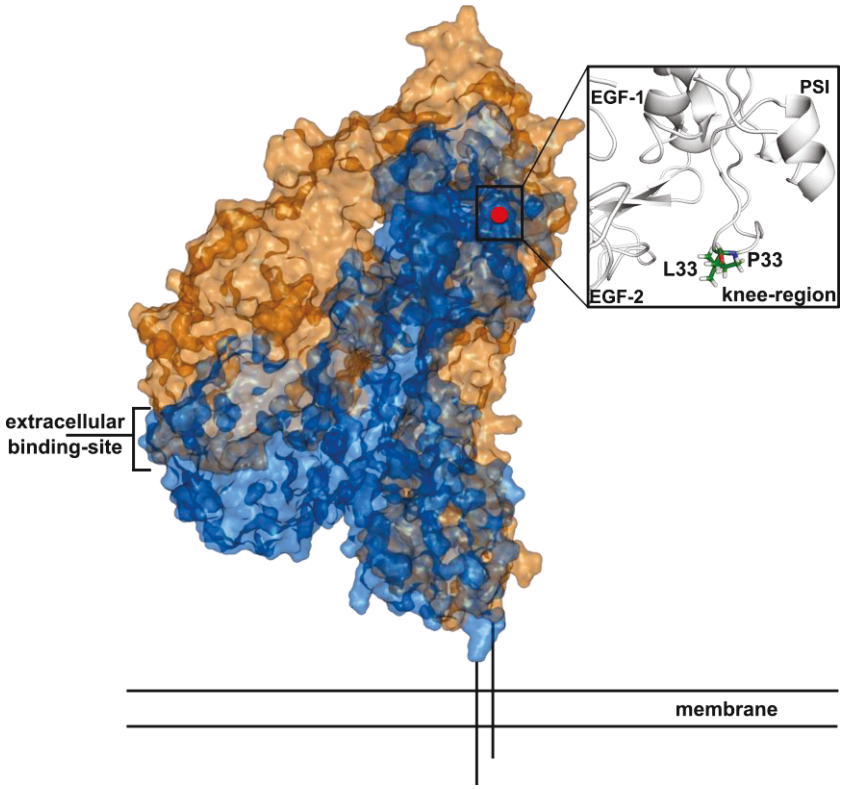

Figure 13 The HPA-1 polymorphism of the integrin $\alpha_{IIb}\beta_3$ arises from a Leu→Pro exchange at residue 33. The position of the HPA-1 polymorphism is highlighted by a red dot on the crystal structure of integrin $\alpha_{IIb}\beta_3$ (PDB ID 3FCS), depicted in surface representation, Residue 33 is > 80 Å away from both the extracellular binding site and the transmembrane domain. Close-up view of the box content shows the Leu→Pro exchange at the knee region, formed at the interface between the PSI domain and the EGF-1/EGF-2 domains.

2.3.4 Do platelet integrins get activated in the same way?

I would like to conclude this first part of my thesis regarding the biology of integrins by introducing one more aspect that has recently become an important object of study. Thus far, I discussed the mechanism of activation as if it would apply for all integrin members without distinction. However, albeit its underlying general core is unified, integrins are known to have different activation set points [84], as well as different basal activities [246]. Interestingly, also members of the same subfamily have been shown to be greatly different among each other. For example, integrin $\alpha_{IIb}\beta_3$ is basally inactive, while integrin $\alpha_v\beta_3$ is partially active [39, 247]. Differences exist also among subfamilies, as integrin $\alpha_5\beta_1$ is considered basally active [84]. Currently, there is an on-going research, which is trying to correlate specific molecular features of integrin isoforms to their activation specificity. In this sense, an interesting approach is that applied by Springer and co-authors, in which an understanding of the conformational equilibrium of integrin is obtained through a quantification of thermodynamic properties and elucidation of the integrin energy landscape

[72, 83, 84, 157]. This way, after assessing the equilibrium constants of the three main conformational states of integrin, it also becomes possible to understand which state is predominant (and so the basal activity) and how much energy is required to allow the transition from one state to another [84]. Likewise, extending this type of analysis to different cell types, it becomes feasible to understand the role played by the "environment" together with the specific properties of integrins [248]; for example, to clarify why integrin $\alpha_v\beta_3$ is considered active in only determined cell types [39, 247]. The interplay between structural features, dynamics aspects, and energetics properties has represented also part of the work here presented and described in **section 6**.

2.4 COMPUTATIONAL METHODS

2.4.1 Molecular dynamics (MD) simulations

Molecular dynamics (MD) simulation is a computational technique used to explore the conformational space of molecules. This tool allows the description of the dynamic properties of molecules as function of time providing detailed information on the fluctuations and conformational changes by simulating the natural motions of the atoms in a structure. The MD method is based on the Newton's second law, or equation of motion, **F** = **ma**, where **F** is the force exerted on the particle, **m** is its mass and **a** is the acceleration [3]. MD simulations generate a sequence of points on the potential energy surface (PES) as a function of time, and the integration of the equation of motion then yields to a trajectory that describes the position, velocities and accelerations of the particles as they vary with time [249]. Thanks to the knowledge of the dynamics of a system it becomes more feasible to identify the structural key elements in all the aspects of protein functions.

Among the different computational techniques that have developed during the last decade, all-atom MD simulation has become an appreciate tool to analyze the dynamics and function of biomolecules [250]. Since the main objective of the work here presented was to understand the complex regulation of integrin in atomic detail, I also preferentially made used of all-atom MD simulations throughout my research. The contribution given by this technique in fostering our understanding in the field of the structural biology is undeniable. Likewise, computer simulations have proven to be a valid complementary method to gain insights into the structural mechanisms of integrin activation. In the following paragraph, I will describe the contribution given by this technique in investigating the behavior of integrin taking into account also the limitations and difficulties intrinsic of this method.

2.4.2 Common pitfalls in MD simulations

Size and time limitation

Thanks to the computational resources nowadays available, large biological systems and long timescale simulations are becoming a much easier problem to deal with than in the past [250, 251]. To cite a few, it was possible to simulate large macromolecular systems as the ribosome [252, 253], or entire viral capsids [254, 255]. So for integrin, taking advantage of the possibility of using the advance supercomputer Anton [256], the group of Filizola *et al.* successfully performed microseconds-long MD simulations (~ 5 μs) on a highly complex model of integrin TMD and CT in complex with cytoplasmic effectors (i.e. Talin) [257]. However, the time scale in which biological events occur, as for example the process of integrin activation (~ 1 s), is still far beyond the time scale usually reached by MD simulations (time scale of microseconds [258, 259]). In the case of integrins, this implies that the magnitude of changes that can be normally observed will be smaller than those associated to a complete extension of integrin [32]. However, these changes, albeit small, can still be indicative of an overall trend for the investigated system, as shown in two studies on integrin $\alpha_5\beta_1$ ectodomains performed by Gohlke *et al*., which were based on MD simulations of 200 ns length [175, 260]

Coarse-grained mixed models and steered MD next to all-atom models of integrins

However, to the best of my knowledge, the majority of the computational studies on integrin were performed using a multiscale MD simulation approach, combining coarse-grained (CG) MD simulations [261] with atomistic MD simulations, and through steered molecular dynamics simulations (SMD) [262]. In the former, it means that the authors preferred the possibility to run longer in time simulations over more precision, thus partly losing the atomic detail [263]. Multiscale simulations, represented the method chosen by Kalli *et al.* in studies focused on the heterodimers α/β TMD in both the presence and absence of Talin [264, 265]. In contrast, in the SMD investigations, external pulling forces are added to the system to enforce a change that potentially could spontaneously happen, but it would require much longer simulation time to be detected. To cite a few, in the case of integrin, the opening of the headpiece of integrin $\alpha_v\beta_3$ was successfully fastened through the application of ligand-binding mechanical forces [151, 172]. Similarly, in the study by Chen *et al.*, the authors were applying external forces and managed to observe the unbending of integrin $\alpha_v\beta_3$ and thus shed light on the mechanism underlying the process of integrin activation [266]. In summary,

all-atom MD simulations are computationally more expensive [267] and the system size and time-scale represent real limitations [268]; at the same time, they work as a computational microscope able to capture the atomic detail [263]. In virtue of this, all atom MD simulations are arguably the most accurate way to simulate a biomolecule [267].

Convergence and reproducibility

Convergence is used as an expression to indicate that the system will no longer change, even considering a simulation time that approaches infinity [251, 269]. As such, demonstrating the convergence of an MD simulation is essential to ensure the quality and validity of the results [269]. MD simulation is a conformational search method and, as such, it is used to sample the conformational space of a biological molecule [249]. In other words, it is used to localize energetically preferred conformations that a molecule can adopt while sampling on the energy landscape [249]. The equivalent in mathematical function is to find minima of the energy function. At this point, it is legitimate to ask how long an MD simulation is supposed to run in order to produce meaningful results [269]. However, as explained by Alan Grossfield and co-authors [251], this is all but a simple question. In fact, based on the information collected until that point, one is asked to rule out the possibility that additional transitions or states may still exist [251], i.e. the presence of an energy minimum point, in which the system resides for long time so that a particular state will be more frequently sampled [269].

RAC and KLD functions

In the work here presented, I applied the method described by Cheatham and co-authors [270] to assess the convergence of the performed MD simulations. To start, I measured the RAC, which stands for "RMS average correlation" and is an autocorrelation-like function for structural deviations (RMSD) of the system along the trajectory [270]. The underlying idea is simple and is based on deriving the average structure from the ensemble of conformations obtained during a simulation run [251]. As the sampling time increases, no large deviations are expected to be seen in the average structures that will be further generated [251]. Essentially, the RAC parameter works in the same way, as a running average structure is generated at given time frames of a single trajectory until the total simulation time is reached (Eq. 1):

$$RAC_{(\tau)} = \frac{\sum_{t=0}^{N} RMSD\big(AvgCrd(t, t+\tau)\big)}{N - \tau + 1}$$

(Eq 1)

where N is the total length of the MD simulation and τ indicates the time interval or lag. For each τ, an average structure (AvgCrd) is generated and then fit to a given reference structure, and the average RMSD of all the average structures at τ is calculated. Graphically (Figure 14), it can be seen as a curve that, while approaching zero (RMSD = 0 Å), is indicative of the absence of larger deviations in the newly generated structures as the MD simulation time increases.

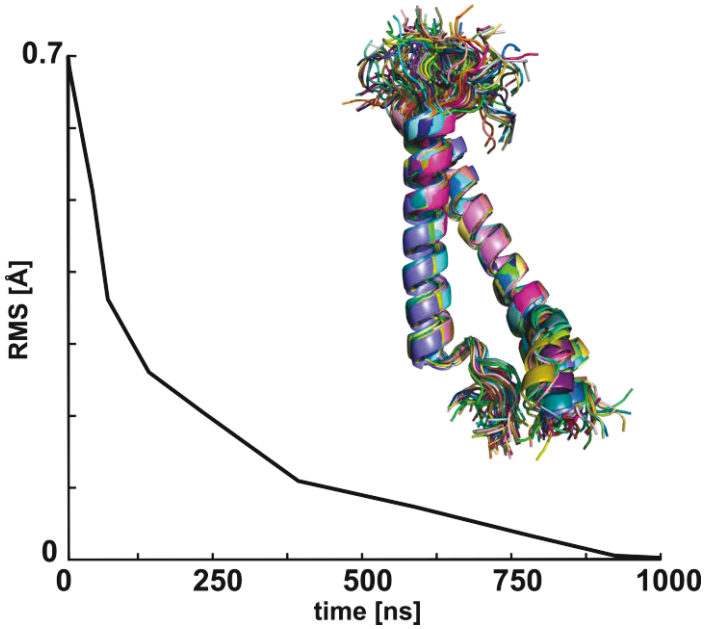

Figure 14 RAC analysis. Exemplary of RAC measurement (normalized RMS in Å, y-axis) as a function of simulation time (here 800 ns, x-axis). The curve decays towards zero as the simulation time increases, thus indicating that no further changes are expected. Within the plot, an exemplary of the overlap of running average structures of integrin $\alpha_{IIb}\beta_3$ (PDB ID: 2K9J) at consecutive intervals of time is shown.

While RAC is a way to assess convergence within one single MD simulation, it is also useful to compare how multiple MD simulations behave with respect to each other [270]. In fact, reproducibility represents the second way of testing the statistical significance and robustness of the outcomes [271]. Repeating experiments in order to replicate the results multiple times is more easily achievable in an experimental setting [251]. Replicating

microsecond-long MD simulations multiple times is still computationally very expensive and time consuming [251]. In the present work, I performed three MD simulations in each case and applied the Kullback-Leibler divergence [272], or KLD, to evaluate the convergence of each trajectory with respect to the others [270]. This method considers the structural dynamics of the system, with the internal motions described in terms of principal components (PC). The PC analysis (or PCA) is an efficient method for evaluating the atomic fluctuations [251, 273]. It is based on the diagonalization of the covariance-matrix of the internal atomic fluctuations of the system (C_{ij}), from which eigenvectors (and respective eigenvalues) are derived. The former represent the atomic displacement, while the latter indicate the magnitude of the displacement (Eq.2):

$$C_{ij} = \langle (x_i - x_i^o)(x_j - x_j^o) \rangle \qquad \text{(Eq.2)}$$

The subscript 'o' denotes equivalent atomic coordinates (x) of the reference structure, and C is the covariance matrix calculated as averaged ensemble [251]. Once the PCs are derived, it is possible to use them to calculate the KLD (Eq.3):

$$KLD(t) = \sum_{i=0}^{M} ln\left(\frac{hPC1_N(t,i)}{hPC2_N(t,i)}\right) hPC1_N(t,i) \qquad \text{(Eq.3)}$$

The underlying idea is that at each time frame (t), one takes the histogram (M defines the total number of bins) created for each trajectory of the PC projection values for a given PC (1,2 . . . N) and uses the KLD to measure the resulting overlap between the histograms [270]. From it, it is possible to estimate how well different MD simulations are convergent.

Statistical inefficiency

It is common practice to discard the initial portion of an MD simulation production run and consider it as *equilibration* (t_o) in order reduce the bias of a property ⟨A⟩ of interest caused by initial conditions (e.g., atypical starting structure) [274]. In the present work, I used the RMSD analysis of the C_α atoms to determine the portion of trajectory to be considered as equilibration. In **Publication I**, I performed all-atom MD simulations of 500 ns length, but in the analysis of the trajectories I considered the first 150 ns as equilibration and discarded this initial portion. In **Publication II**, I performed all-atom MD simulations of 1 μs length,

but in the analysis of the trajectories I considered the first 200 ns as equilibration and discarded this initial portion. I presented each measurement included in both the publications in terms of arithmetic means ± the standard error of the mean (SEM), calculated according to the law of error propagation (Eq. 4):

$$SEM_{tot} = \sqrt{SEM_1^2 + SEM_2^2 + SEM_3^2}$$

(Eq.4)

Where the subscripts i={1, 2, 3} refers to the three trajectories. However, the procedure used to calculate the SEM_i (i.e. considering N as the actual sample size) in **Publication II** received some criticism. In particular, doubts were raised with respect to the validity of the SEM_{tot} used in the statistical analyses (i.e. Student *t*-test) performed by myself; a large sample size can lead to small SEM values, thus potentially affecting the statistical significance of a measurement (e.g. in comparing a wild type system with a mutated one as it was done here). As such, in order to defend the validity of our outcomes, we decided to re-perform all the calculations through the analysis of correlation functions to obtain the decorrelation time, and from it determine the effective number of independent frames (N_{eff}) within each trajectory (N=N_{eff}). To do so, I followed the procedure described by Chodera [274, 275] and used the *detectEquilibration*() function available within the Python module *timeseries* of the *pymba*r package [274, 275]: first, the portion of trajectory considered as equilibration is discarded, and only the sample for an interval of time [t_o, T] is kept, second the statistical inefficiency (g) is used to compute the effective number of uncorrelated MD frames for the interval of time [t_o, T] [274] via (Eq.5):

$$g \equiv 1 + 2\tau_{ac}$$

(Eq.5)

Where τ_{ac} is the integrated autocorrelation time, obtained via (Eq.6):

$$\tau_{ac} \equiv \sum_{t=1}^{T-1} \left(1 - \frac{t}{T}\right) C_t$$

(Eq.6)

And C_t indicates the discrete-time fluctuation autocorrelation function calculated via (Eq.7):

$$C_t \equiv \frac{\langle a_n a_{n+t} \rangle - \langle a_n \rangle^2}{\langle a_n^2 \rangle - \langle a_n \rangle^2}$$

(Eq.7)

Where a_t corresponds to the timeseries of observations of a property <A>.

From g, I obtained the N_{eff} used for calculating the SEM$_i$ for each property <A> discussed in **Publication II** and **Publication III** via (Eq.8):

$$N_{eff} \equiv (T - t_0 + 1)/g_{t0}$$

(Eq.8)

Where N_{eff} indicates the total number of uncorrelated frames within a trajectory.

2.4.3 MD simulation and integrin- part I

Why explicit solvent model is arguably the best way to simulate integrin

Atomistic MD simulations are usually divided into two groups: those that consider the solvent explicitly (explicit-solvent models) and those that consider the solvent implicitly (implicit-solvent models) [276-278]. An analogue division exists in the case of MD simulation performed in the presence of a lipid bilayer (explicit membrane models and implicit membrane models) [267]. The former is based on the particle mesh Edwald (PME) approximation [270] to treat the solvent, and calculate explicitly the interactions between the solute and solvent atoms. Whereas, in the case of is based on the generalized Born (GB) approximation to consider the solvent as a continuum with a specific dielectric constant (ε=80) [279]. The analytical formula of the PME and GB approximation can be found elsewhere [276]. Here, I want to focus on the advantages and disadvantages of both the models. In principle, by neglecting the solvent contribution from the calculation, one would expect a valuable improvement of the algorithm speedup (efficiency) [276]. Indeed, a 2-20-fold average increase in the simulation time step for processor (CPU) time [276] has been recorded in several studies in which GB implicit simulations were compared to PME explicit simulations [280-283]. In the absence of solvent, all the potential interactions made by the solvent atoms are not counted and thus the total number of calculations performed during a run of simulation is reduced. As such, implicit models represent an appreciate method of sample of the conformational space of a molecule [280-282, 284]. As explained in better

detail in ref. [276], this is mainly due to the fact that solvent viscosity is reduced without having, in principle, any effect on the energy landscape [276]. Thus far, it sounds like the implicit models represent a rather good approximation, both in terms of accuracy and computational costs. So why do the MD simulations in the present work were all done in explicit-solvent? In answering, one has to take into account the actual system size and, with respect of it, the scaling efficiency of the PME *vs* GB models [276]. The former (in the most common form of TIP3P-PME [285]) scales as $\sim N\log N$, whereas the latter scales as $\sim n^2$, where N is the total number of solute and solvent atoms and n is only the number of solute atoms [276]. Due to the fact that n^2 grows faster than $\sim N\log N$, the algorithmic speedup of the GB model decreases with the sample size in comparison to the TIP3P-PME model. In conclusion, based on this assumption (here only briefly and yet not completely discussed), neglecting the solvent is not always and necessarily an advantage as in the case of a large biological system as integrin.

2.4.4 MD simulation and integrin- part II

Integrins belong to the class of membrane proteins. Typically, this type of protein is in charge of two main biological events, known as substrate transport and signal transduction into the cell [267]. As described in the previous paragraphs, integrins, in being signaling receptors [8], fall into the second category. Moreover, the event of signal transduction across the plasma membrane has been associated to large-scale conformational change of the membrane protein itself [286-288]. This is indeed also the case for integrin (see **paragraph 2.2**). As for the proteins, so biological membranes, in creating a barrier between the extracellular and intracellular environment, are involved in the regulation of a wide range of biological processes, including signaling [289]. Biological membranes are complex structures composed by lipids, water, protein and cholesterol [290]. A lipid molecule is formed by a hydrophilic head group attached to two hydrophobic, acyl chains. Through assembling together of a number of lipids is grounded a lipid bilayer, in which the hydrophilic heads point towards the outside, while the hydrophobic part faces the interior [267]. The first simulation of a peptide embedded in membrane dates back to 1994 [291] and before the 2000, lipid bilayers were usually formed by dipalmitoylphosphatidylcholine (DPPC) or dimyristoylphosphatidylcholine (DMPC) [292-294]. Nowadays MD simulations performed in explicit solvent and in the presence of a bilayer of different type of lipids [290, 295-297] summing up to more than 100,000 atoms constitute a routine practice [290].

However, in this type of models, before setting up the simulation, it is of crucial importance to correctly pack the protein structure inside the lipid bilayer [250]. This also means to carefully inspect that the protein has the right orientation with respect to the bilayer plane [267]. Generally, there are two different methods used to embed a protein in a lipid bilayer, the "replacement method" and the "insertion method" [291, 298-301]. The former is a two-step process, as initially pseudo atoms are sequentially placed around the protein and, only in a second time, replaced by real lipid molecules. The advantage of this method is to be in the hand of the user, as the number of lipids and the system size can be manually defined. In the latter, a protein is inserted within a pre-created hole in a pre-equilibrated bilayer of protein. However, this approach, despite being faster, is more convenient only in case of cylindrical and regular proteins that can adjust within the hole without the need of post-processing modifications [302]. The optimal orientation of a protein with respect to the normal of the membrane is achieved by minimizing its transfer energy, $\mathbf{\Delta G_{transfer}}$, from water to the hydrophob ic layer with respect to the system coordinates [303]. Although in principle it is feasible to calculate it manually [304], automated methods such as the "orientations of proteins in membranes" (OPM) database [305], represent a fast, and easy alternative Figure 15).

As in the previous paragraph, I introduced the concept of implicit and explicit solvent MD simulation, it is also worth mentioning that an important difference between an implicit solvent lipid model and explicit solvent lipid model lies in the biomembranes being intrinsically anisotropic systems [306] and, therefore, highly influenced by the macroscopic boundary conditions [307]. In principle, MD simulations can be equally run in constant volume (NVT) or constant pressure (NPT) environment [249]. In the former, the pressure will fluctuate during the simulation, while in the latter the box volume will change to allow the pressure to remain constant. However, there is a general agreement in preferring the NPT ensemble over the NVT approach [307, 308]. The NPT environment is achieved by means of a barostat, which keeps the pressure constant, despite the inherently property of the Newton's equation would be to keep the volume constant. The Berendsen, or weak-coupling method, [309] is the most common used barostat. Here, a target pressure is used as reference, and any deviation from it is compensated by modulating the simulation box and particle positions. Accordingly, volume fluctuations also affect the thickness and overall area of a membrane. This artifact can be avoided by creating a tension-free lipid bilayer and enabling tensionless simulations [295]. AMBER lipid [310] is the force field used in the present work, and it is grounded on this method.

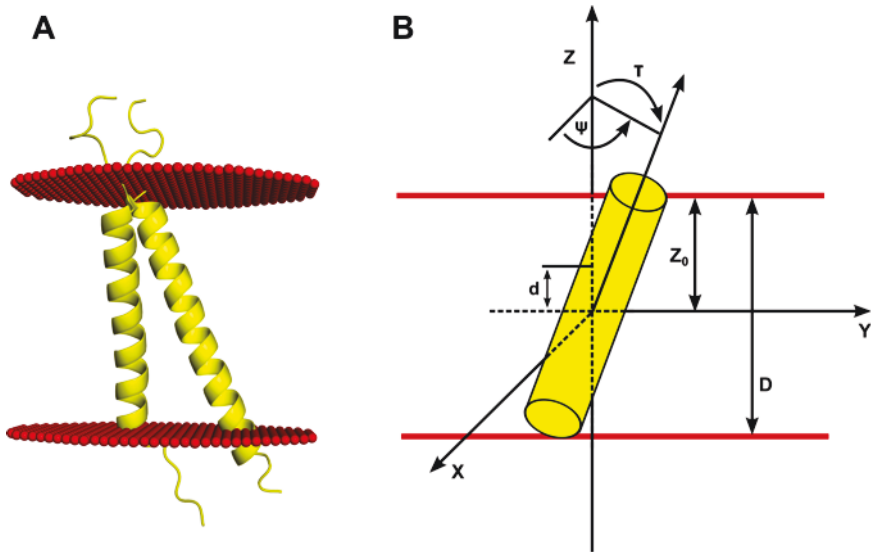

Figure 15 Orientation of a transmembrane protein in a membrane. (**A**) Integrin $\alpha_{IIb}\beta_3$ TMD (PDB ID 2K9J) in cartoon representation and the two lipid slabs in red spheres (output from the PPM server [305]). (**B**) Orientation of a transmembrane protein in a lipid bilayer is obtained with respect to an ensemble of variables in a system of coordinates xyz, where z corresponds to the normal of the bilayer, and D indicates the level of thickness of the membrane. Tilting of the TM segment is indicated by the variable τ, its rotation is obtained through the variable ψ, and a possible shift through the variable d. Figure adapted from reference [303].

2.4.5 Umbrella sampling and potential of mean force

Albeit the methodological improvements, not every biomolecule and biological event can be fully characterized by means of all atom MD simulation. To overcome this limitation, a number of alternative methods have been developed, including replica exchange MD simulations [311] and umbrella sampling simulations [312].

Umbrella sampling (US) is a type of biased MD simulations [313] and represents the chosen method to address part of the work done in **Publication III**. First introduced by Torrie and Valleau in 1997 [314], it is efficiently used to investigate the dynamic evolution of a molecular system as the system moves on the potential energy landscape from an energy minimum to another. By defining a reaction coordinate (ξ), it becomes possible to investigate and characterize biological processes happening along a chosen pathway [312]. In one or multiple dimensions, any parameter, i.e. distance or angle, can in principle be used as reaction coordinate [312]. Umbrella sampling works by dividing the pathway along the chosen reaction coordinate into a series of consecutive windows [312]. Each window has a defined reference point (ξ_i^{ref}) around which sampling is restrained by means of a bias function. For a window *i,* the bias potential ω_i is commonly an harmonic bias of strength *K* (Eq. 9) [312]:

$$\omega_i(\xi) = K/2\left(\xi - \xi_i^{\mathrm{ref}}\right)^2$$

(Eq. 9)

The definition of consecutive ξ_i^{ref} leads to the overlap between the individual windows, thus ensuring the sampling over the whole reaction coordinate $P^u(\xi)$, where the subscript 'b' indicates biased quantities [312]. Single US simulations are: i) unbiased to obtain the global (unbiased) distribution $P_i^u(\xi)$ where the subscript 'u' indicates unbiased quantities, ii) combined together to generate the unbiased distribution along the chosen reaction coordinate $P_i^{\mathrm{u}}(\xi)$. One way to do it is by using the Weighted Histogram Analysis Method (WHAM) [315], in which the biasing potential $\omega_i(\xi)$ is removed from each window (Eq. 10):

$$P_i^u(\xi) = P_i^b(\xi) exp\left(\frac{\omega_i(\xi)}{kT}\right) \langle exp\left(\frac{\omega_i(\xi)}{k_B T}\right)\rangle$$

(Eq. 10)

Where < > indicates the ensemble average, and k_B is the Boltzmann factor. Next, the singular $P_i^u(\xi)$ are combined by WHAM, through which the global (unbiased) distribution $P^u(\xi)$ is obtained as average distribution of the windows *i* (Eq. 11):

$$P^u(\xi) = \sum_i^{window} p_i\,(\xi) P_i^u(\xi)$$

(Eq. 11)

Where p_i are the weights introduced to reduce the statistical error of P^u and are calculated via (Eq 12):

$$p_i(\xi) = N_i exp\left(-\frac{\omega_i(\xi) + F_i}{k_B T}\right)$$

(Eq. 12)

Where N_i is the number of steps within each window *i*, and F_i is the free energy constant calculated via (Eq. 13):

$$exp\left(-\frac{F_i}{K_B T}\right) = \int P_i^u(\xi)\ exp\left(-\frac{\omega_i(\xi)}{K_B T}\right) d(\xi)$$

(Eq. 13)

An iteration of (Eq.11- Eq.13) until convergence must occur as $P_i^u(\xi)$ enters (Eq. 13) and F_i enters (Eq. 11) via (Eq. 12) [312].

Usually, this procedure, based on running umbrella sampling simulations in combination with WHAM, is done to extract the potential of mean force (PMF) [316], through which it is possible to compute the ΔG of a biological event (e.g. ligand-binding), or to derive the free energy profile of an investigated biological process as function of the reaction coordinate (ξ) (Eq. 14):

$$F(\xi) = -k_B T ln[P(\xi)] + C$$

(Eq. 14)

Where T is the temperature and C is a constant.

3 SCOPE OF THE THESIS

Over the past decade, there has been increasing interest in studying integrins, particularly for their involvement in the pathogenesis of a variety of human diseases. In this context, the availability of structural information is essential to shed lights on the structure-function relationship of integrins, and the subunit specificity of the various integrin isoforms.

Hence, in this thesis I applied a structure-based approach to derive structural information on integrin that may serve as basis for further studies (e.g. development of novel therapeutic strategies as discussed in **paragraph 2.3.3** and **section 4**), analyze the molecular nature underlying a phenotype associated to a pathological condition (i.e. the human platelet antigen-1 as discussed in **paragraph 2.3.4** and **section 5**), or investigate how specific molecular characteristics can account for differences in the activity and function detected in different integrin isoforms (e.g. integrin $\alpha_{IIb}\beta$, $\alpha_v\beta_3$ and $\alpha_5\beta_1$ as discussed in **paragraph 2.3.5** and **section 6**).

Publication I. Integrin isoform $\alpha_{IIb}\beta$, the predominant isoform of integrins on platelet, is a validated target for antithrombotic therapy with three approved drugs. The discovery of the involvement of platelets in the pathogenesis of Alzheimer's disease has opened up the way to the application of the antithrombotic therapy also in the case of neurodegenerative disorders. The $A\beta_{40}$ peptide is a ligand for integrin $\alpha_{IIb}\beta_3$, which leads to integrin activation and deposit of $A\beta_{40}$ in brain parenchyma and cerebral vessels are a sign for Alzheimer's disease. However, $A\beta_{40}$ peptide expresses a RHD sequence in place of the RGD-ligand integrin recognition sequence. Consequently, in order to use this target to develop a novel therapeutic strategy, it is important to answer the following questions:

- Is the mechanism of $A\beta_{40}$ binding the same as for the RGD ligands?
- What are the ligand-induced consequences on the structural dynamics of integrin?

Publication II. Integrin isoform $\alpha_{IIb}\beta$ is the carrier of the HPA-1 polymorphism, arising from a Leu→Pro exchange and resulting in Leu33 (HPA-1a) and Pro33 (HPA-1b) platelets. There is an ongoing debate concerning the exact nature of this polymorphism, and whether it effectively leads to an increased thrombogenicity of the Pro33 platelets, as otherwise hypothesized. In addition, due to the distant location of this amino acid exchange from the relevant functional domains of integrin, the way by which it can influence integrin function

represents an intriguing question. Consequently, in order to clarify the consequences of the HPA-1 polymorphism, the following questions were posed:

- Does the Leu→Pro exchange shift the conformational equilibrium from the inactive to the active state?
- What is the molecular mechanism through which this exchange contributes to integrin activation?

Publication III. Integrin $\alpha_{IIb}\beta_3$, together with the isoform $\alpha_v\beta_3$, forms the β_3 subfamily of integrins, and both of them with the addition of the isoform $\alpha_5\beta_1$ are contained on platelets. These three isoforms show a high sequence identity, but different activation points and different basal activities. Broadly speaking, integrin activation is coupled to a large-scale reorientation of the ectodomain and structural changes in the TMD. Consequently, in order to elucidate the origin of subunit-specific sensitivity to activation, the following questions were posed:

- How is the TMD association disrupted during integrin activation?
- How do subunit-specific interactions between the TMDs modulate the activation of these three integrin isoforms?

4 PUBLICATION I - Blood platelets contribute to the formation of amyloid deposits in cerebral vessels via integrin alphaIIbbeta3 induced outside-in signaling and clusterin release

Donner, L., Fälker, K., Gremer, L., Klinker, S., **Pagani**, **G**., Ljungberg, L. U., Lothmann, K., Rizzi, F., Schaller, M., Gohlke, H., Willbold, D., Grenegard, M., Elvers, M.

Sci. Signal. (2016), 9, RA52.

4.1 Background

Integrin $\alpha_{IIb}\beta_3$ recognizes ligands containing an arginine-glycine-aspartate (RGD) motif and, through an interplay of specific and well described interactions (see **paragraph 2.1.4**), binds them in the head region at the interface formed between the α- and β-subunits [317]. Upon ligand binding, conformational changes are allosterically transmitted from the head across the entire structure leading to integrin activation [12, 164, 318]. Already in the early 90s, researchers provided evidences that ligands that contain an arginine-histidine-aspartate (RHD) sequence can bind to integrins in a way that closely resembles the RGD-dependent ligand recognition [234]. The $A\beta_{40}$ peptide is believed to bind integrin $\alpha_{IIb}\beta_3$ via its RHD motif. As a direct consequence of binding, $A\beta_{40}$ induces integrin activation via outside-in signaling, which leads to the release of a chaperone protein responsible for modulation of soluble Aβ into Aβ neurotoxic fibrils [319, 320]. This is of particular importance, considering that the event of fibril formation has been associated to neurotoxicity, and deposits of $A\beta_{40}$ in brain parenchyma and cerebral vessels have been linked to Alzheimer's disease [18, 227, 321, 322]. This publication is the result of a collaboration between different research groups*, in which the computational investigation provided a support to the *in vitro* and *in vivo* experiments. The overreaching goal pursued here was to reach a deeper understanding of the consequences of $A\beta_{40}$ binding on the biological function of integrin $\alpha_{IIb}\beta_3$. Together, these findings are expected to improve the

* The experiments were performed in the laboratories of Prof. Dr. M. Elvers and Prof. Dr. D. Willbold.

understanding of the contribution of platelets via integrin $\alpha_{IIb}\beta_3$ to cerebral amyloid angiopathy, which is the pathological hallmark of Alzheimer's disease [227].

4.2 Results

Integrin $\alpha_{IIb}\beta_3$ is relevant for Aβ fibril formation

Fibrinogen binding to integrin $\alpha_{IIb}\beta_3$ is believed to be related to Aβ aggregation and consequent fibril formation. Hence, mouse and human platelets, in which fibrinogen binding to integrin $\alpha_{IIb}\beta_3$ was blocked, were analyzed. In both platelets, an increase in the release of the chaperone protein CLU was detected when cultured with $A\beta_{40}$. Likewise, analyses carried out on platelets from patients affected by Glanzmann's thrombasthenia revealed that the capability of modulating Aβ fibril formation is strictly dependent on the abundance of integrin $\alpha_{IIb}\beta_3$.

$A\beta_{40}$ binding to integrin $\alpha_{IIb}\beta_3$ induces outside-in signaling

Upon extracellular ligand binding, a cascade of signals is triggered within the cell leading to the release of different kinases, i.e. SYK or PLCγ2. By means of Western blot analyses, it was possible to observe a positive impact on the phosphorylation of the aforementioned kinases. In contrast, the presence of Tirofiban, which was shown to affect the Aβ-induced platelet aggregation, reduces the phosphorylation of SYK or PLCγ2.

Fibrinogen binds to platelet-bound of $A\beta_{40}$

Flow cytometry experiments revealed that, by increasing the amount of $A\beta_{40}$, also the binding of fibrinogen is induced. In addition, kinetic analyses confirmed $A\beta_{40}$ binding to fibrinogen, with an initial dissociation constant (K_D) of 15nM. Likewise, from the preincubation of platelets with fibrinogen for 30min, a reduction of binding of fluorescent-tagged $A\beta_{40}$ was not observed, thus indicating $A\beta_{40}$ binding to the fibrinogen-integrin complex.

Thus far, I summarized the part done by the co-authors of this work. In the following part, I will describe the part of work done by myself, and based on the atomic level investigation of $A\beta_{40}$ binding to integrin $\alpha_{IIb}\beta_3$.

$A\beta_{1\text{-}40}$ binds with the RHD sequence to integrin $\alpha_{IIb}\beta_3$

In order to characterize the underlying mechanism of binding of $A\beta_{40}$ at an atomistic level, I generated two additional versions of the peptide with an inverted (RHDS → SDHR) and scrambled (RHDS→HRSD) motif and introduced them into the crystal structure of the

ectodomain of integrin $\alpha_{IIb}\beta_3$ in a bent conformation (PDB ID 3FCS). The resulting integrin $\alpha_{IIb}\beta_3$ bound to $A\beta_{40native}$, $A\beta_{40inverted}$ and $A\beta_{scrambled}$ was used as model system and subjected to replicate all-atom MD simulations of 500 ns length each, summing up to a total aggregate time of 4.5 μs. Keeping in mind the time scale of integrin activation (< 1 s [75]), I was aware of the fact the magnitudes of the changes visible during 500 ns of MD simulations would not correspond to those describing the full extension of integrins. For this reason, I decided to further reduce the computational costs of the MD simulations, by decreasing the level of complexity of the model system without the risk of losing precision. Only the domains forming the headpiece (β-propeller and βA plus the hybrid domains for the α and β subunits, respectively) [13] were maintained in the model. In addition, since my aim was to specifically assess the RHD contribution to the binding, I also used a shortened version of the $A\beta_{40}$ peptide (14 residues) (Figure 16). Nevertheless, such setting would still allow me to detect the conformational changes occurring in the head of the protein and that have been linked to integrin activation (**paragraph 2.2.2**). As a first step, I verified the structural integrity of the system as well as of the $A\beta_{40}$ peptide within the binding pocket. In both the cases, root-mean-square deviation (RMSD) values below 3.5 Å confirmed that the system remained intact with only minor deviations from the starting structure. However, it also provided a first indication of a different behavior in the three cases, with both the $A\beta_{40inverted}$ and $A\beta_{40scrambled}$ complexes showing the largest deviations.

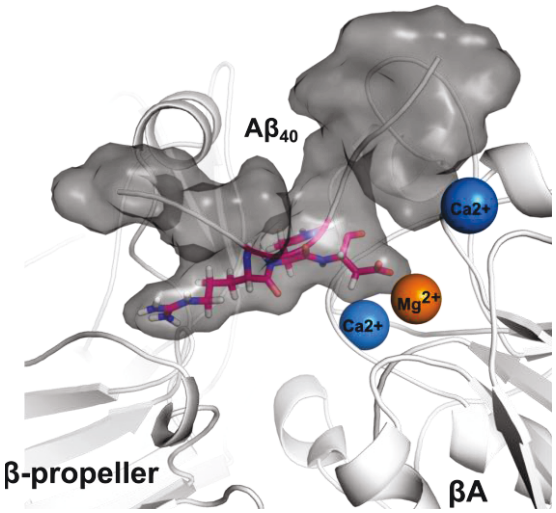

Figure 16 $A\beta_{40}$ binding to integrin $\alpha_{IIb}\beta_3$. Model of $A\beta_{40}$ peptide bound into the crevice between the β-propeller and βA domains, which corresponds to the extracellular binding site of integrin.

Structural rearrangements linked to integrin activation

Integrins $\alpha_{IIb}\beta_3$ binds $A\beta_{40}$ at the interface between the β-propeller and βA domain. As described in **Paragraph 2.1.4**, upon ligand-binding, this interface undergoes a structural rearrangement, including the increase of the hinge angle formed between the βA and hybrid domains. To test this, first I evaluated the binding interface in terms of the distance between the β-propeller and βA domains and geometric parameters within the βA domain (T-junction formation) (Figure 17). Results from the simulations indicate that a significantly more pronounced shift of the βA domain relative to the β-propeller occurs when in complex with the $A\beta_{40native}$. So for the T-junction formation: the smaller distance between the center of helix α1 and the N-terminus of helix α7 indicates tighter hydrophobic interactions in the case of $A\beta_{40native}$, than in $A\beta_{40inverted}$ and $A\beta_{40scrambled}$ complexes.

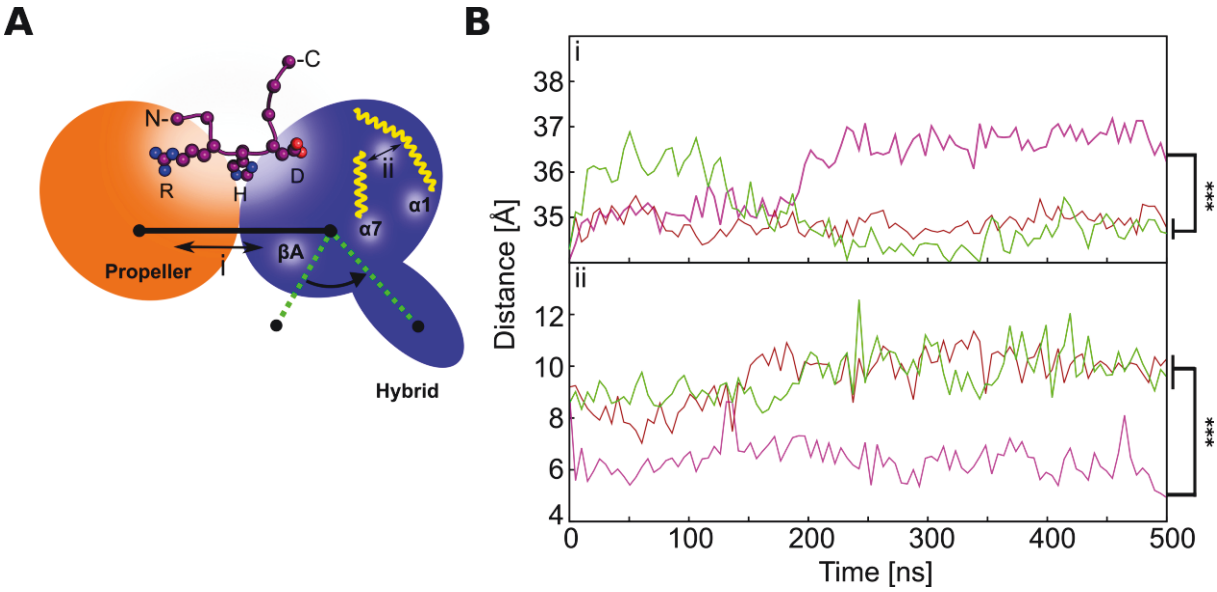

Figure 17 Consequences of $A\beta_{40}$ binding to integrin $\alpha_{IIb}\beta_3$. (**A**) Schematic representation of model system used for the MD simulation and formed by the headpiece (β-propeller, βA and hybrid domain, respectively) in complex with the first 14 amino acid residues of $A\beta_{40}$ (in ball and sticks representation, and colored in purple). The two double arrows indicate the distance between the center of mass of the β-propeller and βA domain (i), and between the center of helix α1 and the N-terminus of helix α7 colored in yellow (ii). The green dashed lines indicate the increase of the hinge angle, which has been linked to integrin activation. (**B**) Time series of the mean distances (i and ii) calculated over three MD simulations. Stars denote the statistical significance ($p < 0.001$ according to the Student's t-test).

4.3 Conclusion and significance

In this study, it was possible to verify that $A\beta_{40}$ binding to integrin $\alpha_{IIb}\beta_3$ induces the release of the chaperone CLU involved in the conversion of a soluble Aβ into Aβ fibrils, responsible for the vascular Aβ deposits.

In detail:

- $A\beta_{40}$ via its RHD motif binds to integrin $\alpha_{IIb}\beta_3$ and induces the release of CLU, in turn, responsible for Aβ aggregation and fibril formation.
- The kinetic analysis revealed that $A\beta_{40}$ interacts with integrin $\alpha_{IIb}\beta_3$ with high affinity, with a K_D of $A\beta_{40}$ bound similar to the (patho)-physiological concentration of $A\beta_{40}$ in plasma.
- Platelets cultured with Aβ peptides with the RHDS inverted or scrambled resulted in a decreased release of the chaperone CLU and platelet aggregation, thus providing evidences that the binding event is mediated by the RHDS sequence.
- MD simulations confirmed that $A\beta_{40}$ binding leads to the allosteric conformational changes described for integrin activation.

The comparison of the $A\beta_{40native}$ complex with the $A\beta_{40inverted}$ and $A\beta_{40scrambled}$ complexes confirmed the key role played by the RHDS sequence in mediating the $A\beta_{40}$ binding to integrin $\alpha_{IIb}\beta_3$. This, in turn, induces integrin activation and leads to the classical outside-in signaling. This way, partly cause and effect of binding to $A\beta_{40}$, activated platelets contribute to the development of the cerebral amyloid angiopathy.

5 PUBLICATION II – The human platelet antigen-1b variant of $\alpha_{IIb}\beta_3$ allosterically shifts the dynamic conformational equilibrium of the integrin toward an active state

Pagani, **G**., Pereira, J. P. V., Stoldt, V. R., Beck, A., Scharf, R. E., Gohlke, H.
J. Biol. Chem. (2018), DOI: 10.1074/jbc.RA118.002149

5.1 Background

The human platelet antigen-1 (HPA-1) of $\alpha_{IIb}\beta_3$ arises from a Leu→Pro exchange at residue 33 of the mature β_3 subunit resulting in Leu33 (HPA-1a) or Pro33 (HPA-1b) platelets [323]. This mutation is highly relevant from a clinical perspective as patients with coronary artery disease who carry the Pro33 (HPA-1b) allele experience their myocardial infarction five years earlier than in HPA-1a/HPA-1a patients [240]. While these and other experimental observations have shown that the Pro33 (HPA-1b) is a prothrombotic variant of $\alpha_{IIb}\beta_3$, and hence, more easily activated, the molecular mechanism underlying the polymorphism has remained elusive. In this study, I verified the hypothesis that the L33P exchange allosterically shifts the dynamic conformational equilibrium of $\alpha_{IIb}\beta_3$ toward a state closer to the active one. Due to its distant location (> 80 Å) from functional domains of integrin (extracellular binding site and transmembrane domain), a direct influence of the L33P exchange on binding of extracellular, or, even, intracellular agonists (see Figure 13 in **paragraph 2.3.3**) seems reasonable. At the same time, the HPA-1a polymorphism is located within the PSI domain, which forms together with the EGF-1 and EGF-2 domains the knee region of the integrin ectodomain [94]. To probe this hypothesis, I carried out multiple microsecond-long all-atom molecular dynamics (MD) simulations of the $\alpha_{IIb}\beta_3$ ectodomain. Simulations results were then combined with findings from Förster resonance energy transfer (FRET) measurements† of the entire $\alpha_{IIb}\beta_3$-transfected HEK293 cells expressing either isoform, Leu33 (HPA-1a) or Pro33 (HPA-1b). Results from MD simulations indicate that the Leu→Pro exchange affects the inter-domain interface at the

† Experiments were performed in the laboratory of Prof. Dr. Scharf, R.E. at the HHU, Duesseldorf. In particular, FRET measurements were performed by Dr. Joana, P.V. Pereira.

knee region and shifts the dynamic conformational equilibrium of integrin $\alpha_{IIb}\beta_3$ toward a more unbent state. Moreover, time-evolution measurements (inter-domain distances and angles) provide evidence of larger splaying (separation) of the lower legs of integrin $\alpha_{IIb}\beta_3$ ectodomain in the case of Pro33 (HPA-1b) isoform. In parallel, results from FRET analyses, performed taking into account the entire integrin $\alpha_{IIb}\beta_3$, indicate a significantly larger separation between the cytoplasmic tails in the Pro33 (HPA-1b). As such, based on the findings here presented, we confirmed our initial hypothesis, and support the theory that the Leu→Pro exchange confers prothrombotic properties to integrin $\alpha_{IIb}\beta_3$.

5.2 Results

In a previous study, some of the present authors, revealed higher thrombus stability in the case of Pro33 (HPA-1b) platelets than of Leu33 (HPA-1a) platelets [324]. In line with this, in this second study we initially showed that, upon thrombus formation, the flow path becomes narrowed and the shear rates increase due to physical constrictions (see Figure 2 in **Publication II**). Therefore, we also considered the changes of the physiological flow conditions as caused by the increase of the thrombus volume as function of time in the Pro33 isoform, and a sign of an increased thrombus stability in this isoform. In order to explore possible influences on the stability of integrin $\alpha_{IIb}\beta_3$ due to the L33P exchange, I used the available crystal structure of the ectodomain of integrin $\alpha_{IIb}\beta_3$ in the bent conformation as representative structure of the resting state of integrin and model system of the Leu33 isoform for the MD simulations (PDB ID 3FCS). This structure served also as template to model the Pro33 isoform, in which the side chain of Leu33 was replaced by the aromatic ring of Pro. Both models were subjected to replicate MD simulations of 1 μs length each, summing up to a total MD simulation time of 6 μs.

Global conformational changes of the ectodomains of $\alpha_{IIb}\beta_3$

First, I evaluated the structural similarity of the two isoforms with respect to the representative initial structure in terms of RMSD of C_α atoms. Mean values < 3 Å were found after a mass-weighted domain-wise alignment, thus indicating only minor structural changes for each domain in both the isoforms. In contrast, RMSD mean values up to 16 Å were measured after a mass-weighted alignment onto the head (β-propeller and βA domains), with the highest values recorded for the C-terminus domains (calf-2 domain and β-tail domains). Hence, we considered

these values as indicative of movements between the domains (or even subunits), rather than structural changes within each domain. In addition, I evaluated the different level of compactness of the structure of the two isoforms in terms of Radius of gyration (Rg). Albeit rather small (~ 0.7 Å), this difference is statistically significant ($p < 0.05$ Å), and shows that the Pro33 isoform has an overall larger structure than that of the Leu33 isoform. Then, from a visual inspection of the MD trajectories, we hypothesized that the difference in the RMSD values are due to the initial separation between the head region and the legs, as occurring when integrin switches from the inactive to the active state [12, 325]. To probe this hypothesis, I defined a series of geometric parameters across the structure (a similar approach has been already used in related studies of integrins [175, 260]). For investigating that Pro33 isoform adopts a more unbent conformation, I measured the time-evolution of the distance between the N- and C-terminus of each subunit (for simplicity, the βA domain is here considered as the N- terminus of the β_3 subunit), as well as the distance between the two lower legs (calf-2 domain and β-tail for the α and β subunits, respectively). Results from the simulations revealed that the distance between the β-propeller and calf-2 domain is larger by ~ 5 Å, and larger by ~ 9 Å between the βA and β-tail domain in the Pro33 isoform. This implies that the head of integrin $\alpha_{IIb}\beta_3$ is less tightly packed against the lower legs in the Pro33 isoform. Likewise, the distance between the calf-2 and β-tail domains is larger by about 2 Å in the Pro33 isoform, thus suggesting a separation between the two lower legs. Interestingly, in all cases, the differences are significant ($p < 0.05$ Å) up to highly significant ($p < 0.0001$ Å) as shown in Table 2.

Table 2: Distance between the N-terminus and C-terminus of integrin $\alpha_{IIb}\beta_3$ ectodomain.

	Leu33 (HPA-1a) isoform	**Pro33 (HPA-1b) isoform**
βA···β-tail	35.94±0.62[a]	44.76±1.70[a]
	***[b]	
Calf-2···β-tail	27.95±0.56[a]	29.40±0.24[a]
	*[b]	
Calf-2···β-propeller	53.76±0.75[a]	58.51±1.45[a]
	***[b]	

[a] Mean value and SEM, in Å, calculated across three MD simulations.

[b] *< 0.05, **< 0.01, ***: p <0.0001 (according to the t-test for parametric testing).

In addition, I evaluated the unbending of the conformations and legs separation in terms of bending and splaying angle (whose definition is provided in Figure 18). Reference points have been chosen to be similar to those used during the FRET measurements and based on approach previously validated [20, 29]. As shown in Figure 18, the bending angle is larger by ~ 7 Å in the Pro33 isoform, while the splaying angle is larger by ~ 3 Å in Pro33 than the Leu33 isoform.

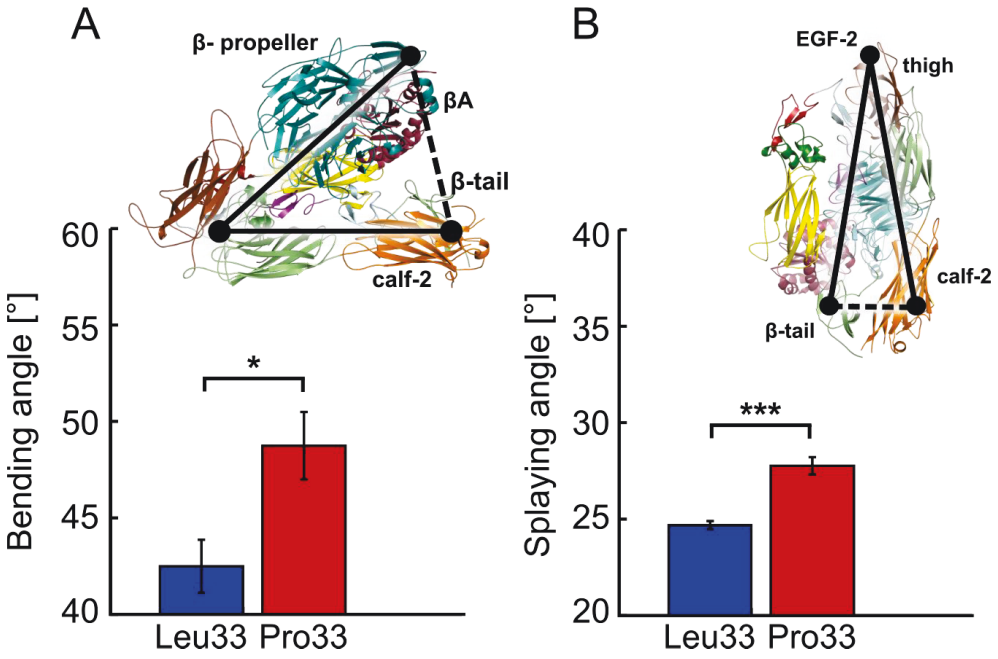

Figure 18 Geometric parameters linked with the opening of the ectodomain. **(A)** On the top of the histograms, definition of the bending angle on the integrin $\alpha_{IIb}\beta_3$ ectodomain starting structure (PDB ID 3FCS), depicted in cartoon drawing with the domains labeled, is given. The black solid lines connect the point triples used for definition: center of mass (COM) of the β-propeller and βA domains; COM of the PSI domain; COM of the calf-2 and β-tail domains. Below the representative structure, histograms of the mean bending angle computed over three MD simulations, with error bars indicating the SEM; stars denote the significant difference between the mean values (*$p < 0.05$); Pro33 variant in red, Leu33 variant in blue. (**B**) As for panel A, on the top of the histograms, definition of the splaying angle by using the point triples: COM of C_α atoms of L788 and G796 in the CALF-2 domain; COM of the C_α atoms of C602 and C608 in the thigh domain; COM of Cα atoms of E1557 and V1561 in the β-tail domain. Below the representative structure, histograms of the mean splaying angle computed over three MD simulations (see panel A for further details).

In parallel, the distance between the two legs was evaluated by means of fusion mVenus and mCherry fluorescent proteins attached to the C-termini of integrin subunits. FRET acceptor photobleaching experiments revealed a significantly higher efficiency of energy transfer between the two subunits in HPA-1a compared to HPA-1b (Figure 19). Thus, both the computational measurements and FRET experiments agree in indicating that the spatial

separation between the cytoplasmic tails in the Leu33 variant is significantly lower than the spatial separation between the cytoplasmic tails in the Pro33 variant.

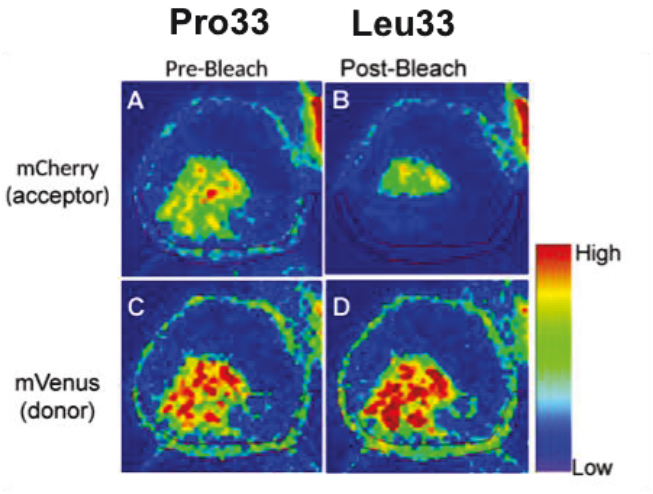

Figure 19 FRET-acceptor photobleaching (APB) experiments. Experiments were performed by Dr. Joana P.V. Pereira on a HEK293 cell transfected with α_{IIb}Venus and β_3Leu33mCherry plasmids and indicate the most pronounced spatial separation in the Pro33 variant.

Short and mid-range consequences of the L33P exchange on $\alpha_{IIb}\beta_3$

In order to evaluate a possible influence of the Leu→Pro exchange on the inter-domain interface at the knee region, first I measured the 2D-RMSD of the C_α atoms of the EGF-1/EGF-2/EGF-3 domains along the MD trajectories (see Figure 5A, **Publication II**). The direct comparison between the two isoforms, with RMSD values up to 8 Å, indicates that, not only, the domains larger deviate from the respective initial structure, but also that they are greatly different in the two isoforms. Next, I examined the atomic mobility of the PSI domain in terms of residue-wise root-mean-square fluctuations (RMSF) (see Figure 5B, **Publication II**). Results revealed an increased mobility of the AB loop carrying P33, with P33 that peaks above the other residues. Albeit this difference is not significant, it is, nevertheless, of great importance as the substitution of L33 with a conformationally restricted residue (proline), would be expected to make this loop more rigid. Moreover, if this increased mobility governs an outward movement of the AB loop, this would also reflect in an increase of the interdomain distance between the PSI with respect to the EGF-1 and EGF-2 domains. To probe this hypothesis, I computed the distance between the C_α atoms of L33P with S469 (EGF-1 domain) and Q481 (EGF-2 domain), respectively. In the former, I found a mean distance larger by ~ 4 Å in the Pro33 isoform, and in the latter larger by ~ 6 Å in Pro33 than the Leu33 isoform (Table 3).

Table 3 Distance at the knee region of the β_3 leg.

	Leu33 (HPA-1a) isoform	Pro33 (HPA-1b) isoform
L33P···S469	8.12±0.40[a]	11.81±0.79[a]
	*[b]	
L33P···Q481	6.65±0.37[a]	12.38±1.02[a]
	***[b]	

[a] Mean value and SEM, in Å, calculated across three MD simulations.

[b] *< 0.05, **< 0.01, ***: p <0.0001 (according to the t-test for parametric testing).

These results provide evidence that the inter-domain interface at the knee region is less tightly packed in the Leu33 isoform compared to the Pro33 isoform (Figure 20). As a further confirmation, I measured the overall number of contacts ("native" and "non-native") formed between the nine residues of the AB loop and all those amino acids located within a distance cut-off of 7 Å. The total number of native contacts is about 20 % lower in Pro33 isoform, and the difference becomes even more consistent in the case of non-native contacts (2-fold more) in the Pro33 isoform (see Figure 6A in **Publication II**). Interestingly, a similar scenario occurs also in the case of specific interactions (hydrogen bonds and salt bridges), with hydrogen bonds only firmly formed in the Leu33 isoform (see Figure S8 in **Publication II**). All together, these findings suggest that the Leu→Pro exchange causes the disruption of stabilizing interactions at the knee region, resulting in an interface less compact in the Pro33 isoform.

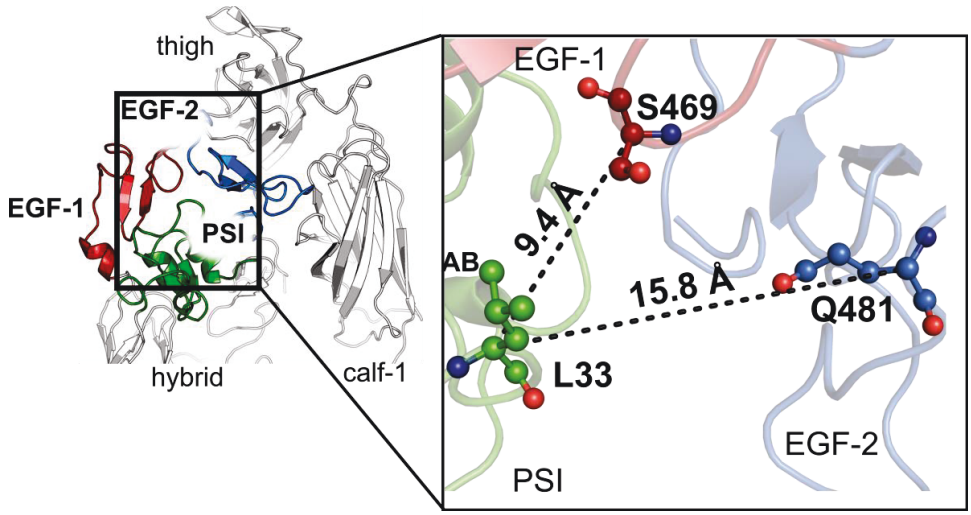

Figure 20 Structural changes within the knee region due to the L33→P33 exchange. Integrin $\alpha_{IIb}\beta_3$ in the bent conformation used as model system (PDB ID 3FCS) in cartoon drawing and colored in grey (with the exception of the PSI domain (green), EGF-1 domain (firebrick), and EGF-2 domain (marine)). Domains are labeled. The close-up view reveals the inter-domain interface at the knee region, with the

distance measurements reported in table 3 as they are measured in the crystal structure. Residues Leu 33 (PSI domain), S469 (EGF-1 domain) and Q481 (EGF-2 domain) are in ball and sticks representation and labeled.

Finally, these findings prompted us to apply the Constraint Network Analysis (CNA) approach [326] to assess whether the influence induced by the polymorphism on the structural stability allosterically spread across the structure. In doing so, we observed that the influence due to the L33P exchange percolates from the knee region further down the leg. Notably, the introduction of a Pro33 reaches the EGF-3 domain, located more than 30 Å from the site of the exchange, which appears to be less stable in the case of Pro33 (Figure 21). This suggests that the L33P exchange has both a short-range and a mid/large range effect on the EGF domains, which are known to be important for locking integrin in the bent conformation.

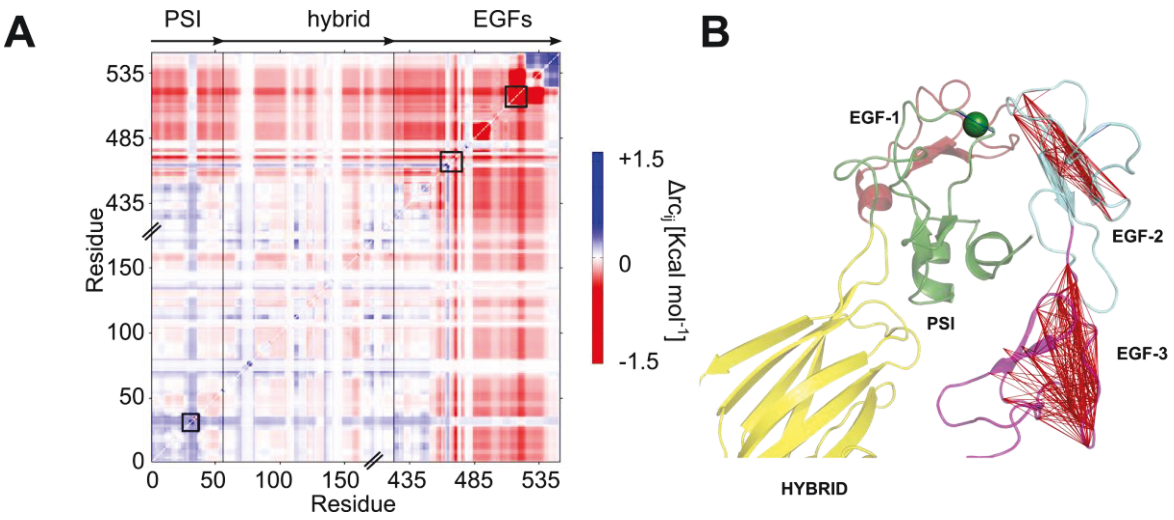

Figure 21 Allosteric influence of the L33→P33 exchange on the structural stability of β_3 leg. (**A**) Difference stability map generated by CNA and averaged over three MD simulations, with a specific focus on the knee region of the β_3 leg. (**B**) Close-up view of the domains analyzed in panel A, with red lines connecting those residues whose mutual stability is lower by –1.5 kcal mol^{-1} in the Pro33 variant.

5.3 Conclusion and significance

This study is grounded on previous clinical and laboratory data indicating, albeit not univocally, that Pro33 (HPA-1b) isoform may be prothrombotic. Results from MD simulations, in being able to scale down to the atomic detail, provide a possible explanation of the molecular nature underlying this genotype, whereas experimental results give strength to the hypothesized shift of the equilibrium towards the active state in the case of Pro33.

In detail:

- Pro33 platelets lead to single thrombi whose mean volume is significantly higher than that formed by Leu33 platelets, thus providing a first evidence of changes in the function and activity of integrin $\alpha_{IIb}\beta_3$.
- Results from MD simulations reveal the tendency of the Pro33 isoform to shift toward a more unbent and splayed state.
- Results from MD simulations in combinations with rigidity analysis suggest the possible underlying molecular mechanism of the prothrombotic phenotype of Pro33 platelets.
- FRET analyses reveal structural changes in the Pro33 isoform that have been linked to the large-scale rearrangement occurring during activation.

Through a direct comparison of the Leu33 (HPA-1a) and Pro33 (HPA-1b) isoforms, we were able to observe changes that, according to the current models, have been linked to the mechanism of activation, and provide a molecular explanation underlying them.

6 PUBLICATION III – On the contributing role of the transmembrane domain for subunit-specific sensitivity of integrin activation

Pagani, **G**., Gohlke, H.
Submitted **(2018)**

6.1 Background

The TMDs of integrin work as a mediator of the transmission of information in both directions across the plasma membrane, leading to outside-in and inside-out signaling [68]. As such, integrin TMDs play a key role during the mechanism of activation [106]. Structural features of the integrin TMD were derived from NMR structures [107, 108, 327], biochemical data and electron microscopy images [37, 66, 156]. The TMD form two short helices [13] and associate in the resting state to form a helix dimer [101, 114, 198]. Two main association motifs, termed the inner membrane clasp (IMC) and outer membrane clasp (OMC), primarily mediate the dimer packing and seem to be required to maintain integrins in a state of low affinity [13]. In addition, single residues are known to make interactions important for the dimer stability, i.e., a salt bridge formed between R995 (α_{IIb} subunit) and D723 (β_3 subunit) and a highly conserved Lys (K716, β_3 subunit), whose importance in the process of integrin activation has been shown by several mutational studies [112, 121]. In this study, we analyzed three different integrin isoforms ($\alpha_{IIb}\beta_3$, $\alpha_v\beta_3$, $\alpha_5\beta_1$), which show a sufficient sequence similarity (> 50%) to allow for initial homology modeling, but at the same time possess characteristic amino acid substitutions, particularly in the OMC, that may be responsible for the proven subunit-specific sensitivity to activation [84, 246, 247]. First, I carried out microsecond long all-atom equilibrium MD simulations of the three TMDs integrin isoforms in an explicit membrane and solvent. Then, I analyzed the energetics of TMD dissociation by means of potential of mean force (PMF) calculations. All together, these findings help shedding lights on how the TMD association is maintained and how the subunit-differences reflect on the subunit-specific sensitivity to activation.

6.2 Results

All-atom MD simulations of integrin $\alpha_{IIb}\beta_3$, $\alpha_v\beta_3$, and $\alpha_5\beta_1$

In order to carry out a comparative analysis of integrin $\alpha_{IIb}\beta_3$, $\alpha_v\beta_3$, $\alpha_5\beta_1$ TMDs, I first generated the initial models starting from the NMR structure of integrin $\alpha_{IIb}\beta_3$ (PDB ID 2K9J) through an homology modeling step (Figure 22). After assessing by means of the QMEAN server [328, 329] the quality of the models, I inserted them within a bilayer of DOPC lipid and performed replicate all-atom MD simulations of 1 μs length each. This sums up to a total aggregate time of 9 μs.

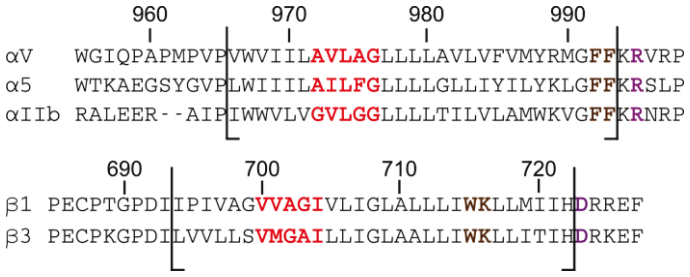

Figure 22 Sequence alignment of $\alpha_{IIb}\beta_3$, $\alpha_v\beta_3$, and $\alpha_5\beta_1$ TMD sequence. Multiple sequence alignment step was carried out to generate the homology models. Numbering refers to the $\alpha_{IIb}\beta_3$ TMD, with black lines added to indicate the TMD border in accordance with reference [330]. Highlighted in red the OMC, in brown the IMC, and in purple the R995-D723 salt bridge, respectively.

First, I assessed the structural integrity of all three systems in terms of RMSD of C_α atoms of the TMDs after a mass-weighted superimpositioning onto the respective starting structure, as well as only of those residues embedded in membrane (see Figure 22). In the former case, I found RMSD mean values up to ~ 7-10 Å, while in the latter case values were only up ~ 2-4 Å. As such, we assumed that the high values must arise from the highly flexible and unstructured N- and C-terminus, while the overall fold of the two helices is conserved over the MD simulation time. Next, I evaluated differences in the TMD topology of each system in terms of changes in the overall number of contacts ("native contacts" and "non-native contacts"). To do this, I applied a cut-off distance of 7 Å between the two helices for each system. In total, I found a reduction of overall contacts by ~10 %, albeit highly significant ($p < 0.0001$), in the total number of contacts of both $\alpha_v\beta_3$ and $\alpha_5\beta_1$ compared to $\alpha_{IIb}\beta_3$. Furthermore, I extracted only those residues belonging to the α subunit and accounting for the native and non-native contacts at the OMC and IMC interface between α and β subunit. This way, I noticed at the OMC a reduction of roughly 20 % in $\alpha_v\beta_3$ TMD and up to 40% in $\alpha_5\beta_1$ TMD compared to $\alpha_{IIb}\beta_3$ TMD (Figure 23).

At the IMC, a smaller difference, albeit significant, of about 10 % was recorded in both $\alpha_v\beta_3$ and $\alpha_5\beta_1$ compared to $\alpha_{IIb}\beta_3$.

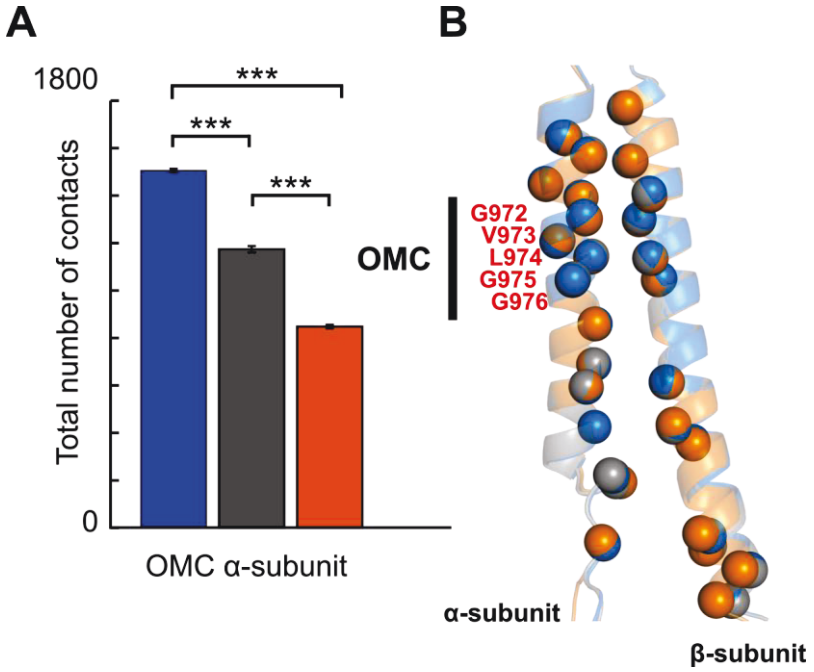

Figure 23 Total number of contacts formed at the OMC. (**A**) Histograms of the averaged total number of contacts formed at the OMC calculated with respect to the residues belonging to the α- subunit as indicated in panel B. The differences are highly significant in all cases ($p < 0.0001$). $\alpha_{IIb}\beta_3$ TMD is colored in blue, $\alpha_v\beta_3$ in gray, and $\alpha_5\beta_1$ in orange. (**B**) A superimposition of the $\alpha_{IIb}\beta_3$, $\alpha_v\beta_3$, and $\alpha_5\beta_1$ TMDs in cartoon drawing and in color code as in panel A. Residues are labeled.

These differences were found to be consistent with respect to the atomic mobility measured in terms of pair residue-wise RMSF. Here, I observed that 60 out of 89 residues of the $\alpha_{IIb}\beta_3$ TMD (~67%) were less mobile than those of $\alpha_v\beta_3$ and $\alpha_5\beta_1$. Hence, together these analyses indicate that the $\alpha_{IIb}\beta_3$ TMD interface is hold by generally more contacts across the TMD interface, which lead to the single residues being less mobile. At this point, we hypothesized that these differences would also reflect on the distances at TMD interface. To do so, I defined the d_{OMC} as the distance between the centers of mass (COM) of the C_α atoms of the G*XXX*G motif (G972-G976) on the α_{IIb} subunit and (V700-I704) on the β_3 subunit. Whereas, I defined the distance d_{IMC} as the minimal distance between the COMs of the aromatic rings of F992 or F993 on the α_{IIb} subunit and the aromatic ring of W715 on the β_3 subunit. The former is 9.3 Å in the NMR structure of $\alpha_{IIb}\beta_3$ TMD (PDB ID 2K9J), while the latter is 7.3 Å in that structure. Although in both the cases, the values found indicate that both the clasps are maintained intact over the

course of the MD simulations (see Figure 2A and 2B in **Publication III**), at the OMC the interface was found to be significantly tighter in the case of $\alpha_{IIb}\beta_3$ TMD, followed by $\alpha_v\beta_3$ and $\alpha_5\beta_1$ TMDs. Then, I evaluated the interface at the membrane-proximal region considering four possible salt bridge combinations that are known to stabilize the membrane-proximal region: R995 *vs* D723 and E726 (and *vice versa*), R997 *vs* D723 and E726 (and *vice versa*). To do so, I measured the minimal distance between the relative amino and carboxyl groups, and applied a cutoff of 4 Å to these distances. We found that R995-D723, as speculated in several studies [36, 121, 124], is the most important salt bridge for the dimer stability to be formed. Additionally, we observed the highest prevalence of this particular interaction in the case $\alpha_{IIb}\beta_3$ TMD. I applied a similar approach for K716, evaluating in parallel the possibility of the hydrogen bond interaction with F992 (α_{IIb} subunit) or a salt bridge interaction with the phospholipid heads from the surrounding lipid bilayer. We found the latter to be the most likely interaction to occur, with a decreasing rank of occurrence from $\alpha_{IIb}\beta_3 < \alpha_v\beta_3 < \alpha_5\beta_1$ TMDs (Figure 24).

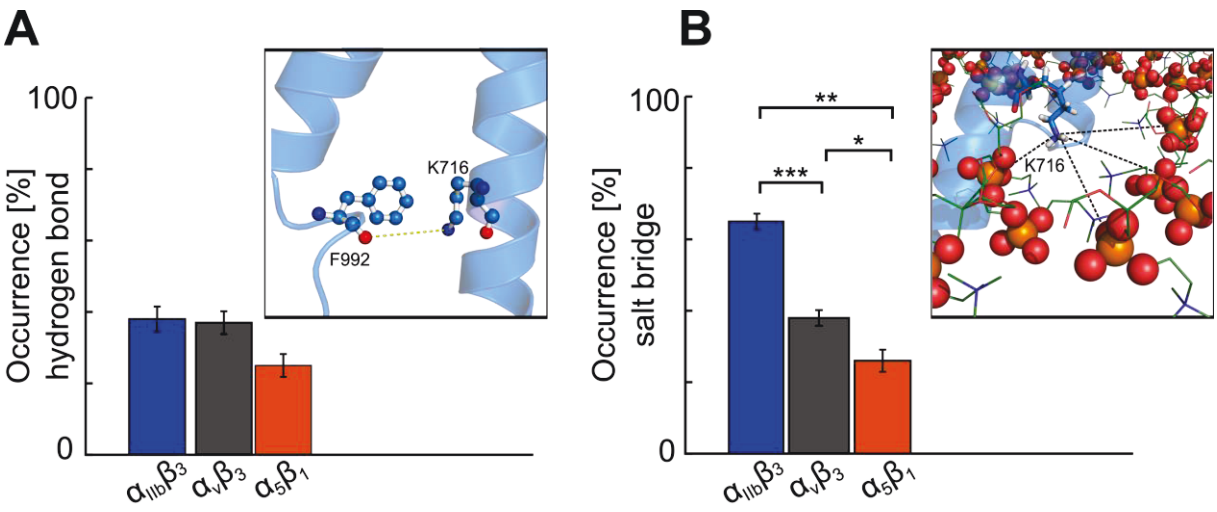

Figure 24 Subunit specific differences at the membrane proximal interface. (**A**) Histograms of the mean relative occurrence of the hydrogen bond between $K716_{N\varepsilon}$ and $F992_O$ obtained applying a distance cutoff of 3.5 Å and an angle cutoff of 120° From left to right, the $\alpha_{IIb}\beta_3$, $\alpha_v\beta_3$, and $\alpha_5\beta_1$ TMDs are colored in blue, grey, and orange, respectively. The box content shows a close-up view of the distance measured onto the structure of integrin $\alpha_{IIb}\beta_3$ TMD depicted in cartoon drawing (PDB ID 2K9J). Residues are labeled. (**B**) Histograms of the mean relative occurrence of the salt bridge between $K716_{N\varepsilon}$ and the oxygens of the phospholipids head groups. The box content shows a close-up view of the distance measured onto the structure of integrin $\alpha_{IIb}\beta_3$ TMD in cartoon drawing (PDB ID 2K9J), with K716 in in ball and sticks representation and the phospholipids head groups shown as spheres. Residues are labeled.

Biased simulations of integrin $\alpha_{IIb}\beta_3$, $\alpha_v\beta_3$, and $\alpha_5\beta_1$

Results from unbiased MD simulations provide a clear indication that the three integrin isoforms show a different strength of association. As an independent approach to explore the TMD dissociation and the corresponding free energy profiles, potential of mean forces (PMF) were computed based on umbrella sampling simulations. To do so, the distance between the centers of mass ($d_{COM\text{-}COM}$) of the embedded sections from the α and β subunits was used as reaction coordinate. Umbrella sampling simulations were performed along the pathway going from the bound state to the unbound state, and WHAM was used to extract the respective free energy profiles [315]. In separating the two helices, we obtained a free energy difference that is about ~4 kcal mol^{-1} larger in $\alpha_{IIb}\beta_3$ TMD, thus confirming a more pronounced tendency to associate for this system. In contrast, integrin $\alpha_5\beta_1$ shows the smallest free energy differences between the associated and dissociated state. In addition, from the PMF profiles, I computed the association free energies, ΔG. Results confirm that $\alpha_{IIb}\beta_3$ TMD is the most stable system, with a ΔG = -3.8 kcal mol^{-1}, followed by $\alpha_v\beta_3$ and $\alpha_5\beta_1$ TMDs (ΔG = -0.8 kcal mol^{-1} and ΔG = 0.5 kcal mol^{-1}, respectively) (Table 4).

Table 4 Thermodynamic quantities for integrin $\alpha_{IIb}\beta_3$, $\alpha_V\beta_3$, and $\alpha_5\beta_1$ TMDs.

System	$\alpha_{IIb}\beta_3$ TMD	$\alpha_v\beta_3$ TMD	$\alpha_5\beta_1$ TMD
$\|\|\Omega\|\|$[a]	0.07	0.05	0.1
ΔG[b]	-3.8	-0.8	-0.5

[a] In radians.

[b] In kcal mol^{-1}.

Thus far, findings from the biased simulations were found to be in good agreement with the results described from the unbiased MD simulations, showing $\alpha_{IIb}\beta_3$ as the most stable system, followed by $\alpha_v\beta_3$ and $\alpha_5\beta_1$.

Finally, to explore a possible mechanism of how the TMD packing changes with increasing helix-helix distances, I evaluated the stability of the OMC/IMC interfaces. To do so, I considered the re-weighted (unbiased) conformations extracted at the free energy minima I-III from the PMF profiles to compute the OMC/IMC distances. Interestingly, we noticed that the

IMC interface remains conserved longer than that of the OMC, thus suggesting a temporal order in the process of clasping/unclasping of the two helices (Figure 25).

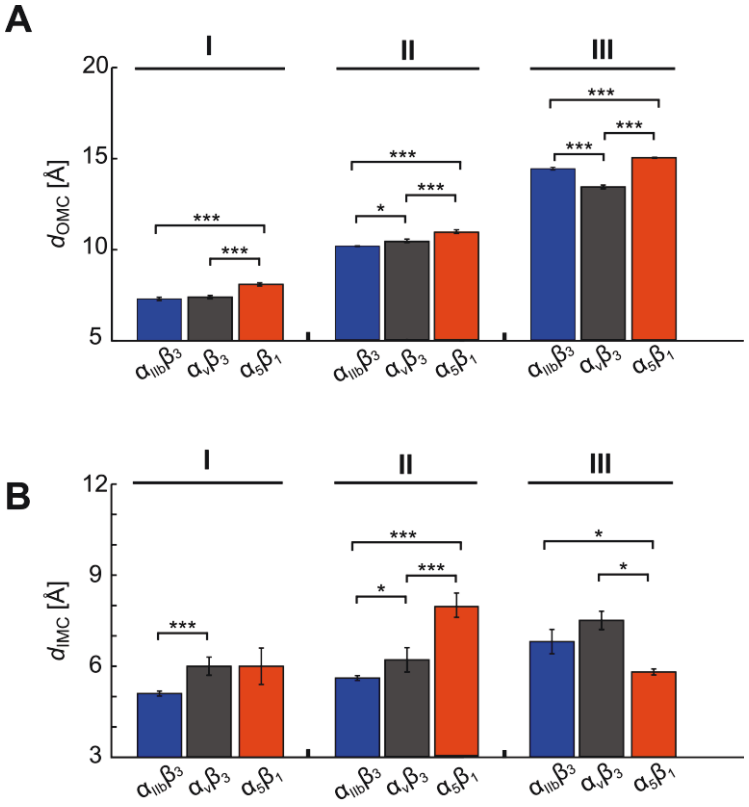

Figure 25 Changes at the OMC/IMC interface with increasing $d_{COM\text{-}COM}$. (**A**) Histograms of the averaged d_{OMC} and d_{IMC} (**B**) calculated from the umbrella sampling windows linked to the free energy minima observed in the PMF profiles of integrin $\alpha_{IIb}\beta_3$, $\alpha_v\beta_3$ and $\alpha_5\beta_1$ TMDs (in blue, grey and orange color, respectively).

6.3 Conclusion and significance

In this study, we carried out a comparative analysis of the TMD of three integrin isoforms ($\alpha_{II}\beta_3$, $\alpha_v\beta_3$ and $\alpha_5\beta_1$), which are known to have different basal activity, by means of all-atom MD simulations and free energy calculations.

In detail:

- Results from equilibrium MD simulations agree in indicating $\alpha_{IIb}\beta_3$ TMD as the most stable system followed by $\alpha_V\beta_3$ and $\alpha_5\beta_1$ TMDs.
- Association free energy extracted from the PMFs are in good agreement with the experimental data, thus giving further strength to the quality and validity of our analyses. Moreover, the order of association found here ($\alpha_{IIb}\beta_3 < \alpha_v\beta_3 < \alpha_5\beta_1$) corresponds with the reported basal activity for the analyzed systems ($\alpha_{IIb}\beta_3 < \alpha_v\beta_3 < \alpha_5\beta_1$).

- Results from biased simulations indicate a temporal order for the OMC/IMC formation, with the OMC being lost before the IMC upon TMD association.

In conclusion, results from both unbiased and biased simulations agree in indicating integrin $\alpha_{IIb}\beta_3$ TMD as the most stable system and $\alpha_5\beta_1$ TMD as the least stable system. Moreover, we identified a series of per-residue subtle differences, which are suggested to be responsible for a different modulation of the way how the TM associate and, consequently, dissociate.

7 SUMMARY AND PERSPECTIVE

In this thesis, I applied all-atom MD simulations in combination with free energy calculations to improve our understanding of the energetics and dynamics of the process of integrin activation.

Integrin $\alpha_{IIb}\beta_3$ is the prototypic and, probably, best characterized integrin isoform [29]. Due to its involvement in a large variety of human diseases, it still remains an attractive target of study. Most importantly, in more recent times, a connection between vascular pathological conditions and the progression of neurodegenerative disorders has been established. Ongoing experiments aim at identifying the contribution played by platelets, whose most abundant receptor is integrin $\alpha_{IIb}\beta_3$, to the progression of Alzheimer's disease. To improve our understanding of the underlying mechanism of $A\beta_{40}$ RHD binding to integrin $\alpha_{IIb}\beta_3$ at the atomic detail, I generated three initial models and subjected them to MD simulations. My computational investigations, in parallel to the experimental investigations, fostered our understanding of the binding event of $A\beta_{40}$ and the structural consequences on integrin $\alpha_{IIb}\beta_3$. However, in the study presented in **section 4**, only a shortened version $A\beta_{40}$ corresponding to the N-terminus of the peptide was used. As such, considering as long-term goal the application of antithrombotic therapy also for neurodegenerative disorders, it would be beneficial to investigate the molecular mechanism of $A\beta_{40}$ binding to integrin $\alpha_{IIb}\beta_3$ using the complete $A\beta_{40}$ peptide.

Integrin $\alpha_{IIb}\beta_3$ is also known as the carrier of the HPA-1 polymorphism [323]. Here we presented a strategy based on the combination of MD simulations with FRET measurements to reveal and quantify the structural changes in the ectodomain of integrin $\alpha_{IIb}\beta_3$ occurring upon the Leu33Pro amino acid exchange. This way, it became possible to shed lights onto the molecular mechanism underlying the HPA-1 polymorphism and provide evidence of the shift of the conformational equilibrium towards the open state. Most importantly, these results give strength to similar predictions based on clinical data [239-241, 243, 331] and experiments [238, 243, 324, 332]. This study, presented in **section 5**, was conducted on integrin $\alpha_{IIb}\beta_3$ in the resting state without the contribution of bound agonists. However, the information derived from this study would open up the way to a follow-up study, in which the two variants would be investigated in complex with immobilized and soluble fibrinogen. Using a similar strategy, based on the combination of MD simulations with FRET measurements, it would be possible to assess the strength of ligand binding, and correlate it to the splaying of the structure upon activation. Results are expected to complete the picture of the integrin $\alpha_{IIb}\beta_3$ behavior in the resting and open conformational state.

MD simulations allowed me to make a link between the structural dynamics, and function of integrin $\alpha_{IIb}\beta_3$. However, in order to foster our understanding of the events upon activation, a comprehension of the underlying energetics is also required. In the study presented in **section 6**, unbiased MD simulations were combined with biased simulations, from which the PMF of three integrin isoforms was derived and a quantitative assessment of the TMDs in terms of free binding energies was obtained. The analyses presented here show that subtle differences at the sequence level impact the way different TMD associate, and greatly influence the conformational free energy of each integrin. This workflow used in combination with experiments can lead to a substantial improvement of our knowledge of the physiological state of different integrins. As such, it would be of great interest to repeat this study in the presence of intracellular effectors, such as Talin. Albeit computationally expensive, such model system would allow the investigation of the influence of Talin-binding on the TMDs association and foster our understanding of the ligand-induced conformational changes undergone by integrin TMDs. Moreover, it would be interesting to further extend this study repeating the MD simulations in the presence of different lipid bilayers to elucidate the role of the membrane environment on integrin TMD interaction.

8 ACKNOWLEDGEMENT

Once somebody told me that all the best things happen in Duesseldorf. Today, I think he was right. It started as a PhD, and it turned out to be the most challenging, yet rewarding journey of my life.

First and foremost, I would like to thank my supervisor Prof. Dr. Holger Gohlke for believing in me and giving me this opportunity. I am deeply grateful for his guidance, support and never-ending enthusiasm. For all our truly enjoyable discussions, scientific and not.

I am very grateful to my dear colleagues in the CPC Lab, for the help and for being a little, warm family. In particular I would like to thank Dr. Christian Hanke and Michele Bonus for being the best roommates that one could ever wished to have. Furthermore, I am thankful to them, to Stephan Schott, to David Bickel, to Dr. Denis Schmidt, to Dr. Daniel Ciupka for their help and advices. To Neha, Susanne, Anuseema, Bastian, Nicola, Markus, Tobias and Daniel for the nice moments spent together.

I am deeply grateful to Karo, who helped me out when lost in translation.

I am thankful to Emanuele, Susanne, Dennis, Roberto and Friedrich for the beautiful memories bound to this city.

A special thanks to Elisa, this PhD is also yours!

..and to Christian, without whom nothing would have been the same.

Knowing already that I am missing someone, I would like to thank (in sparse order) Blerina, Sara, Stefania, Jacqueline, for being by my side, always. Moreover, I would like to thank Danny and Jutta for the unforgettable memories that bound me to them.

To my family. Thank you! For all you did for me and for making my dreams coming true.

Last, but not least, sincere thanks to Oleksandr, “Sasha”, for his never-ending energy, contagious enthusiasm and optimism, which guided me throughout these final, difficult steps of my PhD.

Grazie!

9 PUBLICATIONS

Reprint permissions for publications

PUBLICATION I

Reprinted from "*Blood platelets contribute to the formation of amyloid deposits in cerebral vessels via integrin $\alpha_{IIb}\beta_3$ induced outside-in signaling and clusterin release.*" Donner, L., Fälker, K., Gremer, L., Klinker, S., Pagani, G., Ljungberg, L. U., Lothmann, K., Rizzi, F., Schaller, M., Gohlke, H., Willbold, D., Grenegard, M., Elvers, M., **Sci. Signal.** 2016, 9, RA52. DOI: 10.1126/scisignal.aaf6240. This is the author's version of the work. It is posted here by permission of the AAAS for personal use, not for redistribution. The definitive version was published in Science Journal.

PUBLICATION II

Reprinted from "*The human platelet antigen-1b variant of $\alpha_{IIb}\beta_3$ allosterically shifts the dynamic conformational equilibrium of this integrin toward the active state."* Pagani, G., Pereira, J. P. V., Stoldt, V. R., Beck, A., Scharf, R. E., Gohlke, H., **J. Biol. Chem.** 2018, DOI: 10.1074/jbc.RA118.002149, Copyright (2018), with permission from The American Society for Biochemistry and Molecular Biology, Inc.

PUBLICATION III

Reprinted from "On the contributing role of the transmembrane domain for subunit-specific sensitivity of integrin activation." Pagani, G., Gohlke, H., **Sci. Rep.** 2018 DOI:10.1038/s41598-018-23778-5. This work is licensed under a Creative Commons Attribution 4.0 International License, which permits unrestricted use, distribution, and reproduction in any medium.

PUBLICATION I

Blood platelets contribute to the formation of amyloid deposits in cerebral vessels via integrin $\alpha_{IIb}\beta_3$ induced outside-in signaling and clusterin release

Donner, L., Fälker, K., Gremer, L., Klinker, S., **Pagani**, **G**., Ljungberg, L. U., Lothmann, K., Rizzi, F., Schaller, M., Gohlke, H., Willbold, D., Grenegard, M., Elvers, M.

Sci. Signal. 2016, 9, RA52.

RESEARCH ARTICLE

PHYSIOLOGY

Platelets contribute to amyloid-β aggregation in cerebral vessels through integrin $\alpha_{IIb}\beta_3$–induced outside-in signaling and clusterin release

Lili Donner,[1] Knut Fälker,[2] Lothar Gremer,[3,4] Stefan Klinker,[3] Giulia Pagani,[5] Liza U. Ljungberg,[2] Kimberley Lothmann,[3] Federica Rizzi,[6,7,8] Martin Schaller,[9] Holger Gohlke,[5] Dieter Willbold,[3,4] Magnus Grenegard,[2] Margitta Elvers[1]*

Cerebral amyloid angiopathy (CAA) is a vascular dysfunction disorder characterized by deposits of amyloid-β (Aβ) in the walls of cerebral vessels. CAA and Aβ deposition in the brain parenchyma contribute to dementia and Alzheimer's disease (AD). We investigated the contribution of platelets, which accumulate at vascular Aβ deposits, to CAA. We found that synthetic monomeric Aβ40 bound through its RHDS (Arg-His-Asp-Ser) sequence to integrin $\alpha_{IIb}\beta_3$, which is the receptor for the extracellular matrix protein fibrinogen, and stimulated the secretion of adenosine diphosphate (ADP) and the chaperone protein clusterin from platelets. Clusterin promoted the formation of fibrillar Aβ aggregates, and ADP acted through its receptors $P2Y_1$ and $P2Y_{12}$ on platelets to enhance integrin $\alpha_{IIb}\beta_3$ activation, further increasing the secretion of clusterin and Aβ40 binding to platelets. Platelets from patients with Glanzmann's thrombasthenia, a bleeding disorder in which platelets have little or dysfunctional $\alpha_{IIb}\beta_3$, indicated that the abundance of this integrin dictated Aβ-induced clusterin release and platelet-induced Aβ aggregation. The antiplatelet agent clopidogrel, which irreversibly inhibits $P2Y_{12}$, inhibited Aβ aggregation in platelet cultures; in transgenic AD model mice, this drug reduced the amount of clusterin in the circulation and the incidence of CAA. Our findings indicate that activated platelets directly contribute to CAA by promoting the formation of Aβ aggregates and that Aβ, in turn, activates platelets, creating a feed-forward loop. Thus, antiplatelet therapy may alleviate fibril formation in cerebral vessels of AD patients.

INTRODUCTION

Alzheimer's disease (AD) is an age-related neurodegenerative disorder that is the most common form of senile dementia and is characterized by deposits of amyloid-β (Aβ) in the brain (*1*–*6*). About 35 million people worldwide are affected by this progressive cognitive decline, and by 2050, the number of AD patients is predicted to increase to >115 million people or 1% of the total population (*7*). Aβ misfolding, oligomerization, and aggregation are crucial events in the pathogenesis of AD (*5*, *8*) leading to the formation of extracellular plaques containing mostly self-aggregating 40– to 43–amino acid residue peptides of Aβ and intracellular neurofibrillary tangles (*9*–*11*). The Aβ peptides are generated from amyloid precursor protein (APP), which belongs to an evolutionarily conserved family of type 1 transmembrane glycoproteins (*12*, *13*). APP can undergo amyloidogenic processing, which occurs mainly on the surface of cells to induce Aβ generation, and nonamyloidogenic processing in intracellular compartments (*14*–*17*). Aβ is ubiquitously present, but clinically relevant Aβ deposition occurs only in the brain. The factors that promote Aβ deposition or inhibit its clearance in the brain are still uncertain. Several studies provide evidence that AD is a more intriguing disorder than was previously appreciated and is related to vascular diseases such as stroke (*18*, *19*), atherosclerosis (*2*, *20*, *21*), and hypertension (*22*). Vascular risk factors are predicted to increase the risk for AD (*19*), and cerebrovascular dysfunction with impaired blood flow develops in AD patients (*23*–*26*). Formation of Aβ deposits in AD patients occurs not only in brain parenchyma but also in blood vessels in the brain in a condition called cerebral amyloid angiopathy (CAA) (*27*). CAA is characterized by the deposition of Aβ peptides, mainly Aβ(1–40) in the tunica media, smooth muscle cells (SMCs), and adventitia of cortical and leptomeningeal arteries, causing the destruction of the vessel wall and contributes to the severity of AD pathology (*10*, *27*–*29*). The incidence of CAA increases with age and develops sporadically or as a result of mutations in the genes encoding APP, presenilin 1 (PS1) or PS2, or possession of the epsilon 4 allele of apolipoprotein E (APOE-ε4). APOE-ε4 is a member of apolipoproteins involved in the lipid metabolism in atherosclerosis and is the major known genetic risk factor for AD (*27*, *30*). Cerebral vessels show loss of SMCs, luminal narrowing, vessel wall thickening, microaneurysm formation, and intracerebral microhemorrhage (*31*, *32*). More than 95% of AD patients develop CAA that may contribute to neurodegeneration and thus to cognitive decline (*33*).

Platelets are essential mediators of hemostasis but also play a dominant role in the development of arterial thrombosis (*34*, *35*). Platelets are also recognized to play a role in the pathology of neurodegenerative diseases, such as Parkinson's disease (*36*), schizophrenia (*37*), and AD (*2*). Platelets contain high amounts of APP and display the complete enzymatic machinery to process APP proteins into Aβ peptides (*2*). Platelets are thus a

[1]Department of Clinical and Experimental Hemostasis, Hemotherapy and Transfusion Medicine, Heinrich Heine University, 40225 Düsseldorf, Germany. [2]Cardiovascular Research Centre, Örebro University, SE-701 82 Örebro, Sweden. [3]Institute of Physical Biology, Heinrich Heine University, 40225 Düsseldorf, Germany. [4]Institute of Structural Biochemistry (ICS-6), Research Centre Jülich, 52425 Jülich, Germany. [5]Institute for Pharmaceutical and Medicinal Chemistry, Department of Mathematics and Natural Sciences, Heinrich Heine University, 40225 Düsseldorf, Germany. [6]Department of Biomedical, Biotechnological, and Translation Sciences, University of Parma, Via Volturno 39/a, 43126 Parma, Italy. [7]Centre for Molecular and Translational Oncology (COMT), University of Parma, Parco Area delle Scienze 11/a, 43124 Parma, Italy. [8]National Institute of Biostructure and Biosystems (INBB), Viale Medaglie d'Oro 305, 00136 Rome, Italy. [9]Department of Dermatology, University of Tübingen, 72076 Tübingen, Germany.
*Corresponding author. Email: margitta.elvers@med.uni-duesseldorf.de

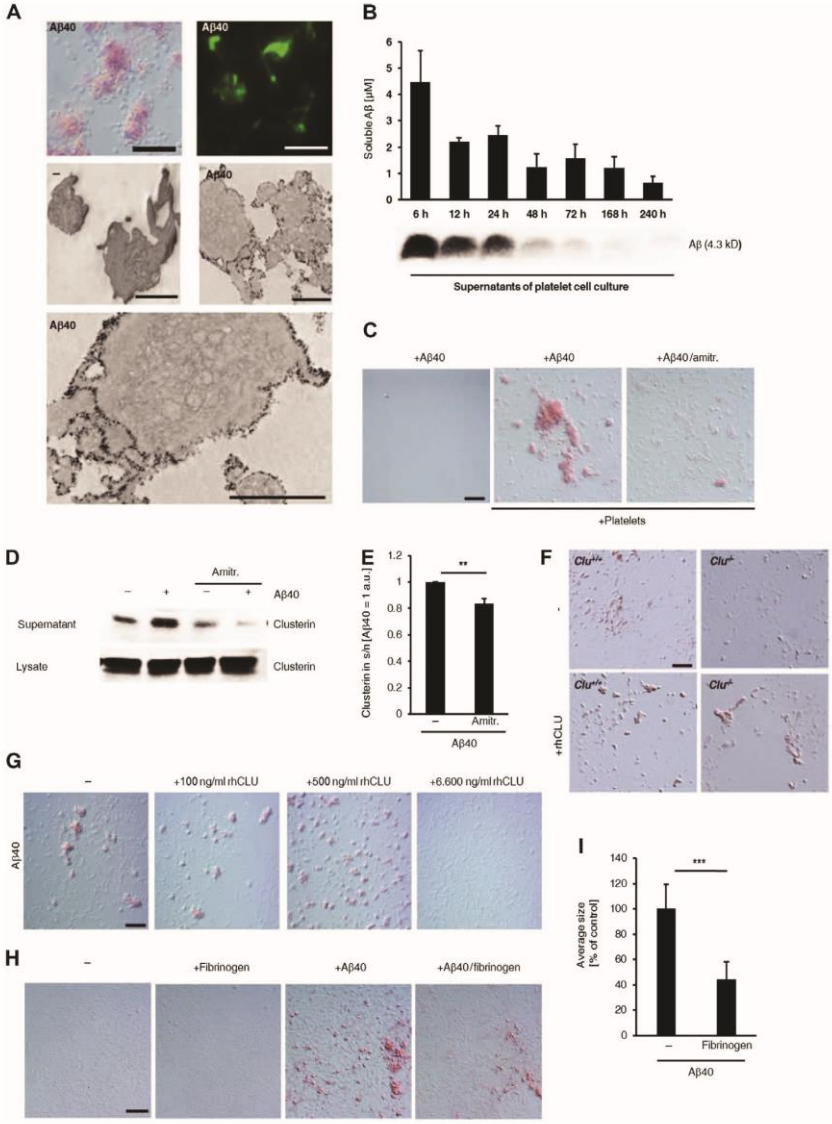

Fig. 1. Amyloid aggregate formation is modulated by platelet CLU release in culture. (**A**) Congo red staining of amyloid fibrils (top left; scale bar, 20 μm), immunofluorescence staining with the Aβ antibody 6E10 (top right; scale bar, 10 μm), and transmission electron microscopy (middle and rotated zoom below; scale bars, 1 μm) in different cultures of human platelets before (–) or after incubation with soluble, synthetic Aβ40 for 3 days. (**B**) Western blot analysis of supernatants from human platelet cultures incubated with Aβ40 for the indicated time. (**C**) Congo red staining of human platelets cultured in the presence of amitriptyline (amitr.). Scale bar, 50 μm. (**D** and **E**) Images (D) and quantification (E) of Western blotting of supernatants (s/n) and lysates of amitriptyline-treated platelets after stimulation with Aβ40. α-tubulin, loading control. a.u., arbitrary unit. (**F**) Congo red staining in cultures of platelets from $Clu^{-/-}$ and $Clu^{+/+}$ mice after stimulation with Aβ40 in the absence (–) or presence of recombinant human CLU (+rhCLU) (200 ng/ml). (**G**) Congo red staining of human platelets cultured in the presence of rhCLU. (**H** and **I**) Images (H) and quantification (I) of Congo red staining in human platelet cultures incubated with fibrinogen. Scale bar, 50 μm. Data are means ± SEM of three (E) or four (I) experiments. $^{**}P < 0.01$, $^{***}P < 0.001$, Student's *t* test. Images and blots in (A) to (C) and (F) and (G) are representative of three experiments.

major source of Aβ in the blood stream, which might contribute to the accumulation of Aβ in the brain and cerebral vessels (*38*–*40*). Aβ activates platelets and enhances platelet aggregation in vitro (*41*, *42*). Moreover, the adhesion of platelets to immobilized Aβ was observed under both static and flow conditions (*41*, *43*). In AD patients, platelet activation is enhanced (*44*), and in mice with carotid artery injury, the injection of Aβ enhances platelet adhesion to the injured vessel (*41*). Analysis of platelet function in the APP transgenic mouse strain APP23 revealed that these mice have an increased risk for arterial thrombosis (*45*), exhibit platelet accumulation at Aβ deposits in cerebral vessels (*41*, *45*), and develop CAA (*46*). Thus, platelets appear to have an important contribution to AD. Here, we investigated the molecular mechanisms mediated by platelets in the development of CAA and its implication for the progression of AD.

RESULTS

Aβ aggregate formation is stimulated by clusterin release from platelets

Platelets modulate soluble Aβ peptides into fibrillar Aβ structures and induce fibrillar Aβ aggregate formation in culture (*41*). To identify the molecular mechanisms behind this effect, we cultured human platelets with

soluble, synthetic Aβ40 for 3 days and analyzed the modulation of Aβ by Congo red staining and differential interference contrast microscopy (Fig. 1A, upper left panel). The presence of Congo red–positive Aβ deposits in platelet cell culture was confirmed by staining for fibrillar Aβ aggregates using an Aβ antibody (Fig. 1A, upper right panel). Aβ fibrils were detected on the surface of human platelets incubated with soluble, synthetic Aβ40 (Fig. 1A). The supernatant of Aβ-stimulated platelets alone was not sufficient to induce fibrillar Aβ aggregate formation (fig. S1A), suggesting that Aβ binding to platelets is a prerequisite for the formation of Aβ fibrils in platelet cell culture. To characterize the formation of Aβ deposits

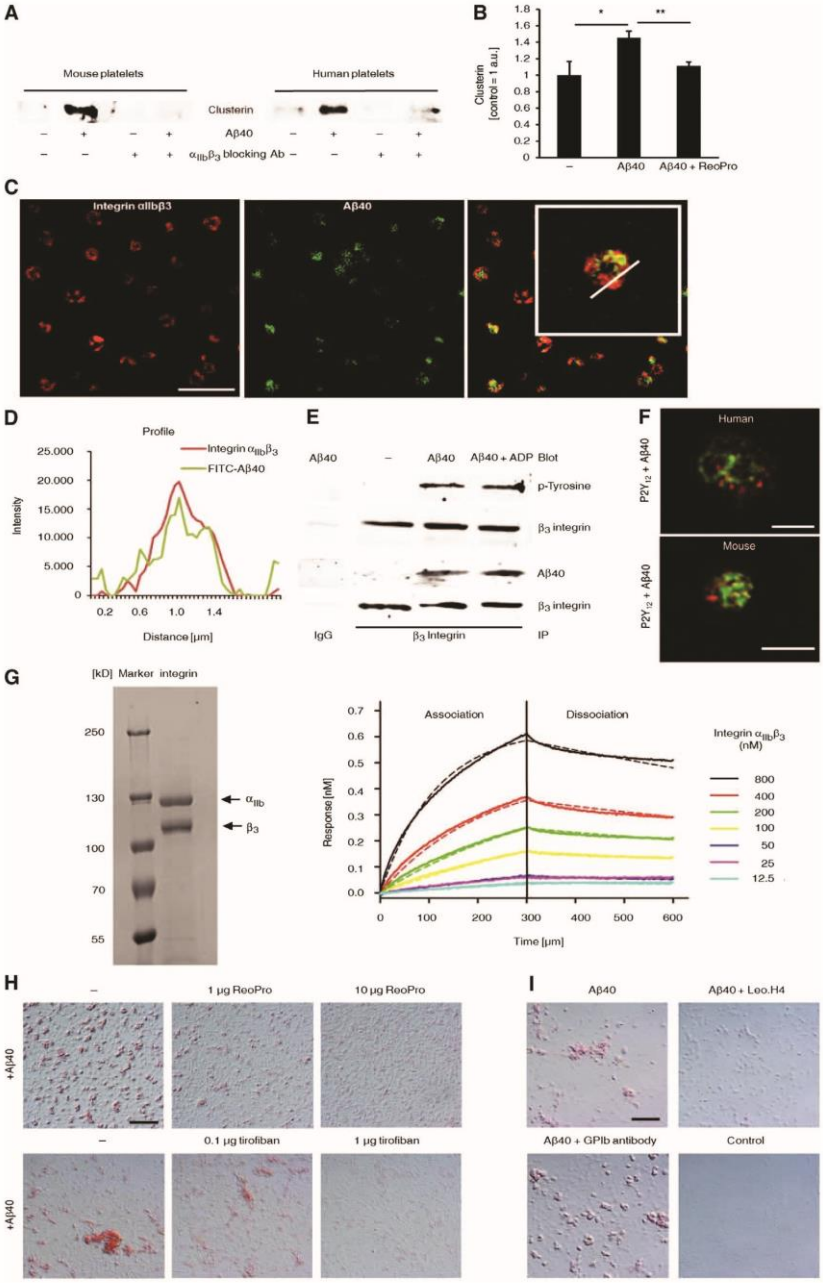

Fig. 2. **Aβ binds to integrin $\alpha_{IIb}\beta_3$ to induce CLU release and amyloid aggregate formation.** (**A**) Representative Western blots of supernatants of human and mouse platelets treated with integrin-blocking antibody (Ab), ReoPro, or Leo.H4, respectively. (**B**) Quantification of human CLU Western blots ($n = 4$). (**C** and **D**) Immunofluorescence staining (C) of integrin $\alpha_{IIb}\beta_3$ (red) and Aβ40 (green) shows colocalization (yellow). Line scan (D) was recorded along the white line in (C). (**E**) Human platelets were stimulated with Aβ40 and ADP (adenosine diphosphate) as indicated and immunoprecipitated with anti-β_3 integrin antibody. Immunoprecipitates were blotted with antiphosphotyrosine (p-tyrosine) and anti-Aβ antibody, respectively. (**F**) Immunostaining of $P2Y_{12}$ (red) and Aβ40 (green) in human and mouse platelets. Scale bars, 5 μm. (**G**) Right panel: BLI revealed direct binding of Aβ40 to integrin $\alpha_{IIb}\beta_3$. Values are means of four independent BLI experiments. Dashed lines represent global fitting curves using a 1:1 binding model. Left panel: purity of integrin $\alpha_{IIb}\beta_3$ preparation used for BLI is shown after SDS–polyacrylamide gel electrophoresis (SDS-PAGE) and Coomassie brilliant blue staining. (**H**) Representative Congo red stainings of amyloid aggregate formation in the presence of ReoPro and tirofiban, respectively, in human cell culture. (**I**) Aβ aggregation in murine platelet cell culture in the presence of blocking antibodies (integrin $\alpha_{IIb}\beta_3$ antibody, Leo.H4, or GPIb antibody as a control). Scale bar, 50 μm.

in more detail, we analyzed fibrillar Aβ aggregates with thioflavin staining (fig. S1B) and electron microscopy (Fig. 1A, middle and lower panels) and performed Western blot analysis to determine the remaining soluble Aβ40 in culture over time. We found that the amount of soluble Aβ40 decreased after 6 hours and was hardly detectable after 10 days (Fig. 1B). In line with this result, Aβ aggregate formation in these cultures was observed by 6 hours and increased over time (fig. S1C).

Treatment of platelets with the acid sphingomyelinase (ASM) inhibitor amitriptyline, which impairs the secretion of adenosine triphosphate (ATP) and P-selectin from platelets (*47*), significantly reduced Aβ aggregate formation (Fig. 1C and fig. S1D). Clusterin (CLU), a chaperone glycoprotein, is associated with the severity and risk of AD (*48*). The amount of CLU that platelets secreted increased in response to Aβ40, as measured by enzyme-linked immunosorbent assay (ELISA) (fig. S1E). To investigate whether CLU plays a role in platelet-mediated formation of fibrillar Aβ aggregates, we performed Western blot analysis and confirmed CLU release from platelets upon Aβ and thrombin stimulation (fig. S1F), whereas amitriptyline treatment markedly reduced CLU release (Fig. 1, D and E). Cultures of platelets from CLU knockout mice ($Clu^{-/-}$) displayed markedly reduced Aβ aggregate formation (Fig. 1F) but unaltered integrin $\alpha_{IIb}\beta_3$ abundance and activation upon Aβ40 stimulation (fig. S2, A and B). Platelet activation as measured by P-selectin exposure, a marker for degranulation of α-granules and integrin $\alpha_{IIb}\beta_3$ activation upon stimulation with standard agonists such as collagen-related peptide (CRP) and thrombin, was not substantially different between wild-type ($Clu^{+/+}$) and $Clu^{-/-}$ platelets (fig. S2, C and D). In addition, Western blot analysis revealed a greater amount of remaining soluble Aβ40 in supernatants from CLU-deficient platelets cultured with Aβ40 than in those from controls (fig. S2E).

To further explore the effects of CLU, we performed cell culture experiments with rhCLU (Fig. 1G). Control experiments without platelets confirmed that CLU alone did not induce Aβ aggregate formation in solution in vitro (fig. S2F). High amounts of rhCLU were not toxic to cultured platelets (fig. S2G). Addition of rhCLU increased Aβ aggregate formation in $Clu^{+/+}$ and $Clu^{-/-}$ platelets (Fig. 1F). Aβ aggregate formation was also enhanced in human platelets treated with rhCLU (Fig. 1G) or amitriptyline (fig. S2H). High amounts of rhCLU (6600 ng/ml), however, abolished fibrillar Aβ aggregate formation (Fig. 1G and fig. S2H). These data suggested that CLU promotes platelet-mediated Aβ aggregation.

Aβ40 binds to integrin $\alpha_{IIb}\beta_3$ to induce CLU release and fibrillar Aβ aggregate formation

Previous studies indicate that fibrinogen may contribute to AD pathology (*49*). When platelets were preincubated with human fibrinogen, subsequent Aβ aggregate formation was reduced (Fig. 1, H and I), suggesting that fibrinogen binding, presumably to its physiological receptor (integrin $\alpha_{IIb}\beta_3$), might prohibit Aβ binding to platelets and subsequently the formation of Aβ fibrils. To investigate whether integrin $\alpha_{IIb}\beta_{3i}$ is involved, we blocked the fibrinogen binding site in integrin $\alpha_{IIb}\beta_3$ using antibodies. Treating mouse platelets with Leo.H4 (a monoclonal antibody against mouse integrin $\alpha_{IIb}\beta_3$) or incubating human platelets with ReoPro [also known as abciximab, which binds integrin $\alpha_{IIb}\beta_3$ (also known as glycoprotein IIb/IIIa) as well as $\alpha_v\beta_3$] markedly impaired the release of CLU from platelets cultured with Aβ (Fig. 2, A and B), suggesting that integrin $\alpha_{IIb}\beta_3$ promotes the release of CLU from platelets in response to Aβ. To investigate this further, we cultured platelets with Aβ40 for 1 hour and found that Aβ colocalized with integrin $\alpha_{IIb}\beta_3$, as analyzed by confocal microscopy (Fig. 2, C and D). Moreover, immunoprecipitation of the β_3 subunit from platelets revealed phosphorylation (activation) of the β_3 subunit and pulldown of Aβ when platelets were incubated with Aβ40 (Fig. 2E), suggesting a functional interaction between Aβ and the β_3 subunit (Fig. 2E), supporting our confocal microscopy data. After a period of incubation, flow cytometry analysis detected fluorescent-tagged Aβ40 bound to the surface of platelets that express $\alpha_{IIb}\beta_3$ integrin (fig. S3, A and B). Tirofiban, the small synthetic nonpeptide blocker of glycoprotein IIb/IIIa (integrin $\alpha_{IIb}\beta_3$), significantly reduced platelet binding by Aβ and, as a control, fibrinogen (fig. S3B). Subsequent kinetic analysis by bio-layer interferometry (BLI) confirmed direct binding of monomeric Aβ40 to purified integrin $\alpha_{IIb}\beta_3$ with nanomolar affinity [dissociation constant (K_d) of 43.8 ± 18.8 nM; association rate constant (k_{on}) of $9.05 \times 10^3\ M^{-1}\ s^{-1} \pm 2.22 \times 10^3\ M^{-1}\ s^{-1}$; dissociation rate constant (k_{off}) of $3.86 \times 10^{-4}\ s^{-1} \pm 1.09 \times 10^{-4}\ s^{-1}$] (Fig. 2G). The formation of Aβ fibrils was inhibited by ReoPro or tirofiban in cultures of human platelets (Fig. 2H) and by Leo.H4 in cultures of murine platelets (Fig. 2I), together suggesting a prominent role for integrin $\alpha_{IIb}\beta_3$ in platelet-mediated modulation of Aβ peptides. In contrast, a blocking antibody to glycoprotein Ib (GPIb), a subunit of the von Willebrand factor (vWF) receptor on platelets, did not alter Aβ aggregate formation in murine platelet cultures (Fig. 2I), suggesting that this receptor does not play a role.

Platelets from Glanzmann's thrombasthenia patients display reduced or no ability to modulate Aβ in a manner correlated with the abundance of integrin $\alpha_{IIb}\beta_3$

To further investigate the impact of integrin $\alpha_{IIb}\beta_3$ in the formation of fibrillar Aβ aggregates, we used platelets from patients with Glanzmann's thrombasthenia (GT). GT platelets have either dysfunctional integrin $\alpha_{IIb}\beta_3$ or low amounts of the protein. As a result, platelet aggregation via fibrinogen bridging of platelets to other platelets cannot occur or is not adequate, respectively, resulting in significantly prolonged bleeding time. Clinical characteristics and flow cytometry analysis of all GT patients are shown in Table 1. GT is classified into three subtypes according to the abundance of integrin $\alpha_{IIb}\beta_3$ on platelets (*50*). To determine the subtype of the patients from whom platelets were isolated, we measured $\alpha_{IIb}\beta_3$ abundance by flow cytometry (Fig. 3A and Table 1) as well as binding of the antibody PAC1, which detects only active integrin, to determine the platelets' qualitative defects. In cultures of platelets from a patient with GT subtype I, in which integrin $\alpha_{IIb}\beta_3$ abundance was <5% that of control platelets (Fig. 3B), almost no Aβ fibrils were detectable after 3 days in culture with Aβ40 (Fig. 3D). In contrast, on platelets from a patient with GT subtype II, in which $\alpha_{IIb}\beta_3$ abundance was 5 to 25% that of controls, and from patients with GT subtype III, in which $\alpha_{IIb}\beta_3$ abundance was >25% that of controls, Aβ fibril formation was observed (Fig. 3D) despite no detectable integrin activation based on PAC1 binding (Fig. 3B). Together, these data indicate that the abundance of integrin $\alpha_{IIb}\beta_3$ determines the ability of these platelets to modulate soluble Aβ because all patients who were analyzed in this study showed qualitative defects (no PAC1 binding). In controls and types II and III GT platelets, pretreatment with ReoPro prevented aggregation of Aβ40 (Fig. 3D), indicating that Aβ aggregation was dependent on the fibrinogen receptor in these cells. The reduced formation of Aβ aggregates in GT platelet cultures was paralleled by absent (GT type I) or almost normal (GT type III) CLU abundance in the respective supernatants (Fig. 3E), meaning that CLU is a major determinant in platelet-induced Aβ aggregation.

ADP promotes Aβ aggregate formation

In contrast to our results for integrin $\alpha_{IIb}\beta_3$, immunofluorescence of cultured human and murine platelets indicated no colocalization of Aβ with the ADP receptor $P2Y_{12}$ (Fig. 2F). However, Aβ binding to platelets was enhanced by the addition of ADP (fig. S3A), suggesting that although the ADP receptor was not the interacting partner for Aβ,

Table 1. Characteristics of Glanzman thrombasthenia (GT) patients. Clinical characteristics and flow cytometry analysis in GT patients. p, protein; dup, duplication; 558C>A, substitution. Nomenclature according to the Human Genome Variation Society version 2.121101.

Patient (year of birth)	Bleeding severity	CD61 anti-β_3, %	CD42a, anti-GPIbIX, %	Mutation
No.1: Adult female (1969)	Bleeding tendency (moderate) Bruising	35	211	ITGA2B 3012dup9; p.(Val^{971}_Val^{973}dup) homozygous
No. 2: Adult male (1983)	Bleeding tendency (moderate)	4.5	255	ITGA2B 558C>A, p.(Tyr^{186*}) 558>A, (Y155X)
No. 3: Adult female (1981)	No bleeding tendency Bruising	29	70	ITGA2B 3004_3012dup9; p.(Val^{971}_Val^{973}dup) homozygous
No. 4: Adult female (1982)	Repeated epistaxis	75	187	Not known
No. 5: Adult male (1945)	Bleeding tendency (moderate) Bruising	8	123	Not known

ADP may contribute to the interaction. Administering the ADP scavenger apyrase, which is an ADPase, and clopidogrel, which antagonizes the ADP receptor $P2Y_{12}$, before Aβ stimulation dose-dependently reduced the formation of fibrillar Aβ aggregates that was induced by platelets from healthy volunteers (Fig. 3, F and H), whereas addition of ASA, an antithrombotic, did not appear to inhibit Aβ aggregation (Fig. 3F). Accordingly, Aβ-stimulated CLU release was substantially reduced after platelets were treated with apyrase or clopidogrel (Fig. 3G and fig. S4D) but not with ASA (Fig. 3G). When platelets were preincubated with both ASA and either apyrase or clopidogrel to prevent the release of the second wave mediators thromboxane A2 and ADP, the formation of Aβ fibrils was markedly diminished (fig. S4, A to C). Accordingly, CLU release was substantially reduced (fig. S4D). In line with these results, the addition of ADP to Aβ-stimulated platelets enhanced CLU release that appeared to be prevented by pretreatment with ReoPro (Fig. 3I). These data suggest that ADP plays an essential role in platelet-mediated Aβ aggregation.

Aβ40 binding to integrin $\alpha_{IIb}\beta_3$ induces platelet adhesion and outside-in signaling

Aβ stimulation neither induced up-regulation nor enhanced ADP-mediated induction of integrin $\alpha_{IIb}\beta_3$ abundance on the platelet surface (Fig. 4A). However, PAC1 binding was increased by treating platelets with Aβ in combination with ADP compared to ADP alone (Fig. 3B). Studies have shown that platelets adhere to immobilized Aβ under both static and dynamic flow conditions (*41*, *43*). To investigate whether integrin $\alpha_{IIb}\beta_3$ is involved in platelet adhesion to Aβ, platelets were incubated with Aβ40 and increasing amounts of ReoPro in a static solution. Platelet adhesion was dose-dependently inhibited by ReoPro as observed in control experiments using collagen and fibrinogen (Fig. 4B).

Integrin $\alpha_{IIb}\beta_3$–mediated cell adhesion to the extracellular matrix transmits signals within the cell that stimulates cell spreading, retraction, migration, and proliferation. The binding of different ligands, such as fibrinogen, to integrin $\alpha_{IIb}\beta_3$ induces a signaling cascade into the cell (called "outside-in signaling") leading to the phosphorylation and activation of various signaling molecules, including the kinase SYK or PLCγ2. Western blot analysis revealed that upon platelet stimulation with Aβ, prominent phosphorylation of SYK and PLCγ2 was detected with a maximum abundance at 120 s of incubation (Fig. 4, C to E). PLCγ2 phosphorylation was dependent on the kinase SRC as well as SYK (Fig. 4F). Furthermore, Aβ-induced platelet aggregation and calcium (Ca^{2+}) mobilization in platelets were dependent on SYK (Fig. 4G and fig. S5A). Further, tirofiban significantly reduced Aβ-induced platelet aggregation, as did the control collagen (Fig. 4H). In contrast to CLU release (Fig. 3I) and Aβ binding to platelets (fig. S3A), ADP did not enhance platelet aggregation, ATP release, or PLCγ2 phosphorylation in response to Aβ (fig. S5, A to C). The phosphorylation of SYK and PLCγ2 was markedly reduced in the presence of tirofiban or ReoPro, respectively (Fig. 4I). Reduced phosphorylation of SYK and PLCγ2 was also observed after Aβ stimulation of platelets from GT patients (Fig. 4J). The abundance of phosphorylated SYK and PLCγ2 appeared to be relatively greater in platelets from GT type III than GT type I patients (Fig. 4J), which reflects low integrin abundance, CLU release, and extent of Aβ aggregation (Fig. 3, A to E).

Fibrinogen binds to platelet-bound Aβ40

Thus far, we have found that Aβ binds to integrin $\alpha_{IIb}\beta_3$ and induces platelet aggregation. Therefore, we asked whether fibrinogen can bridge platelets by analyzing fibrinogen binding to platelet-bound Aβ. Increasing concentrations of Aβ40 induced the binding of fibrinogen, as measured by flow cytometry (Fig. 5A). ADP did not enhance Aβ-induced fibrinogen binding, whereas ReoPro induced a significant reduction (Fig. 5B). Subsequent kinetic analysis confirmed binding of monomeric Aβ40 to fibrinogen with a K_d of 15 nM and of 5-hour-oligomerized Aβ40 with a K_d of 27 nM (Fig. 5C). Monomeric Aβ42 showed a K_d of 104 nM, and 2.5-hour-oligomerized Aβ42 showed a K_d of 265 nM (Fig. 5C); these were used as a positive control (*51*). In contrast to the above experiments (Fig. 1H), preincubation of platelets with fibrinogen for 30 min did not reduce binding of fluorescent-tagged Aβ40 as measured by flow cytometry (Fig. 5D), suggesting that Aβ can bind to the fibrinogen-integrin complex.

Aβ40 binds with its RHDS sequence to integrin $\alpha_{IIb}\beta_3$ to induce outside-in signaling

APP and its derivative proteolytic fragment peptides contain an RHDS sequence at the amino acid residues 5 to 8 of the Aβ domain (*52*). To investigate whether Aβ binds with its RHDS sequence to the RGDS binding domain of integrin $\alpha_{IIb}\beta_3$, as does fibrinogen (*53*), we used mutated Aβ40 peptides that had either an inverted (SDHR) or a scrambled (HRSD) motif, respectively. Neither $Aβ40_{inverted}$ nor $Aβ40_{scrambled}$ induced PLCγ2 phosphorylation, Ca^{2+} mobilization, or platelet aggregation (Fig. 6, A to C). Moreover, CLU release was strongly reduced (Fig. 6D). Accordingly, platelets cultured with mutated Aβ peptides failed to induce the formation of Aβ fibrils (Fig. 6E).

To investigate the structural consequences of Aβ40 binding to integrin $\alpha_{IIb}\beta_3$ at an atomistic level, we performed all-atom molecular dynamics (MD) simulations of a complex of the propeller, βA, and hybrid domains of integrin $\alpha_{IIb}\beta_3$ bound to the first 14 residues of Aβ40, $Aβ40_{inverted}$, or $Aβ40_{scrambled}$ (Fig. 6, F and G) of 500-ns length each. The simulations

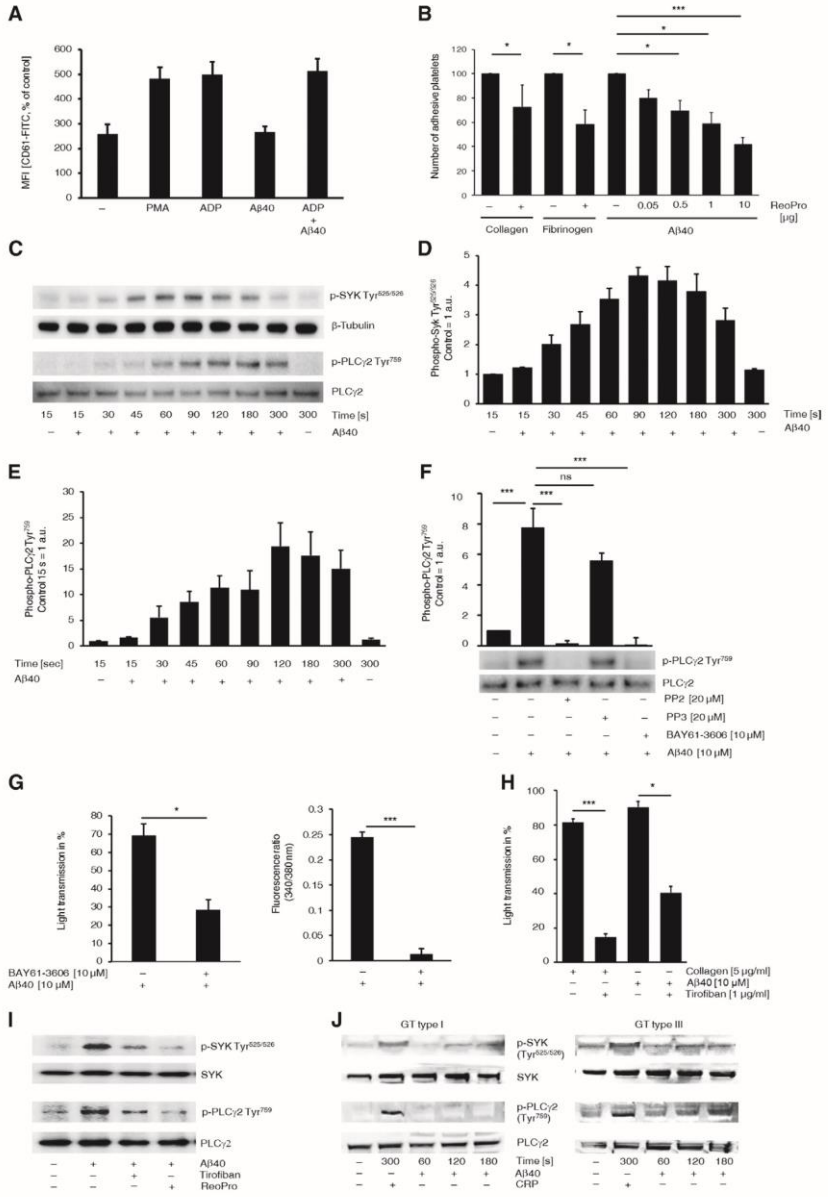

Fig. 4. **Aβ binding to integrin $\alpha_{IIb}\beta_3$ induces platelet adhesion and outside-in signaling.** (**A**) $\alpha_{IIb}\beta_3$ abundance assessed by flow cytometry [mean fluorescence intensity (MFI) CD61–FITC (fluorescein isothiocyanate)] in platelets stimulated with PMA (phorbol 12-myristate 13-acetate), ADP, Aβ40, or ADP and Aβ40 (n = 6 experiments). (**B**) Platelet adhesion to immobilized Aβ40 under static conditions in the presence or absence of ReoPro. Coverslips with collagen and fibrinogen served as positive controls (n = 3 to 4 experiments). (**C** to **E**) Representative Western blots (C) and quantification (D and E) for phosphorylated spleen tyrosine kinase (SYK) and phospholipase Cγ2 (PLCγ2) in platelets stimulated with Aβ40 (n = 4 experiments). (**F**) Western blotting assessing the effects of inhibitors of SRC (PP2) or SYK (BAY61-3606) on Aβ40-induced phosphorylation of PLCγ2 Tyr^{759} (n = 4 experiments). (**G**) Effects of BAY61-3606 on platelet aggregation (left) and Ca^{2+} mobilization (right) (n = 3 to 4 experiments). (**H**) Platelet aggregation of human platelets in response to collagen (control) and Aβ40 (n = 3 experiments). (**I**) Representative Western blots of phosphorylated SYK and PLCγ2. PLCγ2 and SYK were used as loading control (n = 3 experiments). (**J**) Western blot analysis of phospho-SYK and phospho-PLCγ2 in platelets from GT patients after stimulation with CRP or Aβ40 (n = 1 patient of GT types I and II, n = 3 patients of GT type III). Data are means ± SEM. *P < 0.05, ***P < 0.001, t test; ns, not significant.

region of the center of helix α1 and the N terminus of helix α7: the Aβ40 complex shows tighter hydrophobic interactions ("T-junction formation") (*54*, *55*) than the complexes of $A\beta40_{inverted}$ and $A\beta40_{scrambled}$ (Fig. 6I). Furthermore, the Aβ40 complex showed a significantly more pronounced shift of the βA domain relative to the propeller domain (Fig. 6H). T-junction formation (*54*, *55*) and a shift of the βA domain (*56*, *57*) have been suggested previously to lead to a change in the interdomain βA/hybrid domain hinge angle (Fig. 6G) (*58*), which is considered to result in integrin activation (Fig. 6F) (*59*). Together, the MD simulations reveal that Aβ40 bound via its RHDS motif leads to conformational changes in the headpiece of $\alpha_{IIb}\beta_3$ that have been linked to integrin activation.

Antiplatelet therapy reduces vascular Aβ plaques (CAA) in cerebral vessels of APP23 transgenic mice

To explore the effects of platelets on Aβ fibril formation in vivo, we treated APP23 transgenic mice, which develop CAA (*60*), with an antiplatelet

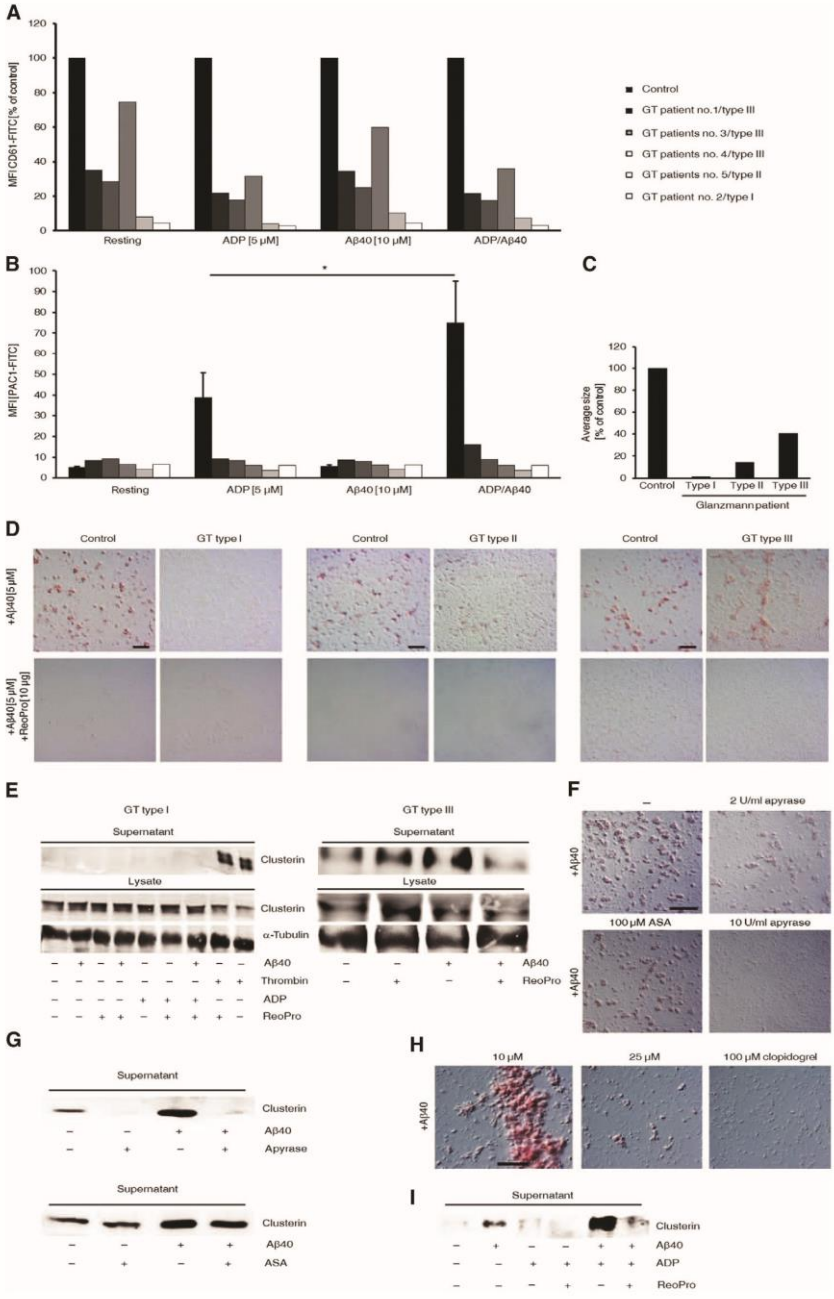

Fig. 3. Platelets from GT patients failed to modulate Aβ or display reduced Aβ aggregate formation. (**A** and **B**) Flow cytometry analysis of platelets from GT patients to examine (A) expression and (B) activation of integrin $\alpha_{IIb}\beta_3$ upon Aβ stimulation. (**C** and **D**) Quantification of fibrillar Aβ aggregates (C) and representative images of Congo red staining (D) in platelets from patients with different subtypes of GT incubated with Aβ40 for 3 days in the absence or presence of ReoPro. Scale bar, 50 μm. (**E**) Western blot analysis for CLU in supernatants and lysates of platelets from GT patients (n = 1 patient of GT types I and II, n = 3 patients of GT type III; controls n = 6). (**F**) Platelet-induced amyloid aggregate formation in the presence of acetylsalicylic acid (ASA) or apyrase in platelets from healthy volunteers (n = 3 experiments). Scale bar, 50 μm. (**G**) Western blots of supernatants from human platelets treated with apyrase or ASA before stimulation with Aβ40 (n = 3 experiments). (**H**) Amyloid aggregate formation in the presence of clopidogrel (n = 3 experiments). Scale bar, 50 μm. (**I**) Representative Western blots of CLU in supernatants of human platelets in the presence and absence of ReoPro (n = 3 experiments). Data are means ± SEM. *P < 0.05, **P < 0.01, Student's t test.

revealed overall minor structural differences when considering the integrin domains separately [root mean square deviation (RMSD) over all C_α atoms <3.5 Å; fig. S6], indicating stable simulations. The Aβ40 variants remained in the binding region between the propeller and βA domains (RMSD, <2 Å), with $A\beta40_{inverted}$ and $A\beta40_{scrambled}$ showing larger structural differences than Aβ40 (figs. S7 and S8). Significant structural variations were found between the βA domain of the Aβ40 complex and the $A\beta40_{inverted}$ and $A\beta40_{scrambled}$ complexes, respectively, in the

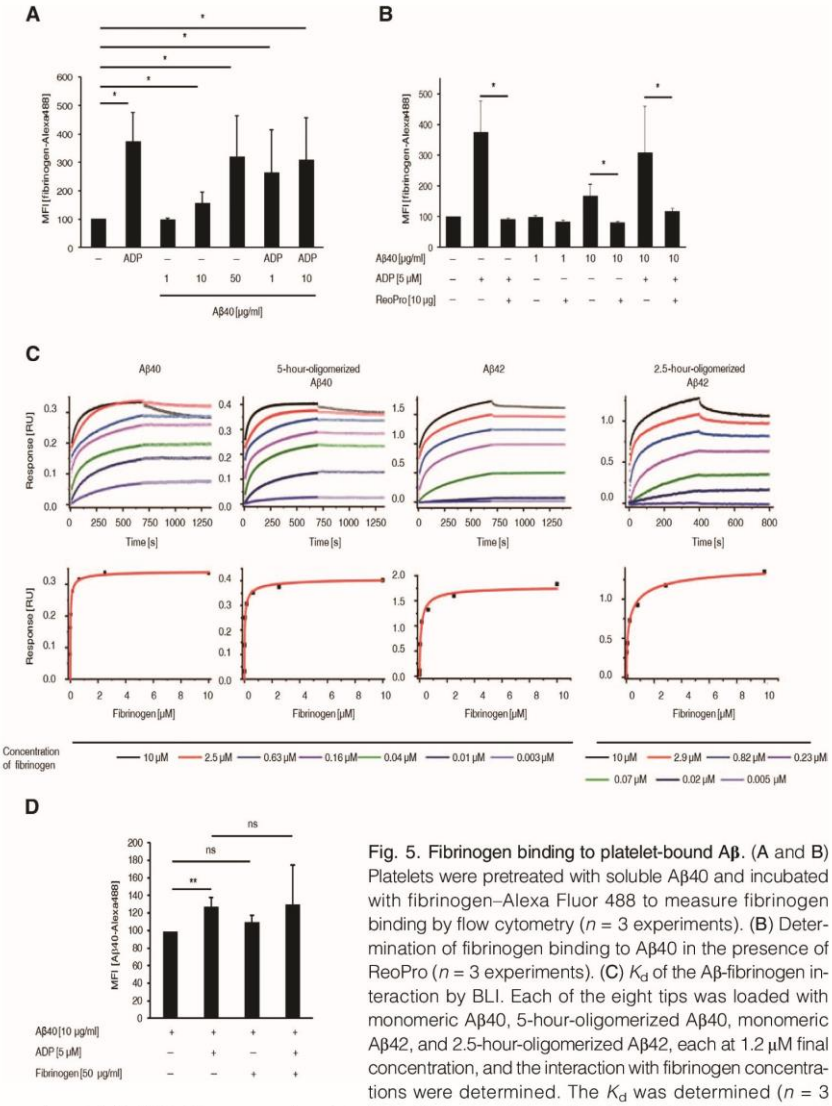

Fig. 5. Fibrinogen binding to platelet-bound Aβ. (**A** and **B**) Platelets were pretreated with soluble Aβ40 and incubated with fibrinogen–Alexa Fluor 488 to measure fibrinogen binding by flow cytometry ($n = 3$ experiments). (**B**) Determination of fibrinogen binding to Aβ40 in the presence of ReoPro ($n = 3$ experiments). (**C**) K_d of the Aβ-fibrinogen interaction by BLI. Each of the eight tips was loaded with monomeric Aβ40, 5-hour-oligomerized Aβ40, monomeric Aβ42, and 2.5-hour-oligomerized Aβ42, each at 1.2 μM final concentration, and the interaction with fibrinogen concentrations were determined. The K_d was determined ($n = 3$ experiments). (**D**) Platelets were preincubated with fibrinogen followed by incubation with Aβ40–Alexa Fluor 488. Aβ40 binding to platelets was measured by flow cytometry ($n = 3$ experiments). Data are means ± SEM. $^*P < 0.05$, $^{**}P < 0.01$, Student's t test.

therapy. Because treatment of mice with ReoPro is not feasible (*61*), we used tirofiban injections to inhibit platelet activation. However, tirofiban was not satisfying because platelet inhibition in mice was only temporary and returned to normal levels within 2 hours (fig. S9). Thus, we decided to treat APP23 mice with clopidogrel, which was previously shown to effectively inhibit platelet activation (*62*) for a period of 3 months. We then assessed Aβ deposition by immunohistochemistry. It is well known that a robust increase in brain Aβ40 begins at the age of 8 months in the frontal cortex. At 12 months of age and later, there is a progressive increase in plaque number and size in different brain regions of APP23 mice (*29*). Immunohistochemistry of clopidogrel-treated and untreated APP23 mice revealed the appearance of senile and diffuse Aβ plaques in the hippocampus and cortex of both groups. Plaque size in the cortex of clopidogrel-treated APP23 mice was comparable to mice that did not receive therapy (Fig. 7, A and B). However, we did see reduced Aβ deposits in the hippocampus of clopidogrel-treated mice, although this did not reach statistical significance (Fig. 7, A and B).

Analysis of CAA was performed by confocal microscopy and Aβ staining with appropriate antibodies to visualize Aβ plaque formation in cerebral vessels (Fig. 7C), as well as Congo red staining (Fig. 7D) to identify Aβ-positive vessels. The 6E10 antibody used in this study is an amyloid-specific pan-Aβ antibody detecting both Aβ40 and Aβ42 (*63*) that has been utilized in different in vitro and in vivo studies (*64*–*66*). The number of cerebral vessels that were affected by CAA, the total area of CAA, and the number of affected vessels were significantly reduced in mice treated with clopidogrel (Fig. 7, C to E). Reduced CAA in clopidogrel-treated APP23 transgenic mice was coincident with strongly reduced platelet activation (Fig. 7G) and significantly reduced plasma CLU levels (Fig. 7F). Together, the inhibition of platelet activation reduced Aβ plaque formation in cerebral vessels of APP23 mice.

DISCUSSION

The present study discloses an important role of platelets in the development of vascular Aβ deposits (CAA). According to the present observations, Aβ40 bound with its RHDS sequence to platelet integrin $\alpha_{IIb}\beta_3$ and induced the release of CLU resulting in Aβ fibril formation, a key event in the development of CAA. CLU is a chaperone protein involved in rapid progression of AD because CLU influences the structure and toxicity of Aβ peptides and Aβ deposition. Aβ-induced outside-in signaling of platelet integrin $\alpha_{IIb}\beta_3$ resulted in ADP release that played an important role in CLU-mediated Aβ aggregate formation because treatment with clopidogrel prevented platelet-induced formation of Aβ aggregates in culture and reduced CAA in APP23 transgenic mice in vivo. The analysis of platelets from GT patients confirmed the relevance of integrin $\alpha_{IIb}\beta_3$ for platelet-mediated Aβ fibril formation and CLU release. Besides, Aβ40 binding to integrin $\alpha_{IIb}\beta_3$ induced platelet adhesion and platelet aggregation via fibrinogen binding that might play an important role in the occlusion of CAA-affected cerebral vessels. Aβ-induced signaling in platelets and functional consequences were summarized in a schematic illustration (Fig. 7H).

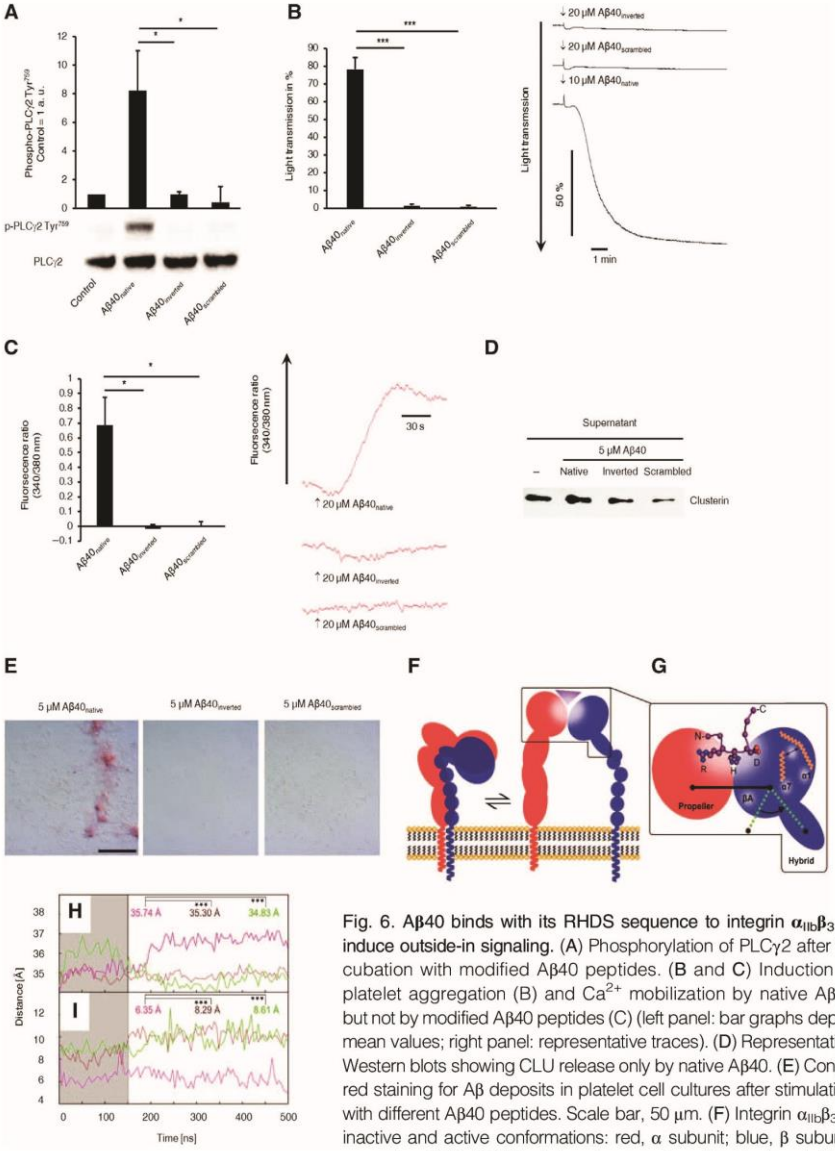

Fig. 6. Aβ40 binds with its RHDS sequence to integrin $\alpha_{IIb}\beta_3$ to induce outside-in signaling. (A) Phosphorylation of PLCγ2 after incubation with modified Aβ40 peptides. (B and C) Induction of platelet aggregation (B) and Ca^{2+} mobilization by native Aβ40 but not by modified Aβ40 peptides (C) (left panel: bar graphs depict mean values; right panel: representative traces). (D) Representative Western blots showing CLU release only by native Aβ40. (E) Congo red staining for Aβ deposits in platelet cell cultures after stimulation with different Aβ40 peptides. Scale bar, 50 μm. (F) Integrin $\alpha_{IIb}\beta_3$ in inactive and active conformations: red, α subunit; blue, β subunit; magenta, Aβ40. (G) Headpiece in complex with shortened Aβ40 used for MD simulations. Double arrow, distance between helix α1 and helix α7; black line, distance between centers of mass (COM) of propeller and βA domains. Green lines, change in interdomain βA/hybrid domain hinge angle. (H and I) Distance between COM of propeller and βA domains (H) and between helices α1 and α7 (I) computed from trajectories of the $\alpha_{IIb}\beta_3$ headpiece bound to Aβ40 (magenta). $A\beta40_{scrambled}$ (brown), $A\beta40_{inverted}$ (green), initial 150 ns were disregarded for analyses. Numbers in (H) and (I) depict averages over three replicates each SEM < 0.02 Å. Data are means ± SEM. $^*P < 0.05$, $^{***}P < 0.001$, Student's *t* test.

Aβ fibril formation in cell culture occurs at sites of activated platelets and results from platelet-mediated modulation of soluble Aβ (*41*). Reduced platelet secretion upon inhibition of ASM as well as addition of fibrinogen, which competed for integrin binding with Aβ, reduced fibril formation, suggesting that platelet degranulation and integrin $\alpha_{IIb}\beta_3$ played a pivotal role in platelet-mediated Aβ oligomerization. The crucial role of integrin $\alpha_{IIb}\beta_3$ was supported by inhibitory experiments with ReoPro, tirofiban (human platelets), and Leo.H4 (murine platelets). Cell culture experiments using platelets from GT patients confirmed the results with integrin-inhibiting antibodies and demonstrated that integrin expression level determined the ability of platelets to induce Aβ fibril formation. Platelets from GT type I did not induce Aβ oligomerization and displayed no CLU release, whereas platelets from GT types II and III induced moderate Aβ aggregate formation and CLU release. Because platelets from GT types II and III showed almost no PAC1 binding, it is tempting to speculate that Aβ binds to activated and nonactivated integrin $\alpha_{IIb}\beta_3$. This is in line with the results of our all-atom MD simulations suggesting that Aβ binds to nonactivated integrin. In contrast, flow cytometric analysis revealed that Aβ40–Alexa Fluor 488 does not bind to nonactivated integrin with a similar binding property as fibrinogen. Moreover, platelets became activated in the platelet culture model used in this study probably because the surface of the chamber has adhesive properties for platelets that might lead to integrin activation. However, according to our data, it is not entirely clear if Aβ is able to bind to nonactivated integrins or if a conformational change of integrins is necessary. This issue still needs further investigation and will be of major interest because Aβ40 would bind to integrins on circulating platelets in an arbitrary manner if no conformational change of integrin $\alpha_{IIb}\beta_3$ is necessary for Aβ binding to platelets.

Our data revealed that Aβ40 interacts with integrin $\alpha_{IIb}\beta_3$ with high affinity because we determined a K_d of Aβ40 that is near the (patho-)physiological concentration of Aβ40 in plasma. Furthermore we provided evidence that Aβ40 binding to integrin $\alpha_{IIb}\beta_3$ is mediated via its RHDS sequence. Earlier, it has been reported that the sequence RHDS (amino acids 5 to 8 of Aβ) is responsible

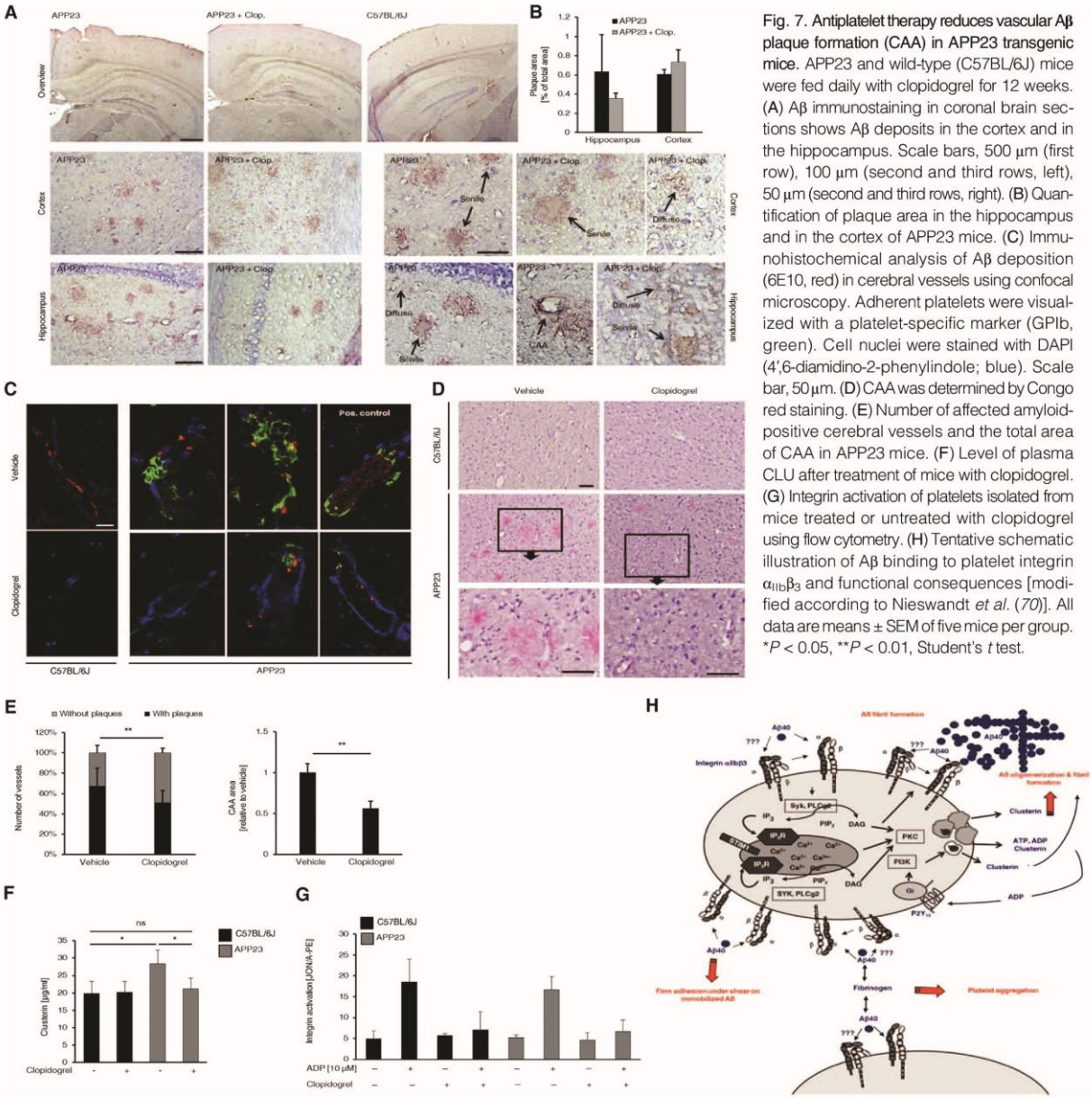

Fig. 7. **Antiplatelet therapy reduces vascular Aβ plaque formation (CAA) in APP23 transgenic mice.** APP23 and wild-type (C57BL/6J) mice were fed daily with clopidogrel for 12 weeks. (**A**) Aβ immunostaining in coronal brain sections shows Aβ deposits in the cortex and in the hippocampus. Scale bars, 500 µm (first row), 100 µm (second and third rows, left), 50 µm (second and third rows, right). (**B**) Quantification of plaque area in the hippocampus and in the cortex of APP23 mice. (**C**) Immunohistochemical analysis of Aβ deposition (6E10, red) in cerebral vessels using confocal microscopy. Adherent platelets were visualized with a platelet-specific marker (GPIb, green). Cell nuclei were stained with DAPI (4′,6-diamidino-2-phenylindole; blue). Scale bar, 50 µm. (**D**) CAA was determined by Congo red staining. (**E**) Number of affected amyloid-positive cerebral vessels and the total area of CAA in APP23 mice. (**F**) Level of plasma CLU after treatment of mice with clopidogrel. (**G**) Integrin activation of platelets isolated from mice treated or untreated with clopidogrel using flow cytometry. (**H**) Tentative schematic illustration of Aβ binding to platelet integrin $\alpha_{IIb}\beta_3$ and functional consequences [modified according to Nieswandt *et al.* (*70*)]. All data are means ± SEM of five mice per group. $^*P < 0.05$, $^{**}P < 0.01$, Student's *t* test.

for an adhesion-promoting activity of Aβ (*67*) that might involve platelet membrane integrin receptors (*68*). Besides integrin $\alpha_{IIb}\beta_3$, platelets contain $\alpha_V\beta_3$ and $\alpha_5\beta_1$ integrins, which engage extracellular matrix ligands that contain the canonical Arg-Gly-Asp (RGD) motif (*69*, *70*). Thus, these integrins might also act as receptors for Aβ representing an alternative mechanism. Future work is needed to address whether Aβ is able to bind to other integrins via the RGD motif and whether that results in related cellular consequences.

Our all-atom MD simulations confirmed Aβ40 binding to the head region of integrin $\alpha_{IIb}\beta_3$ to introduce an allosteric conformational change that has been linked to integrin activation before (*54*, *55*). The C-terminal domain of Aβ protruded from the Aβ/integrin complex, which might allow further binding of Aβ40 molecules to induce Aβ oligomerization and Aβ fibril formation at the surface of platelets. Recent studies propose that the main aggregation seems to happen via the C terminus of Aβ40 and that fibril formation is known to take place at residues 16 to 20 (*71*, *72*).

CLU is associated with the severity, pathology, and progression of AD and can influence the structure and toxicity of Aβ. Various clinical trials show that increased concentrations of plasma CLU correlate with the rate of clinical progression in AD (*48*, *73*, *74*). CLU has an ambivalent role in AD because it displays anti- and pro-AD properties. Cell culture experiments suggest that CLU-mediated effects are determined by the concentration of the protein (*73*). The fact that increased CLU levels in APP23 transgenic mice were reduced to normal levels by antiplatelet therapy suggests that platelets may be the major source of plasma CLU and not astrocytes (*73*) and emphasizes the crucial role of platelet-derived CLU in CAA. Knockout of CLU reduced but does not prevent Aβ plaques in the brain of PDAPP mice (*75*). In line with previous reported results, Aβ stimulation of CLU-deficient platelets resulted in significantly reduced but not absent platelet-mediated Aβ fibril formation, suggesting an important but not essential role for CLU in platelet-induced Aβ fibril formation.

Absent colocalization of Aβ and the ADP receptor $P2Y_{12}$ proposed that not Aβ binding to the ADP receptor but ADP itself plays a pivotal role in platelet-mediated Aβ fibril formation. Both the ADP scavenger apyrase and the $P2Y_{12}$ inhibitor clopidogrel reduced CLU release and prevented Aβ aggregate formation in vitro, and clopidogrel decreased CAA in APP23 transgenic mice in vivo. Moreover, ADP increased binding of Aβ40 to platelets and amplified the release of CLU upon stimulation of platelets with Aβ. Aβ-induced platelet activation and aggregation are already shown in different studies (*41*–*44*, *68*, *76*). We observed no priming of Aβ-induced effects on platelet activation by ADP. However, Aβ40 enhanced PAC1 binding upon ADP stimulation of platelets. Fibrinogen binding to Aβ might explain the ability of Aβ to induce platelet aggregation and suggests that fibrinogen bridges Aβ/integrin $\alpha_{IIb}\beta_3$ complexes of platelets. Here, we determined the binding affinity of fibrinogen and Aβ40 and found slightly lower K_d values for monomeric compared to oligomeric Aβ40. Recent studies show that depletion of fibrinogen is successful to reduce CAA in AD mice (*49*). The authors provide evidence for Aβ mediated oligomerization of fibrinogen playing a critical role in AD (*51*). According to the present observations, we assume that Aβ-induced platelet aggregation and fibrinogen binding play a critical role in CAA because increased platelet activation in APP23 mice (*45*) may lead to enhanced fibrinogen binding that is critically involved in the occlusion of cerebral vessels. We previously observed occlusion of cerebral vessels in AD transgenic mice (*41*).

To date, the reason for the increase of Aβ within the cerebral vessel is unclear. Increased production or altered clearance of Aβ might cause CAA. Moreover, SMCs in the media support the deposition of Aβ in the vessel wall (*77*), but the onset of Aβ deposition occurs at the outer basement membrane (*27*). According to our data, we suggest that platelets are responsible to induce the onset of CAA. This idea is supported by antiplatelet therapy of APP23 mice leading to inhibited platelet activation, reduced CLU release, and significantly reduced CAA with less adherent platelets at Aβ deposits. Most noteworthy, GT patients are described to not suffer from neurodegenerative diseases, strongly suggesting that platelets and integrin $\alpha_{IIb}\beta_3$ are markedly involved in the pathology of AD (*78*). Here, we did not observe alterations in Aβ deposition in brain parenchyma, although a reduction of Aβ plaques was observed in the hippocampus without reaching statistical significance. This might be due to the short period (for 3 months) or late start of clopidogrel treatment of APP23 mice. Here, mice were treated from 13 months of age because the onset of CAA is around 12 months of age. However, parenchymal Aβ deposition at this time point is already prominent (*29*, *46*). Thus, our in vivo findings support the mechanism suggested by cell culture and other in vitro experiments and suggest that antiplatelet therapy may alleviate fibril formation. However, testing a long-term antiplatelet therapy in future experiments will be important to clarify whether this represents a new therapeutic approach to prevent fibril formation and CAA in mice and humans.

Together, our data revealed a critical and direct contribution of platelets in the development of CAA through an interaction with and aggregating effect on Aβ, and we propose that this contributes to the progression of AD.

MATERIALS AND METHODS

Chemicals and antibodies

Soluble Aβ(1–40) (American Peptide, cat. no. 62-0-78A) sequence (single-letter code), DAEFRHDSGYEVHHQKLVFFAEDVGSNKGAIIGLMVGGVV. Synthetic mutated Aβ(1–40) (Innovative Peptide Solutions): Aβ(1–40) scrambled RHDS-Sequence, DAEFHRSDGYEVHHQKLVFFAEDVGSNKG AIIGLMVGGVV (Arg-His-Asp-Ser→His-Arg-Ser-Asp, RHDS→HRSD). Aβ(1–40) inverted RHDS-Sequence, DAEFSDHRGYEVHHQKLVFFAEDV GSNKGAIIGLMVGGVV (Arg-His-Asp-Ser→Ser-Asp-His-Arg, RHDS→SDHR). Stock solutions with a concentration of 1 mg/ml were solved in a sterile tris buffer and stored at −20°C. Before application, peptides were tested for correct sequence and purity by mass spectroscopy (matrix-assisted laser desorption/ionization) and reversed-phase high-performance liquid chromatography analysis. Apyrase (grade III, from potato), fura-2/AM (fura-2 acetoxymethylester), and BAY61-3606 (2-[[7-(3,4-dimethoxyphenyl)-imidazo[1,2-c]pyrimidin-5yl]amino]pyridine-3-carboxamide hydrochloride) were from Sigma. PP2 (3-(4-chlorophenyl) 1-(1,1-dimethylethyl)-1*H*-pyrazolo[3,4-*d*]pyrimidin-4-amine) and PP3 (1-phenyl-1*H*-pyrazolo[3,4-*d*]pyrimidin-4-amine) were from Tocris Bioscience. The phospho-SYK ($Tyr^{525/526}$) antibody (#3584), phospho-PLCγ2 (Tyr^{759}) (#3874), and unmodified PLCγ2 (#2711) antibodies, as well as the horseradish peroxidase (HRP)–conjugated secondary antibodies (#7074 and #7076), were from Cell Signaling Technology. The β-tubulin antibody (clone AA2) (#05-661) was from Upstate/Millipore. All other reagents were of analytical grade.

GT patients

Five patients belonging to unrelated families with a diagnosis of GT were analyzed. Diagnosis of GT was done on the basis of clinical and hematologic parameters. Bleeding characteristics were evaluated by examining available hospital records. CD61 and CD42a expression was performed by flow cytometry. Integrin $\alpha_{IIb}\beta_3$ activation (PAC1 binding) upon Aβ stimulation was determined using PAC1 antibody that specifically recognizes the active form of the integrin. The MFI for each measurement was determined by flow cytometry. The Ethics Committee of the Heinrich Heine University approved the collection of blood samples based on the patients' consent.

Animals

APP23 mice were provided by Novartis Pharma AG. APP23 mice are intensively characterized for their AD phenotype and formation of Aβ plaques in cerebral vessels and brain parenchyma (*60*, *64*–*66*). APP23 mice first develop individual Aβ plaques in the neocortex at 6 months of age. The onset of CAA is at 12 months of age (*46*). For experiments, 13-month-old male or female APP23 transgenic mice (*60*) and age-matched C57BL/6J were used, and antiplatelet therapy with clopidogrel (active enantiomer) for 12 weeks was performed. The mice (five per group) were fed once daily with 2 mg of clopidogrel (Actavis) or vehicle as control. At the age of 16 months, APP23 mice were sacrificed, and brains were removed and analyzed for amyloid plaque formation (CAA). Male and female CLU-deficient mice ($Clu^{-/-}$) were backcrossed to the C57BL/6

strain, and genotype was assessed by polymerase chain reaction as described (*79*). All animal experiments were conducted according to the Declaration of Helsinki and German law for the welfare of animals. The protocol was approved by the Heinrich Heine University Animal Care Committee and by the district government of North Rhine-Westphalia (LANUV, NRW; permit number: 84-02.05.20.12.284; O 86/12; 84-02.04.2012.A405).

Histology

Brains were removed and immersion-fixed for 24 hours in 4% paraformaldehyde and then cryoprotected in 30% sucrose for an additional 24 hours. After freezing in nitrogen-cooled propane, thick coronal sections were cut through the brains using a cryostat. The 25-µm-thick sections were collected in 0.1 M tris-buffered saline and stained immunohistochemically. The antibody 6E10 (1:1000, BioLegend) was used for immunostaining of Aβ, and antibody CD42b (1:100, Xia.G7, emfret ANALYTICS) was used for immunostaining of the platelet-specific GPIb. The 14-µm-thick sections were stained with Congo red according to standard protocols.

Murine platelet preparation

Murine blood from retro-orbital plexus was collected and centrifuged at 250*g* for 5 min at room temperature (RT). To obtain platelet-rich plasma (PRP), the supernatant was centrifuged at 50*g* for 6 min. PRP was washed twice at 650*g* for 5 min at RT, and pellet was resuspended in Tyrode's buffer [136 mM NaCl, 0.4 mM Na_2HPO_4, 2.7 mM KCl, 12 mM $NaHCO_3$, 0.1% glucose, 0.35% bovine serum albumin (BSA) (pH 7.4)] supplemented with prostacyclin (0.5 µM) and apyrase (0.02 U/ml). Before use, platelets were resuspended in the same buffer and incubated at 37°C for 30 min.

Human platelet preparation

Fresh acid citrate dextrose anticoagulated blood was obtained from healthy volunteers between the ages of 18 and 50 years. The blood was centrifuged at 200*g* for 10 min. PRP was separated and added to phosphate-buffered saline (PBS) [pH 6.5, apyrase (2.5 U/ml) (Sigma), 1 µM PGI_2] in 1:1 volumetric ratio and centrifuged at 1000*g* for 6 min. The platelet pellet was resuspended in Tyrode's buffer [140 mM NaCl, 2.8 mM KCl, 12 mM $NaHCO_3$, 0.5 mM Na_2HPO_4, 5.5 mM glucose, 0.1% HIBSA (pH 7.4)]. The platelet count was adjusted as required for the applied functional assay.

Human and murine platelet culture

Human or murine platelets were prepared and incubated for 15 min with 2 µg/10^6 platelets anti-mouse integrin $\alpha_{IIb}\beta_3$ antibody [Leo.H4/Rat, immunoglobulin G2b (IgG2b), emfret ANALYTICS]; 2 µg/10^6 platelets anti-mouse GPIbα (Xia.B2/Rat, IgG2a, emfret ANALYTICS); 5 µg/10^6 platelets ReoPro (Lilly), 0.05/10^6 or 0.5 µg/10^6 tirofiban (Correvio), 10, 25, 50, and 100 µM clopidogrel hydrogen sulfate (active enantiomer, Tocris Bioscience), and apyrase (2 and 10 U/ml)/100 µM ASA, and then adjusted to a final concentration of 2×10^6 platelets per 150 µl of medium (Dulbecco's modified Eagle's medium). Amitriptyline (7 µM) (Sigma), human fibrinogen (250 µg/ml), and rhCLU (100, 200, 500, or 6600 ng/ml) (R&D Systems) were added to the platelet culture. Platelets were stimulated with 5 µM Aβ40 for 3 days. After incubation, unbound platelets were removed by rinsing with PBS, whereas adherent platelets were fixed with 2% paraformaldehyde and stained for fibrillar Aβ aggregates with Congo red according to the manufacturer's protocol (Merck). Thioflavin T staining: fixed platelets were rinsed with distilled water and applied to 1% thioflavin (AppliChem) for 3 min, followed by 1% acetic acid for 10 min, and embedded in glyceringelatine.

Quantitative analysis of fibrillar Aβ aggregates in brain and platelet cell culture

For quantification of plaque load in the brain of APP23 mice, images were captured by an Axiocam 105 color (Zeiss) camera at a magnification of ×2.5 to visualize the entire hippocampus/entorhinal cortex in a single frame as well as by 10×, 20×, or 40× objectives using a Zeiss Axio Observer. Five optical sections from each field of the specimen were recorded with the AxioVision software (Zeiss) and analyzed. Plaque load was calculated blinded to the conditions by determining the area of Aβ plaques (a combination of senile and diffuse plaques) in the parenchyma of the hippocampus and cortex and shown as a percentage of the total area examined. To determine vascular Aβ deposits, Congo red staining was performed, and CAA positive vessels in the cortex and hippocampus were counted. Size of vascular Aβ plaques was calculated using the ZEN software (blue edition, 2012, Zeiss).

Phase-contrast images of fibrillar Aβ aggregates in the platelet cell culture were stained with Congo red according to the manufacturer's protocol (Merck) and recorded with the AxioVision software (Zeiss). Images from different fields of each sample were imported into the ImageJ program (National Institutes of Health). Conversion to grayscale was performed to distinguish between areas of immunoreactivity and background. Total area of immunoreactivity was determined using a standardized histogram-based threshold technique and then subjected to particle analysis.

Cell lysis and immunoblotting for CLU

Platelets (60×10^6) [when indicated, pretreated with anti-mouse integrin $\alpha_{IIb}\beta_3$ antibody (Leo.H4) or ReoPro for 15 min; apyrase (10 U/ml) or 100 µM ASA for 10 min] were stimulated with 5 µM native Aβ40, 5 µM inverted Aβ40, 5 µM scrambled Aβ40, thrombin (0.5 U/ml), and 5 µM ADP in Tyrode's buffer (pH 7.4) for 30 min at 37°C. After incubation, the platelets were centrifuged at 540*g* and then separated in supernatant and pellet. Stimulated platelets were lysed for 15 min on ice with lysis buffer [for human platelets:145 mM NaCl, 20 mM tris-HCl, 5 mM EDTA, 0.5% sodium deoxycholat, 1% Triton X-100, and complete protease inhibitor cocktail (PI); for murine platelets: 15 mM tris-HCl, 155 mM NaCl, 1 mM EDTA (pH 8.05), 0.005% NaN_3, 1% IGPAL and PI]. Platelet lysates and supernatants were prepared with reducing sample buffer (Laemmli buffer) and denatured at 95°C for 5 min, separated on SDS–polyacrylamide gel, and transferred onto nitrocellulose blotting membrane (GE Healthcare Life Sciences). Subsequently, the membrane was blocked using 5% BSA in PBST (PBS with 0.1% Tween 20) and probed with the appropriate antibody. Anti-CLU antibody (for human platelets) (IgG, Proteintech, 1:500) and anti-mouse CLU (for murine platelets) (rabbit, IgG, Sino Biological Solution Inc., 1:500) were used, followed by incubation of membranes with peroxidase-conjugated goat anti-rabbit IgGs (1:2500). Protein bands were visualized by the use of Immobilon Western Chemiluminescent HRP Substrate solution (Bio-Rad).

Immunoblotting of Aβ from cell culture supernatants

Supernatants (12 µl) from the cell culture were prepared with reducing sample buffer (Laemmli buffer) and denatured at 95°C for 5 min, separated on 15 % SDS–polyacrylamide gel, and transferred onto nitrocellulose blotting membrane. Membranes were blocked in 5% nonfat dry milk in tris-buffered saline containing 0.05 % Tween 20 (TBST) and then incubated with 6E10 antibody (Covance, SIG-39320; diluted 1:2,000) followed by goat anti-mouse–horseradish peroxidase (HRP) (Dianova, 115-035-003; diluted 1:5,000). Band intensities were quantified with the Image Lab software (Bio-Rad) relative to a dilution series of Aβ40 present in a mixture of Aβ standard peptides.

Platelet adhesion on immobilized Aβ

Synthetic Aβ40 (200 μg/ml), collagen (200 μg/ml), and fibrinogen (100 μg/ml) were immobilized on a 96-well plate overnight and then blocked with 300 μl of 1% BSA solution for at least 60 min. Humane platelets were prepared, and platelet count was adjusted to 10×10^5 platelets/ml and incubated for 15 min with ReoPro. Platelet adhesion was analyzed under static condition.

Immunoprecipitation

Resting and Aβ40- or ADP-stimulated platelets (400×10^6 platelet/ml) were lysed, and samples were incubated with β_3 integrin antibody (Luc.H11, emfret ANALYTICS). Protein G–Sepharose was washed, and samples were incubated with G-Sepharose overnight at 4°C. The Sepharose pellet was washed before addition of Laemmli sample buffer. Immunoblotting was performed as indicated. Antibody 4G10 (Millipore) was used to analyze tyrosine phosphorylation of the β_3 integrin subunit upon stimulation of platelets with Aβ40 or ADP.

CLU quantification

CLU levels in the plasma of mice were determined using ELISA (mouse CLU ELISA; MCLU00, R&D Systems). For determination of total amount of CLU released by platelets upon stimulation, platelets (2×10^6 platelet per 150 μl of medium) were stimulated with 5 μM Aβ40 for 1 min at RT. The reaction was stopped by the addition of apyrase (2 U/ml) and centrifuged at 650*g* for 5 min. CLU levels were determined using ELISA (human CLU ELISA, DCLU00, R&D Systems).

Flow cytometry

Flow cytometry analysis of murine platelet activation was performed using fluorophore-labeled antibodies for P-selectin (CD62, M130-1, emfret ANALYTICS) expression, the active form of $\alpha_{IIb}\beta_3$ integrin (JON/A-PE, M023-2, emfret ANALYTICS), and for integrin β_3 (CD61, Luc.H11, emfret ANALYTICS) expression. Blood was diluted in Tyrode's buffer and washed twice. Blood samples were mixed with antibodies stimulated with ADP for 15 min at RT. For analysis, washed platelets were diluted in Tyrode's buffer incubated with ADP fluorophore-labeled peptides HiLyte Fluor 488–Aβ(1–40) (AnaSpec) or Alexa Fluor 488–fibrinogen (Life Technologies) for 15 min at RT. The reaction was stopped by the addition of PBS, and samples were immediately analyzed on a FACSCalibur flow cytometer (BD Biosciences). Where indicated, platelets were pretreated with the ReoPro, tirofiban, soluble fibrinogen, or soluble Aβ40.

Electron microscopy of platelet culture with Aβ40

Platelets (2×10^6) were stimulated with 5 μM Aβ40 for 3 days and then was fixed with Karnovsky's fixative [3% formaldehyde, 2.5% glutaraldehyde, 0.1 M phosphate buffer (pH 7.4)] for 10 min at 37°C and stored at 4°C. Postfixation was based on 1.0 % osmium tetroxide containing 1.5 % K-ferrocyanide in 0.1 M cacodylate buffer for 2 hours. After following the standard methods, blocks were embedded in glycide ether and cut using an ultramicrotome (Ultracut, Reichert). Ultra-thin sections (30 nm) were mounted on copper grids and analyzed using a Zeiss LIBRA 120 transmission electron microscope (Carl Zeiss) operating at 120 kV (*80*).

Immunostaining

Murine or human platelets were prepared and incubated with 5 μM Aβ40 or without Aβ40 for 3 days. After incubation, adherent platelets were fixed with PHEM buffer (100 mM PIPES, 5.25 mM HEPES, 10 mM EGTA, 20 mM $MgCl_2$, pH 6.8) for 10 min and then blocked with 5% BSA for 1 hour at RT. After washing with PBS, the slides were incubated with anti-mouse integrin $\alpha_{IIb}\beta_3$ (2 μg/10^6 platelets, Leo.F2, emfret ANALYTICS) and anti-mouse/human $P2Y_{12}$ receptor (TA328648, OriGene) and then stained using the indicated fluorochrome-conjugated secondary antibody (Alexa Fluor 568 goat anti-rat, Invitrogen, Alexa Fluor 555 donkey anti-rabbit) and fluorochrome-conjugated anti-Aβ, 1–16 antibody (6E10, BioLegend) or FITC-β-Ala-Aβ(1–40) (H-6326, Bachem). After washing with PBS, coverslips were mounted with fluorescent mounting medium (Sigma), and fluorescence was detected using a Zeiss Elyra PS microscope with 63× objective.

Bio-layer interferometry

Nonbiotinylated Aβ40 and Aβ42 or N-terminally biotinylated Aβ40 (Bachem) were dissolved in hexafluoroisopropanol (HFIP) for monomerization purpose overnight at RT then aliquoted into Eppendorf low-binding 1.5-ml tubes into the desired amount, typically 50 to 80 μg per tube. The solution was frozen in liquid nitrogen, and afterward, the HFIP was removed in a centrifugal vacuum concentrator. The resulting powder was stored at RT. For interaction studies of Aβ with fibrinogen, nonbiotinylated Aβ40 or Aβ42 was freshly dissolved in PBS [10 mM sodium phosphate buffer, 154 mM NaCl (pH 7.4); PBS] in respective concentrations before use. Fibrinogen from human plasma was purchased from Sigma-Aldrich as 50 to 70% pure powder. It was stored frozen and dry until the intended use. For BLI measurements, fibrinogen was dissolved in PBS to a concentration of 10 μM and dissolved into the respective concentration for measurement in the range of 10 μM to 3 nM. An association and dissociation time of each 700 s (i to iii) or of each 400 s (iv) were chosen. The association phases were fitted with a biexponential-fit $y = y0 + A1*\exp(x/t1) + A2*\exp(-x/t2)$ shown as respectively colored line overlaid to the symbols (upper panel). In the lower panel, the steady-state value of $y0$ was plotted against the concentration of the corresponding sensogram. Black squares show the respective $y0$ value for the concentration. The data points were fitted with the Hill equation $y = \text{end}*(xn/(K_d + xn*))$ shown as line.

For interaction studies of Aβ40 with integrin $\alpha_{IIb}\beta_3$, N-terminally biotinylated Aβ40 was freshly dissolved in 50 mM tris-HCl, 1 mM $CaCl_2$, 1 mM $MgCl_2$ (pH 7.3). Integrin $\alpha_{IIb}\beta_3$ was isolated and purified following published procedures (*81*) from outdated platelet concentrates derived from the blood bank of the University Clinic Düsseldorf. Four independent purifications from four independent platelet concentrates were carried out. The purified integrin $\alpha_{IIb}\beta_3$ derived from the last purification step [size exclusion chromatography with 0.2 % (w/v) Triton X-100, 50 mM tris-HCl, 1 mM $CaCl_2$, 1 mM $MgCl_2$ (pH 7.3) as buffer system] was directly used for interaction analyses.

BLI measurements were performed on an Octet RED96 system (Pall ForteBio). BLI of Aβ/fibrinogen interaction: Aβ40 or 42 aliquots were dissolved in PBS buffer to a concentration of 120 μM. For each peptide, a freshly dissolved monomeric Aβ aliquot ($t = 0$) and an incubated aliquot for oligomerization ($t = 5$ hours, Aβ40; $t = 2.5$ hours, Aβ42; both without shaking at RT) were used. After respective treatment, Aβ proteins were dissolved to 1.2 μM in 10 mM acetate buffer (pH 4.0) and coupled via *N*-hydroxysuccinimide/1-ethyl-3-(3-dimethylaminopropyl)carbodiimide (NHS/EDC)–ester to a series of eight AR2G sensors (fortéBIO) each according to the respective technical note 26 from fortéBIO. The processes of preparation, coupling, and quenching took about 30 min until the start of the first measurement. A series of AR2G tips were NHS/EDC-activated and afterward directly quenched in 1 M ethanolamine (pH 8.5) as reference. The BLI assay with fibrinogen (typically in dilution series from to 10 μM to 3 nM) was performed in PBS buffer, and respective sensorgrams were recorded.

BLI of Aβ40/integrin $\alpha_{IIb}\beta_3$ interaction: N-terminally biotinylated Aβ40 was freshly dissolved to 4 μM in 50 mM tris-HCl, 1 mM $CaCl_2$,

and 1 mM $MgCl_2$ (pH 7.3) and coupled via its biotinyl group to a series of eight Super Streptavidin (SSA) sensors (fortéBIO) to a final level of 2.5 nm. Ligand and reference SSA sensors were quenched with biotin [2 mM in 50 mM tris-HCl, 1 mM $CaCl_2$, 1 mM $MgCl_2$ (pH 7.3)]. Washing and equilibration of loaded SSA sensors and subsequent BLI assay with purified integrin $\alpha_{IIb}\beta_3$ (typically in dilution series from 800 to 12.5 nM) were performed with 0.2% (w/v) Triton X-100, 50 mM tris-HCl, 1 mM $CaCl_2$, 1 mM $MgCl_2$ (pH 7.3) as buffer system. Ligand and reference SSA sensors were regenerated with 50 mM NaOH for 30 s before used in further BLI cycles. Sensorgrams were double-referenced using the biotin reference sensors and a buffer control. Date was analyzed with the fortéBIO data analysis 8.1 kinetics program package. K_d and rate constants k_{on} and k_{off} of the Aβ40/integrin $\alpha_{IIb}\beta_3$ interaction were determined using a 1:1 binding model and global fitting.

Platelet aggregation and ATP release

Measurements were performed using a Chrono-Log dual channel lumi-aggregometer (model 700) at 37°C with stirring at 900 rpm within a final volume of 0.3-ml platelet suspension. Aggregation is expressed as percentage light transmission compared to Tyrode's buffer alone (=100%). Extracellular ATP was assessed applying a luciferin/luciferase bioluminescent assay and calculated using a provided ATP standard (all Chrono-Log).

Immuno Western blotting

Stimulation of platelets were carried out at 37°C in a total volume of 0.2 ml in 2-ml round-bottom tubes in a thermo shaker rotating at 900 rpm, and preincubations at 500 rpm. Reactions were stopped by the addition of 50 µl of 5× SDS sample buffer, and proteins were denaturated at 95°C for 5 min. From these samples, 25 µl was applied for SDS-PAGE. For the detection of phosphorylated SYK, proteins were separated on 4 to 12% NuPAGE Novex Bis-Tris gels with MOPS running buffer; for detecting phosphorylated PLCγ2, proteins were separated on 3 to 8% NuPAGE Tris-Acetate Gels and Tris-Acetate Running buffer (all Invitrogen). To determine apparent molecular protein masses, MagicMark XP Western Protein Standard (Invitrogen) was used. Proteins were blotted onto Immobilon-FL PVDF (polyvinylidene difluoride) membranes (Millipore). For further steps, TBS-T [10 mM tris-HCl (pH 8.0), 150 mM NaCl, 0.1% (w/v) Tween 20] was used. Membranes were incubated with the phospho-SYK antibody (diluted 1:2000) or phospho-PLCγ2 (1:500) followed by peroxidase-conjugated goat anti-rabbit IgGs (1:2000). For reprobing, membranes were stripped and incubated with either the β-tubulin antibody (1:1000) followed by peroxidase-coupled horse anti-mouse IgGs (1:2000) or the PLCγ2 antibody (1:1,000) followed by peroxidase-coupled goat anti-rabbit IgGs (1:2000). Protein bands were visualized by the use of Immobilon Western Chemiluminescent HRP Substrate solution (Millipore), and chemiluminescence was recorded by a LI-COR Odyssey system (LI-COR Biosciences Ltd.).

Measurement of cytosolic Ca^{2+}

Platelets were loaded with fura-2 by incubating PRP with 4 µM fura-2/AM for 45 min at RT in the dark with gentle agitation and subsequently isolated as described above. Platelets were treated as indicated at 37°C with stirring, and fluorescence was recorded using a Hitachi F-7000 spectrofluorometer (Hitachi Ltd.) at 510 nm with simultaneous excitation at 340 and 380 nm. Cytosolic calcium [Ca^{2+}] is expressed in fluorescence ratio (340/380 nm).

Molecular dynamics simulations

Starting structures for MD simulations of integrin $\alpha_{IIb}\beta_3$ in the bent, closed form representing the inactive state bound to Aβ40 variants were obtained from the coordinates of the x-ray structure for the ecotdomain of integrin $\alpha_{IIb}\beta_3$ [Protein Data Bank (PDB) ID: 3FCS] and the nuclear magnetic resonance structure for Aβ40 (PDB ID: 1BA4). Coordinates of a peptidic RGD motif were taken from the x-ray structure of the integrin $\alpha_{IIb}\beta_3$ headpiece bound to a chimeric fibrinogen γ chain peptide (PDB ID: 2VDQ) and served to place Aβ40 via its RHD motif into the binding region between the propeller and βA domains. $A\beta40_{inverted}$ and $A\beta40_{scrambled}$ were generated within the binding region by homology modeling using Aβ40 as a structural template. To reduce the computational complexity, only the propeller, βA, and hybrid domains of integrin $\alpha_{IIb}\beta_3$ and the first 14 residues of Aβ40 were considered for MD simulations. Truncated structures of the integrin ectodomain have been successfully used previously to investigate the influence of solvent (*57*) and agonists (*56*) on integrin activation. See the Supplementary Materials for details on the generation of the starting structures.

Each starting structure was subjected to three replicates of all-atom MD simulations of 500-ns length each in explicit solvent. Conformational changes in the integrin $\alpha_{IIb}\beta_3$ headpiece induced by the Aβ40 variants were assessed after an equilibration phase of 150 ns in terms of the distance between the center of helix α1 and the N terminus of helix α7 and the distance between the centers of mass of the propeller and βA domains. See the Supplementary Materials for details on the protocol of MD simulations and the analyses of the trajectories.

Statistical analysis

Data are provided as arithmetic means ± SEM. Statistical analysis was made by Student's paired *t* test where applicable.

SUPPLEMENTARY MATERIALS

www.sciencesignaling.org/cgi/content/full/9/429/ra52/DC1

Text

Fig. S1. Characterization of platelet-mediated Aβ aggregate formation in culture.

Fig. S2. CLU promotes platelet-mediated Aβ aggregate formation in culture.

Fig. S3. Flow cytometric analysis confirmed Aβ binding to integrin $\alpha_{IIb}\beta_3$.

Fig. S4. Congo red staining of Aβ aggregate formation.

Fig. S5. Aβ-induced aggregation of and ATP release from human platelets.

Fig. S6. Structural stability of domains in integrin $\alpha_{IIb}\beta_3$.

Fig. S7. Structural stability of Aβ peptides bound to integrin $\alpha_{IIb}\beta_3$.

Fig. S8. Hydrogen bond formation of N_ε of His^6 of Aβ40 with the carbonyl group of Asn^{215}.

Fig. S9. Tirofiban treatment of mice is not sufficient because platelet inhibition is temporary.

References (*82*–*94*)

REFERENCES AND NOTES

1. Alzheimer's Association, 2014 Alzheimer's disease facts and figures. *Alzheimers Dement.* **10**, e47–e92 (2014).
2. S. Catricala, M. Torti, G. Ricevuti, Alzheimer disease and platelets: How's that relevant. *Immun. Ageing* **9**, 20 (2012).
3. J. L. Cummings, R. S. Isaacson, F. A. Schmitt, D. M. Velting, A practical algorithm for managing Alzheimer's disease: What, when, and why? *Ann. Clin. Transl. Neurol.* **2**, 307–323 (2015).
4. H. Hampel, R. Frank, K. Broich, S. J. Teipel, R. G. Katz, J. Hardy, K. Herholz, A. L. Bokde, F. Jessen, Y. C. Hoessler, W. R. Sanhai, H. Zetterberg, J. Woodcock, K. Blennow, Biomarkers for Alzheimer's disease: Academic, industry and regulatory perspectives. *Nat. Rev. Drug Discov.* **9**, 560–574 (2010).
5. D. J. Selkoe, The molecular pathology of Alzheimer's disease. *Neuron* **6**, 487–498 (1991).
6. A. Wimo, L. Jönsson, J. Bond, M. Prince, B. Winblad; Alzheimer Disease International, The worldwide economic impact of dementia 2010. *Alzheimers Dement.* **9**, 1–11.e13 (2013).
7. M. Veitinger, B. Varga, S. B. Guterres, M. Zellner, Platelets, a reliable source for peripheral Alzheimer's disease biomarkers? *Acta Neuropathol. Commun.* **2**, 65 (2014).
8. H. F. Langer, J. W. von der Ruhr, K. Daub, T. Schoenberger, K. Stellos, A. E. May, H. Schnell, A. Gauß, R. Hafner, P. Lang, M. Schumm, H.-J. Bühring, K. Klingel, S. Conrad, M. Schaller, M. van Zandvoort, G. Jung, S. Dimmeler, T. Skutella, M. Gawaz, Capture of endothelial progenitor cells by a bispecific protein/monoclonal antibody molecule induces reendothelialization of vascular lesions. *J. Mol. Med.* **88**, 687–699 (2010).

9. D. A. Case, T. E. Cheatham III, T. Darden, H. Gohlke, R. Luo, K. M. Merz Jr., A. Onufriev, C. Simmerling, B. Wang, R. J. Woods, The Amber biomolecular simulation programs. *J. Comput. Chem.* **26**, 1668–1688 (2005).
10. G. G. Glenner, C. W. Wong, Alzheimer's disease: Initial report of the purification and characterization of a novel cerebrovascular amyloid protein. *Biochem. Biophys. Res. Commun.* **120**, 885–890 (1984).
11. C. L. Masters, G. Simms, N. A. Weinman, G. Multhaup, B. L. McDonald, K. Beyreuther, Amyloid plaque core protein in Alzheimer disease and Down syndrome. *Proc. Natl. Acad. Sci. U.S.A.* **82**, 4245–4249 (1985).
12. D. Goldgaber, M. I. Lerman, O. W. McBride, U. Saffiotti, D. C. Gajdusek, Characterization and chromosomal localization of a cDNA encoding brain amyloid of Alzheimer's disease. *Science* **235**, 877–880 (1987).
13. W. Wasco, S. Gurubhagavatula, M. D. Paradis, D. M. Romano, S. S. Sisodia, B. T. Hyman, R. L. Neve, R. E. Tanzi, Isolation and characterization of *APLP2* encoding a homologue of the Alzheimer's associated amyloid β protein precursor. *Nat. Genet.* **5**, 95–100 (1993).
14. K. Beyreuther, P. Pollwein, G. Multhaup, U. Mönning, G. König, T. Dyrks, W. Schubert, C. L. Masters, Regulation and expression of the Alzheimer's β/A4 amyloid protein precursor in health, disease, and Down's syndrome. *Ann. N.Y. Acad. Sci.* **695**, 91–102 (1993).
15. Y. Ling, K. Morgan, N. Kalsheker, Amyloid precursor protein (APP) and the biology of proteolytic processing: Relevance to Alzheimer's disease. *Int. J. Biochem. Cell Biol.* **35**, 1505–1535 (2003).
16. K. S. Vetrivel, G. Thinakaran, Amyloidogenic processing of β-amyloid precursor protein in intracellular compartments. *Neurology* **66** (Suppl. 1), S69–S73 (2006).
17. W. H. Yu, A. M. Cuervo, A. Kumar, C. M. Peterhoff, S. D. Schmidt, J.-H. Lee, P. S. Mohan, M. Mercken, M. R. Farmery, L. O. Tjernberg, Y. Jiang, K. Duff, Y. Uchiyama, J. Näslund, P. M. Mathews, A. M. Cataldo, R. A. Nixon, Macroautophagy—a novel β-amyloid peptide-generating pathway activated in Alzheimer's disease. *J. Cell Biol.* **171**, 87–98 (2005).
18. L. S. Honig, M.-X. Tang, S. Albert, R. Costa, J. Luchsinger, J. Manly, Y. Stern, R. Mayeux, Stroke and the risk of Alzheimer disease. *Arch. Neurol.* **60**, 1707–1712 (2003).
19. J. A. Luchsinger, C. Reitz, L. S. Honig, M. X. Tang, S. Shea, R. Mayeux, Aggregation of vascular risk factors and risk of incident Alzheimer disease. *Neurology* **65**, 545–551 (2005).
20. D. M. Jans, W. Martinet, T. J. L. Van De Parre, A. G. Herman, H. Bult, M. M. Kockx, G. R. Y. De Meyer, Processing of amyloid precursor protein as a biochemical link between atherosclerosis and Alzheimer's disease. *Cardiovasc. Hematol. Disord. Drug Targets* **6**, 21–34 (2006).
21. A. Tedgui, Z. Mallat, Platelets in atherosclerosis: A new role for β-amyloid peptide beyond Alzheimer's disease. *Circ. Res.* **90**, 1145–1146 (2002).
22. M. M. Mielke, P. B. Rosenberg, J. Tschanz, L. Cook, C. Corcoran, K. M. Hayden, M. Norton, P. V. Rabins, R. C. Green, K. A. Welsh-Bohmer, J. C. S. Breitner, R. Munger, C. G. Lyketsos, Vascular factors predict rate of progression in Alzheimer disease. *Neurology* **69**, 1850–1858 (2007).
23. J. Hardy, Does Aβ 42 have a function related to blood homeostasis? *Neurochem. Res.* **32**, 833–835 (2007).
24. C. Iadecola, Neurovascular regulation in the normal brain and in Alzheimer's disease. *Nat. Rev. Neurosci.* **5**, 347–360 (2004).
25. E. E. Smith, S. M. Greenberg, β-Amyloid, blood vessels, and brain function. *Stroke* **40**, 2601–2606 (2009).
26. W. Staffen, J. Bergmann, U. Schönauer, H. Zauner, M. Kronbichler, S. Golaszewski, G. Ladurner, Cerebral perfusion (HMPAO-SPECT) in patients with depression with cognitive impairment versus those with mild cognitive impairment and dementia of Alzheimer's type: A semiquantitative and automated evaluation. *Eur. J. Nucl. Med. Mol. Imaging* **36**, 801–810 (2009).
27. D. R. Thal, W. S. T. Griffin, R. A. I. de Vos, E. Ghebremedhin, Cerebral amyloid angiopathy and its relationship to Alzheimer's disease. *Acta Neuropathol.* **115**, 599–609 (2008).
28. S. A. Gravina, L. Ho, C. B. Eckman, K. E. Long, L. Otvos Jr., L. H. Younkin, N. Suzuki, S. G. Younkin, Amyloid β protein (Aβ) in Alzheimer's disease brain. Biochemical and immunocytochemical analysis with antibodies specific for forms ending at Aβ40 or Aβ42(43). *J. Biol. Chem.* **270**, 7013–7016 (1995).
29. L. F. Maia, S. A. Kaeser, J. Reichwald, M. Lambert, U. Obermüller, J. Schelle, J. Odenthal, P. Martus, M. Staufenbiel, M. Jucker, Increased CSF Aβ during the very early phase of cerebral Aβ deposition in mouse models. *EMBO Mol. Med.* **7**, 895–903 (2015).
30. D. R. Thal, E. Capetillo-Zarate, S. Larionov, M. Staufenbiel, S. Zurbruegg, N. Beckmann, Capillary cerebral amyloid angiopathy is associated with vessel occlusion and cerebral blood flow disturbances. *Neurobiol. Aging* **30**, 1936–1948 (2009).
31. T. I. Mandybur, Cerebral amyloid angiopathy: The vascular pathology and complications. *J. Neuropathol. Exp. Neurol.* **45**, 79–90 (1986).
32. H. V. Vinters, R. Natté, M. L. C. Maat-Schieman, S. G. van Duinen, I. Hegeman-Kleinn, C. Welling-Graafland, J. Haan, R. A. C. Roos, Secondary microvascular degeneration in amyloid angiopathy of patients with hereditary cerebral hemorrhage with amyloidosis, Dutch type (HCHWA-D). *Acta Neuropathol.* **95**, 235–244 (1998).
33. K. A. Jellinger, J. Attems, Neuropathological evaluation of mixed dementia. *J. Neurol. Sci.* **257**, 80–87 (2007).
34. M. Gawaz, H. Langer, A. E. May, Platelets in inflammation and atherogenesis. *J. Clin. Invest.* **115**, 3378–3384 (2005).
35. Z. M. Ruggeri, Platelets in atherothrombosis. *Nat. Med.* **8**, 1227–1234 (2002).
36. K.-M. Lim, H.-H. Kim, O.-N. Bae, J.-Y. Noh, K.-Y. Kim, S.-H. Kim, S.-M. Chung, S. Shin, H.-Y. Kim, J.-H. Chung, Inhibition of platelet aggregation by 1-methyl-4-phenyl pyridinium ion (MPP^+) through ATP depletion: Evidence for the reduced platelet activities in Parkinson's disease. *Platelets* **20**, 163–170 (2009).
37. E. Asor, D. Ben-Shachar, Platelets: A possible glance into brain biological processes in schizophrenia. *World J. Psychiatry* **2**, 124–133 (2012).
38. A. I. Bush, R. N. Martins, B. Rumble, R. Moir, S. Fuller, E. Milward, J. Currie, D. Ames, A. Weidemann, P. Fischer, G. Multhaup, K. Beyreuther, C. L. Masters, The amyloid precursor protein of Alzheimer's disease is released by human platelets. *J. Biol. Chem.* **265**, 15977–15983 (1990).
39. R. Deane, B. V. Zlokovic, Role of the blood–brain barrier in the pathogenesis of Alzheimer's disease. *Curr. Alzheimer Res.* **4**, 191–197 (2007).
40. A. E. Roher, C. L. Esh, T. A. Kokjohn, E. M. Castaño, G. D. Van Vickle, W. M. Kalback, R. L. Patton, D. C. Luehrs, I. D. Daugs, Y.-M. Kuo, M. R. Emmerling, H. Soares, J. F. Quinn, J. Kaye, D. J. Connor, N. B. Silverberg, C. H. Adler, J. D. Seward, T. G. Beach, M. N. Sabbagh, Amyloid beta peptides in human plasma and tissues and their significance for Alzheimer's disease. *Alzheimers Dement.* **5**, 18–29 (2009).
41. N. S. Gowert, L. Donner, M. Chatterjee, Y. S. Eisele, S. T. Towhid, P. Münzer, B. Walker, I. Ogorek, O. Borst, M. Grandoch, M. Schaller, J. W. Fischer, M. Gawaz, S. Weggen, F. Lang, M. Jucker, M. Elvers, Blood platelets in the progression of Alzheimer's disease. *PLOS One* **9**, e90523 (2014).
42. M. Y. Shen, G. Hsiao, T. H. Fong, H. M. Chen, D. S. Chou, C. H. Lin, J. R. Sheu, C. Y. Hsu, Amyloid beta peptide-activated signal pathways in human platelets. *Eur. J. Pharmacol.* **588**, 259–266 (2008).
43. I. Canobbio, S. Catricalà, L. G. Di Pasqua, G. Guidetti, A. Consonni, D. Manganaro, M. Torti, Immobilized amyloid Aβ peptides support platelet adhesion and activation. *FEBS Lett.* **587**, 2606–2611 (2013).
44. G. Ciabattoni, E. Porreca, C. Di Febbo, A. Di Iorio, R. Paganelli, T. Bucciarelli, L. Pescara, L. Del Re, C. Giusti, A. Falco, A. Sau, C. Patrono, G. Davi, Determinants of platelet activation in Alzheimer's disease. *Neurobiol. Aging* **28**, 336–342 (2007).
45. A. Jarre, N. S. Gowert, L. Donner, P. Munzer, M. Klier, O. Borst, M. Schaller, F. Lang, C. Korth, M. Elvers, Pre-activated blood platelets and a pro-thrombotic phenotype in APP23 mice modeling Alzheimer's disease. *Cell. Signal.* **26**, 2040–2050 (2014).
46. D. T. Winkler, L. Bondolfi, M. C. Herzig, L. Jann, M. E. Calhoun, K.-H. Wiederhold, M. Tolnay, M. Staufenbiel, M. Jucker, Spontaneous hemorrhagic stroke in a mouse model of cerebral amyloid angiopathy. *J. Neurosci.* **21**, 1619–1627 (2001).
47. P. Munzer, O. Borst, B. Walker, E. Schmid, M. A. H. Feijge, J. M. E. M. Cosemans, M. Chatterjee, E.-M. Schmidt, S. Schmidt, S. T. Towhid, C. Leibrock, M. Elvers, M. Schaller, P. Seizer, K. Ferlinz, A. E. May, E. Gulbins, J. W. M. Heemskerk, M. Gawaz, F. Lang, Acid sphingomyelinase regulates platelet cell membrane scrambling, secretion, and thrombus formation. *Arterioscler. Thromb. Vasc. Biol.* **34**, 61–71 (2014).
48. X. Li, Y. Ma, X. Wei, Y. Li, H. Wu, J. Zhuang, Z. Zhao, Clusterin in Alzheimer's disease: A player in the biological behavior of amyloid-beta. *Neurosci. Bull.* **30**, 162–168 (2014).
49. M. Cortes-Canteli, J. Paul, E. H. Norris, R. Bronstein, H. J. Ahn, D. Zamolodchikov, S. Bhuvanendran, K. M. Fenz, S. Strickland, Fibrinogen and β-amyloid association alters thrombosis and fibrinolysis: A possible contributing factor to Alzheimer's disease. *Neuron* **66**, 695–709 (2010).
50. D. Pillitteri, A.-K. Pilgrimm, C. M. Kirchmaier, Novel mutations in the GPIIb and GPIIIa genes in Glanzmann Thrombasthenia. *Transfus. Med. Hemother.* **37**, 268–277 (2010).
51. H. J. Ahn, D. Zamolodchikov, M. Cortes-Canteli, E. H. Norris, J. F. Glickman, S. Strickland, Alzheimer's disease peptide β-amyloid interacts with fibrinogen and induces its oligomerization. *Proc. Natl. Acad. Sci. U.S.A.* **107**, 21812–21817 (2010).
52. S. M. Saporito-Irwin, W. E. Van Nostrand, Coagulation factor XIa cleaves the RHDS sequence and abolishes the cell adhesive properties of the amyloid β-protein. *J. Biol. Chem.* **270**, 26265–26269 (1995).
53. E. Ruoslahti, M. D. Pierschbacher, New perspectives in cell adhesion: RGD and integrins. *Science* **238**, 491–497 (1987).
54. E. Puklin-Faucher, V. Vogel, Integrin activation dynamics between the RGD-binding site and the headpiece hinge. *J. Biol. Chem.* **284**, 36557–36568 (2009).
55. T. Xiao, J. Takagi, B. S. Coller, J.-H. Wang, T. A. Springer, Structural basis for allostery in integrins and binding to fibrinogen-mimetic therapeutics. *Nature* **432**, 59–67 (2004).
56. H. Gohlke, B. Schmitz, A. Sommerfeld, R. Reinehr, D. Häussinger, $\alpha_5\beta_1$-integrins are sensors for tauroursodeoxycholic acid in hepatocytes. *Hepatology* **57**, 1117–1129 (2013).
57. R. Reinehr, H. Gohlke, A. Sommerfeld, S. Vom Dahl, D. Häussinger, Activation of integrins by urea in perfused rat liver. *J. Biol. Chem.* **285**, 29348–29356 (2010).
58. B.-H. Luo, C. V. Carman, T. A. Springer, Structural basis of integrin regulation and signaling. *Annu. Rev. Immunol.* **25**, 619–647 (2007).
59. J.-P. Xiong, T. Stehle, S. L. Goodman, M. A. Arnaout, A novel adaptation of the integrin PSI domain revealed from its crystal structure. *J. Biol. Chem.* **279**, 40252–40254 (2004).

60. C. Sturchler-Pierrat, D. Abramowski, M. Duke, K.-H. Wiederhold, C. Mistl, S. Rothacher, B. Ledermann, K. Bürki, P. Frey, P. A. Paganetti, C. Waridel, M. E. Calhoun, M. Jucker, A. Probst, M. Staufenbiel, B. Sommer, Two amyloid precursor protein transgenic mouse models with Alzheimer disease-like pathology. *Proc. Natl. Acad. Sci. U.S.A.* **94**, 13287–13292 (1997).
61. M. Schwarz, G. Meade, P. Stoll, J. Ylanne, N. Bassler, Y. C. Chen, C. E. Hagemeyer, I. Ahrens, N. Moran, D. Kenny, D. Fitzgerald, C. Bode, K. Peter, Conformation-specific blockade of the integrin GPIIb/IIIa: A novel antiplatelet strategy that selectively targets activated platelets. *Circ. Res.* **99**, 25–33 (2006).
62. A. Afek, E. Kogan, S. Maysel-Auslender, A. Mor, E. Regev, A. Rubinstein, G. Keren, J. George, Clopidogrel attenuates atheroma formation and induces a stable plaque phenotype in apolipoprotein E knockout mice. *Microvasc. Res.* **77**, 364–369 (2009).
63. R. U. Bodani, U. Sengupta, D. L. Castillo-Carranza, M. J. Guerrero-Muñoz, J. E. Gerson, J. Rudra, R. Kayed, Antibody against small aggregated peptide specifically recognizes toxic Aβ-42 oligomers in Alzheimer's disease. *ACS Chem. Neurosci.* **6**, 1981–1989 (2015).
64. Y. S. Eisele, U. Obermüller, G. Heilbronner, F. Baumann, S. A. Kaeser, H. Wolburg, L. C. Walker, M. Staufenbiel, M. Heikenwalder, M. Jucker, Peripherally applied Aβ-containing inoculates induce cerebral β-amyloidosis. *Science* **330**, 980–982 (2010).
65. G. Heilbronner, Y. S. Eisele, F. Langer, S. A. Kaeser, R. Novotny, A. Nagarathinam, A. Åslund, P. Hammarström, K. P. R. Nilsson, M. Jucker, Seeded strain-like transmission of β-amyloid morphotypes in APP transgenic mice. *EMBO Rep.* **14**, 1017–1022 (2013).
66. A. Nagarathinam, P. Höflinger, A. Bühler, C. Schäfer, G. McGovern, M. Jeffrey, M. Staufenbiel, M. Jucker, F. Baumann, Membrane-anchored Aβ accelerates amyloid formation and exacerbates amyloid-associated toxicity in mice. *J. Neurosci.* **33**, 19284–19294 (2013).
67. J. Ghiso, A. Rostagno, J. E. Gardella, L. Liem, P. D. Gorevic, B. Frangione, A 109-amino-acid *C*-terminal fragment of Alzheimer's-disease amyloid precursor protein contains a sequence, -RHDS-, that promotes cell adhesion. *Biochem. J.* **288**, 1053–1059 (1992).
68. M. A. Kowalska, K. Badellino, β-Amyloid protein induces platelet aggregation and supports platelet adhesion. *Biochem. Biophys. Res. Commun.* **205**, 1829–1835 (1994).
69. A. Kasirer-Friede, M. L. Kahn, S. J. Shattil, Platelet integrins and immunoreceptors. *Immunol. Rev.* **218**, 247–264 (2007).
70. B. Nieswandt, D. Varga-Szabo, M. Elvers, Integrins in platelet activation. *J. Thromb. Haemost.* **7** (Suppl. 1), 206–209 (2009).
71. M. Schmidt, C. Sachse, W. Richter, C. Xu, M. Fändrich, N. Grigorieff, Comparison of Alzheimer Aβ(1–40) and Aβ(1–42) amyloid fibrils reveals similar protofilament structures. *Proc. Natl. Acad. Sci. U.S.A.* **106**, 19813–19818 (2009).
72. L. O. Tjernberg, D. J. E. Callaway, A. Tjernberg, S. Hahne, C. Lilliehöök, L. Terenius, J. Thyberg, C. Nordstedt, A molecular model of Alzheimer amyloid β-peptide fibril formation. *J. Biol. Chem.* **274**, 12619–12625 (1999).
73. T. Nuutinen, T. Suuronen, A. Kauppinen, A. Salminen, Clusterin: A forgotten player in Alzheimer's disease. *Brain Res. Rev.* **61**, 89–104 (2009).
74. M. Thambisetty, A. Simmons, L. Velayudhan, A. Hye, J. Campbell, Y. Zhang, L.-O. Wahlund, E. Westman, A. Kinsey, A. Güntert, P. Proitsi, J. Powell, M. Causevic, R. Killick, K. Lunnon, S. Lynham, M. Broadstock, F. Choudhry, D. R. Howlett, R. J. Williams, S. I. Sharp, C. Mitchelmore, C. Tunnard, R. Leung, C. Foy, D. O'Brien, G. Breen, S. J. Furney, M. Ward, I. Kloszewska, P. Mecocci, H. Soininen, M. Tsolaki, B. Vellas, A. Hodges, D. G. M. Murphy, S. Parkins, J. C. Richardson, S. M. Resnick, L. Ferrucci, D. F. Wong, Y. Zhou, S. Muehlboeck, A. Evans, P. T. Francis, C. Spenger, S. Lovestone, Association of plasma clusterin concentration with severity, pathology, and progression in Alzheimer disease. *Arch. Gen. Psychiatry* **67**, 739–748 (2010).
75. R. B. DeMattos, M. A. O'dell, M. Parsadanian, J. W. Taylor, J. A. K. Harmony, K. R. Bales, S. M. Paul, B. J. Aronow, D. M. Holtzman, Clusterin promotes amyloid plaque formation and is critical for neuritic toxicity in a mouse model of Alzheimer's disease. *Proc. Natl. Acad. Sci. U.S.A.* **99**, 10843–10848 (2002).
76. I. Canobbio, G. F. Guidetti, B. Oliviero, D. Manganaro, D. Vara, M. Torti, G. Pula, Amyloid β-peptide-dependent activation of human platelets: Essential role for Ca^{2+} and ADP in aggregation and thrombus formation. *Biochem. J.* **462**, 513–523 (2014).
77. H. M. Wisniewski, J. Frackowiak, B. Mazur-Kolecka, In vitro production of β-amyloid in smooth muscle cells isolated from amyloid angiopathy-affected vessels. *Neurosci. Lett.* **183**, 120–123 (1995).
78. A. T. Nurden, M. Fiore, P. Nurden, X. Pillois, Glanzmann thrombasthenia: A review of *ITGA2B* and *ITGB3* defects with emphasis on variants, phenotypic variability, and mouse models. *Blood* **118**, 5996–6005 (2011).
79. L. McLaughlin, G. Zhu, M. Mistry, C. Ley-Ebert, W. D. Stuart, C. J. Florio, P. A. Groen, S. A. Witt, T. R. Kimball, D. P. Witte, J. A. K. Harmony, B. J. Aronow, Apolipoprotein J/clusterin limits the severity of murine autoimmune myocarditis. *J. Clin. Invest.* **106**, 1105–1113 (2000).
80. A. Fotinos, M. Klier, N. S. Gowert, P. Münzer, C. Klatt, S. Beck, O. Borst, P. Billuart, M. Schaller, F. Lang, M. Gawaz, M. Elvers, Loss of oligophrenin1 leads to uncontrolled Rho activation and increased thrombus formation in mice. *J. Thromb. Haemost.* **13**, 619–630 (2015).
81. G. A. Rivas, J. J. Calvete, J. González-Rodríguez, A large-scale procedure for the isolation of integrin GPIIb/IIIa, the human platelet fibrinogen receptor. *Protein Expr. Purif.* **2**, 248–255 (1991).
82. J. Zhu, B.-H. Luo, T. Xiao, C. Zhang, N. Nishida, T. A. Springer, Structure of a complete integrin ectodomain in a physiologic resting state and activation and deactivation by applied forces. *Mol. Cell* **32**, 849–861 (2008).
83. UniProt Consortium, UniProt: A hub for protein information. *Nucleic Acids Res.* **43**, D204–D212 (2015).
84. T. A. Springer, J. Zhu, T. Xiao, Structural basis for distinctive recognition of fibrinogen γC peptide by the platelet integrin $\alpha_{IIb}\beta_3$. *J. Cell Biol.* **182**, 791–800 (2008).
85. M. Coles, W. Bicknell, A. A. Watson, D. P. Fairlie, D. J. Craik, Solution structure of amyloid β-peptide(1–40) in a water-micelle environment. Is the membrane-spanning domain where we think it is? *Biochemistry* **37**, 11064–11077 (1998).
86. N. Guex, M. C. Peitsch, SWISS-MODEL and the Swiss-Pdb Viewer: An environment for comparative protein modeling. *Electrophoresis* **18**, 2714–2723 (1997).
87. A. Fiser, R. K. G. Do, A. Šali, Modeling of loops in protein structures. *Protein Sci.* **9**, 1753–1773 (2000).
88. A. Fiser, A. Sali, ModLoop: Automated modeling of loops in protein structures. *Bioinformatics* **19**, 2500–2501 (2003).
89. W. D. Cornell, P. Cieplak, C. I. Bayly, I. R. Gould, K. M. Merz Jr., D. M. Ferguson, D. C. Spellmeyer, T. Fox, J. W. Caldwell, P. A. Kollman, A second generation force field for the simulation of proteins, nucleic acids, and organic molecules *J. Am. Chem. Soc.* 1995, *117,* 5179–5197. *J. Am. Chem. Soc.* **118**, 2309–2309 (1996).
90. C. Simmerling, B. Strockbine, A. E. Roitberg, All-atom structure prediction and folding simulations of a stable protein. *J. Am. Chem. Soc.* **124**, 11258–11259 (2002).
91. W. L. Jorgensen, J. Chandrasekhar, J. D. Madura, R. W. Impey, M. L. Klein, Comparison of simple potential functions for simulating liquid water. *J. Chem. Phys.* **79**, 926–935 (1983).
92. T. Darden, D. York, L. Pedersen, Particle mesh Ewald: An *N*·log(*N*) method for Ewald sums in large systems. *J. Chem. Phys.* **98**, 10089–10092 (1993).
93. P. Gonnet, P-SHAKE: A quadratically convergent SHAKE in $O(n^2)$. *J. Comput. Phys.* **220**, 740–750 (2007).
94. D. R. Roe, T. E. Cheatham III, PTRAJ and CPPTRAJ: Software for processing and analysis of molecular dynamics trajectory data. *J. Chem. Theory Comput.* **9**, 3084–3095 (2013).

Acknowledgments: We thank M. Spelleken, B. Fehrenbacher, and E. Reinartz for providing outstanding technical assistance and B. Bomke for recruiting GT patients. We are grateful to M. Thomaier for expert assistance on BLI and C. von Gall for technical support. **Funding:** This work was maintained by the Stiftung für Altersforschung of the Heinrich Heine University, Düsseldorf (M.E.). We are grateful to the Zentrum für Informations und Medientechnologie (ZIM) at Heinrich Heine University Düsseldorf for computational support and to the Jülich Supercomputing Center for granting computing time on the supercomputers JUROPA and JURECA (NIC project ID: HDD11) to us. **Author contributions:** L.D., K.F., S.K., G.P., L.U.L., L.G., K.L., and F.R. performed experiments and analyzed the data; L.D., K.F., L.G., M.S., H.G., D.W., and M.G. discussed the data and contributed to writing of the manuscript; M.E. analyzed the data, designed the research, and wrote the manuscript. **Competing interests:** The authors declare that they have no competing interests. **Data and materials availability:** Acquisition of the APP23 mice required a material transfer agreement from Novartis Pharma AG.

Submitted 4 March 2016
Accepted 6 May 2016
Final Publication 24 May 2016
10.1126/scisignal.aaf6240
Citation: L. Donner, K. Fälker, L. Gremer, S. Klinker, G. Pagani, L. U. Ljungberg, K. Lothmann, F. Rizzi, M. Schaller, H. Gohlke, D. Willbold, M. Grenegard, M. Elvers, Platelets contribute to amyloid-β aggregation in cerebral vessels through integrin $\alpha_{IIb}\beta_3$–induced outside-in signaling and clusterin release. *Sci. Signal.* **9**, ra52 (2016).

Science Signaling
AAAS

www.sciencesignaling.org/cgi/content/full/9/429/ra52/DC1

Supplementary Materials for

Platelets contribute to amyloid-β aggregation in cerebral vessels through integrin $\alpha_{IIb}\beta_3$–induced outside-in signaling and clusterin release

Lili Donner, Knut Fälker, Lothar Gremer, Stefan Klinker, Giulia Pagani, Liza U. Ljungberg, Kimberley Lothmann, Federica Rizzi, Martin Schaller, Holger Gohlke, Dieter Willbold, Magnus Grenegard, Margitta Elvers*

*Corresponding author. Email: margitta.elvers@med.uni-duesseldorf.de

Published 24 May 2016, *Sci. Signal.* **9**, ra52 (2016)
DOI: 10.1126/scisignal.aaf6240

The PDF file includes:

Details of the MD simulations

Generation of the starting structures

For the generation of the starting structures for MD simulations, the crystal structure of the ectodomain of integrin αIIbβ3 in a bent, closed conformation (PDB ID 3FCS (82)) was used for the integrin part. To reduce the computational complexity, we only used the headpiece of the protein: For the αIIb subunit, only the propeller domain was used (residues 1 to 451); for the β_3 subunit, the βA domain (residues 56 to 108) and the hybrid domain (residues 109 to 433) were used. Integrin sequence numbers are according to Uniprot (83). No further modifications of the protein structure were required.

Onto this crystal structure, the crystal structure of a chimeric fibrinogen gamma chain peptide in complex with integrin αIIbβ3 (PDB ID 2VDQ (84)) was overlaid in order to use the coordinates of the RGD motif of fibrinogen to subsequently orient the Aβ peptides within the binding site between the propeller and βA domains. Accordingly, the RHD motif of the NMR structure of Aβ40 (PDB ID 1BA4 (85)) was overlaid onto the RGD motif of fibrinogen. The RHD motif was refined using the Swiss PDB Viewer (86) and selecting the best rotamer for histidine.

For the complex structure of integrin αIIbβ3 headpiece / Aβ40, only residues 1 to 14 of PDB ID 1BA4 were used, which contain the RHDS motif. These residues are unstructured in the NMR structure. This alleviates the need to identify an initial binding position for residues 15 to 40 of which residues 15 to 36 are alpha-helical.

From this structure, complex structures of integrin αIIbβ3 headpiece / $A\beta40_{scrambled}$ and integrin αIIbβ3 headpiece / $A\beta40_{inverted}$ were generated by homology modeling using MODELLER (v9.9) (87).

For the final generation of the starting structures for the MD simulations, the first four residues of the Aβ peptides preceding the RHDS sequence and the following seven residues were refined using the Web server ModLoop (88).

General settings

MD simulations were performed with the AMBER 14 suite of programs (9), together with the ff99SB force field by Cornell *et al.* (89) considering the modifications by Simmerling *et al.* (90). Na^+ counter-ions were added to neutralize the total charge of the system using *Leap*. The resulting system of ~300,000 atoms was placed into an octahedral period box of TIP3P water molecules (91) with a distance of (at least) 8 Å between the edges of the water box and the closest atom of the protein. Before launching the production phase of MD simulations, each system was minimized by 50 steps of steepest descent minimization followed by 450 steps of conjugate gradient minimization. The particle mesh Ewald method (92) was used to treat long-range electrostatic interactions, and bond lengths involving bonds to hydrogen atoms were constrained using the SHAKE algorithm (93). The time step for all molecular (MD) dynamics was 2 fs with a direct space, non-bonded cut-off of 8 Å. Applying harmonic restraints with force constants of 5 kcal mol^{-1} $Å^{-2}$ to all solute atoms, NVT-MD was carried out for 50 ps, during which the system was heated from 100 to 300 K. Subsequent NPT-MD was used for 150 ps to adjust the solvent density. Finally, the force constant of the harmonic restraints on solute atom positions were gradually reduced to zero during 100 ps of NVT-MD. The following 500 ns of NVT-MD at 300 K with a time constant of 10 ps for heat bath coupling were used for analysis, with conformations extracted every 20 ps.

Three independent MD simulations of 500 ns length were performed for each system, summing up to a total of 3 x 3 x 500 ns = 4.5 µs of MD simulations for production.

Analyses

The MD trajectories were analyzed using the *cpptraj/ptraj* tool (94) from the AmberTools suite of programs (9). Trajectories were combined applying a mass-weighted root mean square fitting of the coordinates of the Cα atoms of the propeller and βA domains using the starting structure as reference. The initial 150 ns of each trajectory were considered equilibration phase and, hence, not used for the analyses.

The root mean square deviations (RMSD) of the Cα atoms with respect to the starting structures were calculated to evaluate structural deviations over the course of the MD simulations. For the integrin headpiece simulations, RMSD was computed for all three domains (propeller, βA, hybrid) separately. For Aβ, the RMSD of the Cα atoms of the RHDS motif was computed after superimposing the integrin headpiece.

Changes in the inter-domain interface between the propeller and the βA domains were quantified by measuring the distance between the centers of mass of each domain. In order to monitor a potential helix α1/α7 T-junction formation (54, 55), the distance between the Cβ atoms of Leu138 on helix α1and Val332 on helix α7 was measured.

Statistics

Results from three independent simulations are expressed as mean ± SEM (standard error of the mean) calculated over the time. The overall SEM for each system "X" was calculated accordingly to the law of error propagation:

$$SEM_X = \sqrt{\mathrm{SEM}_1^2 + \mathrm{SEM}_2^2 + \mathrm{SEM}_3^2} \quad (1)$$

where {1, 2, 3} indicates a single trajectory.

The Student's t-test was used to evaluate the computational findings, and $p < 0.001$ was considered significant. Statistical analysis was performed using the program R.

Figure preparation

The crystal structure of integrin $\alpha_{IIb}\beta_3$ (PDB ID 3FCS) was used to represent the protein, together with conformations extracted from the MD trajectories. Pymol (The PyMOL Molecular Graphics System, Version 1.7.4 Schrödinger, LLC) was used to generate figures, and graphs were prepared using Gnuplot. For the sake of clarity, results are plotted applying a smoothing representation as implemented in Gnuplot.

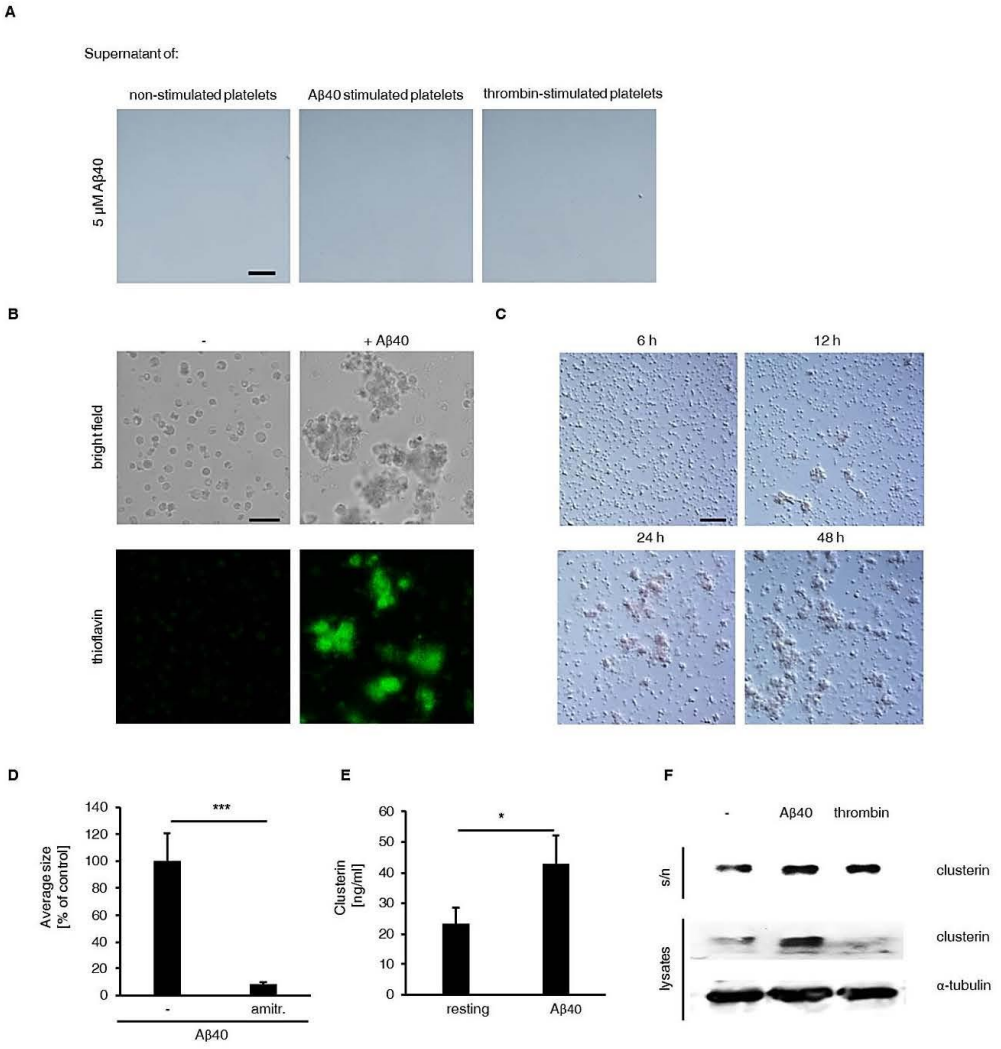

Fig. S1. Characterization of platelet-mediated Aβ aggregate formation in culture. (**A**) Supernatants of stimulated platelets with Aβ40 or thrombin were incubated with 5 μM Aβ40 for 3 days in culture. Scale bar 50 μm. (**B**) Amyloid fibril detection in the platelet cell culture by Thioflavin-T stain. Scale bar 10 μm. (**C**) Congo red staining for amyloid fibrils in platelet cell cultures over time. Scale bar 50 μm. h, hours. (**D**) Quantification of amyloid aggregates in platelet cell culture in the presence of amitriptyline (n = 3). (**E**) The amount of platelet-released clusterin after stimulation with 5 μM Aβ40 for 1 min. (**F**) Representative Western blots of supernatants (s/n) and lysates of platelets using anti-clusterin antibody after stimulation with Aβ40. α-tubulin was used as a loading control. Data are means ± SEM from 3 experiments. **P*<0.05, ****P*<0.001, by a student's paired t-test. All blots and microscopy images are representative of 3 independent experiments. Amitr. = amitriptyline.

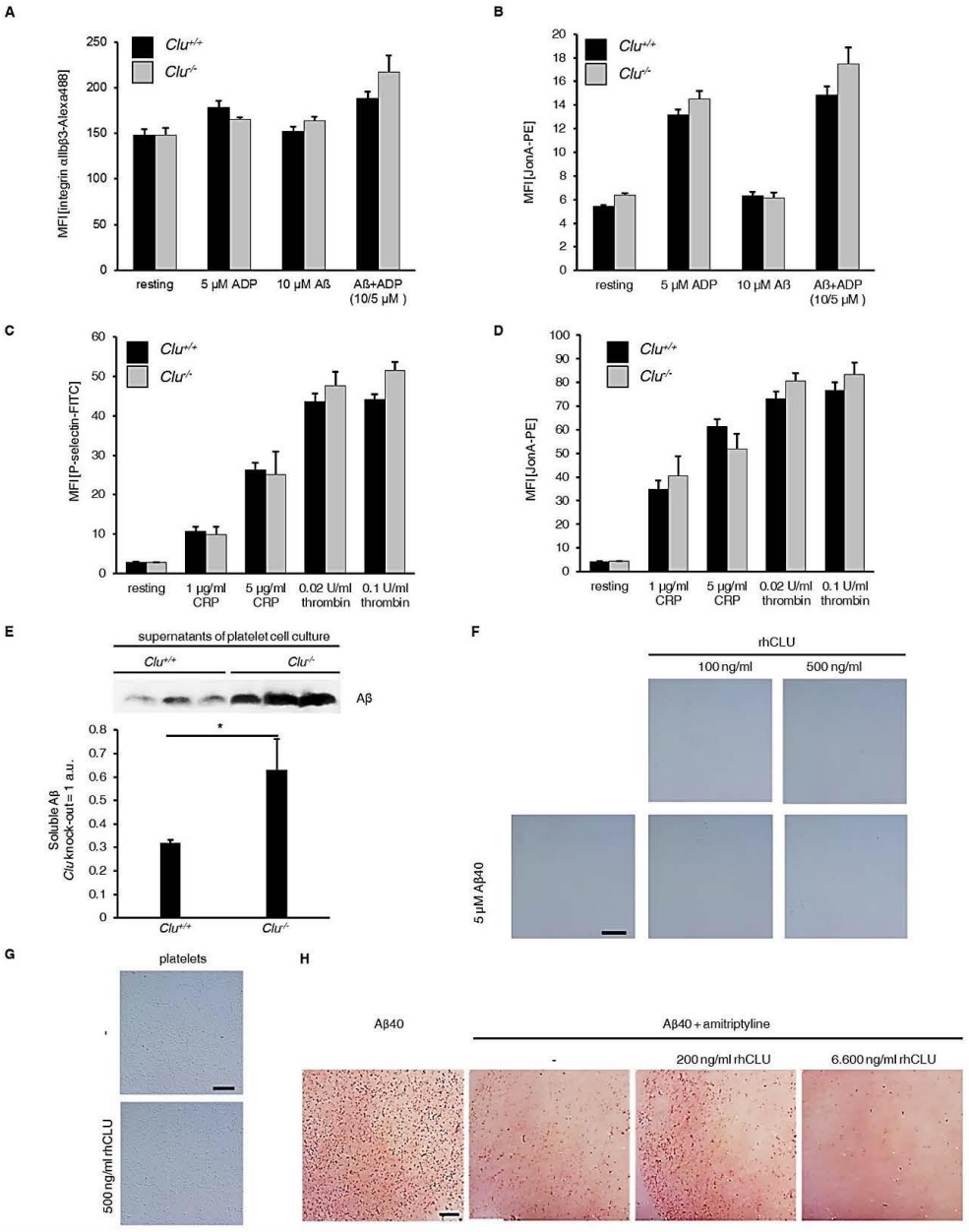

Fig. S2. Clusterin promotes platelet-mediated Aβ fibril formation in culture. (**A-D**) Blood from clusterin knock-out (*Clu*$^{-/-}$) or wild-type (*Clu*$^{+/+}$) mice was washed twice and incubated with ADP, Aβ40, ADP/Aβ40, CRP or thrombin as indicated for 15 min in the presence of antibodies against P-selectin and integrin $\alpha_{IIb}\beta_3$ (JON/A-PE). Platelets were gated by their forward and side characteristics. The mean flourescence intensity (MFI) for each measurement is shown (n=5-6 mice per group). (**E**) Western blot analysis for Aβ (6E10 antibody) in the supernatants of clusterin knock-out (*Clu*$^{-/-}$) and wild-type (*Clu*$^{+/+}$) platelet cell culture after stimulation with Aβ40 for 3 days. (**F**) Noting the absence of aggregates after

incubation of Aβ40 with rhCLU in a platelet-free solution for 3 days. Scale bar, 50 µm (**G**) Visual assessment of morphology indicates that high amounts of human recombinant (rh) clusterin (rhCLU) are not toxic for platelets after 3 days in cell culture. Scale bar, 50 µm. (**H**) Human platelets stimulated with Aβ40 alone, with amitriptyline, or with amitriptyline and recombinant human (rh) clusterin (CLU) for 3 days. Representative images of Congo red-stained Aβ fibrils. Scale bar, 500 µm. Data are means ± SEM from 3 experiments. **P*<0.05by a student's paired t-test. All blots and microscopy images are representative of 3 independent experiments.

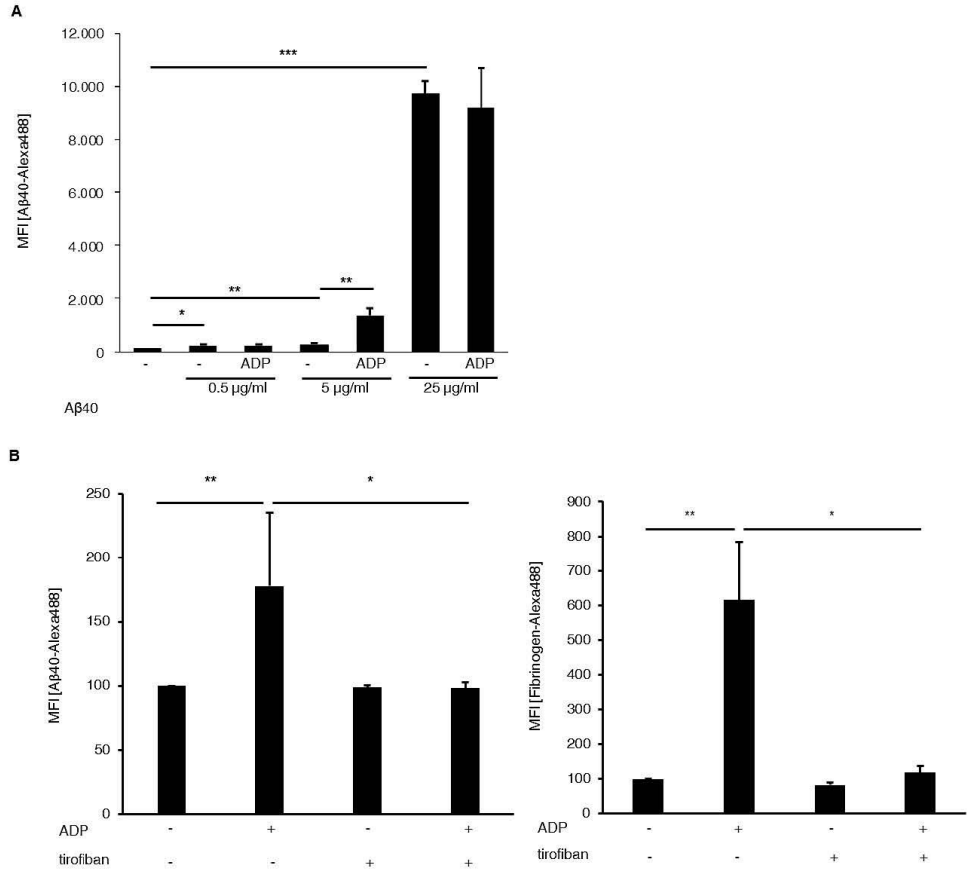

Fig. S3. Flow cytometric analysis confirmed Aβ binding to integrin $\alpha_{IIb}\beta_3$. (**A**) Platelets were incubated with Aβ40-Alexa488 with or without ADP for 15 minutes and analyzed by flow cytometry (n = 3-5). MFI, mean fluorescence intensity. (**B**) Platelets were pre-treated with the antiplatelet, glycoprotein IIb/IIIa inhibitor tirofiban for 15 min and then incubated with Aβ40-Alexa488 (left panel). Determination of fibrinogen (fibrinogen-Alexa488) binding to platelets served as positive control (right panel, n = 3). Data are means ± SEM from 3 experiments. **P*<0.05, ***P*<0.01 by a student's paired t-test.

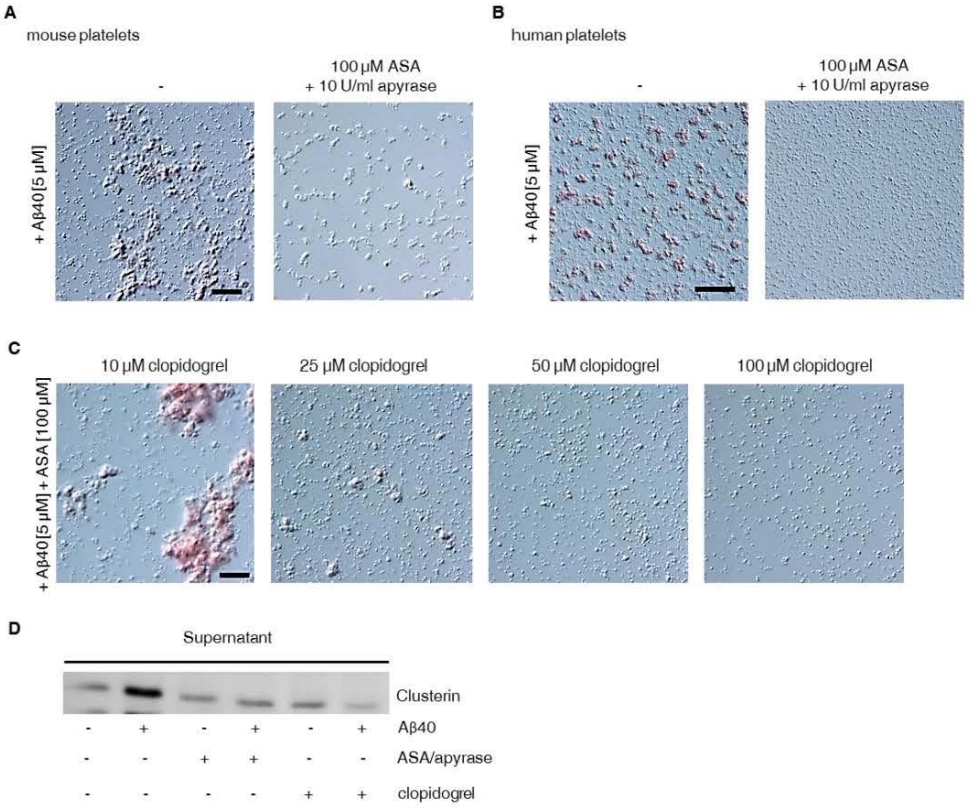

Fig. S4. Congo red staining of Aβ aggregate formation. (**A-B**) Murine platelets (**A**) and human platelets (**B**) were incubated with Aβ40 for 3 days in the presence of ASA and apyrase. (**C**) Human platelets were incubated with Aβ40 in the presence of ASA and increasing concentrations of clopidogrel. (**D**) Human platelets were treated with ASA/apyrase or clopidogrel followed by stimulation with Aβ40, respectively. Western blots of supernatants of human platelets using anti-clusterin antibody. Blots and images are representative of 3 experiments.

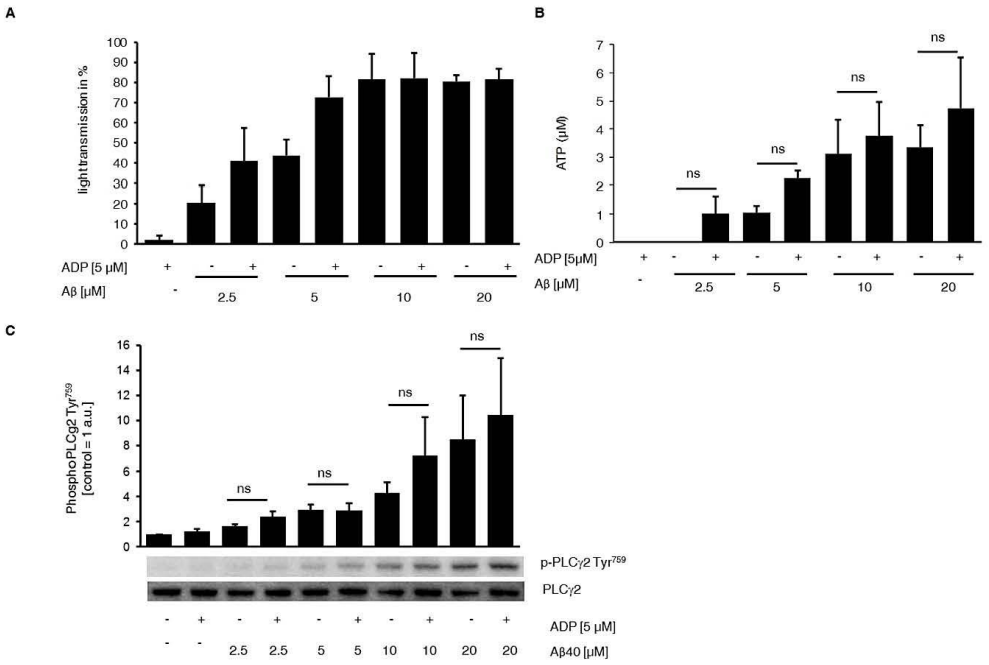

Fig. S5. Aβ-induced aggregation of and ATP release from human platelets. (**A** and **B**) Human platelets were incubated with indicated concentrations of Aβ40 in the absence or presence of ADP for 120 sec, and platelet aggregation (**A**) and ATP release (**B**) was determined. (**C**) Effects of "priming" human platelets with ADP (for 120 sec) on Aβ40-induced phosphorylation PLCγ2 at Tyr^{759}. Samples were analyzed by Western blot and probed with antibodies recognizing phosphorylated or total PLCγ2. Data are means ± SEM of 3 experiments. ns = not significant, by a student's paired t-test.

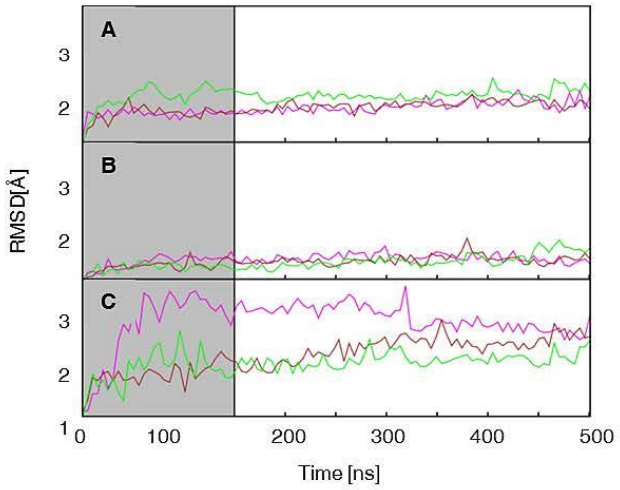

Fig. S6. Structural stability of domains in integrin $\alpha_{IIb}\beta_3$. Time series of the RMSD of Cα atoms of the propeller (**A**), βA (**B**), and hybrid (**C**) domains of integrin $\alpha_{IIb}\beta_3$ bound to Aβ40 with respect to the starting structure. Brown, green, and magenta colors represent the three independent trajectories. Data are representative of 3 independent experiments.

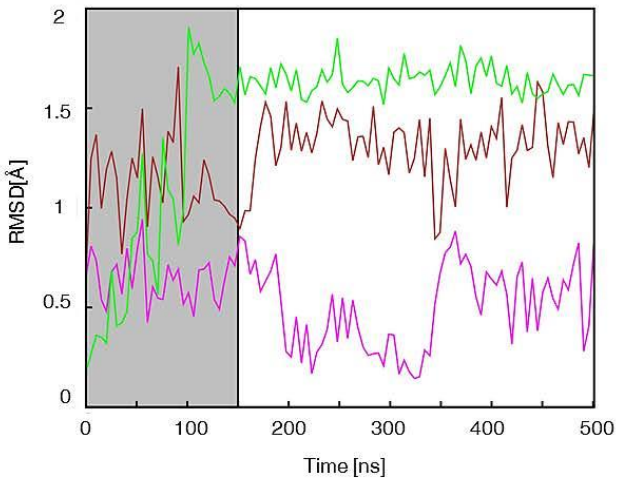

Fig. S7. Structural stability of Aβ peptides bound to integrin $\alpha_{IIb}\beta_3$. Time series of the RMSD of Cα atoms of the RHDS sequence of Aβ40 (magenta), $A\beta40_{scrambled}$ (brown), and $A\beta40_{inverted}$ (green) bound to integrin $\alpha_{IIb}\beta_3$ with respect to the starting structure after superimposing only the integrin part. Shown are representative results from one MD trajectory each; the two other MD trajectories for each case confirm these data. Data are representative of 3 independent experiments.

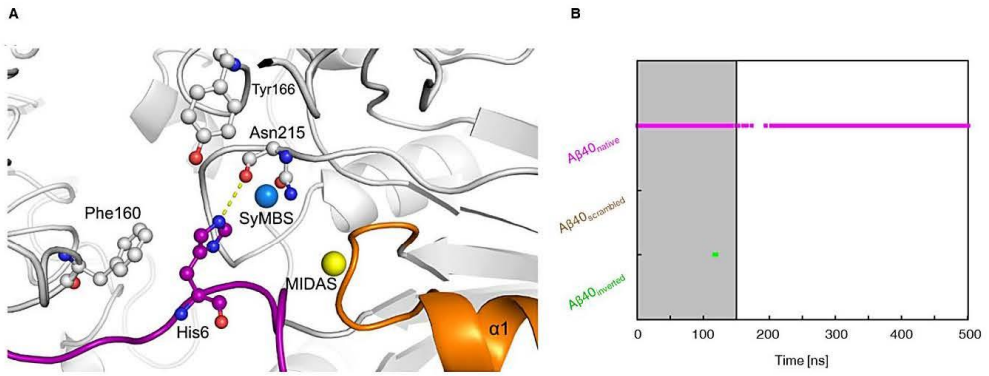

Fig. S8. Hydrogen bond formation of N_ε of His^6 of Aβ40 with the carbonyl group of Asn^{215}. (**A**) Representation of the interaction (dashed line) in the closest-to-average structure from the last 350 ns of the MD simulations of Aβ40 bound to integrin $\alpha_{IIb}\beta_3$. Metal ions are represented by spheres (yellow and marine for Mg^{2+} and Ca^{2+} ions, respectively). (**B**) Frequency of occurrence of the hydrogen bond between His^6 and Asn^{215}. Magenta, brown, and green colors indicate the three Aβ40 variants. Shown are representative results from one MD trajectory each; the two other MD trajectories for each case confirm these data.

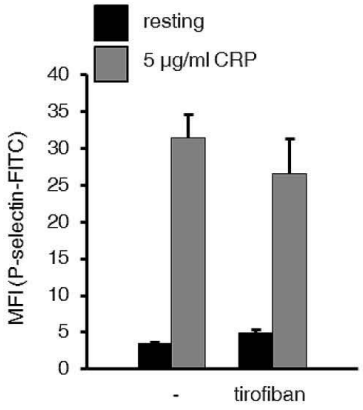

Fig. S9. Tirofiban treatment of mice is not sufficient, because platelet inhibition is temporary. Wild-type (C57BL/6J) mice were injected with tirofiban (1 µg/g body weight) or 0.9 % NaCl (vehicle, "-"). Two hours after injection, platelet activation upon stimulation with collagen-related peptide (CRP) was determined by flow cytometric analysis using fluorophore-labeled antibody for P-selectin expression. Data are means ± SEM of 3 experiments. MFI, mean fluorescence intensity.

PUBLICATION II

The human platelet antigen HPA-1b variant of $\alpha_{IIb}\beta_3$ allosterically shifts the dynamic conformational equilibrium of this integrin toward the active state

Pagani, **G.**, Pereira, J. P. V., Stoldt, V. R., Beck, A., Scharf, R. E., Gohlke, H.

J. Biol. Chem. 2018, DOI: 10.1074/jbc.RA118.002149

JBC ARTICLE

The human platelet antigen-1b (Pro^{33}) variant of $\alpha_{IIb}\beta_3$ allosterically shifts the dynamic conformational equilibrium of this integrin toward the active state

Received for publication, January 31, 2018, and in revised form, February 8, 2018 Published, Papers in Press, February 9, 2018, DOI 10.1074/jbc.RA118.002149

Giulia Pagani[‡], **Joana P. V. Pereira**[§1], **Volker R. Stoldt**[§1], **Andreas Beck**[¶], **Rüdiger E. Scharf**[§‖2], **and Holger Gohlke**[‡**2,3]

From the [‡]*Institute for Pharmaceutical and Medicinal Chemistry,* [¶]*Institute of Informatics, and* [‖]*Biological Medical Research Center, Heinrich Heine University Düsseldorf, 40225 Düsseldorf, Germany,* [§]*Division of Experimental and Clinical Hemostasis, Hemotherapy and Transfusion Medicine, Institute of Transplantation Diagnostics and Cell Therapeutics, Heinrich Heine University Medical Center, 40225 Düsseldorf, Germany, and* ***John von Neumann Institute for Computing (NIC), Jülich Supercomputing Centre (JSC), and Institute for Complex Systems-Structural Biochemistry (ICS 6), Forschungszentrum Jülich GmbH, 52425 Jülich, Germany*

Edited by Norma M. Allewell

Integrins are heterodimeric cell-adhesion receptors comprising α and β subunits that transmit signals allosterically in both directions across the membrane by binding to intra- and extracellular components. The human platelet antigen-1 (HPA-1) polymorphism in $\alpha_{IIb}\beta_3$ arises from a Leu → Pro exchange at residue 33 in the genu of the β_3 subunit, resulting in Leu^{33} (HPA-1a) or Pro^{33} (HPA-1b) isoforms. Although clinical investigations have provided conflicting results, some studies have suggested that Pro^{33} platelets exhibit increased thrombogenicity. Under flow-dynamic conditions, the Pro^{33} variant displays prothrombotic properties, characterized by increased platelet adhesion, aggregate/thrombus formation, and outside-in signaling. However, the molecular events underlying this prothrombotic phenotype have remained elusive. As residue 33 is located >80 Å away from extracellular binding sites or transmembrane domains, we hypothesized that the Leu → Pro exchange allosterically shifts the dynamic conformational equilibrium of $\alpha_{IIb}\beta_3$ toward an active state. Multiple microsecond-long, all-atom molecular dynamics simulations of the ectodomain of the Leu^{33} and Pro^{33} isoforms provided evidence that the Leu → Pro exchange weakens interdomain interactions at the genu and alters the structural dynamics of the integrin to a more unbent and splayed state. Using FRET analysis of fluorescent proteins fused with $\alpha_{IIb}\beta_3$ in transfected HEK293 cells, we found that the Pro^{33} variant in its resting state displays a lower energy transfer than the Leu^{33} isoform. This finding indicated a larger spatial separation of the cytoplasmic tails in the Pro^{33} variant. Together, our results indicate that the Leu → Pro exchange allosterically shifts the dynamic conformational equilibrium of $\alpha_{IIb}\beta_3$ to a structural state closer to the active one, promoting the fully active state and fostering the prothrombotic phenotype of Pro^{33} platelets.

Integrins are heterodimeric cell-adhesion receptors formed of α and β subunits. Each subunit is divided into three parts: a large extracellular domain (ectodomain), a single-pass transmembrane domain, and a short cytoplasmic tail connecting the extracellular to the intracellular environment (1). In addition to their biomechanical role (2), integrins transmit signals allosterically (3) in both directions across the membrane (termed "outside-in" and "inside-out" signaling) by binding to intra- and extracellular components (4). In the present study, we focused on $\alpha_{IIb}\beta_3$ (5–8), which is expressed on the platelet surface and essential for platelet aggregation (8).

The ectodomain can be divided into two parts (9, 10) (Fig. 1). The "head" of the receptor is formed by the β-propeller and βA domains, and the "legs" are formed by the thigh and calf domains (α_{IIb} subunit) as well as EGF domains together with the β-tail domain (β_3 subunit) (4). The genu located between the thigh and calf-1 domain as well as the EGF-1 and EGF-2 domains in the α_{IIb} and β_3 subunits, respectively, forms a region of interdomain flexibility (11). Integrin structural dynamics is characterized by at least three states: a closed, bent, low-affinity state; a closed, extended, low-affinity state; and an open, extended, high affinity state (12). Although the magnitude of conformational changes has remained a matter of discussion (6, 10, 13), the majority of crystal structures of $\alpha_v\beta_3$ (14), $\alpha_{IIb}\beta_3$ (9), and $\alpha_x\beta_2$ (15) integrins show their ectodomain in a bent conformation (14, 16, 17). Here, the head is flexed toward the membrane at an angle of 135° (7) related to the legs, with the genu being the angle's vertex.

According to current models, the genu plays a critical role in conformational transitions between the three structural states as a straightening in the genu region leads to a separation of the head from the legs and thus an unbending of the conformation. This motion is associated with reduced interactions between the two subunits, resulting in a spatial separation ("splaying") of the α and β subunit legs (18). With respect to our study, the role

This work was supported by a grant from the Deutsche Forschungsgemeinschaft (Sonderforschungsbereich 612, Project B2) (to R. E. S. and V. R. S.). The authors declare that they have no conflicts of interest with the contents of this article.

This article contains supporting methods, Figs. S1–S8, and Tables S1–S10.

[1] Present address: Dept. of General, Visceral and Pediatric Surgery, Heinrich Heine University Medical Center and Faculty of Medicine, Heinrich Heine University Düsseldorf, 40225 Düsseldorf, Germany.

[2] Both authors share senior authorship.

[3] To whom correspondence should be addressed: Institute for Pharmaceutical and Medicinal Chemistry, Heinrich Heine University Düsseldorf, Universitätsstr. 1, D-40225 Düsseldorf, Germany. Tel.: 49-211-81-13662; Fax: 49-211-81-13847; E-mail: gohlke@uni-duesseldorf.de or h.gohlke@fz-juelich.de.

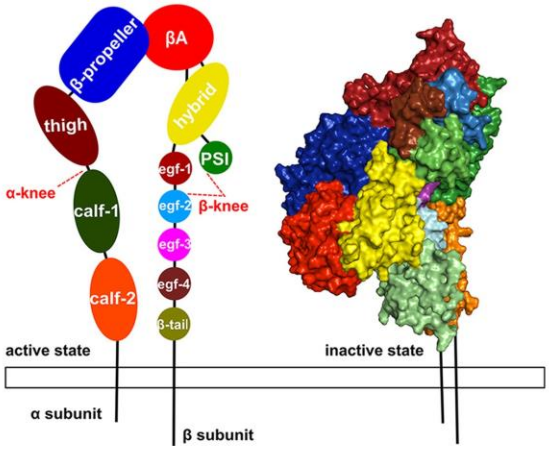

Figure 1. Representation of the domain organization of integrin $\alpha_{IIb}\beta_3$. On the *left*, the open conformation is depicted as a schematic with the α subunit divided into four different domains and the β subunit divided into eight domains. Each domain is colored and labeled. The knees of the protein are highlighted by *red dashed lines* and lie between the thigh and calf-1 domains and between the PSI and EGF-1/EGF-2 domains of the α and β subunits, respectively. On the *right*, the $\alpha_{IIb}\beta_3$ ectodomain starting structure (Protein Data Bank code 3FCS) in the bent conformation is depicted in surface representation (*right*) with domains colored as on the *left*.

of the plexin-semaphorin-integrin (PSI)[4] domain, which is part of the β_3 genu (5), is of particular interest in integrin activation. Located >80 Å away from the extracellular binding site and >90 Å away from the membrane (estimated from Protein Data Bank code 3FCS), the domain's involvement in integrin activation has been demonstrated (19, 20). Specifically, the domain is believed to have a biomechanical role in the allosteric signal transmission across the structure (21).

The human platelet antigen-1 (HPA-1) polymorphism of the β_3 gene of $\alpha_{IIb}\beta_3$ arises from a Leu → Pro exchange at residue 33 of the mature β_3 subunit (22, 23), resulting in Leu^{33} (HPA-1a) or Pro^{33} (HPA-1b) platelets. This amino acid exchange, located within the PSI domain, leads to an inherited dimorphism that can be of clinical relevance (22). For example, the HPA-1b allele was significantly more frequent among young patients with acute coronary syndrome than among age-matched healthy subjects (24). In the Ludwigshafen Risk and Cardiovascular Health (LURIC) trial, an association study including more than 4,000 individuals, we documented that patients with coronary artery disease (CAD), who are carriers of the HPA-1b allele, experience their myocardial infarction 5 years earlier in life than CAD patients who are HPA-1b–negative (22, 23). In a prospective study on CAD patients undergoing saphenous-vein coronary-artery bypass grafting, we demonstrated that HPA-1b is a hereditary risk factor for bypass occlusion, myocardial infarction, or death after coronary-artery bypass surgery (25). These results suggest that the Leu → Pro exchange may modulate functional properties of $\alpha_{IIb}\beta_3$, resulting in a prothrombotic integrin variant. Prothrombotic properties are also displayed by Pro^{33} platelets under flow-dynamic conditions (26). However, the molecular mechanism underlying the suggested prothrombotic phenotype of the Pro^{33} (HPA-1b) variant has remained elusive.

We hypothesized that the Leu → Pro exchange allosterically shifts the dynamic conformational equilibrium of $\alpha_{IIb}\beta_3$ toward an active state. This shift, in turn, would facilitate reaching the fully active state in the presence of integrin ligands. To examine this hypothesis, we performed multiple microsecond-long all-atom molecular dynamics (MD) simulations of the ectodomain and Förster resonance energy transfer (FRET) measurements of $\alpha_{IIb}\beta_3$-transfected HEK293 cells expressing either the Leu^{33} (HPA-1a) or Pro^{33} (HPA-1b) isoform. Our MD simulations provide evidence that the Leu → Pro exchange weakens interdomain interactions at the genu and alters the structural dynamics of the integrin to a more unbent and splayed state, resulting in overall conformational changes that have been linked to integrin activation (18, 27). In accord with these results, FRET analyses of $\alpha_{IIb}\beta_3$ transfectants reveal that the Pro^{33} (HPA-1b) variant in the resting state displays a significantly lower energy transfer than the Leu^{33} (HPA-1a) variant.

Results

Platelet thrombus size in relation to $\alpha_{IIb}\beta_3$ HPA-1 isoforms under flow conditions in vitro

Given the prothrombotic phenotype of Pro^{33} platelets, we initially focused on platelet thrombus formation under arterial flow conditions comparing Leu^{33} (HPA-1a) with Pro^{33} (HPA-1b) platelets. To study the dynamics of platelet thrombus formation, mepacrine-labeled citrated whole blood from healthy volunteers genotyped for HPA-1 of $\alpha_{IIb}\beta_3$ and α_2C807T of $\alpha_2\beta_1$ (see supporting methods) was perfused at shear rates >500 s^{-1} through a flow chamber coated with collagen type I. Image acquisition was achieved by a series of stacks corresponding to confocal sections from the bottom to the apex of forming platelet thrombi. For quantitation of thrombus formation *in vitro*, we applied a voxel-based method for 3D visualization of real time-resolved volume data using ECCET software (www.eccet.de)[5] (28). As depicted in Fig. 2*A*, ECCET allows determination of the number, bottom area, height, and volume of single platelet thrombi formed *in vitro*.

Using these tools, we detected that, upon perfusion over 10 min, platelets homozygous for Pro^{33} (HPA-1b) formed single thrombi that were significantly higher than those of platelets homozygous for Leu^{33} (HPA-1a) (Fig. 2*B*). This difference in mean single thrombus volume was due to an increased thrombus height, whereas the number and bottom area of thrombi

[4] The abbreviations used are: PSI, plexin-semaphorin-integrin; APB, acceptor photobleaching; APC, allophycocyanin; CAD, coronary artery disease; CNA, Constraint Network Analysis; GP, glycoprotein; HPA-1, human platelet antigen-1; MD, molecular dynamics; NPT, constant number of particles, pressure, and temperature; NVT, constant number of particles, volume, and temperature; RMSD, root-mean-square deviation; RMSF, root-mean-square fluctuation; R_g, radius of gyration; VWF, von Willebrand factor; PC, principal component; SyMBS, synergistic metal-binding site; MIDAS, metal ion–dependent adhesion site; ADMIDAS, adjacent to MIDAS.

[5] Please note that the JBC is not responsible for the long-term archiving and maintenance of this site or any other third party-hosted site.

Allosteric changes of $\alpha_{IIb}\beta_3$ induced by the Pro^{33} variant

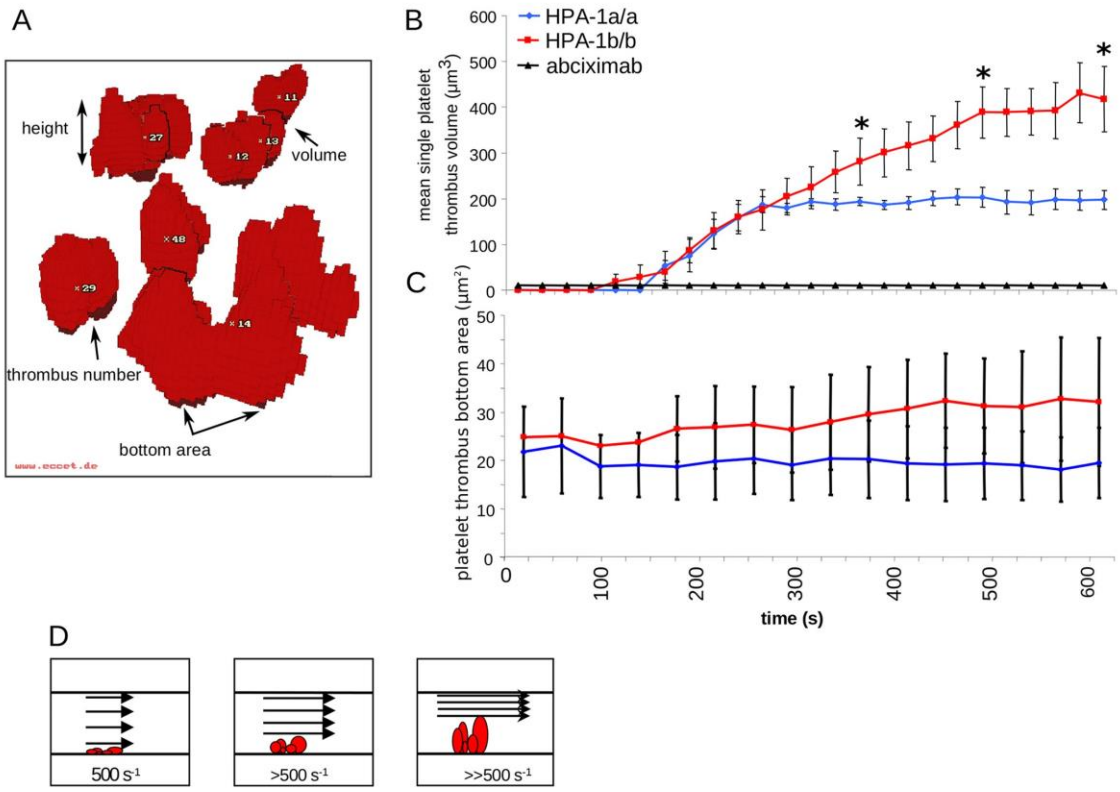

Figure 2. Dynamics and volumetric analysis of platelet thrombus formation under flow-dynamic conditions. A rectangular flow chamber coated with collagen type I (3 mg/ml) at the lower surface was perfused with mepacrine-labeled citrated whole blood for 10 min at an initial near-wall shear rate of 500 s^{-1}, simulating arterial flow conditions. Fluorescence signals were detected by confocal laser scanning microscopy, and digital imaging was processed as described under "Experimental procedures". Volumetry of forming platelet thrombi was assessed by real-time 3D visualization. *A*, a reconstruction of formed platelet thrombi obtained from a stack of 30 images by confocal laser scanning microscopy and subsequent data processing by ECCET. *B* and *C*, initial platelet thrombus formation and subsequent thrombus growth were recorded in 25-s intervals for each single thrombus. Addition of abciximab (4 μg/ml), an inhibitory antibody to $\alpha_{IIb}\beta_3$, abrogated any platelet thrombus formation. *B* shows the mean single platelet thrombus volume, and *C* shows the corresponding thrombus bottom area. *D*, schematic illustrating the narrowing of the flow path within the perfusion chamber with a resulting increase in shear rates upon apical thrombus growth. *Blue diamonds*, homozygous Leu^{33} (HPA-1a) platelets ($n = 8$); *red squares*, homozygous Pro^{33} (HPA-1b) platelets ($n = 8$); *black rectangles*, control in the presence of abciximab ($n = 2$). *Error bars* indicate mean ± S.E. *Asterisks* indicate statistical significance (*, $p < 0.05$).

(Fig. 2*C*) did not differ between the HPA-1 isoforms. Platelet adhesion and subsequent aggregate/thrombus formation under flow were abrogated by the monoclonal antibody LJ-Ib1 (a gift from Dr. Z. M. Ruggeri, La Jolla, CA) that completely inhibits binding of von Willebrand factor (VWF) to the platelet glycoprotein (GP) Ib-IX-V complex or by the monoclonal antibody 5C4 (a gift from Dr. M. Gawaz, Tübingen, Germany) that blocks the platelet collagen receptor GPVI (data not shown). As depicted in the schematic illustration (Fig. 2*D*), with increasing time, the flow path of the perfusion chamber becomes narrowed as the thrombi are growing. Consequently, shear rates gradually increase, and formed platelet thrombi, especially at their apex, are exposed to higher shear than initially applied. Thus, the difference in mean single thrombus volumes between the HPA-1 isoforms can be indicative of a higher thrombus stability of Pro^{33} (HPA-1b) than Leu^{33} (HPA-1a) platelets as reported before (29).

Structural variability of $\alpha_{IIb}\beta_3$ HPA-1 isoforms in MD simulations of the integrin ectodomain

To provide an atomistic view on the effect of the Leu → Pro exchange, the Leu^{33} (HPA-1a) and Pro^{33} (HPA-1b) isoforms were investigated by all-atom MD simulations using the respective integrin ectodomains in the bent conformation as starting structures. The quality of the crystal structure used as a starting structure for the Leu^{33} isoform and to model the Pro^{33} isoform was validated by MolProbity (30), yielding a percentile score of 1.70, equal to a 99th percentile rank, where a 0th percentile rank indicates the worst and a 100th percentile rank indicates the best structure among structures with comparable resolution (~2.55 Å in the case of Protein Data Bank code 3FCS). For generating the Pro^{33} isoform from the crystal structure, the Leu^{33} side chain was mutated using the best rotamer of Pro at this position according to Swiss-PdbViewer (31). For this structure, the quality of the PSI domain in complex with the EGF-1

and EGF-2 domains (genu of the β_3 subunit) was assessed by MolProbity, yielding a percentile score of 1.30, equal to a 98th percentile rank.

Three independent MD simulations of 1-μs length each were carried out. The convergence of the MD simulations was tested by computing the root-mean-square deviation (RMSD) average correlation as described previously (32) (Fig. S1). The root-mean-square average correlation is a measure of the time scales on which structural changes occur in MD simulations. From the bumps in the curves, we can estimate that observed structural changes occur within ~50–200 ns. For time intervals >200 ns, the curves are smooth, suggesting that no large structural changes happen during the investigation period.

In addition, we analyzed the overlap of histograms of principal component (PC) projections obtained in a pairwise manner from each simulation for a given isoform as a function of time (Fig. S2). The PC analysis was performed on the whole protein after a mass-weighted fitting on the β-propeller and βA domains. The results reveal that, overall, the Kullback-Leibler divergence between histograms of the respective first three PCs becomes small (<0.02) after ~600 ns of simulation time, whereas values in the first 100 ns can be as high as ~0.1. Hence, the analyses indicate that, in the given simulation times, rather similar conformational spaces were sampled by MD simulations of one isoform. However, in some cases, a small increase in the Kullback-Leibler divergence is observed toward the end of the simulation time; this behavior is not unexpected because the MD simulations were started from bent conformations of the isoforms that can relax to more open conformations (33). Given that, in the absence of force, the timescale of integrin activation is on the order of 10^{-3} (34) to 1 s (35), one cannot expect that the MD simulations are converged with respect to the bent-open conformational equilibrium of $\alpha_{IIb}\beta_3$ integrin. In total, differences in structural parameters between both isoforms that we report below relate to differences in the tendency of the ectodomains to go from a bent to an open state. Unless stated otherwise, all results of the MD simulations are expressed as arithmetic means calculated over time, and we considered only uncorrelated instances for S.E. calculations (see "Experimental procedures").

The βA domain contains three metal ion–binding sites (Fig. S3). To assess their structural integrity during the MD simulations, we monitored the time evolution of distances between the SyMBS, MIDAS, and ADMIDAS metal ions and the respective coordinating residues (Table S3 and Fig. S3). The results reveal that during the production runs the distances remain almost unchanged with S.E. <0.1 Å in almost all cases. Thus, the local geometry of the metal ion–binding sites is well preserved throughout the MD simulations.

The structural similarity of the conformations obtained by MD simulations with respect to the starting structure was explored in terms of the RMSD of C^α atoms after mass-weighted superimpositioning. Similar to our previous MD studies performed on integrin $\alpha_5\beta_1$ (18, 27), the simulations revealed minor structural changes of the single domains as mirrored by RMSD values that were largely below 3 Å with the exception of the calf-2 and EGF domains and the β-tail (RMSD up to 5 Å) (Table S4 and Fig. S4). Although the β-tail has been characterized as highly flexible (14), the larger RMSD of the calf-2 domain, in part, is due to the presence of long flexible loops (9); furthermore, the larger RMSD may result from simulating the ectodomain only; *i.e.* at the C-terminal ends of each subunit, the transmembrane domains are missing. As to the EGF domains, visual inspection of the MD trajectories revealed that the larger RMSD resulted in part from motions of the domains relative to each other.

In contrast, when aligning only the head region, the mean RMSD increased up to ~17 Å (Table S5 and Fig. S5) with the highest values found for the calf-2 and β-tail domains of the legs. Hence, these larger structural changes must arise from relative movements of the domains (or subunits) with respect to each other, considering that the single domains were structurally rather invariant. Comparing both isoforms of $\alpha_{IIb}\beta_3$, a larger mean RMSD (~9.2 ± 0.34 Å) was found for Pro^{33} than Leu^{33} (~6.6 ± 0.83 Å) (Fig. 3*A*). In accord with that, the mean radius of gyration (R_g) of the overall structure was larger for the Pro^{33} (~40.3 ± 0.22 Å) than the Leu^{33} isoform (~39.6 ± 0.09 Å) (Fig. 3*A*). Taken together, the sampled conformational space of both $\alpha_{IIb}\beta_3$ isoforms varied significantly with respect to the difference of the mean values of these structural parameters (Table S6). To conclude, the Pro^{33} variant displayed significantly larger structural deviations from the bent starting structure and became less compact than the Leu^{33} isoform during MD simulations.

Conformational changes of the ectodomains of $\alpha_{IIb}\beta_3$ HPA-1 isoforms toward a more open, extended conformation

To further characterize the structural differences between the $\alpha_{IIb}\beta_3$ isoforms, we monitored geometric parameters along the MD trajectories that have been linked with conformational changes of the ectodomain from an inactive to an active state (18, 27) (Fig. S6 and Table S7). First, we investigated possible variations in the region of the center of helix α1 and the N terminus of helix α7 (27, 37). This region was shown to form a "T-junction" upon activation (21, 27). We computed the kink angle of helix α1 (Fig. 3*B*), which revealed a mean value over three MD trajectories that is larger by 15° in the Pro^{33} (~153 ± 1.5°) than the Leu^{33} isoform (~138 ± 2.8°) (Fig. 3*B*). Hence, helix α1 straightens more in Pro^{33} and thus shows a stronger tendency to form the T-junction than in Leu^{33}. The spread in the mean values found for Pro^{33} (Table S7) resulted from a rapid and pronounced increase of the kink angle, which was initially ~143° (calculated from Protein Data Bank code 3FCS), within the first 200 ns in two of the three MD simulations (Fig. S6A).

Second, we evaluated the unbending of the structure in terms of the separation of the head region and the terminal part of the legs (calf-2 domain and β-tail) (Fig. 3*C*). Furthermore, we monitored the spatial separation (splaying) of the integrin's legs (Fig. 3*D*). Similar parameters were successfully used previously (18). The bending angle was ~7° larger in the Pro^{33} (~49 ± 1.8°) than in the Leu^{33} isoform (~42 ± 1.4°) (Fig. 3*C*, Fig. S6*B*, and Table S7). The splaying angle was ~3° larger in Pro^{33} (~28 ± 0.5°) than in Leu^{33} (~25 ± 0.2°) (Fig. 3*D*, Fig. S6*C*, and Table S7). In the latter case, in two MD simulations, the time evolution of the splaying angle revealed a decrease of ~22° within the last 200 ns

Allosteric changes of $\alpha_{IIb}\beta_3$ induced by the Pro^{33} variant

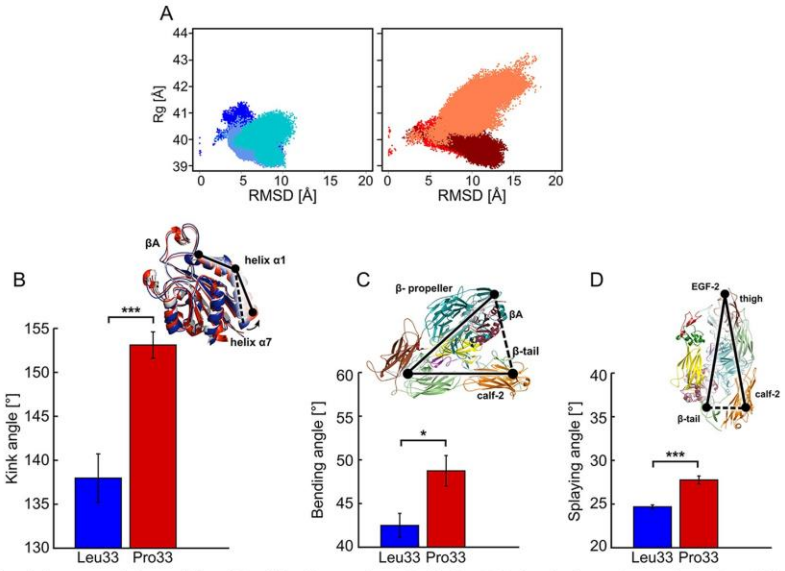

Figure 3. Conformational changes of the Leu^{33} and Pro^{33} isoforms of $\alpha_{IIb}\beta_3$ during MD simulations. *A*, two-dimensional histogram of the RMSD of C$^{\alpha}$ atoms of the entire ectodomain after mass-weighted fitting on the β-propeller and βA domains of the starting structure *versus* R_g for the ectodomains. *Bluish* colors represent the three MD simulations of the Leu^{33} isoform, and *reddish* colors represent those of the Pro^{33} variant. *B–D*, histograms of the kink, bending, and splaying angles averaged over three MD simulations with *error bars* showing the S.E. and *asterisks* indicating the statistical significance (*, $p < 0.05$; ***, $p < 0.0001$). Above the plots, the definitions of the angles are given: *B*, kink angles as *black solid line* connecting the three points (center of mass of C$^{\alpha}$ atoms of Lys^{112} and Ile^{118}, center of mass of C$^{\alpha}$ atoms of Gln^{119} and Lys^{125}, and center of mass of C$^{\alpha}$ atoms of Leu^{126} and Leu^{132}) on both isoforms; *C*, bending angle as a *black solid line* connecting the three points (center of mass of the β-propeller and βA domains, center of mass of the PSI domain, and center of mass of the calf-2 and β-tail domains); *D*, splaying angle as a *black solid line* connecting the three points (center of mass of C$^{\alpha}$ atoms of Leu^{788} and Gly^{796} in the calf-2 domain, center of mass of the C$^{\alpha}$ atoms of Cys^{602} and Cys^{608} in the thigh domain, and center of mass of C$^{\alpha}$ atoms of Glu^{1557} and Val^{1561} in the β-tail domain).

of the simulation (Fig. S6C). The differences between angles in the Leu^{33} and Pro^{33} isoforms were significant in all cases (Table S7). As additional indicators of structural changes, we evaluated the opening of the structure in terms of changes in internal distances between the N and C termini of each subunit and between the C termini of the two subunits (Fig. S6D). All evaluated distances were larger in the Pro^{33} than the Leu^{33} isoform, and the differences between respective distances were significant in all cases (Table S8). To conclude, our results revealed significant differences in the conformational states of both $\alpha_{IIb}\beta_3$ isoforms with the ectodomain of Pro^{33} displaying a stronger tendency to move toward the extended conformation with more splayed legs.

Experimental evidence for spatial rearrangements of the cytoplasmic tails of $\alpha_{IIb}\beta_3$ upon Leu → Pro exchange

To investigate a possible influence of the Leu → Pro exchange on the spatial separation of α and β subunits, we performed FRET acceptor photobleaching (APB) analyses in individual cells transfected with α_{IIb}mVenus and β_3Leu^{33} mCherry (HPA-1a) (Table S1) or β_3Pro^{33}mCherry (HPA-1b) (Table S2) plasmids, respectively. Using FRET, the spatial separation of the subunits is inferred from the amount of energy transferred between the fluorescent proteins mVenus and mCherry attached to the cytoplasmic tails of the subunits.

By fluorescence microscopy performed 48 h after transfection, we verified that both subunits were colocalized at the cell membrane (Fig. 4*A*). Concordant with the presence of the integrin at the plasma membrane, we detected the complete $\alpha_{IIb}\beta_3$ receptor (recognized by a complex-specific anti-$\alpha_{IIb}\beta_3$ antibody, anti-CD41, clone MEM-06) by flow cytometry. Functional integrity of both integrin isoforms and correct membrane insertion were documented by intact activation of $\alpha_{IIb}\beta_3$ in transfected cells upon phorbol 12-myristate 13-acetate–induced stimulation of protein kinase C and specific binding of Alexa Fluor 647-fibrinogen to $\alpha_{IIb}\beta_3$ upon inside-out activation (38). Notably, flow cytometry measurements of CD41 expression upon five independent transfection experiments indicated that the levels of $\alpha_{IIb}\beta_3$ expressing either the Leu^{33} (HPA-1a) or the Pro^{33} (HPA-1b) isoform did not differ more than 10% from each other (Fig. 4*B*).

Using these transfectants, photobleaching of mCherry at 561 nm on a defined cellular region (region of interest) encompassing part of the cell membrane led to a complete loss of energy transfer and, consequently, to an increase in mVenus fluorescence intensity (Fig. 4*C*). For a control, cells were transfected with α_{IIb}mVenus and β_3Leu^{33} or β_3Pro^{33} plasmids (without mCherry), a condition that abrogated any energy transfer (data not shown). To focus on non-activated $\alpha_{IIb}\beta_3$ transfectants, as evidenced by absence of binding of Alexa Fluor 647-fibrinogen or PAC1, an activation-dependent anti-$\alpha_{IIb}\beta_3$ monoclonal antibody (data not shown), cells were left resting on chamber slides with culture medium for 24 h prior

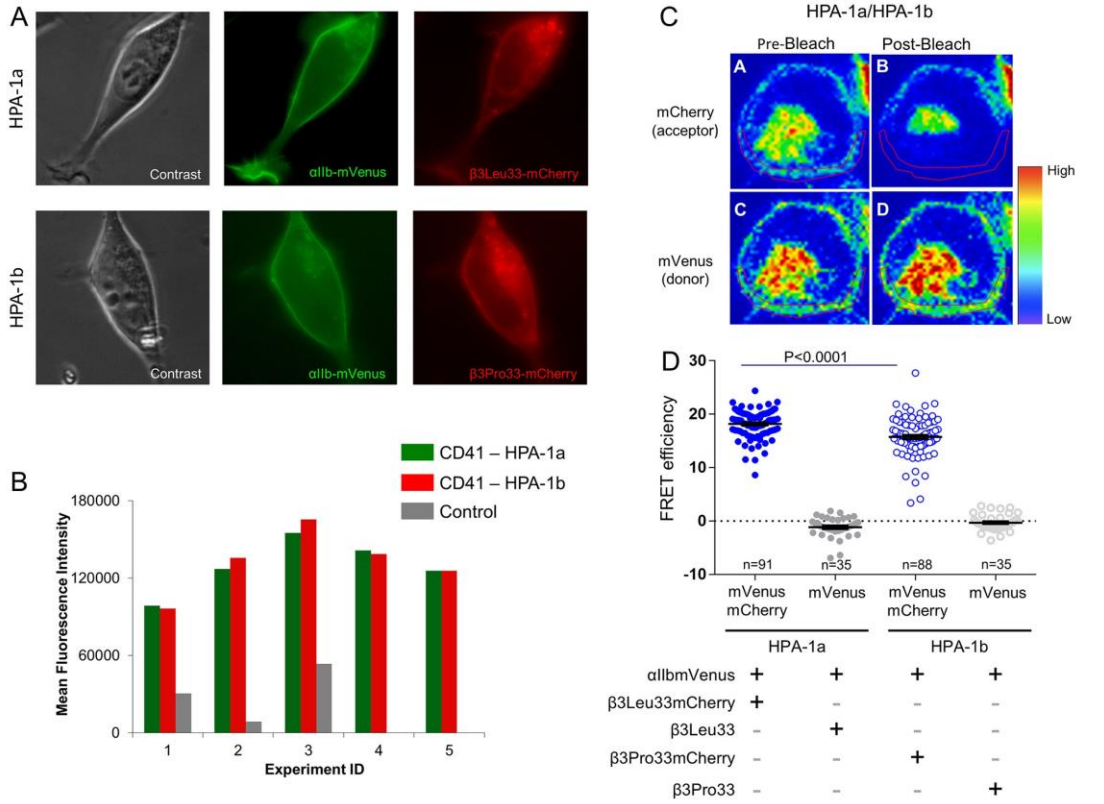

Figure 4. Transient expression of the complete $\alpha_{IIb}\beta_3$ receptor in HEK293 cells. *A*, phase-contrast and fluorescence microscopy images of a representative HEK293 cell transfected with α_{IIb}mVenus and β_3Leu^{33}mCherry plasmids (*upper panel*) and a representative HEK293 cell transfected with α_{IIb}mVenus and β_3Pro^{33}mCherry plasmids (*lower panel*). *B*, flow cytometric analyses of $\alpha_{IIb}\beta_3$ (CD41), expressing either isoform Leu^{33} (HPA-1a) or Pro^{33} (HPA-1b), performed 48 h after transfection in five independent experiments. Of note, the transfectants displayed less than 10% difference in $\alpha_{IIb}\beta_3$ expression of either Leu^{33} (HPA-1a) or Pro^{33} (HPA-1b) isoform. Values represent mean fluorescence intensity after staining of the transfectants with APC-conjugated CD41 antibody, a complex-specific anti-$\alpha_{IIb}\beta_3$ antibody. *C*, FRET-APB measurements in a representative HEK293 cell transfected with α_{IIb}mVenus and β_3Leu^{33}mCherry plasmids. *D*, results of FRET efficiency of fused individual Leu^{33} (HPA-1a) or Pro^{33} (HPA-1b) cells and respective donor controls. To determine the efficiency of energy transfer, the fluorescence of mVenus was measured in a defined region of the membrane (*red circled*) before and after photobleaching of mCherry at 561 nm (39, 40). Details are given under "Experimental procedures." The *error bars* indicate mean ± S.E.

to FRET analyses, all of which were subsequently carried out with minimal manipulation of the cells to prevent any possible cellular activation.

FRET-APB analyses were performed in a total of 249 single cells: 91 Leu^{33} cells, 88 Pro^{33} cells, 35 Leu^{33} donor control cells, and 35 Pro^{33} donor control cells. FRET-APB efficiency was computed according to Equation 2 (see "Experimental procedures" and Refs. 39 and 40). Notably, FRET-APB efficiency between mVenus and mCherry in Leu^{33} cells (mean ± S.E., 18.20 ± 0.276) was significantly higher ($p < 0.0001$) than in HPA-1b cells (15.74 ± 0.395) (Fig. 4*D*). This difference in energy transfer upon photobleaching of both $\alpha_{IIb}\beta_3$ isoforms suggested a larger spatial separation in the Pro^{33} than the in Leu^{33} isoform when both isoforms were examined in their bent conformation. This observation is indicative of a state more prone to activation as a consequence of the Leu → Pro exchange at residue 33 in the ectodomain of the β subunit of $\alpha_{IIb}\beta_3$.

Short- and mid-range structural, dynamics, and stability changes induced by the Leu → Pro exchange

The two-dimensional (2D) RMSD of C$^\alpha$ atoms of the EGF-1/EGF-2/EGF-3 domains along the MD trajectories was computed after mass-weighted superimposition onto the respective starting structures of the domains. The 2D RMSD values indicated that the domains showed larger differences from the initial starting structure in the Pro^{33} than in the Leu^{33} isoform (see also Table S4) but also that the two isoforms adopted conformational states that largely deviated from each other (RMSD up to 8 Å) (Fig. 5*A*). Next, we computed the residue-wise root-mean-square fluctuations (RMSFs) of the PSI domain, a measure of atomic mobility, to identify differences in the conformational variations associated with the Leu → Pro exchange. The results revealed a marked increase in atomic mobility for residues Glu^{29}–Pro^{37} of the loop between strands A and B in the PSI domain (Fig. 5*B*) with a ~0.6-Å difference found at residue

Allosteric changes of $\alpha_{IIb}\beta_3$ induced by the Pro^{33} variant

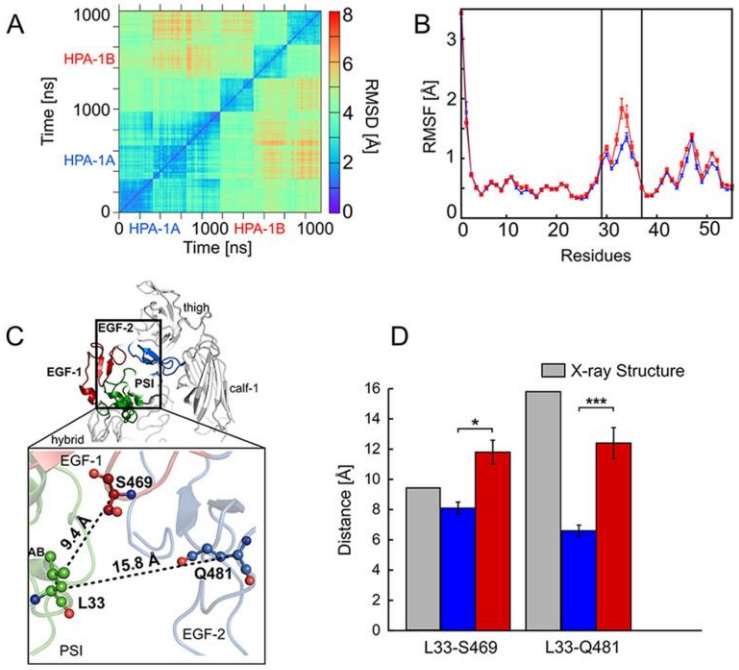

Figure 5. Short- and mid-range structural and dynamics changes induced by the Leu → Pro exchange. *A*, 2D RMSD plot calculated for the C$^{\alpha}$ atoms of the EGF-1, EGF-2, and EGF-3 domains after superimposing onto the respective domains. All trajectories accounting for an aggregate simulation time of 2 × 3 μs were considered together in the analysis, excluding the first 200 ns of each trajectory and extracting frames at intervals of 100 ns. *B*, residue-wise mean backbone RMSF of the PSI domain after a mass-weighted fitting onto the starting structure. *Error bars* denote S.E. *Blue* and *red curves* represent the Leu^{33} and Pro^{33} isoforms, respectively; the *two black lines* delineate the AB loop (residues Glu^{29}–Pro^{37}). *C*, $\alpha_{IIb}\beta_3$ is shown in schematic representation and colored in *light gray* (with the exception of the PSI domain (*green*), EGF-1 domain (*firebrick*), and EGF-2 domain (*marine*)). Domains are labeled. The enlargement shows the location of the Leu → Pro exchange in the PSI domain within the genu interface of the β_3 subunit. *Black dashed lines* indicate distances computed in *D* with the distance values of the starting structure reported next to them. Residues Leu^{33} (PSI domain), Ser^{469} (EGF-1 domain), and Gln^{481} (EGF-2 domain) are depicted in *ball-and-stick* representation. *D*, mean distances between the C$^{\alpha}$ atoms of Leu^{33}/Pro^{33} as well as Ser^{469} (EGF-1) and Gln^{481} (EGF-2) calculated for the Leu^{33} isoform (*blue boxes*) and the Pro^{33} variant (*red boxes*) and measured in the crystal structure (Protein Data Bank code 3FCS; *gray boxes*). *Error bars* indicate mean ± S.E., and *asterisks* denote a significant difference (*, $p < 0.05$; ***, $p < 0.0001$) between the two isoforms of $\alpha_{IIb}\beta_3$.

33 (Leu or Pro). Beyond this region, the amino acid exchange did not affect the atomic mobility (Fig. 5*B*). Likewise, we did not detect significant differences in the secondary structure propensity of the AB loop residues between the Leu^{33} and Pro^{33} isoform except for a small decrease of the α-helix propensity in the helix C-terminal to the loop (Fig. S7). To conclude, in both isoforms, the PSI domain did not undergo marked changes in structure (see also Table S4) as a consequence of the polymorphism at residue 33 of the β_3 subunit. This was in contrast to the EGF domains, which revealed marked structural changes in Pro^{33}. However, the structural dynamics of the AB loop of the PSI domain increased in the Pro^{33} variant.

As this loop faces the EGF-1 and EGF-2 domains (41), the Leu → Pro exchange may also impact the structure, interactions, and stability of this interface. Therefore, we monitored the time evolution of the distance between the C$^{\alpha}$ atoms of residue Leu^{33} or Pro^{33} and Ser^{469} and Gln^{481} to investigate the level of compactness of the interface between the PSI domain and the EGF-1/EGF-2 domains (Fig. 5*C*). In the bent conformation of $\alpha_{IIb}\beta_3$, the C$^{\alpha}$ atom at residue 33 is separated by 9.4 and 15.8 Å from the C$^{\alpha}$ atoms of Ser^{469} and Gln^{481} (calculated from Protein Data Bank code 3FCS), respectively.

Comparing both isoforms of $\alpha_{IIb}\beta_3$, we found a mean value for the Leu/Pro^{33}···Ser^{469} distance that is smaller by ~3.7 Å in Leu^{33} (~8.1 ± 0.40 Å) than in Pro^{33} (~11.8 ± 0.79 Å). A mean value smaller by ~5.8 Å in Leu^{33} (~6.6 ± 0.37 Å) than in Pro^{33} (~12.4 ± 1.02 Å) was found for the Leu/Pro^{33}···Gln^{481} distance. The differences between distances in the Leu^{33} and Pro^{33} isoforms were significant in all cases (Fig. 5*D* and Table S9). The pronounced decrease from the initial structure observed in the Leu^{33} isoform (~9 Å) for the Leu^{33}···Gln^{481} distance is in line with the description of a contact area between these two domains in the closed, low-affinity, bent state (41). This contact is lost in the extended conformation (41). These results indicated that the interface between the PSI domain and the EGF-1/EGF-2 domains is more tightly packed in the Leu^{33} than in the Pro^{33} isoform.

In addition, we computed the number of contacts present in the starting structure ("native contacts") and those formed over the course of the MD simulations ("non-native contacts"). Contacts were evaluated between the nine residues of the AB loop and residues of the adjacent EGF-1 and EGF-2 domains, applying a distance cutoff of 7 Å between the side-chain atoms. In all three MD simulations of the Pro^{33} variant, the total number of

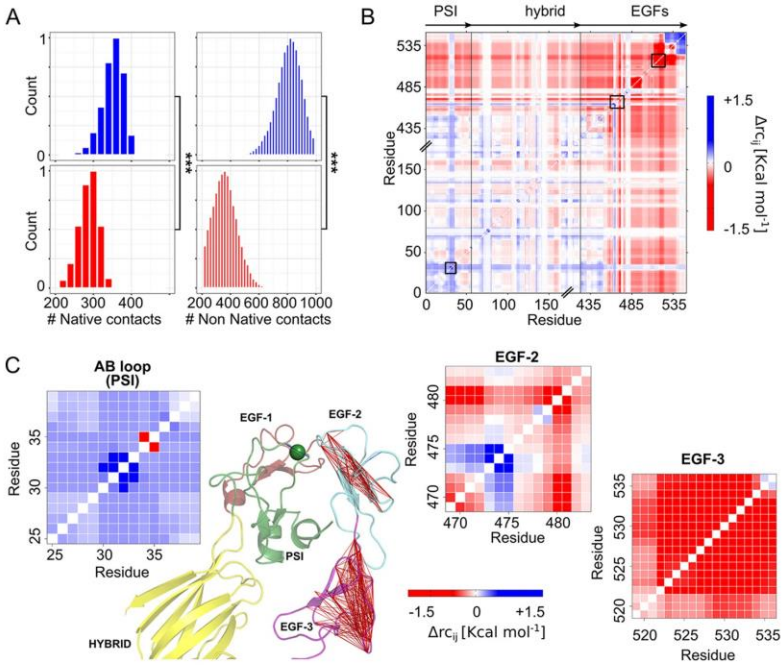

Figure 6. Changes within the PSI/EGF domain interface and in the structural stability between the Leu^{33} and Pro^{33} isoforms. *A*, shown are the active contacts (*left*) and non-native contacts (*right*) formed between the AB loop (PSI domain) and all the side chains located within a distance range of 7 Å. Mean values were computed over three MD simulations of the Leu^{33} isoform (*blue* histograms) and Pro^{33} variant (*red* histograms). *Asterisks* denote a significant difference (***, $p < 0.0001$) between the two isoforms of $\alpha_{IIb}\beta_3$. *B*, difference stability map generated by CNA and averaged over three MD simulations showing the difference in structural stability between both isoforms, focusing on the β_3 genu region. The color gradient indicates residues with lower structural stability in the Leu^{33} (*blue*) or Pro^{33} isoform (*red*). *C*, enlargements of three areas highlighted within the difference stability map by *black boxes* (*B*) and corresponding to the AB loop (PSI domain), residues Ser^{469}–Asp^{484} (loop connecting the EGF-1 domain to the EGF-2 domain), and residues Gly^{519}–Cys^{536} (EGF-3 domain), exemplifying changes in structural stability due to the Leu → Pro exchange. The results for the latter two regions are also displayed on the structure of the hybrid (*yellow*), PSI (*green*), EGF-1 (*firebrick*)/EGF-2 (*light blue*)/EGF-3 (*purple*) domains of $\alpha_{IIb}\beta_3$ (*green sphere*, C^{α} atom of residue 33) in terms of lines connecting residues whose mutual stability has decreased in the Pro^{33} isoform ($\Delta rc_{ij} > -1.5$ kcal mol^{-1}).

contacts was significantly lower than in the Leu^{33} isoform (Fig. 6*A* and Table S10). This difference became even more pronounced when only non-native contacts were considered (2-fold decrease). The same holds true for specific interactions (hydrogen bonds and salt bridges) that were conserved in the Leu^{33} isoform only (Fig. S8). In the segment connecting the EGF-1 domain with the EGF-2 domain, Gln^{481} is hydrogen-bonded to Ser^{469} with a high occupancy (~70% along the MD trajectories) and/or with Gln^{470} (~27%). Additional stable intradomain hydrogen bond interactions (>60%) were found within the EGF-2 domain that involve Cys^{492}, which also forms a disulfide bridge with Cys^{473} of the EGF-1 domain (Fig. S8). To conclude, the Leu → Pro exchange leads to a less compact interface between the PSI domain and EGF-1/EGF-2 domains. Moreover, fewer interactions across the interface and within the EGF-1/EGF-2 domains were found in the Pro^{33} variant compared with the Leu^{33} isoform.

Changes in structural stability of the EGF domains occur at long range from residue 33

To analyze changes in the structural stability of the interface between the PSI domain and EGF-1/EGF-2 domains resulting from the Leu → Pro exchange, we performed Constraint Network Analysis (CNA) on the β_3 leg (hybrid domain/PSI and EGF domains) of both $\alpha_{IIb}\beta_3$ isoforms, Leu^{33} and Pro^{33}. In CNA (42), a molecular system is represented as a network of nodes (atoms) connected by constraints (non-covalent bonds). This network is analyzed applying rigidity theory (43), revealing rigid (*i.e.* structurally stable) clusters and flexible links in between (44). By rigidity analysis, long-range effects on the stability of distant structural parts due to a local structural change can be detected (45). Performing a constraint dilution simulation (46), a stability map (42), rc_{ij} (where i and j are residue numbers), is obtained that reports on the hierarchy of structural stability of the molecular system. The difference stability map calculated as rc_{ij} (Leu^{33}) − rc_{ij} (Pro^{33}) then reports on the influence on structural stability due to the Leu → Pro exchange (*blue* (*red*) colors in Fig. 6, *B* and *C*, indicate residues that were less stable in the Leu^{33} (Pro^{33}) isoform, respectively). The AB loop showed a local increase in structural stability, which results from the overconstrained five-membered ring of Pro^{33} compared with the flexible side chain of Leu^{33} (48) (Fig. 6, *B* and *C*). By contrast, the loop connecting the EGF-1 to the EGF-2 domain and pointing toward the AB loop (21), which is >15 Å apart from residue 33, became less stable in the Pro^{33} variant (Fig. 6, *B* and *C*; the

segment formed by residues Ser^{469}–Gln^{481} is highlighted). The EGF-3 domain, although not directly interacting with the PSI domain, has been suggested to be important for keeping the integrin in its bent conformation (20). Residues Gly^{519}–Cys^{536} of the EGF-3 domain >30 Å apart from residue 33 became less structurally stable in the Pro^{33} variant. To conclude, the Leu → Pro exchange leads to long-range decreases in the structural stability of the EGF domains.

Discussion

In this study, we provide evidence that indicates that the Pro^{33} variant of $\alpha_{IIb}\beta_3$ allosterically shifts the dynamic conformational equilibrium of the integrin toward a more active state. This finding can provide an explanation for the prothrombotic phenotype of Pro^{33} platelets that has been suggested in several clinical association studies (22–25) but also in experimental settings (26, 38, 49).

Both clinical and laboratory data regarding a possible impact of the HPA-1 polymorphism of $\alpha_{IIb}\beta_3$ on modulating platelet function have been discussed controversially. Specifically, it has been debated whether or not the Leu → Pro exchange at residue 33 of the β_3 subunit induces an increased thrombogenicity of Pro^{33} platelets. We therefore initially studied the dynamics of platelet thrombus formation using a collagen type I matrix in an established perfusion system, simulating arterial flow conditions. Quantitation of thrombus growth *in vitro* demonstrated that the mean volume of single thrombi formed by Pro^{33} platelets is significantly higher than that of the Leu^{33} platelets (Fig. 2). The initial adhesion of circulating platelets with a collagen matrix is complex, involving platelet capture ("tethering") by immobilized VWF via GPIbα of the platelet GPIb-IX-V complex, subsequent GPIb-IX-V– dependent signaling, and direct interaction with collagen via $\alpha_2\beta_1$ and GPVI, the platelet collagen receptors, inducing platelet activation (50, 51). To block some of these interactions, we therefore used specific monoclonal antibodies such as LJ-Ib1 that completely inhibits VWF binding to the platelet GPIb-IX-V complex or 5C4 that blocks the platelet GPVI receptor (data not shown). The expression of $\alpha_2\beta_1$ on the platelet surface is genetically controlled and modulated by nucleotide polymorphisms in the α_2 gene (52). Moreover, because the $\alpha_2$807TT genotype of $\alpha_2\beta_1$ has also been suggested to be a prothrombotic integrin variant (22), volunteers of this series of experiments were carefully selected by recruiting only carriers of the $\alpha_2$807CC genotype.

A specific feature of the experiments summarized in Fig. 2 is that the difference in single thrombus volumes between Pro^{33} and Leu^{33} platelets is due to differences in apical thrombus growth (Fig. 2*B*). This is remarkable, especially because apical thrombus segments become exposed to increasing shear over time, exceeding an initial near-wall shear rate of 500 s^{-1} (Fig. 2*D*). Our finding is indicative of a higher thrombus stability of Pro^{33} than Leu^{33} platelets as reported before (29). By contrast, considering the fact that neither the number nor the bottom area of formed thrombi differs between both isoforms of $\alpha_{IIb}\beta_3$, it appears rather unlikely that the initial adhesive interactions between the collagen matrix and platelets under flow had a significant effect on the results.

Assuming that the difference in thrombus volumes between both $\alpha_{IIb}\beta_3$ isoforms is indeed due to increased thrombus stability in the Pro^{33} variant, it would be an attractive assumption that the Leu → Pro exchange has an impact on the mechanotransduction mediated by the integrin. Such a contention is in line with previous observations documenting a significantly more stable adhesion of Pro^{33} than of Leu^{33} platelets onto immobilized fibrinogen at shear rates ranging from 500 to 1,500 s^{-1} (26). Moreover, it has been shown that the Pro^{33} variant displays increased outside-in signaling (53). These findings suggest that the HPA-1 polymorphism of $\alpha_{IIb}\beta_3$ modulates the function and activity of the integrin.

However, the molecular nature underlying this modulation has remained elusive so far. In this context, a marked concern in the past has been that the point mutation at residue 33 of the β_3 subunit is located >80 Å away from relevant functional domains of $\alpha_{IIb}\beta_3$ such as extracellular binding sites or transmembrane domains. Conversely, due to its distant location, it appears quite appropriate to exclude that the Leu → Pro exchange would directly influence interactions with ligands at the extracellular or even intracellular binding sites. It is more likely that an increased activity of $\alpha_{IIb}\beta_3$ results from a change in the structural dynamics of the integrin. To probe this assumption, we performed microsecond-long MD simulations on the ectodomains of both $\alpha_{IIb}\beta_3$ isoforms, Leu^{33} and Pro^{33}. The ectodomains of either isoform initially only differed in the side chains of residue 33.

Ectodomains of integrins have been successfully used by us (18, 27) and others (34, 54) in previous studies as model systems to explore possible influences of structure and solvent on integrin activation. For the MD simulations, we used established parameterizations for the solvent (55) and the protein (56, 57), which we had applied successfully in other integrin simulations (18, 27, 37), although we note that more recent protein force fields have become available (58, 59). The impact of force field deficiencies on our results is expected to be small due to cancellation of errors when comparatively assessing the two isoforms. Furthermore, we expect the deficiency of the ff99SB force field (56, 57) to destabilize helical structures (60) to not have a decisive influence on our results because the mutation site (residue 33) is located in a loop region. Finally, ff99SB was also shown to have some issues with side-chain torsions (61). As Leu^{33} is located at the vertex of the AB loop, with the side chain facing away from the β_3 subunit, we do not expect imperfect leucine torsions to impact structural properties markedly however.

The present simulations were started from the bent conformation with closed legs as present in the crystal structure (62), representing a low-affinity, inactive state of the integrin (63). As depicted, our simulation findings reveal that the Pro^{33} variant displays significantly larger structural deviations from the bent starting structure and becomes less compact than the Leu^{33} isoform (Fig. 3). Furthermore, we evaluated geometric parameters within the βA domain ("T-junction formation" between helices α1 and α7; Fig. 3*B*) and variables characterizing the bending and splaying of the structure (Fig. 3, *C* and *D*), which had been used successfully in related studies to characterize inactive-to-active transitions (27, 37, 64). The results display

significant differences in the conformational states of both isoforms of $\alpha_{IIb}\beta_3$ with the ectodomain of the Pro^{33} variant showing a stronger tendency to move toward an open, extended conformation with more splayed legs than the Leu^{33} isoform. We performed triplicate MD simulations for both isoforms, which allows probing for the influence of the starting conditions and determining the significance of the computed results by statistical testing and rigorous error estimation. As to the latter, we paid close attention to only consider uncorrelated instances for the S.E. calculations (Equations 1 and 2).

The results are consistent across three independent MD simulations for each isoform. This demonstrates the robustness of our approach. We are aware that the magnitudes of the changes of the bending or splaying angles do not correspond to those described for a fully open, extended ectodomain conformation (8). However, in consideration of the simulation times used here, this finding is in complete accord with the timescale of integrin activation in the absence of biomechanical forces, ranging from microseconds to seconds (34, 35).

As an independent approach to explore the impact of the Leu → Pro exchange on the structural dynamics of full-length $\alpha_{IIb}\beta_3$ integrin, FRET measurements on α_{IIb}mVenus and β_3Leu^{33}mCherry or β_3Pro^{33}-mCherry transiently cotransfected in HEK293 cells were performed (Fig. 4, *A–C*). HEK293 cells have previously been shown to be a suitable cellular model for functional studies involving $\alpha_{IIb}\beta_3$ (65, 66). The transfectants display a significantly higher efficiency of energy transfer between the α and β subunits in the Leu^{33} than in the Pro^{33} isoform. This difference is indicative of a smaller spatial separation between the cytoplasmic tails of the Leu^{33} isoform in its resting state. Conversely, the lower energy transfer obtained in the Pro^{33} variant reflects a larger spatial separation of its cytoplasmic domains that is already present in the resting state (Fig. 4*D*). A limitation of the FRET method is that it furnishes indirect information. However, the level of evidence is consistent, and the observation is in good agreement with the findings of the MD simulations. A direct study comparing activity and stability of both receptor isoforms using purified protein would provide complementary information about receptor conformations but was beyond the scope of the present work.

Taken together, both the MD simulations and FRET experiments reveal structural changes in the ectodomain of $\alpha_{IIb}\beta_3$ or the full-length integrin for the Pro^{33} variant that relate to a conformational change from a closed, bent structural state with closed legs to a more open, extended state with splayed legs. According to current models (14, 16, 33), such a conformational change is required for integrin activation. Considering that in both the MD simulations and FRET measurements the integrin has been examined in the resting state, our results provide evidence that the Leu → Pro exchange can shift the dynamic conformational equilibrium of $\alpha_{IIb}\beta_3$ in such a way that a structural state more similar to the active conformation is present.

The effect of the Leu → Pro exchange appears to have some similarity to stimulatory monoclonal antibodies, which have been suggested to shift the dynamic conformational equilibrium in favor of those forms that lead to an increase in the proportion of a high-affinity integrin (62). As the effect induced by the amino acid substitution manifests in regions far away from the mutation site, the influence of the Leu → Pro exchange must be allosteric. Our results clearly go beyond a previous study (67) that used MD simulations of the β_3 subunit only to investigate possible effects of the HPA-1 polymorphism on the structure of the β_3 subunit.

To explore a possible mechanism of how the Leu → Pro exchange exerts an allosteric effect, applying MD simulations and rigidity analyses, we examined short- and mid-range structural, dynamics, and stability changes in the PSI domain and neighboring domains. Although the overall architecture of the PSI domain remains largely unchanged by the amino acid substitution, particularly the EGF domains show marked structural alterations in the Pro^{33} variant (Fig. 5). The EGF-1 and EGF-2 domains, although sequentially distant from the mutation located at residue 33, are spatially close to the AB loop of the PSI domain in the bent state, which carries the HPA-1 polymorphism (5, 19, 21). Parts of the AB loop are markedly more mobile in the Pro^{33} variant (Fig. 5*B*). Related to these changes, our analyses reveal that the Leu → Pro exchange leads to a less compact interface between the PSI domain and EGF-1/EGF-2 domains (Fig. 5, *C* and *D*). Specifically, fewer native and nonnative contacts are formed across the interface and within the EGF-1/EGF-2 domains in the Pro^{33} variant than in the Leu^{33} isoform (Fig. 6*A*). These conformational and dynamic alterations are related to a change in the structural stability of the EGF-1 and EGF-2 domains that percolates from the interface region through these domains (Fig. 6, *B* and *C*).

Notably, similar changes in these regions have been related to integrin activation before. For example, the displacement of the PSI domain of about 70 Å, described to act as a mechanical lever upon outside-in signaling (21), alters the interface formed with the EGF-1 and EGF-2 domains (68). Furthermore, activating mutations have been identified in the N-terminal part of the PSI domain, the EGF-2 domain, and parts of the EGF-3 domain of $\alpha_x\beta_2$ integrin (20). These regions are thought to form the area of contact between α and β subunits in the bent conformation. Finally, when generating an integrin chimera by combining α and β subunits from different species, direct interactions between the subunits could not be formed, and the integrin no longer appeared locked in the closed conformation (20).

The results of this study provide an explanation for the prothrombotic phenotype of the Pro^{33} variant of $\alpha_{IIb}\beta_3$. Specifically, the shift of the dynamic conformational equilibrium of the Pro^{33} variant toward an active state may promote a fully active state in the presence of immobilized adhesive ligands such as fibrinogen or VWF and, consequently, favor outside-in signaling. This, in turn, may facilitate and accelerate platelet aggregation and subsequent formation of stable platelet thrombi. Thus, our results lend support to previous clinical (22–25, 29, 49) and experimental findings (26, 29, 38, 49) suggesting that the Leu → Pro exchange confers prothrombotic properties to $\alpha_{IIb}\beta_3$.

Experimental procedures

Blood collection

Blood was collected through a 21-gauge needle from 15 healthy, medication-free volunteers into vacutainer tubes (BD Biosciences) containing sodium citrate (0.38%, w/v). The volunteers were recruited by the Düsseldorf University Blood Donation Center. Written informed consent was obtained from the volunteers according to the Helsinki Declaration. The Ethics Committee of the Faculty of Medicine, Heinrich Heine University Düsseldorf, approved the study (study number 1864).

Parallel plate flow chamber

A custom-made rectangle flow chamber was used (flow-channel width, 5 mm; height, 80 μm; length, 40 mm). Glass coverslips forming the lower surface of the chamber were flame-treated, cooled, and coated with 0.04 μml/mm^2 collagen type S (concentration, 3 mg/ml) containing 95% type I and 5% type III collagen (Roche). The perfusion system was flushed and filled with PBS buffer (pH 7.3) containing 2% BSA to block unspecific adhesion onto the glass slides. A syringe pump (Harvard Apparatus Inc., Holliston, MA) was used to aspirate mepacrine-labeled citrated whole blood through the flow chamber for 10 min at a constant flow rate of 9.6 ml h^{-1}, producing an initial near-wall shear rate of 500 s^{-1}.

Labeling of platelets

Platelets were stained in whole blood by direct incubation with the fluorescent dye mepacrine (quinacrine dihydrochloride; 10 μM final concentration). Although this dye also labels leukocytes, these cells could be readily distinguished from platelets by their relatively large size and sparsity; moreover, leukocyte attachment to the surface tested was negligible under the conditions used. Mepacrine accumulates in the dense granules of platelets and had no effect on normal platelet function at the concentration used. Platelet secretion after adhesion did not prevent their visualization. Furthermore, mepacrine did not affect platelet adhesion or platelet aggregate/thrombus formation.

Picture acquisition and digital image processing

The fluorescence signal of mepacrine-stained platelets was detected by a Zeiss Axiovert 100 M/LSM 510 confocal laser scanning microscope (Jena, Germany). During the flow period of 10 min, 25 stacks of images were acquired. One stack consisted of 30 slices with a height of 30 μm. Digitized images had a standard size of 512 × 512 pixels and an optical resolution of 1 μm.

Volumetry of single platelet thrombi

The stacks were reconstructed three-dimensionally and analyzed with the custom-made software package ECCET (www.eccet.de).[5] The software integrated the slices of every stack and divided the three-dimensional space into multiple "voxels" (three-dimensional equivalent to a pixel). All fluorescence signals were smoothed by a separate linear Gaussian filter in all three planes (filter σ2). Voxels with a gray value >10 were marked as thrombus; voxels with lower gray values were disregarded. Thus, background noise of fluorescence signals from adjacent focus planes and single platelets was suppressed. Thrombi were then categorized by volume, and only platelet aggregates exceeding the cutoff volume of 100 μm^3 were assessed to avoid interference by non-stationary objects, *e.g.* moving platelets.

Starting structures for molecular dynamics simulations

The starting structure for MD simulations of $\alpha_{IIb}\beta_3$ in the bent, closed form representing the inactive state of the Leu^{33} isoform was obtained from the coordinates of the X-ray structure of the ectodomain of $\alpha_{IIb}\beta_3$ integrin (Protein Data Bank code 3FCS) (9). In the Protein Data Bank entry, the α_{IIb} subunit contains two unresolved regions within the calf-2 domain (residues 764–774 (AB loop) and 840–873 (XY loop)), and the β_3 subunit has two unresolved regions within the EGF domains (residues 75–78 and 477–482). Residues unresolved in the α_{IIb} subunit were not included in the starting structures, consistent with our previous studies on integrin (18, 27). The apparently high flexibility of these residues implies that they will not contribute significantly to stabilizing the bent conformation of the $\alpha_{IIb}\beta_3$ integrin. The short regions of unresolved residues of the β_3 subunit were modeled and refined using the automatic loop refinement server ModLoop (69). The structure was finally refined by reverting the engineered residues Cys^{598} and Cys^{688} to the natural residues Leu^{598} and Pro^{688}, respectively. MODELLER version 9.9 (70) was applied, allowing the modeling of the two Cys residues only. The Pro^{33} variant was obtained by mutating residue Leu^{33} to Pro^{33}, using Swiss-PdbViewer (31), without changing the coordinates of any of the other amino acids. As a final step, we capped the charges at the N-terminal residues Glu^{764} and Gly^{840} and the C-terminal residues Asp^{774} and Gln^{873} using the leap module of Amber 12 (71). All structural ions present in the protein were modeled as Mg^{2+} ions. Integrin sequence numbers used throughout this study are according to UniProt.

Molecular dynamics simulations

Each starting structure of the two HPA-1 isoforms, Leu^{33} and Pro^{33}, was subjected to three replicates of all-atom MD simulations of 1-μs length each in explicit solvent summing up to 6 μs of aggregate simulation time for production. MD simulations were performed with the Amber 12 suite of programs (71) using the force field ff99SB, initially described by Cornell *et al.* (56) and modified according to Simmerling and co-workers (57). Parameters for the Mg^{2+} ions were taken from Aqvist (72). The total charge of the system was neutralized by adding eight Na^+ counter-ions with the leap module of Amber 12 (71), and the solutes were placed into an octahedral period box of TIP3P water molecules (55). The distance between the edges of the water box and the closest atom of the protein was at least 11 Å, resulting in systems of ~200,000 atoms. The particle mesh Ewald method (73) was used to treat long-range electrostatic interactions, and bond lengths involving bonds to hydrogen atoms were constrained using the SHAKE algorithm (74). The time step for integrating Newton's equations of motion was 2 fs with a direct-space, non-bonded cutoff of 8 Å. Applying har-

monic restraints with force constants of 5 kcal mol^{-1} $Å^{-2}$ to all solute atoms, MD simulations in the NVT (constant number of particles, volume, and temperature) ensemble was carried out for 50 ps, during which the system was heated from 100 to 300 K. Subsequent MD simulations in the NPT (constant number of particles, pressure, and temperature) ensemble were used for 150 ps to adjust the solvent density. Finally, the force constant of the harmonic restraints on solute atom positions was gradually reduced to zero during 100 ps of NVT MD simulations. Subsequently, we performed a 1-μs unrestrained simulation; the first 200 ns were discarded, and the following 800 ns were used for analysis with the programs ptraj/cpptraj (75) with conformations extracted every 20 ps. The production MD simulations were performed with the graphics processing unit (GPU) version of the program pmemd (76).

Analysis of the trajectories

For the analysis of the trajectories, ptraj/cpptraj (75) of the AmberTools suite of programs (71) were applied. For investigating structural deviations along the MD trajectories, the RMSD of all C^α atoms was computed after minimizing the mass-weighted RMSD of the C^α atoms of the βA and β-propeller domains with respect to the starting structure. In addition, to investigate the structural changes of a domain, the C^α atom RMSD of each domain was computed after superimposing the respective domain. To evaluate the level of compactness of the structure, the R_g was calculated with respect to the complete ectodomain. To examine atomic mobility, RMSFs were computed for the backbone atoms of the PSI domain. An analysis of the secondary structure of the PSI domain was carried out to monitor variations in the content of the two helices bordering the AB loop. Structural changes in the ectodomain were characterized as reported previously (18, 27). The kinking of the helix α1 was measured by the three points (center of mass of C^α atoms of Lys^{112} and Ile^{118}, center of mass of C^α atoms of Gln^{119} and Lys^{125}, and center of mass of C^α atoms of Leu^{126} and Leu^{132}). The unbending of the structure was evaluated using the angle formed by the centers of mass of the β-propeller, βA, and PSI domains, and the splaying of the two legs was evaluated using the angle formed by the centers of mass of the calf-2, thigh, and β-tail domains. Changes in the β_3 genu region were first quantified by computing the distances between the C^α atom of residue 33 and the C^α atom of Ser^{469} (EGF-1 domain) and with the C^α atom of Gln^{481} (EGF-2 domain). To identify a network of interactions keeping the interdomain interface stable, a maximal distance of 3.5 Å and a minimal angle of 120° were used as exclusion criteria to identify hydrogen bond formation.

The CNA software package was used to provide a link between structure and rigidity/flexibility of the HPA-1 isoforms (77). To derive information of the effect of Pro^{33} on a local level, we first generated an ensemble of 400 equally distributed structures from the 200–1,000-ns intervals of each MD simulation, considering only the hybrid, PSI, and EGF block domains. Thermal unfolding simulations of the Leu^{33} and Pro^{33} isoforms were then carried out with CNA to identify differences in the structural stability within the β_3 genu region following established protocols (77). For each isoform, we generated three different stability maps and three different neighbor stability maps; from them we calculated the mean values used to build a final stability map and neighbor stability map for Leu^{33} and Pro^{33}. Finally, a difference stability map was calculated as rc_{ij} (Leu^{33} isoform) − rc_{ij} (Pro^{33} isoform).

Statistical analysis

Results from three independent MD simulations are expressed as arithmetic means ± S.E. calculated over the time. The overall S.E. for each simulated system was calculated according to the law of error propagation (Equation 1),

$$S.E._{total} = \sqrt{S.E._1^2 + S.E._2^2 + S.E._3^2} \quad \text{(Eq. 1)}$$

where the subscripts $i = \{1, 2, 3\}$ indicate the three trajectories. $S.E._i$ was computed following Ref. 78 and applying the multiple Bennett acceptance ratio method (79), which allows detecting the decorrelation time of an investigated variable along each MD simulation. From it, the effective sample size is established, and the $S.E._i$ is derived.

In the case of hydrogen bond and contact analyses, S.E. is calculated from the S.D. of the three means of the three MD simulations according to Equation 2, assuming that the three MD simulations are statistically independent.

$$S.E. = S.D. / \sqrt{3} \quad \text{(Eq. 2)}$$

Differences between mean values are considered statistically significant if $p < 0.05$ and $p < 0.001$ (indicated as * and **, respectively, in figures and tables) and highly statistically significant if $p < 0.0001$ (indicated as ***) according to the Student's t test for parametric testing. The statistical analysis was performed using R software (80) and the pymbar module for multiple Bennett acceptance ratio (79).

The FRET efficiency results obtained performing the FRET-AB experiments are expressed as means ± S.E. For statistical analysis, the unpaired t test was applied using GraphPad Prism version 6.00 for Windows (GraphPad Software, La Jolla, CA).

Figure preparation

The crystal structure of the $\alpha_{IIb}\beta_3$ integrin (Protein Data Bank code 3FCS) was used to represent the protein together with conformations extracted from the MD trajectories. PyMOL was used to generate molecular figures (36), and graphs were prepared using Gnuplot (47).

Live-cell imaging of $\alpha_{IIb}\beta_3$-transfected HEK 293 cells expressing either isoform Leu^{33} or Pro^{33}

Live-cell imaging was performed to examine the cellular distribution of $\alpha_{IIb}\beta_3$-transfected HEK 293 cells expressing either isoform Leu^{33} or Pro^{33}. 24 h after transfection, 3.7×10^4 cells in complete culture medium were allowed to settle for more 24 h in individual chambers in a μ-slide 4-well ibiTreat chamber slide (Ibidi, Martinsried, Germany) previously coated with 50 μg/ml fibrinogen from human plasma (Sigma-Aldrich) in PBS without Ca^{2+} and Mg^{2+} for 1 h at 37 °C. Live-cell imaging was performed with an Axiovert S100 inverted fluorescence microscope (Zeiss) equipped with a 12.0 Monochrome without IR-18

monochromatic camera (Diagnostic Instruments, Inc, Sterling Heights, MI) and an LEJ EBQ 100 isolated lamp (Leistungselektronik Jena GmbH, Jena, Germany). Images were obtained with a 63× oil immersion objective lens using a 5,000-ms exposure time for mVenus, 100 ms for mCherry, and 300 ms for brightfield. Image acquisition was performed with MetaMorph software (version 7.7.7.0). Background subtraction and image processing were performed using Adobe Photoshop CS3 software (Adobe, San Jose, CA).

Flow cytometry

Transfected cells at 70–80% confluence were harvested 24, 48, and 72 h after transfection. Subsequently, cells were pelleted by centrifugation at 400 × *g* for 7 min and suspended again in 100 μl of Dulbecco's phosphate-buffered saline (PBS). Staining with allophycocyanin (APC)-conjugated mouse anti-human CD41 monoclonal antibody (clone MEM-06; Exbio, Praha, Czech Republic; 0.15 μg/ml) was performed for 30 min at room temperature protected from light. After staining, cells were washed once in Dulbecco's PBS and analyzed on a FACS Canto II flow cytometer (BD Biosciences) equipped with 488 and 633 nm lasers for excitation and FITC, phycoerythrin, and APC filters for detection of mVenus, mCherry, and APC, respectively. The collected data were analyzed with FACSDiva software version 6.1.3 (BD Biosciences). PAC1 was obtained from BD Biosciences, and Alexa Fluor 647-fibrinogen was from Thermo Fisher Scientific (Dreieich, Germany).

FRET measurements using APB

24 h after transfection, cells were harvested and seeded in a μ-slide 8-well ibiTreat chamber slide (Ibidi). Subsequently, 24 h later (48 h after transfection) and before measuring FRET efficiency, the culture medium was substituted by identical medium but containing phenol red–free Fluorobrite™ DMEM (Thermo Fisher, formerly Life Technologies).

Live cells were examined with an LSM 780 (Zeiss) inverted microscope equipped with a C-Apochromat 40×/1.20 W Corr (from correction ring) M27 water-immersion objective lens, an AxioCam camera, and an HPX 120C lamp. FRET acceptor photobleaching experiments including image acquisition, definition of regions of interest for bleaching, and data readout were performed using the LSM software package ZEN 2012 (Zeiss). The chamber slide containing the live cells was mounted on a heating frame within a large incubation chamber (PeCon, Erbach, Germany) set to 37 °C. mVenus was excited with the 488 nm line of an argon multiline laser and detected between 513 and 558 nm using a gallium arsenide phosphide detector, whereas mCherry was excited at 561 nm using a diode-pumped solid-state laser and detected between 599 and 696 nm. The beam splitter was MBS 488/561/633. In total, a time series of 20 frames (128 × 128 pixels; pixel size, 0.33 μm) at a pixel time of 2 μs/pixel was acquired for each FRET experiment. The entire measurement including bleaching of mCherry was finished within 3.5 s. After the fifth frame, an area corresponding to half of a cell, with a constant dimension of 42 × 42 pixels (region of interest), was bleached by 30 iterations of the mCherry excitation wavelength (561 nm) using 100% laser power. After bleaching, 15 additional frames were recorded. The mean intensity of mVenus fluorescence at the cell membrane within the bleached area was extracted and analyzed according to Equation 3,

$$\text{FRET efficiency} = \frac{(I_{\text{after}} - I_{\text{before}})}{I_{\text{after}}} \times 100 \qquad \text{(Eq. 3)}$$

where I_{before} (intensity of mVenus before bleaching) and I_{after} (intensity of mVenus after bleaching) correspond to the mean intensity values of mVenus fluorescence of five images before and after bleaching within the bleached area at the cell membrane (39, 40).

Author contributions—G. P. and J. P. P. data curation; G. P., J. P. P., V. R. S., R. E. S., and H. G. formal analysis; G. P., J. P. P., and V. R. S. validation; G. P. and J. P. P. investigation; G. P. and J. P. P. visualization; G. P., J. P. P., and V. R. S. writing-original draft; G. P., J. P. P., R. E. S., and H. G. writing-review and editing; V. R. S., R. E. S., and H. G. supervision; A. B. software; A. B. methodology; R. E. S. and H. G. conceptualization; R. E. S. and H. G. funding acquisition; R. E. S. and H. G. project administration; H. G. resources.

Acknowledgments—We are grateful for computational support and infrastructure provided by the Zentrum für Informations und Medientechnologie (ZIM) at the Heinrich Heine University Düsseldorf and the computing time provided by the John von Neumann Institute for Computing (NIC) to H. G. on the supercomputers JUROPA and JURECA at Jülich Supercomputing Center (JSC) (Projects 6710, 8348, and 10307; user, HDD11). We thank Dr. Rainer B. Zotz and Beate Maruhn-Dembowski for genotyping HPA-1 of $\alpha_{IIb}\beta_3$ and α_2C807T of $\alpha_2\beta_1$. The assistance of Bianca Maassen-Weingart and Jan Peveling-Oberhag in the platelet experiments is also gratefully acknowledged. The FRET measurements were performed at the Center of Advanced Imaging at Heinrich Heine University Düsseldorf. We thank Dr. Stefanie Weidtkamp-Peters for scientific assistance.

References

1. Hynes, R. O. (2002) Integrins: bidirectional, allosteric signaling machines. *Cell* **110,** 673–687 CrossRef Medline
2. Coppolino, M. G., and Dedhar, S. (2000) Bi-directional signal transduction by integrin receptors. *J. Biochem. Cell Biol.* **32,** 171–188 Medline
3. Mould, A. P. (1996) Getting integrins into shape: recent insights into how integrin activity is regulated by conformational changes. *J. Cell Sci.* **109,** 2613–2618 Medline
4. Arnaout, M. A. (2002) Integrin structure: new twists and turns in dynamic cell adhesion. *Immunol. Rev.* **186,** 125–140 CrossRef Medline
5. Arnaout, M. A., Goodman, S. L., and Xiong, J. P. (2007) Structure and mechanics of integrin-based cell adhesion. *Curr. Opin. Cell Biol.* **19,** 495–507 CrossRef Medline
6. Luo, B. H., Carman, C. V., and Springer, T. A. (2007) Structural basis of integrin regulation and signaling. *Annu. Rev. Immunol.* **25,** 619–647 CrossRef Medline
7. Askari, J. A., Buckley, P. A., Mould, A. P., and Humphries, M. J. (2009) Linking integrin conformation to function. *J. Cell Sci.* **122,** 165–170 CrossRef Medline
8. Bennett, J. S., Berger, B. W., and Billings, P. C. (2009) The structure and function of platelet integrins. *J. Thromb. Haemost.* **7,** Suppl. 1, 200–205 CrossRef Medline
9. Zhu, J., Luo, B. H., Xiao, T., Zhang, C., Nishida, N., and Springer, T. A. (2008) Structure of a complete integrin ectodomain in a physiologic resting state and activation and deactivation by applied forces. *Mol. Cell* **32,** 849–861 CrossRef Medline
10. Springer, T. A., and Dustin, M. L. (2012) Integrin inside-out signaling and the immunological synapse. *Curr. Opin. Cell Biol.* **24,** 107–115 CrossRef Medline

11. Bledzka, K., Smyth, S. S., and Plow, E. F. (2013) Integrin $\alpha_{IIb}\beta_3$: from discovery to efficacious therapeutic target. *Circ. Res.* **112,** 1189–1200 CrossRef Medline
12. Luo, B. H., and Springer, T. A. (2006) Integrin structures and conformational signaling. *Curr. Opin. Cell Biol.* **18,** 579–586 CrossRef Medline
13. Arnaout, M. A., Mahalingam, B., and Xiong, J. P. (2005) Integrin structure, allostery, and bidirectional signaling. *Annu. Rev. Cell Dev. Biol.* **21,** 381–410 CrossRef Medline
14. Xiong, J. P., Stehle, T., Diefenbach, B., Zhang, R., Dunker, R., Scott, D. L., Joachimiak, A., Goodman, S. L., and Arnaout, M. A. (2001) Crystal structure of the extracellular segment of integrin $\alpha_V\beta_3$. *Science* **294,** 339–345 CrossRef Medline
15. Xie, C., Zhu, J., Chen, X., Mi, L., Nishida, N., and Springer, T. A. (2010) Structure of an integrin with an αI domain, complement receptor type 4. *EMBO J.* **29,** 666–679 CrossRef Medline
16. Takagi, J., Petre, B. M., Walz, T., and Springer, T. A. (2002) Global conformational rearrangements in integrin extracellular domains in outside-in and inside-out signaling. *Cell* **110,** 599–611 CrossRef Medline
17. Beglova, N., Blacklow, S. C., Takagi, J., and Springer, T. A. (2002) Cysteine-rich module structure reveals a fulcrum for integrin rearrangement upon activation. *Nat. Struct. Biol.* **9,** 282–287 CrossRef Medline
18. Reinehr, R., Gohlke, H., Sommerfeld, A., Vom Dahl, S., and Häussinger, D. (2010) Activation of integrins by urea in perfused rat liver. *J. Biol. Chem.* **285,** 29348–29356 CrossRef Medline
19. Xiong, J. P., Stehle, T., Goodman, S. L., and Arnaout, M. A. (2004) A novel adaptation of the integrin PSI domain revealed from its crystal structure. *J. Biol. Chem.* **279,** 40252–40254 CrossRef Medline
20. Zang, Q., and Springer, T. A. (2001) Amino acid residues in the PSI domain and cysteine-rich repeats of the integrin β_2 subunit that restrain activation of the integrin $\alpha_X\beta_2$. *J. Biol. Chem.* **276,** 6922–6929 CrossRef Medline
21. Xiao, T., Takagi, J., Coller, B. S., Wang, J. H., and Springer, T. A. (2004) Structural basis for allostery in integrins and binding to fibrinogen-mimetic therapeutics. *Nature* **432,** 59–67 CrossRef Medline
22. Zotz, R. B., Winkelmann, B. R., Müller, C., Boehm, B. O., März, W., and Scharf, R. E. (2005) Association of polymorphisms of platelet membrane integrins $\alpha_{IIb}\beta_3$ (HPA-1b/Pl) and $\alpha_2\beta_1$ (α807TT) with premature myocardial infarction. *J. Thromb. Haemost.* **3,** 1522–1529 CrossRef Medline
23. Zotz, R. B., Winkelmann, B. R., Nauck, M., Giers, G., Maruhn-Debowski, B., März, W., and Scharf, R. E. (1998) Polymorphism of platelet membrane glycoprotein IIIa: human platelet antigen 1b (HPA-1b/PIA2) is an inherited risk factor for premature myocardial infarction in coronary artery disease. *Thromb. Haemost.* **79,** 731–735 Medline
24. Weiss, E. J., Bray, P. F., Tayback, M., Schulman, S. P., Kickler, T. S., Becker, L. C., Weiss, J. L., Gerstenblith, G., and Goldschmidt-Clermont, P. J. (1996) A polymorphism of a platelet glycoprotein receptor as an inherited risk factor for coronary thrombosis. *N. Engl. J. Med.* **334,** 1090–1094 CrossRef Medline
25. Zotz, R. B., Klein, M., Dauben, H. P., Moser, C., Gams, E., and Scharf, R. E. (2000) Prospective analysis after coronary-artery bypass grafting: platelet GP IIIa polymorphism (HPA-1b/PIA2) is a risk factor for bypass occlusion, myocardial infarction, and death. *Thromb. Haemost.* **83,** 404–407 Medline
26. Loncar, R., Stoldt, V., Hellmig, S., Zotz, R. B., Mihalj, M., and Scharf, R. E. (2007) HPA-1 polymorphism of $\alpha_{IIb}\beta_3$ modulates platelet adhesion onto immobilized fibrinogen in an *in-vitro* flow system. *Thromb. J.* 10.1186/1477-9560-1185-1182
27. Gohlke, H., Schmitz, B., Sommerfeld, A., Reinehr, R., and Häussinger, D. (2013) $\alpha_5\beta_1$-integrins are sensors for tauroursodeoxycholic acid in hepatocytes. *Hepatology* **57,** 1117–1129 CrossRef Medline
28. Aurich, V., and Beck, A. (2002) ECCET: Ein System zur 3D-Visualisierung von Volumendaten mit Echtzeitnavigation, in *Bildverarbeitung für die Medizin 2002* (Meiler, M., Saupe, D., Kruggel, F., Handels, H., and Lehmann, T. M., eds) pp. 389–392, Springer, Berlin
29. Scharf, R. E., Hasse, M., Reiff, E., Gyenes, M., and Stoldt, V. R. (2009) CD40 ligand (CD40L) increases thrombus stability and outside-in signaling through integrin $\alpha_{IIb}\beta_3$. In Abstracts of the XXII Congress of the International Society of Thrombosis and Haemostasis, Boston, MA, July 11–16, 2009, Suppl. 2, AS-TH-060 CrossRef
30. Chen, V. B., Arendall, W. B., 3rd, Headd, J. J., Keedy, D. A., Immormino, R. M., Kapral, G. J., Murray, L. W., Richardson, J. S., and Richardson, D. C. (2010) MolProbity: all-atom structure validation for macromolecular crystallography. *Acta Crystallogr. D Biol. Crystallogr.* **66,** 12–21 CrossRef Medline
31. Guex, N., and Peitsch, M. C. (1997) SWISS-MODEL and the Swiss-PdbViewer: an environment for comparative protein modeling. *Electrophoresis* **18,** 2714–2723 CrossRef Medline
32. Galindo-Murillo, R., Roe, D. R., and Cheatham, T. E., 3rd. (2015) Convergence and reproducibility in molecular dynamics simulations of the DNA duplex d(GCACGAACGAACGAACGC). *Biochim. Biophys. Acta* **1850,** 1041–1058 CrossRef Medline
33. Li, J., Su, Y., Xia, W., Qin, Y., Humphries, M. J., Vestweber, D., Cabañas, C., Lu, C., and Springer, T. A. (2017) Conformational equilibria and intrinsic affinities define integrin activation. *EMBO J.* **36,** 629–645 CrossRef Medline
34. Chen, W., Lou, J., Hsin, J., Schulten, K., Harvey, S. C., and Zhu, C. (2011) Molecular dynamics simulations of forced unbending of integrin $\alpha_V\beta_3$. *PLoS Comput. Biol.* **7,** e1001086 CrossRef Medline
35. Puklin-Faucher, E., and Sheetz, M. P. (2009) The mechanical integrin cycle. *J. Cell Sci.* **122,** 179–186 CrossRef Medline
36. DeLano, W. L. (2012) *The PyMOL Molecular Graphics System*, version 1.5.0.1, Schroedinger, LLC, New York
37. Donner, L., Fälker, K., Gremer, L., Klinker, S., Pagani, G., Ljungberg, L. U., Lothmann, K., Rizzi, F., Schaller, M., Gohlke, H., Willbold, D., Grenegard, M., and Elvers, M. (2016) Platelets contribute to amyloid-β aggregation in cerebral vessels through integrin $\alpha_{IIb}\beta_3$-induced outside-in signaling and clusterin release. *Sci. Signal.* **9,** ra52 CrossRef Medline
38. El Khattouti, A., Stoldt, R. V., and Scharf, R. E. (2010) The HPA-1b (Pro33) isoform of platelet integrin $\alpha_{IIb}\beta_3$ is a prothrombotic variant: characterization by fluorescence resonance energy transfer. *Blood* **116,** 2028
39. Bleckmann, A., Weidtkamp-Peters, S., Seidel, C. A., and Simon, R. (2010) Stem cell signaling in *Arabidopsis* requires CRN to localize CLV2 to the plasma membrane. *Plant Physiol.* **152,** 166–176 CrossRef Medline
40. Karpova, T. S., Baumann, C. T., He, L., Wu, X., Grammer, A., Lipsky, P., Hager, G. L., and McNally, J. G. (2003) Fluorescence resonance energy transfer from cyan to yellow fluorescent protein detected by acceptor photobleaching using confocal microscopy and a single laser. *J. Microsc.* **209,** 56–70 CrossRef Medline
41. Shi, M., Foo, S. Y., Tan, S. M., Mitchell, E. P., Law, S. K., and Lescar, J. (2007) A structural hypothesis for the transition between bent and extended conformations of the leukocyte β_2 integrins. *J. Biol. Chem.* **282,** 30198–30206 CrossRef Medline
42. Pfleger, C., Radestock, S., Schmidt, E., and Gohlke, H. (2013) Global and local indices for characterizing biomolecular flexibility and rigidity. *J. Comput. Chem.* **34,** 220–233 CrossRef Medline
43. Jacobs, D. J., and Thorpe, M. F. (1995) Generic rigidity percolation: the pebble game. *Phys. Rev. Lett.* **75,** 4051–4054 CrossRef Medline
44. Hermans, M. A., Pfleger, C., Nutschel, C., Hanke, C. A., and Gohlke, H. (2017) Rigidity theory for biomolecules: concepts, software, and applications. *Wiley Interdiscip. Rev. Comput. Mol. Sci.* **7,** e1311 CrossRef
45. Thorpe, M., Jacobs, D., and Djordjevic, B. (1996) Generic rigidity percolation. *J. Phys. Condens. Matter* **11,** 407–424
46. Radestock, S., and Gohlke, H. (2008) Constraint network analysis: exploiting the link between protein rigidity and thermostability. *Eng. Life Sci.* **8,** 507–522 CrossRef
47. Williams, T., and Kelley, C. (2011) *Gnuplot 4.5: an Interactive Plotting Program*, SourceForge, La Jolla, CA
48. Whiteley, W. (2005) Counting out to the flexibility of molecules. *Phys. Biol.* **2,** S116–S126 CrossRef Medline
49. Stoldt, V. R., Peveling, J., Loncar, R., Beck, A., Aurich, V., and Scharf, R. E. (2005) Evaluation of platelet thrombus formation under flow. *Blood* **106,** 3964
50. Savage, B., and Ruggeri, Z. M. (2013) The basis for platelet adhesion, in *Hemostasis and Thrombosis. Basic Principles and Clinical Practice*

(Marder, V. J., Aird, W., Bennett, J. S., Schulman, S., and White, G. C., eds) 6th Ed., pp. 400–409, Lippincott Williams & Wilkins, Philadelphia
51. Watson, S. P., Farndale, R. W., Moroi, M., and Jung, S. M. (2013) Platelet collagen receptors, in *Haemostasis and Thrombosis. Basic Principles and Clinical Practice* (Marder, V. J., Aird, W., Bennett, J. S., Schulman, S., and White, G. C., eds) 6th Ed., pp. 420–430, Lippincott Williams & Wilkins, Philadelphia
52. Kritzik, M., Savage, B., Nugent, D. J., Santoso, S., Ruggeri, Z. M., and Kunicki, T. J. (1998) Nucleotide polymorphisms in the α_2 gene define multiple alleles that are associated with differences in platelet $\alpha_2\beta_1$ density. *Blood* **92,** 2382–2388 Medline
53. Vijayan, K. V., Liu, Y., Sun, W., Ito, M., and Bray, P. F. (2005) The Pro33 isoform of integrin β_3 enhances outside-in signaling in human platelets by regulating the activation of serine/threonine phosphatases. *J. Biol. Chem.* **280,** 21756–21762 CrossRef Medline
54. Puklin-Faucher, E., Gao, M., Schulten, K., and Vogel, V. (2006) How the headpiece hinge angle is opened: new insights into the dynamics of integrin activation. *J. Cell Biol.* **175,** 349–360 CrossRef Medline
55. Jorgensen, W. L., Chandrasekhar, J., Madura, J. D., Impey, R. W., and Klein, M. L. (1983) Comparison of simple potential functions for simulating liquid water. *J. Chem. Phys.* **79,** 926–935 CrossRef
56. Cornell, W. D., Cieplak, P., Bayly, C. I., Gould, I. R., Merz, K. M., Ferguson, D. M., Spellmeyer, D. C., Fox, T., Caldwell, J. W., and Kollman, P. A. (1995) A 2nd generation force-field for the simulation of proteins, nucleic-acids, and organic-molecules. *J. Am. Chem. Soc.* **117,** 5179–5197 CrossRef
57. Hornak, V., Abel, R., Okur, A., Strockbine, B., Roitberg, A., and Simmerling, C. (2006) Comparison of multiple Amber force fields and development of improved protein backbone parameters. *Proteins* **65,** 712–725 CrossRef Medline
58. Perez, A., MacCallum, J. L., Brini, E., Simmerling, C., and Dill, K. A. (2015) Grid-based backbone correction to the ff12SB protein force field for implicit-solvent simulations. *J. Chem. Theory. Comput.* **11,** 4770–4779 CrossRef Medline
59. Maier, J. A., Martinez, C., Kasavajhala, K., Wickstrom, L., Hauser, K. E., and Simmerling, C. (2015) ff14SB: improving the accuracy of protein side chain and backbone parameters from ff99SB. *J. Chem. Theory Comput.* **11,** 3696–3713 CrossRef Medline
60. Best, R. B., and Hummer, G. (2009) Optimized molecular dynamics force fields applied to the helix-coil transition of polypeptides. *J. Phys. Chem. B* **113,** 9004–9015 CrossRef Medline
61. Lindorff-Larsen, K., Piana, S., Palmo, K., Maragakis, P., Klepeis, J. L., Dror, R. O., and Shaw, D. E. (2010) Improved side-chain torsion potentials for the Amber ff99SB protein force field. *Proteins* **78,** 1950–1958CrossRef Medline
62. Campbell, I. D., and Humphries, M. J. (2011) Integrin structure, activation, and interactions. *Cold Spring Harb. Perspect. Biol.* **3,** a004994CrossRef Medline
63. Xiong, J. P., Stehle, T., Goodman, S. L., and Arnaout, M. A. (2003) New insights into the structural basis of integrin activation. *Blood* **102,** 1155–1159 CrossRef Medline
64. Puklin-Faucher, E., and Vogel, V. (2009) Integrin activation dynamics between the RGD-binding site and the headpiece hinge. *J. Biol. Chem.* **284,** 36557–36568 CrossRef Medline
65. Vijayan, K. V., Goldschmidt-Clermont, P. J., Roos, C., and Bray, P. F. (2000) The Pl(A2) polymorphism of integrin β_3 enhances outside-in signaling and adhesive functions. *J. Clin. Investig.* **105,** 793–802 CrossRef Medline
66. Abraham, D. G., Nutt, E. M., Bednar, R. A., Bednar, B., Gould, R. J., and Duong, L. T. (1997) Arginine-glycine-aspartic acid mimics can identify a transitional activation state of recombinant $\alpha_{IIb}\beta_3$ in human embryonic kidney 293 cells. *Mol. Pharmacol.* **52,** 227–236 CrossRef Medline
67. Jallu, V., Poulain, P., Fuchs, P. F., Kaplan, C., and de Brevern, A. G. (2012) Modeling and molecular dynamics of HPA-1a and -1b polymorphisms: effects on the structure of the β_3 subunit of the $\alpha_{IIb}\beta_3$ integrin. *PLoS One* **7,** e47304 CrossRef Medline
68. Bennett, J. S. (2005) Structure and function of the platelet integrin $\alpha_{IIb}\beta_3$. *J. Clin. Investig.* **115,** 3363–3369 CrossRef Medline
69. Fiser, A., and Sali, A. (2003) ModLoop: automated modeling of loops in protein structures. *Bioinformatics* **19,** 2500–2501 CrossRef Medline
70. Webb, B., and Sali, A. (2014) Comparative protein structure modeling using MODELLER. *Curr. Protoc. Bioinformatics* **47,** 5.6.1–32 CrossRef Medline
71. Case, D. A., Cheatham, T. E., 3rd, Darden, T., Gohlke, H., Luo, R., Merz, K. M., Jr., Onufriev, A., Simmerling, C., Wang, B., and Woods, R. J. (2005) The Amber biomolecular simulation programs. *J. Comput. Chem.* **26,** 1668–1688 CrossRef Medline
72. Aqvist, J. (1992) Modeling of ion ligand interactions in solutions and biomolecules. *J. Mol. Struct.* **88,** 135–152
73. Cheatham, T. E., Miller, J. L., Fox, T., Darden, T. A., and Kollman, P. A. (1995) Molecular dynamics simulations on solvated biomolecular systems: the particle mesh Ewald method leads to stable trajectories of DNA, RNA, and proteins. *J. Am. Chem. Soc.* **117,** 4193–4194 CrossRef
74. Ryckaert, J. P., Ciccotti, G., and Berendsen, H. J. C. (1977) Numerical integration of cartesian equations of motion of a system with constraints: molecular dynamics of *n*-alkanes. *J. Comput. Phys.* **23,** 327–341 CrossRef
75. Roe, D. R., and Cheatham, T. E., 3rd (2013) PTRAJ and CPPTRAJ: software for processing and analysis of molecular dynamics trajectory data. *J. Chem. Theory Comput.* **9,** 3084–3095 CrossRef Medline
76. Salomon-Ferrer, R., Götz, A. W., Poole, D., Le Grand, S., and Walker, R. C. (2013) Routine microsecond molecular dynamics simulations with AMBER on GPUs. 2. Explicit solvent particle mesh Ewald. *J. Chem. Theory Comput.* **9,** 3878–3888 CrossRef Medline
77. Pfleger, C., Rathi, P. C., Klein, D. L., Radestock, S., and Gohlke, H. (2013) Constraint Network Analysis (CNA): a Python software package for efficiently linking biomacromolecular structure, flexibility, (thermo-)stability, and function. *J. Chem. Inf. Model.* **53,** 1007–1015 CrossRef Medline
78. Chodera, J. D. (2016) A simple method for automated equilibration detection in molecular simulations. *J. Chem. Theory Comput.* **12,** 1799–1805 CrossRef Medline
79. Shirts, M. R., and Chodera, J. D. (2008) Statistically optimal analysis of samples from multiple equilibrium states. *J. Chem. Phys.* **129,** 124105 CrossRef Medline
80. R Development Core Team (2010) *R: a Language and Environment for Statistical Computing*, R Foundation for Statistical Computing, Vienna, Austria

Supporting Information

The Pro33 variant (HPA-1b) of $\alpha_{IIb}\beta_3$ allosterically shifts the dynamic conformational equilibrium of the integrin towards an active state

Giulia Pagani[1], Joana P. V. Pereira[2§], Volker R. Stoldt[2§], Andreas Beck[3], Rüdiger E. Scharf[2,4#], Holger Gohlke[1,5#*]

[1]Institute for Pharmaceutical and Medicinal Chemistry, Heinrich Heine University Düsseldorf, Düsseldorf, Germany

[2]Division of Experimental and Clinical Hemostasis, Hemotherapy and Transfusion Medicine, Institute of Transplantation Diagnostics and Cell Therapeutics, Heinrich Heine University Düsseldorf Medical Center, Düsseldorf, Germany

[3]Institute of Informatics, Heinrich Heine University Düsseldorf, Düsseldorf, Germany

[4]Biological Medical Research Center, Heinrich Heine University Düsseldorf, Düsseldorf, Germany

[5]John von Neumann Institute for Computing (NIC), Jülich Supercomputing Centre (JSC) & Institute for Complex Systems - Structural Biochemistry (ICS 6), Forschungszentrum Jülich GmbH, Jülich, Germany

[§]Current affiliation: Dept. of General, Visceral and Pediatric Surgery, Heinrich Heine University Medical Center & Faculty of Medicine, Heinrich Heine University Düsseldorf, Düsseldorf, Germany

[#]Share senior authorship

[*]Address: Universitätsstr. 1, D-40225 Düsseldorf, Germany.

Phone: (+49) 211 81 13662; Fax: (+49) 211 81 13847

E-mail: gohlke@uni-duesseldorf.de or h.gohlke@fz-juelich.de

Table of Contents

Supplemental Methods

Determination of HPA-1 alleles of $\alpha_{IIb}\beta_3$ and α_2 C807T genotypes of $\alpha_2\beta_1$

Prior to blood collection for this study, genotyping of HPA-1 and α_2C807T had been performed. Genomic DNA was extracted from whole blood using the QIAmp blood kit (Qiagen, Hilden, Germany). Upon amplification by polymerase chain reaction, genotypes were determined by allele-specific restriction enzyme analysis (1). The results of genotyping were confirmed by a second analysis using the LightCycler™ system (Roche Diagnostics, Mannheim, Germany) (2) and the results of both procedures were in 100% concordance.

Donor population

Homozygous carriers of either allele, Leu33 (HPA-1a) or Pro33 (HPA-1b), which did not carry the $\alpha_2$807CT or $\alpha_2$807TT genotype of $\alpha_2\beta_1$, were selected for the subsequent experiments. Group A (HPA-1a/1a) consisted of 8 individuals (5 males, 3 females, mean age: 38.8 yrs., range: 21 to 58 yrs.); group B consisted of 7 individuals (4 males, 3 females, mean age: 45.3 yrs., range: 35 to 54 yrs.).

Compounds

Abciximab 4µg/ml (c7E3, ReoPro, Centocor, Inc/Eli Lilly, Indianapolis, IN, USA) is a murine-human chimeric monoclonal antibody fragment directed against human $\alpha_{IIb}\beta_3$. A complex-specific anti-$\alpha_{IIb}\beta_3$ antibody, anti-CD41 (clone MEM-06, Exbio, Praha, Czech Republic) was used for flow cytometric analysis of transfected HEK293 cells. For calibration of the flow cytometer and quantitation of $\alpha_{IIb}\beta_3$ expression, fluorescent microspheres (F-36905, Molecular Probes, Eugene, OR, USA) were used.

Design and construction of plasmids

Two plasmids were generated first by cloning the cDNA of the α_{IIb} human integrin gene (ITGA2B), a gift from Dr. S. Shattil (University of California, San Diego, CA, USA), and the cDNA of the β_3 human integrin gene (ITGB3), a gift from Dr. J. Jones (Northwestern University Medical School, Chicago, IL, USA), downstream the cytomegalovirus promoter in the pcDNA3.1(-) plasmid (Thermo Fisher, formerly Invitrogen, Waltham, MA, USA). A third plasmid, containing the Pro-for-Leu substitution in the β_3 subunit was generated by site-directed mutagenesis, as reported by Kunkel (3). Subsequently, the coding sequence of mVenus (plasmid # 27794), a gift from S. Vogel (Addgene, Cambridge, MA, USA) was cloned downstream the α_{IIb} coding sequence, and the coding sequence of mCherry (Clontech Laboratories, Takara Bio, Mountain View, CA, USA) was cloned downstream the β_3Leu33 and β_3Pro33 coding sequences in the respective plasmids. In initial fusion constructs, the length of the linker between the C-terminus of each subunit and the N-terminus of the corresponding fluorescent protein (mVenus or mCherry) was varied (4), and combinations of these constructs were tested in transiently transfected HEK293 cell by acceptor-photobleaching to determine optimal basal FRET efficiency. Accordingly, the construct containing a linker of 39 amino acids between α_{IIb} (C-terminus) and mVenus (N-terminus),

and a linker of 6 amino acids between β_3Leu33 or β_3Pro33 (C-terminus) and mCherry (N-terminus), was chosen.

Importantly, mVenus and mCherry coding sequences were cloned in frame with the integrin subunits coding sequences with removal of the original stop codon of the integrin subunits (4) for expression as fusion proteins. The sequences of the three resulting plasmids were confirmed by Sanger sequencing (Biological Medical Research Center, Heinrich Heine University Düsseldorf), using the primers listed in **Tables S1** and **S2**.

Cell line culture and transfection

HEK293 cells were purchased from the Leibniz Institute DSMZ - German Collection of Microorganisms and Cell Cultures (DSMZ, Braunschweig, Germany) and cultured according to the recommended conditions (DMEM supplemented with 10% of fetal bovine serum (FBS) and 1% penicillin-streptomycin (PCN-STR). DMEM, FBS, and PCN-STR were obtained from Thermo Fischer Scientific (Waltham, MA, USA). To achieve expression of the complete $\alpha_{IIb}\beta_3$ receptor complex of either isoform, Leu33 (HPA-1a) or Pro33 (HPA-1b), in HEK293 cells, a double transient transfection was performed with the plasmids α_{IIb}mVenus and β_3Leu33mCherry or β_3Pro33mCherry, respectively. HEK293 cells transfected with an empty vector DNA were used as controls in the flow cytometry analyses, and cells double transfected with αIIbmVenus and β_3Leu33 or β_3Pro33 plasmids (without mCherry) served as controls in FRET-APB experiments. The transfection protocol was performed using the Effectene® Transfection Reagent (Qiagen, Hilden, Germany). 24 h prior to transfection, $1.6x10^5$ cells were seeded on a 6-well plate (Greiner Bio-one, Frickenhausen, Germany) in culture medium. On the next day, 0.4 µg of integrin α_{IIb} encoding plasmid and 0.4 µg of each β_3 encoding plasmids were diluted in EC (Enhancer and DNA condensation) buffer (total final volume of 100 µl), 3.2 µl of transfection enhancer was added and the mixture incubated

at RT for 5 min. Subsequently, 10 µl of Effectene® was added and the mixture incubated at RT for 10 min. Finally, 200 µl of cell culture medium was added, and the mixture was carefully pipetted into the wells containing the cells. 24 h after transfection, the medium was replaced by standard cell culture medium (DMEM supplemented with 10% FBS and 1% PCN-STR).

Image acquisition was achieved by using the Metamorph Software (v. 7.7.7.0), and image processing was performed with Adobe Photoshop CS3 (Adobe, USA) software.

FRET acceptor-photobleaching (APB) analyses

mVenus fluorescence intensity measured in the ROI varied between 11 and 134 (mean ± SEM, 37.85±1.992) for cells transfected with α_{IIb}mVenus and β_3Leu33mCherry plasmids and between 7 and 93 (35.27 ± 2.048) for cells transfected with αIIbmVenus and β3Pro33mCherry plasmids, respectively; mCherry fluorescence intensity varied between 12 and 120 (54.37 ± 2.284) for cells transfected with α_{IIb}mVenus and β_3Leu33mCherry plasmids and between 12 and 99 (44.90 ± 2.159) for cells transfected with α_{IIb}mVenus and β_3Pro33mCherry plasmids. Transfected cells were randomly chosen for analysis.

Supplemental Tables

Table S1: Primers for α_{IIb}mVenus.

T7minus1	AATACGACTCACTATAGGG
Seq-p101-I	TGGGACAAGCGTTACTGTG
Seq-p101-II	GACCGGGATGGCTACAATG
Seq-p101-III	TCGAGATGAGGCAGACTTC
Seq-p101-IV	CAGCAGAAGAAGGTGAGAG
Seq-p101-mVenus	GGCAACTAGAAGGCACAGTC
RPC	ACAGCTATGACCATGATTACG
Seq-p101-Hyg-fw	ACAGCTATGACCATGATTACG
pEGFP-RP	AACAGCTCCTCGCCCTTG

Table S2: Primers for β_3mCherry.

pEGFP-FP	TTTAGTGAACCGTCAGATC
Seq-p106-I	CTTGCCCATGTTTGGCTAC
Seq-p106-II	GGCCTCAAGTCTTGTATGG
Seq-p106-III	TGGCAGCTGTGTCTGTATC
pEGFP_C2-RP	TTTAAAGCAAGTAAAACCTC
Seq-p106-Zeo	GAACAAACGACCCAACAC

Table S3: Local geometry of the metal ion binding sites.

	Leu33 (HPA-1a) isoform			Pro33 (HPA-1b) isoform		
	SimI[a]	SimII[a]	SimIII[a]	SimI[a]	SimII[a]	SimIII[a]
SyMBS···P219$_O$	2.03±0.00	2.02±0.00	2.02±0.00	2.03±0.01	2.05±0.01	2.02±0.00
	2.05±0.01[b]			2.03±0.01[b]		
SyMBS···E220$_{\varepsilon1}$	1.95±0.00	1.96±0.00	1.95±0.00	1.05±0.004	1.95±0.00	1.94±0.002
	1.95±0.00[b]			1.95±0.01[b]		
MIDAS···E220$_{\varepsilon2}$	4.02±0.01	4.06±0.00	4.07±0.01	4.00±0.01	4.01±0.03	4.09±0.00
	4.05±0.01[b]			4.03±0.04[b]		
MIDAS···D119$_{\delta2}$	1.99±0.00	2.00+0.01	1.99±0.01	2.03±0.007	2.04±0.05	1.99±0.00
	1.99±0.01[b]			2.02±0.05[b]		
AMIDAS···D126$_{\delta1}$	2.07±0.01	2.14±0.02	2.17±0.02	2.35±0.04	1.95±0.00	2.81±0.05
	2.13±0.04[b]				2.37±0.07[b]	
AMIDAS···D127$_{\delta1}$	1.95±0.00	1.95±0.00	1.95±0.01	2.28±0.29	2.58±0.10	1.95±0.00
	1.95±0.01[b]			2.27±0.31[b]		

[a] Mean value and SEM, in Å, calculated for each MD simulation.
[b] Mean value and SEM, in Å, calculated across three MD simulations.

Table S4: RMSD of $\alpha_{IIb}\beta_3$ domains after domain-wise alignment.

		Leu33 (HPA-1a) isoform			Pro33 (HPA-1b) isoform		
	Domain	**Sim I[a]**	**Sim II[a]**	**Sim III[a]**	**Sim I[a]**	**Sim II[a]**	**Sim III[a]**
Sub α_{IIb}	**β-propeller**	1.71±0.01	2.04±0.04	1.91±0.01	2.33±0.03	1.94±0.01	2.17±0.01
		1.89±0.04[b]			2.15±0.0[b]3		
	thigh	1.86±0.05	1.99±0.13	1.95±0.03	1.75±0.02	1.78±0.04	1.82±0.03
		1.94±0.14[b]			1.78±0.06[b]		
	calf-1	1.71±0.12	2.39±0.03	2.16±2.09	2.15±0.10	1.89±0.02	1.86±0.07
		2.09±0.13[b]			1.78±0.12[b]		
	calf-2	1.85±0.16	2.56±0.13	1.43±0.01	3.39±0.12	2.15±0.14	2.02±0.03
		1.95±0.13[b]			2.52±0.19[b]		
Sub β_3	**βA**	2.37±0.03	1.43±0.01	2.06±0.07	1.50±0.05	1.63±0.01	2.65±0.01
		1.96±0.07[b]			1.92±0.05[b]		
	hybrid	2.60±0.15	2.56±0.02	2.63±0.05	2.91±0.03	2.59±0.05	2.69±0.08
		2.51±0.16[b]			2.73±0.10[b]		
	PSI	1.60±0.03	1.62±0.03	1.60±0.02	1.72±0.03	3.97±0.07	1.61±0.04
		1.60±0.05[b]			2.43±0.09[b]		
	EGFs	2.58±0.03	2.44±0.09	2.33±0.23	3.31±0.04	4.23±0.08	3.89±0.06
		2.45±0.25[b]			3.81±0.09[b]		
	β-tail	4.55±0.03	5.96±0.09	4.26±0.04	4.24±0.17	4.91±0.04	4.43±0.03
		4.93±0.11[b]			4.53±0.17[b]		

[a] Mean value and SEM, in Å, calculated for each MD simulation.
[b] Mean value and SEM, in Å, calculated across three MD simulations.

Table S5: RMSD of the $\alpha_{IIb}\beta_3$ integrin domains after alignment of the head region.

		Leu33 (HPA-1a) isoform			Pro33 (HPA-1b) isoform		
	Domain	**Sim I[a]**	**Sim II[a]**	**Sim III[a]**	**Sim I[a]**	**Sim II[a]**	**Sim III[a]**
Sub α_{IIb}	**β-propeller**	2.82±0.37	2.53±0.03	2.27±0.07	2.71±0.03	2.34±0.02	2.74±0.04
		2.54±0.37[b]			2.60±0.06[b]		
	thigh	5.70±0.09	5.41±0.34	6.64±0.11	9.84±0.15	10.75±1.11	8.45±0.45
		5.91±0.37[b]			9.68±1.20[b]		
	calf-1	7.48±0.85	5.79±0.41	8.61±0.37	10.73±0.08	12.79±0.52	11.31±0.49
		7.90±1.02[b]			11.61±0.72[b]		
	calf-2	8.93±0.44	8.18±0.74	11.39±0.19	13.25±0.24	16.35±0.38	21.13±2.65
		9.50±0.89[b]			16.91±2.69[b]		
Sub β_3	**βA**	4.00±0.30	2.75±0.15	2.91±0.06	2.39±0.11	2.35±0.04	3.34±0.05
		3.22±0.34[b]			2.70±0.13[b]		
	hybrid	6.49±0.61	7.62±0.26	8.21±0.05	5.66±0.12	8.36±0.31	6.52±0.22
		7.29±0.67[b]			6.85±0.40[b]		
	PSI	11.72±0.82	12.03±0.30	12.53±1.98	10.82±0.15	18.15±0.79	6.58±0.600
		12.09±2.16[b]			11.85±1.01[b]		
	EGFs	9.25±0.97	10.03±1.34	9.77±0.67	9.89±0.09	14.41±0.70	8.40±0.21
		9.68±1.78[b]			10.73±0.73[b]		
	β-tail	17.10±0.21	7.87±0.50	19.55±0.34	7.88±0.15	19.30±0.12	16.65±0.46
		14.83±0.64[b]			14.61±0.50[b]		

[a] Mean value and SEM, in Å, of the C_α atom RMSD of $\alpha_{IIb}\beta_3$ domains with respect to the starting structure after a mass-weighted alignment onto the β-propeller and βA domains, calculated for each MD simulation.
[b] Mean value and SEM, in Å, of the C_α atom RMSD of $\alpha_{IIb}\beta_3$ domains with respect to the starting structure after a mass-weighted alignment onto the β-propeller and βA domains, calculated across three MD simulations.

Table S6: RMSD and R_g of $\alpha_{IIb}\beta_3$.

	Leu33 (HPA-1a) isoform			Pro33 (HPA-1b) isoform		
	SimI[a]	**SimII**[a]	**SimIII**[a]	**SimI**[a]	**SimII**[a]	**SimIII**[a]
RMSD_ALL	6.76±0.41	5.68±0.54	7.46±0.47	7.55±0.07	10.40±0.30	9.55±0.14
	6.64±0.83[b]			9.17±0.34[b]		
	** [c]					
Rg_ALL	39.75±0.04	39.68±0.08	39.39±0.02	40.04±0.03	39.67±0.05	41.25±0.21
	39.61±0.09[b]			40.32±0.22[b]		
	* [c]					

[a] Mean value and SEM, in Å, calculated for each MD simulation.
[b] Mean value and SEM, in Å, calculated across three MD simulations.
[c] *: p <0.05, **: p < 0.001, ***: p < 0.0001 (according to the t-test for parametric testing).

Table S7: Kink, bending, and splaying angles.

	Leu33 (HPA-1a) isoform			Pro33 (HPA-1b) isoform		
	SimI[a]	SimII[a]	SimIII[a]	SimI[a]	SimII[a]	SimIII[a]
Kink[°]	137.38±2.33	136.99±1.43	139.55±0.36	140.02±0.56	154.06±1.35	165.25±0.35
	137.97±2.76[b]			153.11±1.50[b]		
	*** [c]					
Bending[°]	45.91±1.30	42.92±0.45	38.64±0.11	48.82±0.45	44.78±0.33	54.92±1.66
	42.49±1.38[b]			48.74±1.75[b]		
	* [c]					
Splaying[°]	22.85±0.15	27.16±0.13	24.05±0.06	26.88±0.08	28.65±0.44	27.76±0.08
	24.69±0.21[b]			27.76±0.45[b]		
	*** [c]					

[a] Mean value and SEM, in °, calculated for each MD simulation.
[b] Mean value and SEM, in °, calculated across three MD simulations.
[c] *: p <0.05, **: p < 0.001, ***: p < 0.0001 (according to the t-test for parametric testing).

Table S8: Distance between the N-terminus and C-terminus.

	Leu33 (HPA-1a) isoform			Pro33 (HPA-1b) isoform		
	SimI[a]	SimII[a]	SimIII[a]	SimI[a]	SimII[a]	SimIII[a]
βA···β-tail	35.70±0.33	40.81±0.52	31.30±0.05	43.45±0.24	42.86±1.51	47.95±0.75
	35.94±0.62			44.76±1.70		
	***					
calf-2···β-tail	29.65±0.10	28.31±0.55	25.92±0.03	29.03±0.08	31.00±0.22	28.17±0.04
	27.95±0.56			29.40±0.24		
	*					
calf-2···β-propeller	53.54±0.47	53.87±0.51	52.81±0.28	57.21±0.27	52.58±0.10	65.75±1.42
	53.07±0.75			58.51±1.45		
	*** [c]					

[a] Mean value and SEM, in Å, calculated for each MD simulation.
[b] Mean value and SEM, in Å, calculated across three MD simulations.
[c] *: p <0.05, **: p < 0.001, ***: p < 0.0001 (according to the t-test for parametric testing).

Table S9: Distance at the interface between PSI and the EGF-1/EGF-2 domains

	Leu33 (HPA-1a) isoform			Pro33 (HPA-1b) isoform		
	SimI[a]	**SimII**[a]	**SimIII**[a]	**SimI**[a]	**SimII**[a]	**SimIII**[a]
L33P···S469	7.32±0.28	8.45±0.10	8.59±0.28	12.60±0.21	11.49±0.47	11.34±0.60
	8.12±0.40			11.81±0.79		
	*					
L33P···Q481	6.45±0.28	6.63±0.35	6.77±0.24	13.75±0.21	10.03±0.54	13.38±0.84
	6.65±0.37			12.38±1.02		
	***					

[a] Mean value and SEM, in Å, calculated for each MD simulation.
[b] Mean value and SEM, in Å, calculated across three MD simulations.
[c] *: p <0.05, **: p < 0.001, ***: p < 0.0001 (according to the t-test for parametric testing).

Table S10: Native and non-native contacts involving the AB loop

	Leu33 (HPA-1a) isoform			Pro33 (HPA-1b) isoform		
	SimI[a]	**SimII**[a]	**SimIII**[a]	**SimI**[a]	**SimII**[a]	**SimIII**[a]
Native	374±4	279±7	357±4	295±6	247±4	301±2
	336±9			281±6		
	***					
Non-Native	869±13	977±13	726±32	191±6	538±9	436±37
	857±37			388±39		
	***					

[a] Mean value and SEM calculated for each MD simulation.
[b] Mean value and SEM calculated across three MD simulations.
[c] *: p <0.05, **: p < 0.001, ***: p < 0.0001 (according to the t-test for parametric testing).

Supplemental Figures

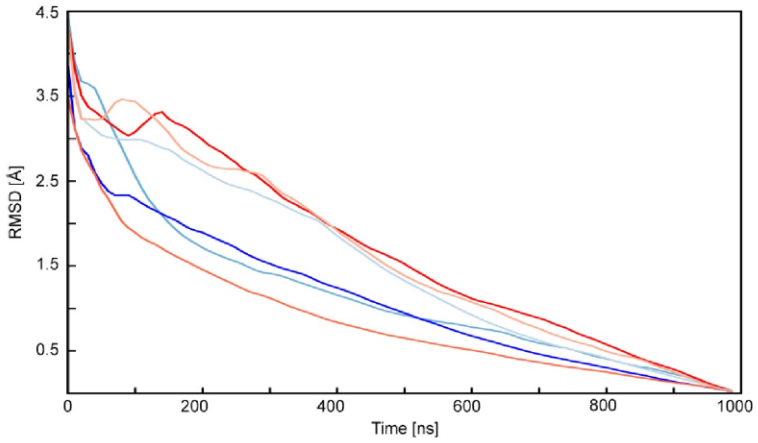

Fig. S1: RMSD average correlation.

RMSD average correlation (RAC) computed for the three independent MD simulations of $\alpha_{IIb}\beta_3$ expressing Leu33 (HPA-1a) (colored in three different shades of blue) or Pro33 (HPA-1b) (colored in three different shades of red) isoforms, respectively, as described in ref. (5). The structures were mass-weighted fitted on the C_α atoms of the head part (propeller domain and βA domain), excluding the first 200 ns from the trajectories, applying an offset of 250 frames, and using as reference the running average calculated over each time interval.

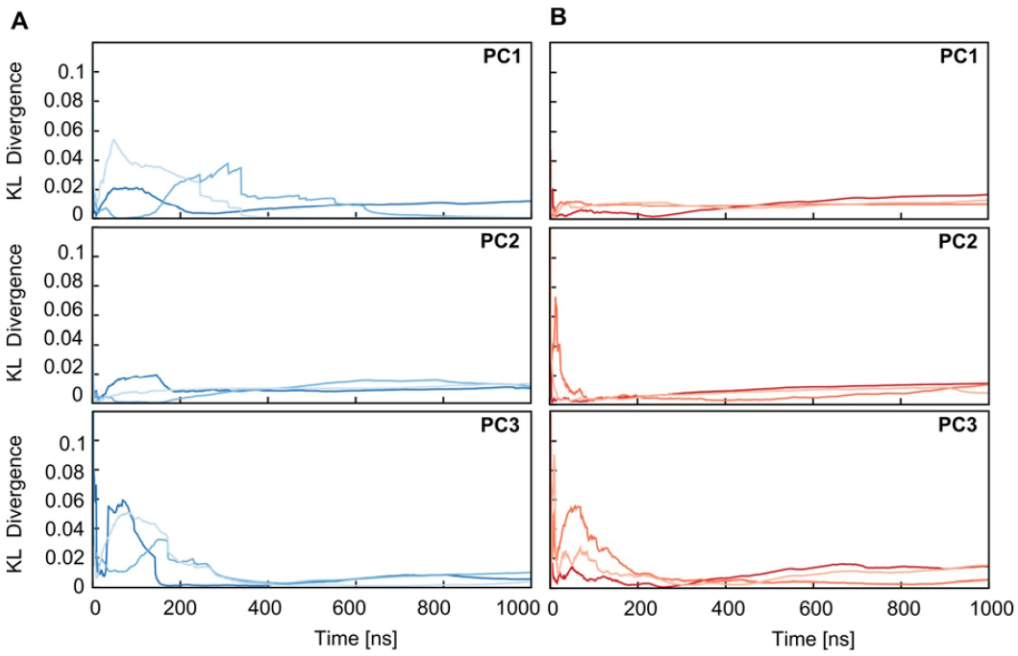

Fig S2: Convergence of internal motions in unbiased MD simulations.

Kullback-Leibler (KL) divergence[3] as a parameter to evaluate the convergence of the three independent MD simulations of Leu33 (HPA-1a) (**A**) and Pro33 (HPA-1b) (**B**). The KL divergence was computed for pair-wise comparisons of replicates of MD simulations in terms of histograms describing the projection of snapshots onto the given principal component (PC). The principal component analysis was performed on all the C_α atoms after alignment onto the β-propeller and βA domains. Lines colored in three different shades of blue and three different shades of red are used to represent the Leu33 (**A**) and Pro33 (**B**) isoforms, respectively.

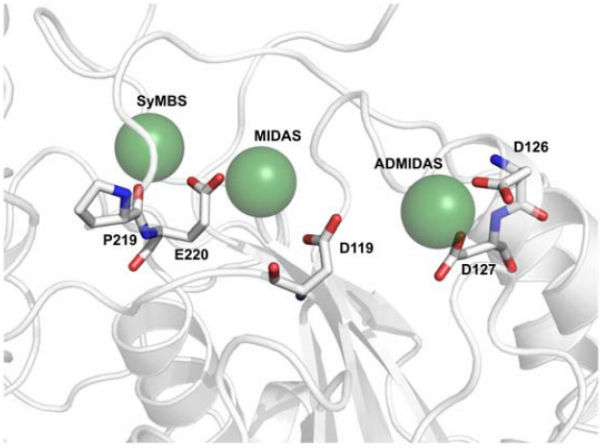

Fig S3: Metal ion binding sites

Close-up view of the metal binding sites within the βA domain. Metal ions are depicted as green spheres and labeled. Residues projecting from the βA domain (in cartoon drawing) involved in the metal coordination are shown in ball and sticks representation and labeled.

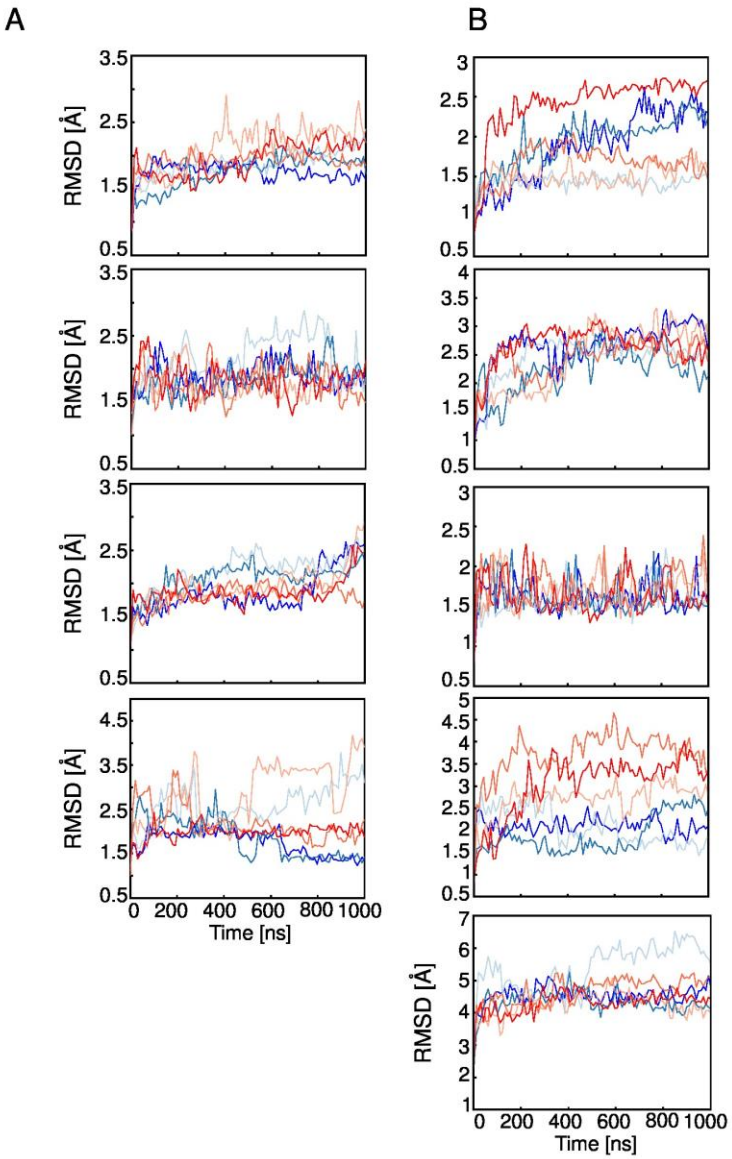

Fig. S4: Internal changes of $\alpha_{IIb}\beta_3$ domains: RMSD profiles.

RMSD of the C_α atoms of each domain of $\alpha_{IIb}\beta_3$ as a function of time with respect to the starting structure after a mass-weighted superimposition on the respective domain. From top to bottom, **(A)** the RMSD of the propeller domain, thigh domain, calf-1 and calf-2 domains is depicted, as is **(B)** the RMSD of the βA domain, hybrid domain, PSI domain, EGF block, and β-tail domains. Three different shades of blue and three different shades of red are used to represent the Leu33 and Pro33 isoforms, respectively.

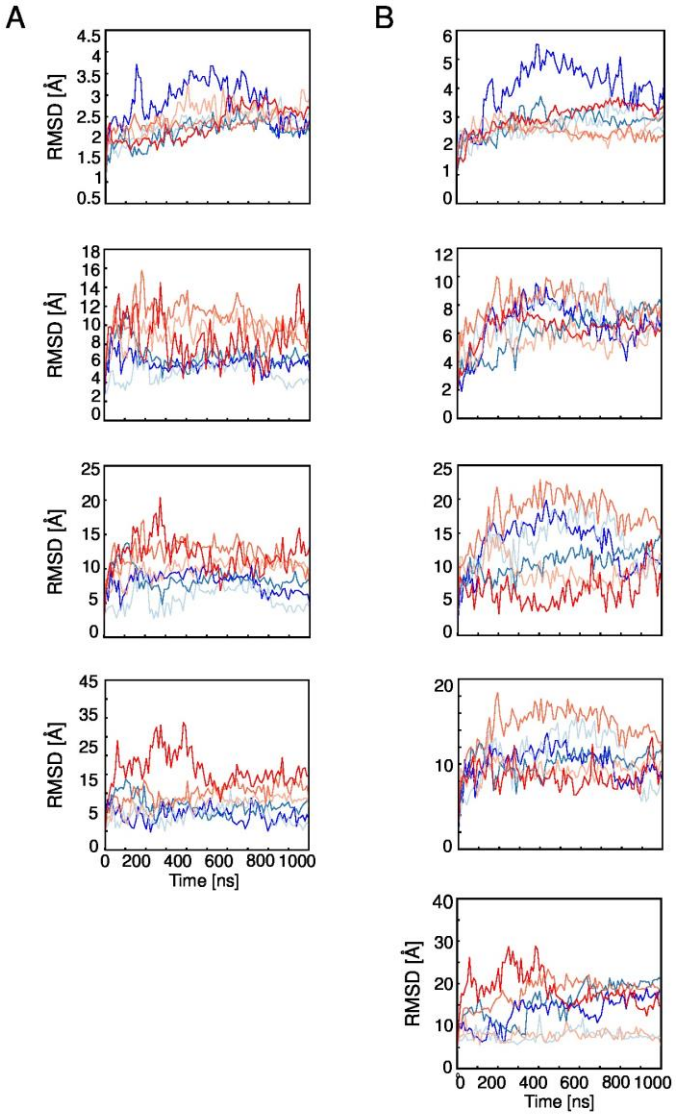

Fig. S5: Global changes of $\alpha_{IIb}\beta_3$ domains: RMSD profiles.

RMSD of the Cα atoms of each domain of $\alpha_{IIb}\beta_3$ as a function of time with respect to the starting structure after a mass-weighted superimposition on the head part (propeller domain and βA domain). From top to bottom, **(A)** the RMSD of the propeller domain, thigh domain, calf-1 and calf-2 domains is shown, as is **(B)** the RMSD of the βA domain, hybrid domain, PSI domain, EGF block, and β-tail domain. Three different shades of blue and three different shades of red are used to represent the Leu33 and Pro33 isoforms, respectively.

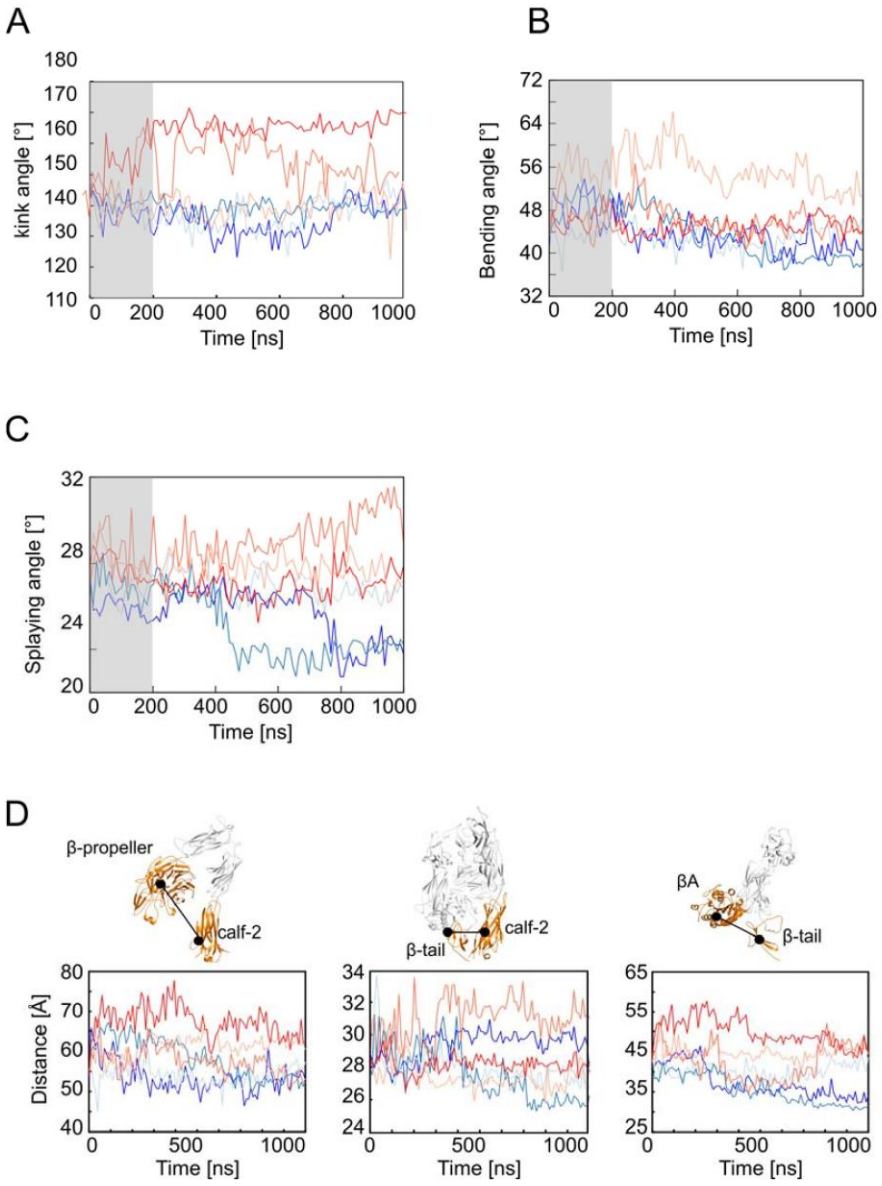

Fig. S6: Time series of geometric parameters.

(A, B, C) Time evolution of the kink angle, bending angle, and splaying angle defined as in the Methods section. Blue and red lines are used for the Leu33 (HPA-1a) isoform and Pro33 (HPA-1b) isoform, respectively. **(D)** Time evolution of the distances indicated in panel D. Above each panel, the initial structure of the respective MD simulations is depicted in cartoon representation. Domains involved in the measurements are labeled and highlighted in orange; the black line indicates the calculated distance between the COM of the domains (shown in black circles). Lines in color code as in panels (A)-(C).

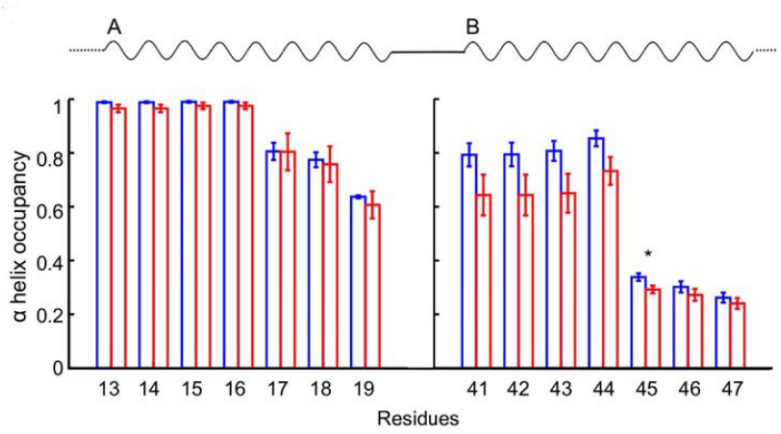

Fig. S7: Secondary structure analysis.

Normalized distribution of the helix content of **(A)** residues Cys13 to Met19 and **(B)** residues Leu40 to Asp47. Mean values calculated over three MD simulations are given, with error bars indicating SEM. The star indicates $p = 0.1$ for the difference. Blue and red colors represent the Leu33 and Pro33 isoforms, respectively.

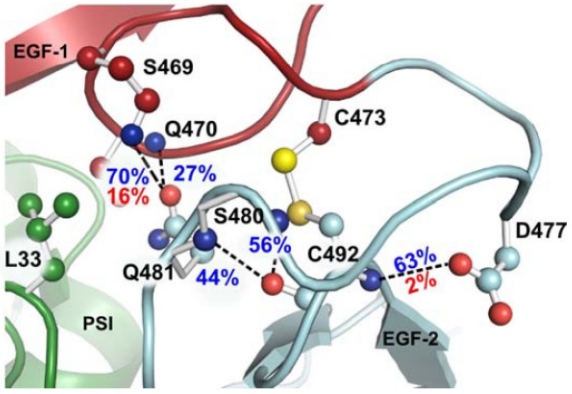

Fig. S8: Hydrogen bond network.

Mean occupancy of hydrogen bonds during three MD simulations each for the Leu33 (HPA-1a) and Pro33 (HPA-1b) isoform shown as labels next to the hydrogen bond marked by black dashed lines in the closest-to-average structure calculated from one simulation of the Leu33 (HPA-1a) isoform; occupancy values < 1% are not reported. For the sake of clarity, only the PSI (green), EGF-1 (firebrick), and EGF-2 (marine) domains of $\alpha_{IIb}\beta_3$ are shown. Residues Leu33 (PSI domain), Ser469-Gln470-Cys473 (EGF-1 domain), and Asp477-Ser480-Gln481-Cys492 (EGF-2 domain) are depicted in ball-and-sticks representation.

Supplemental References

1. Unkelbach, K., Kalb, R., Santoso, S., Kroll, H., Mueller-Eckhardt, C., and Kiefel, V. (1995) Genomic RFLP typing of human platelet alloantigens Zw(PlA), Ko, Bak and Br (HPA-1, 2, 3, 5). *Br. J. Haematol.* **89**, 169-176
2. Nauck, M. S., Gierens, H., Nauck, M. A., Marz, W., and Wieland, H. (1999) Rapid genotyping of human platelet antigen 1 (HPA-1) with fluorophore-labelled hybridization probes on the LightCycler. *Br. J. Haematol.* **105**, 803-810
3. Kunkel, T. A. (1985) Rapid and efficient site-specific mutagenesis without phenotypic selection. *Proc. Natl. Acad. Sci. U. S. A.* **82**, 488-492
4. Kim, M., Carman, C. V., and Springer, T. A. (2003) Bidirectional transmembrane signaling by cytoplasmic domain separation in integrins. *Science* **301**, 1720-1725
5. Galindo-Murillo, R., Roe, D. R., and Cheatham, T. E., 3rd. (2015) Convergence and reproducibility in molecular dynamics simulations of the DNA duplex d(GCACGAACGAACGAACGC). *Biochim. Biophys. Acta* **1850**, 1041-1058

PUBLICATION III

On the contributing role of the transmembrane domain for subunit-specific sensitivity of integrin activation

Pagani, **G**., Gohlke, H.

Sci. Rep. 2018, 10.1038/s41598-018-23778-5

www.nature.com/scientificreports

OPEN

On the contributing role of the transmembrane domain for subunit-specific sensitivity of integrin activation

Received: 15 January 2018
Accepted: 20 March 2018
Published online: 10 April 2018

Giulia Pagani[1] & Holger Gohlke[1,2]

Integrins are α/β heterodimeric transmembrane adhesion receptors. Evidence exists that their transmembrane domain (TMD) separates upon activation. Subunit-specific differences in activation sensitivity of integrins were reported. However, whether sequence variations in the TMD lead to differential TMD association has remained elusive. Here, we show by molecular dynamics simulations and association free energy calculations on TMDs of integrin $\alpha_{IIb}\beta_3$, $\alpha_v\beta_3$, and $\alpha_5\beta_1$ that $\alpha_{IIb}\beta_3$ TMD is most stably associated; this difference is related to interaction differences across the TMDs. The order of TMD association stability is paralleled by the basal activity of these integrins, which suggests that TMD differences can have a decisive effect on integrin conformational free energies. We also identified a specific order of clasp disintegration upon TMD dissociation, which suggests that the closed state of integrins may comprise several microstates. Our results provide unprecedented insights into a possibly contributing role of TMD towards subunit-specific sensitivity of integrin activation.

Integrins are a major class of heterodimeric adhesion receptors consisting of α and β subunits[1] and are involved in the regulation of many biological events[2]. Each subunit is formed by a large extracellular domain (ectodomain) connected to a short cytoplasmic tail through a single transmembrane domain (TMD)[3]. In providing a physical link between the exterior and the interior of the cell, the TMD serves as a translator of mechanical and biochemical signals in both directions across the plasma membrane, leading to inside-out and outside-in signaling[4–6]. TMDs are directly involved in the mechanism of integrin activation[7] in that the two transmembrane (TM) segments associate in the resting state[8–10] and dissociate upon activation[11–14]. Structural features of the integrin TMD were revealed by nuclear magnetic resonance (NMR) structures[15–17], biochemical data[18,19], and electron microscopy[20–22]. Two structural elements, the inner and outer membrane clasps (IMC and OMC)[23], were recognized as principal mediators of TMD assembly[24], together with electrostatic interactions in the membrane-proximal region. However, despite these unifying principles, there is also evidence for specific ways of helix-helix association among different isoforms[25], and it has remained unclear if and how these differences are linked to the subunit-specific sensitivity of integrin activation[26,27]: Integrin $\alpha_{IIb}\beta_3$ has been described as basally inactive, in contrast to $\alpha_v\beta_3$, which was found to be in the active state by default in certain cell types[28,29], and β_1 integrins, which are considered to be basally active[26], with integrin $\alpha_5\beta_1$ being among the most conformationally flexible integrins containing β_1[27]. In addition, contradicting findings of NMR[24,30] and *in vitro*[31] *versus in vivo*[32] studies with respect to a salt bridge interaction between α_{IIb}-R995 and β_3-D723 might also be related to specific TMD associations (see below for details).

The TMD of a subunit is formed by a short α-helix[33], and two such TMDs are arranged in a right-handed coiled-coil conformation[16] in the resting state of the integrin[9,10,34]. The structure of the TMD of $\alpha_{IIb}\beta_3$ integrin[15] revealed that the TM and membrane-proximal regions of the β_3 subunit form a continuous helical structure that is tilted by ~25° with respect to the membrane normal[16,17]. In contrast, the α_{IIb} subunit is oriented in parallel to the membrane normal, breaks at G991, and bents towards the β_3 TMD. This allows the dimer to be stabilized by the OMC and IMC[23]. The former is a G*XXX*G-like motif[35], while the latter is a highly conserved

[1]Institute of Pharmaceutical and Medicinal Chemistry, Heinrich-Heine-Universität Düsseldorf, 40225, Düsseldorf, Germany. [2]John von Neumann Institute for Computing (NIC), Jülich Supercomputing Centre (JSC) & Institute for Complex Systems - Structural Biochemistry (ICS 6), Forschungszentrum Jülich GmbH, 52425, Jülich, Germany. Correspondence and requests for materials should be addressed to H.G. (email: gohlke@uni-duesseldorf.de)

GFFKR motif[36], with the two Phe residues found in all α subunits[36]. Mutational studies[13], disulphide scanning[11] and Leu scanning[11] experiments confirmed the importance of the OMC, whose alteration prevents correct helix packing and abolishes helix association[36]. However, different compositions of the G*XXX*G motif are found in α subunits, which makes it reasonable to hypothesize that the different OMC interfaces contribute to differential integrin activation. Likewise, the importance of the IMC, and, in particular, the two conserved Phe residues, in maintaining correct TMD packing and restraining integrin in the resting state has been shown[31,37]. In contrast, it has remained controversial whether α_{IIb}-F992 engages β_3-K716 in hydrogen bond formation to support IMC formation[17], or whether K716 "snorkels" towards the lipid head groups[38]. Moreover, NMR spectroscopy[24] revealed the presence of a salt bridge between α_{IIb}-R995 and β_3-D723 at the membrane-proximal region, in immediate vicinity of the IMC, whose functional role in restraining integrin in the inactive state has been demonstrated[24,30,39–41]. However, NMR structures in which both α_{IIb}-F992 and α_{IIb}-R995 point away from the β_3 subunit, thus, not making any interactions with the β_3 subunit, have also been determined[30]. Likewise, mutational studies in which the breaking of the R995-D723 salt bridge did not cause immediate integrin activation were reported[14,39].

In order to provide insights at the atomistic level as to a potential influence of the TMD on the subunit-specific sensitivity of integrin activation, including the role of interactions across the IMC and OMC, here, we performed equilibrium molecular dynamics (MD) simulations in an explicit membrane environment of in total 9 μs length on the associated TMDs of integrins $\alpha_{IIb}\beta_3$, $\alpha_v\beta_3$, and $\alpha_5\beta_1$, respectively, and potential of mean force (PMF) computations of TMD association of in total 3.5 μs sampling time, from which we derived association free energies. Our results show that the TMD of integrin $\alpha_{IIb}\beta_3$ is most stably associated compared to $\alpha_v\beta_3$ and $\alpha_5\beta_1$. We relate these differences to particular interactions across the TMDs, with a focus on the different OMC compositions and an "OMC before IMC" order of clasp disintegration found for TMD dissociation. Our results provide unprecedentedly detailed and comparative insights into a possibly contributing role of the TMD towards subunit-specific sensitivity of integrin activation.

Results

Structural dynamics of the $\alpha_{IIb}\beta_3$, $\alpha_v\beta_3$, and $\alpha_5\beta_1$ TMDs. In order to investigate at an atomistic level possible subunit-specific differences in the association of TMDs of integrins $\alpha_{IIb}\beta_3$, $\alpha_v\beta_3$, and $\alpha_5\beta_1$, the three TMDs were subjected to all-atom MD simulations in an explicit membrane and solvent environment (Fig. 1a). Prior to that, we generated homology models of $\alpha_v\beta_3$ and $\alpha_5\beta_1$ TMDs using the NMR structure of $\alpha_{IIb}\beta_3$ TMD (PDB ID 2K9J)[15] as a template. To estimate the quality of the models, we used the QMEANBrane version[42] of the QMEAN scoring function implemented in the QMEAN server[43]. QMEANBrane employs specifically trained potentials for three different segments (membrane, interface and soluble) in a transmembrane protein model to determine local (*i.e.*, per residue) absolute quality estimates on the basis of a single model. With 1.0 as the optimal score, we found local scores of ~0.8 for the residues embedded in the membrane and ~0.6–0.8 when considering the overall structures (Fig. S1). The NMR structure showed very similar QMEANBrane scores, suggesting a sufficient local structural quality of the models. Sequence identities of 40% to 65% between respective template and target sequences furthermore suggest that the global folds are conserved. Note that we generally refer to the simulated systems as "TMD" here, although the actual TM region is prepended by 9–11 (8) residues of the linker to the calf-2 (β-tail) domain at the N-terminal end of the α (β) subunit, and appended by 5 (6) residues of the respective cytosolic domains at the C-terminal ends (Fig. 1b). For clarity, we furthermore only refer to the sequence numbering of integrin $\alpha_{IIb}\beta_3$ below (Fig. 1b).

Using the three TMD structures as starting structures, we performed three independent MD simulations of 1 μs length for each system, yielding in total 9 μs of simulation time. The structural variability was assessed in terms of root mean square deviations (RMSD) after a mass-weighted superimpositioning onto the respective starting structure. The RMSD of all C_α atoms, including those not embedded in the membrane, raises to values of ~7–10 Å. However, if only the TM region is considered, the RMSD amounts to ~2–4 Å (Fig. 1c). This data indicates that the structural integrity of the two TM helices remains intact throughout the MD simulations, whereas the TMD ends fray at about nine residues at either terminus of either helix. The finding that the overall configuration of the TMD remains intact during our simulations is congruent with a slow dissociation rate found for $\alpha_{IIb}\beta_3$ TMD[44]. In agreement with our findings, NMR spectroscopy revealed a dynamically unstructured α_{IIb} linker[45]. The convergence of the internal motions between independent MD simulations was assessed following ref.[46]. In short, the overlap of histograms of principal component (PC) projections obtained in a pair-wise manner from each simulation for a given TMD system are looked at as a function of time (Fig. S2). The results reveal that the first three PCs are relatively well-converged after ~400 ns for $\alpha_{IIb}\beta_3$ TMD, whereas for $\alpha_v\beta_3$ and $\alpha_5\beta_1$ TMDs it takes ~800 ns to reach a comparable level of convergence.

To conclude, RMSD values of membrane-embedded TMD parts generally below 4 Å reveal that both the secondary structure and overall configuration of the two TM helices remain intact throughout the MD simulations of all three TMDs. The convergence behavior of PC projections suggests larger and/or slower internal motions in $\alpha_v\beta_3$ and $\alpha_5\beta_1$ TMDs than $\alpha_{IIb}\beta_3$ TMD.

Residue-wise analysis of contacts and mobility in the TMD interfaces. Next, we examined differences in the TMD topology of each system in terms of changes in the number of contacts present in the starting structure ("native contacts") and those formed over the MD simulation time ("non-native contacts"). A contact is considered formed between the α and β subunits if any two atoms of two residues come closer than 7 Å[47]. First, for globally comparing the three systems, we computed the average number of overall contacts. The total number of native contacts already present in the NMR structure of $\alpha_{IIb}\beta_3$ TMD (PDB ID 2K9J) is almost equal to that of the initial structure of $\alpha_v\beta_3$ TMD (6217 *versus* 6244), and only ~2% smaller than that of the initial structure of $\alpha_5\beta_1$ TMD (6344). In contrast, compared to $\alpha_{IIb}\beta_3$, both $\alpha_v\beta_3$ and $\alpha_5\beta_1$ reveal a highly significant reduction

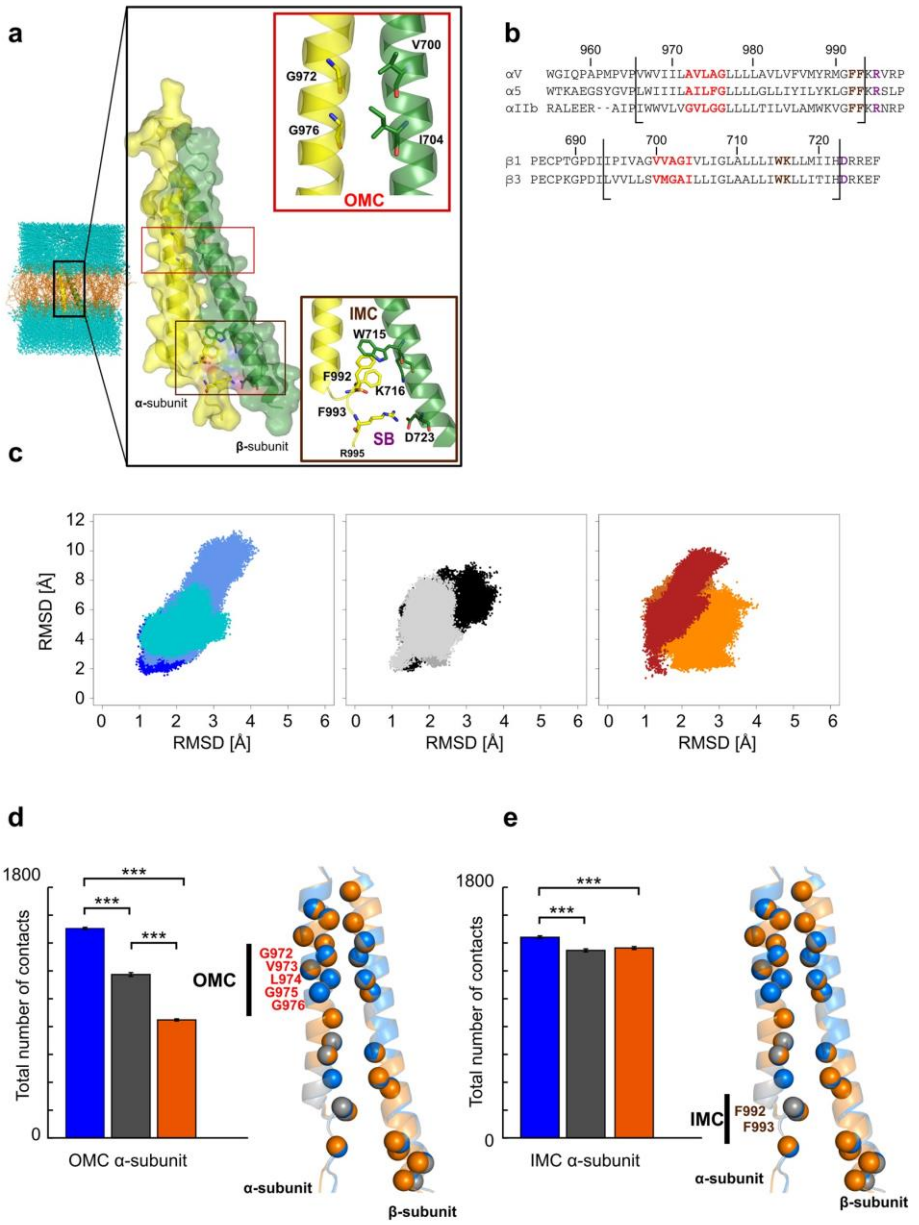

Figure 1. Structural integrity of the membrane-embedded helices throughout the MD simulations and contacts across the interface. (**a**) Exemplary simulation box generated to perform MD simulations including the NMR structure of $\alpha_{IIb}\beta_3$ TMD (PDB ID 2K9J; cartoon and surface representation) with the position of the OMC (red box) and IMC (brown box) indicated; phospholipids are shown as orange sticks, and water layers as blue spheres. Close-up views of the box contents show essential residues mediating the clasps: α_{IIb}-G972/G976 and β_3-V700/I704 for the OMC, α_{IIb}-F992/F993/R995 and β_3-W715/K716/D723 for the IMC plus the putative salt bridge. (**b**) Sequence alignment of the $\alpha_{IIb}\beta_3$, $\alpha_v\beta_3$, $\alpha_5\beta_1$ TMD sequences used to generate the homology models. GXXXG and GFFKR motifs are highlighted in red and brown, respectively, and R995/D723 residues in purple. Black bars indicate the TMD borders as reported in ref.[45]. (**c**) Two dimensional histograms of the RMSD values of all C_α atoms (ordinate values) and only those that are embedded in the membrane (abscissa values) (range of residues considered: P996-V1015 and D718-I747) calculated over three MD simulations. Blue, cornflowerblue, turquoiseblue colored dots represent $\alpha_{IIb}\beta_3$ (MD simulations 1, 2 and 3); darkgrey, black, lightgrey $\alpha_v\beta_3$; chocolate, orange, firebrick $\alpha_5\beta_1$. (**d**,**e**) Histograms of the total number of overall contacts per residue at the OMC and IMC averaged over three MD simulations, with error bars showing the standard error of the mean (SEM; eq. 6) and stars indicating the statistical significance (see Methods section for definition).

Here, only residues of the α subunit are shown (numbering refers to the α_{IIb} subunit). On the right of the plots, a superimposition of the $\alpha_{IIb}\beta_3$, $\alpha_v\beta_3$, and $\alpha_5\beta_1$ TMDs in blue, grey, and orange, respectively, is shown. The C_α atoms of residues considered in the contact analysis are indicated as spheres, and the residues of the α subunit considered in the analyses are labeled.

of overall contacts by ~10% ($p < 0.0001$) (Fig. S3) during the MD simulations. Second, from a list of residues conserved across the three α subunits and the contact map information, we extracted those residues accounting for the native and non-native contacts at the OMC and IMC interface between α and β subunit (Table S1). As to the former, compared to $\alpha_{IIb}\beta_3$ TMD, the overall average number of contacts is ~20% smaller in the $\alpha_v\beta_3$ TMD and ~40% smaller in the $\alpha_5\beta_1$ TMD (Fig. 1d). Both differences are highly significant ($p < 0.0001$). As to the latter, compared to $\alpha_{IIb}\beta_3$ TMD, both $\alpha_v\beta_3$ and $\alpha_5\beta_1$ TMDs reveal a significant reduction of overall contacts by ~10% (Fig. 1e) ($p \approx 0.003$ and 0.006, respectively).

Furthermore, we computed residue-wise root mean square fluctuations (RMSF) as a measure of atomic mobility to identify local differences in the structural dynamics of the three TMD complexes, averaged over the respective three simulations. For both the α and β subunit, the $\alpha_{IIb}\beta_3$ TMD shows less pronounced residue motions, with the RMSF values of 60 out of 89 residues (~67%) being lower than those of $\alpha_v\beta_3$ and $\alpha_5\beta_1$ (Table S2). To conclude, these results demonstrate on a per-residue level that the $\alpha_{IIb}\beta_3$ TMD forms generally more contacts across the TMD interface and shows less mobile residues in the TMD.

Subunit-specific differences in OMC and IMC distances. Both the OMC and IMC are considered necessary to maintain integrin in the low affinity state[2] (Fig. 1a). However, particularly in the OMC, each TMD has subunit-specific amino acids (Fig. 1b) that may be responsible for the above observed differences. The d_{OMC} (distance computed between the centers of mass (COM) of the C_α atoms of the G*XXX*G motif (G972-G976) on the α_{IIb} subunit and V700-I704 on the β_3 subunit) is 9.3 Å in the NMR structure of $\alpha_{IIb}\beta_3$ TMD (PDB ID 2K9J) and 7.3 Å in a structure based on Cys cross-linking results[48]. The distance d_{IMC} computed as the minimal distance between the COMs of the aromatic rings of F992 or F993 on the α_{IIb} subunit and the aromatic ring of W715 on the β_3 subunit is 4.0 Å in the NMR structure and 5.4 Å in the structure based on Cys cross-linking results.

As to the MD simulations, first, the d_{OMC} averaged over three simulations is smaller by ~0.3 Å in the $\alpha_{IIb}\beta_3$ TMD (~6.8 Å, SEM ≈ 0.03 Å) than in the $\alpha_v\beta_3$ TMD (~7.1 Å, SEM ≈ 0.06 Å), and smaller by ~1.5 Å than in the $\alpha_5\beta_1$ TMD (~8.4 Å, SEM ≈ 0.3 Å). All values are well in the range of inter-helical distances found for TM heterodimers containing an OMC-like structural motif[49]. The differences are highly significant in all cases ($p < 0.0001$) (Fig. 2a, Table S3). Hence, the OMC interface is most compact in $\alpha_{IIb}\beta_3$ TMD, followed by $\alpha_v\beta_3$ and $\alpha_5\beta_1$ TMDs. Second, the d_{IMC} averaged over three simulations remains below 7 Å in all cases: $\alpha_{IIb}\beta_3$ (~6.8 Å, SEM ≈ 0.5 Å), $\alpha_v\beta_3$ (~6.3 Å, SEM ≈ 0.9 Å) and $\alpha_5\beta_1$ TMDs (~5.9 Å, SEM ≈ 0.2 Å) (Fig. 2b, Table S3). The differences are not significant ($p \approx 0.6$ for $\alpha_{IIb}\beta_3/\alpha_v\beta_3$, ≈ 0.05 for $\alpha_{IIb}\beta_3/\alpha_5\beta_1$, ≈ 0.5 for $\alpha_v\beta_3/\alpha_5\beta_1$), however. Hence, we conclude that the IMC interface is equally maintained over the course of the MD simulations.

Subunit-specific interactions formed across the TMD interfaces. The IMC interface is adjacent to the membrane-proximal region, which is believed to be mainly stabilized by a salt bridge formed between α_{IIb}-R995 and β_3-D723[2]. First, we computed the minimal distance between the atoms $R995_{N\eta1/N\eta2}$ and $D723_{O\delta1/O\delta2}$ for each system (Table 1). As next to R995 and D723, respectively, R997 is present on the α subunit and E726 on the β subunit, we also analyzed the minimal distances between atoms $R995_{N\eta1/N\eta2}$ and $E726_{O\varepsilon1/O\varepsilon2}$, $R997_{N\eta1/N\eta2}$ and $D723_{O\delta1/O\delta2}$, and $R997_{N\eta1/N\eta2}$ and $E726_{O\varepsilon1/O\varepsilon2}$ (Table 1; $\alpha_5\beta_1$ integrin contains a Leu at position 997 such that the last two distances were not evaluated there). Then, to assess the frequency of occurrence of formed salt bridges, we applied a cutoff of 4 Å to the computed minimal distances, according to a previous study[50] (Table 1): 1) the R995-D723 salt bridge has the highest occupancy in the $\alpha_{IIb}\beta_3$ TMD (~58%), followed by the $\alpha_v\beta_3$ (~37%) and $\alpha_5\beta_1$ TMDs (~39%). The differences between $\alpha_{IIb}\beta_3$ TMD and either $\alpha_v\beta_3$ or $\alpha_5\beta_1$ TMDs are not statistically significant ($p \approx 0.3$ for $\alpha_{IIb}\beta_3/\alpha_v\beta_3$, $\alpha_{IIb}\beta_3/\alpha_5\beta_1$, and ≈ 0.9 for $\alpha_v\beta_3/\alpha_5\beta_1$); 2) the R995-E726 salt bridge (the only alternative interaction that can be formed in $\alpha_5\beta_1$) has the highest occupancy in the $\alpha_5\beta_1$ TMD (~42%), followed by the $\alpha_{IIb}\beta_3$ (~33%) and $\alpha_v\beta_3$ TMDs (~39%). The differences are not significant ($p \approx 0.8$ for $\alpha_{IIb}\beta_3/\alpha_v\beta_3$, $\alpha_{IIb}\beta_3/\alpha_5\beta_1$, and ≈ 0.9 for $\alpha_v\beta_3/\alpha_5\beta_1$); 3) the R997-D723 salt bridge is formed in both the $\alpha_{IIb}\beta_3$ (~47%) and $\alpha_v\beta_3$ TMDs (~48%) to a very similar extent (the difference is not significant ($p \approx 0.9$)); 4) the R997-E726 salt bridge is formed to a lower extent in the $\alpha_{IIb}\beta_3$ (~17%) and $\alpha_v\beta_3$ TMDs (~31%), and the difference is not significant ($p \approx 0.4$). To conclude, our results, in agreement with ref.[24], indicate that R995-D723 is not the only salt bridge that is formed across the TMD interface. In agreement with ref.[51], the R995-D723 salt bridge dissociates intermittently, as indicated by occupancies ≪100%. However, the MD simulations reveal that, among all four possible salt bridges that can form in the membrane-proximal region, R995-D723 is the most prevalent interaction, followed by R995-E726, and R997-E726 is the least prevalent one.

Subunit-specific contribution of K716 to the TMD stability. Finally, we investigated the behavior of K716, monitoring where the residue preferentially places its side chain, i.e., either as part of a hydrogen bond with F992 or by orienting the positive charge of N_ζ towards the negatively charged head groups of the lipid bilayer[38]. In the NMR structure of $\alpha_{IIb}\beta_3$ TMD (PDB ID 2K9J), the distance between N_ζ of K716 and the carbonyl oxygen of F992 is 6.2 Å; in the structure based on Cys cross-linking results, it is 2.9 Å. During the three simulations of each system, the occupancy of the K716-F992 hydrogen bond was investigated applying a distance cutoff of 3.5 Å and an angle cutoff of 120°. On average, the hydrogen bond is formed in a similar manner in the $\alpha_{IIb}\beta_3$ (~38%) and

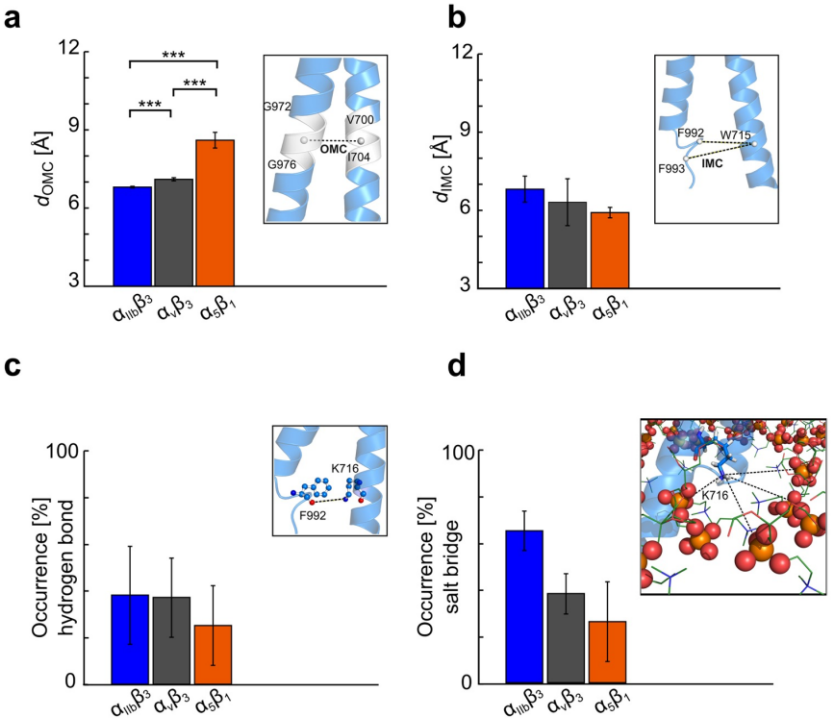

Figure 2. Differences between interdomain interactions in $\alpha_{IIb}\beta_3$, $\alpha_v\beta_3$, and $\alpha_5\beta_1$ TMDs. (**a**,**b**) Histograms of the distances d_{OMC} and d_{IMC} (see main text for definition) averaged over three MD simulations. From left to right, the $\alpha_{IIb}\beta_3$, $\alpha_v\beta_3$, and $\alpha_5\beta_1$ TMDs are displayed in blue, grey, and orange, respectively. Within each plot, a close-up view of the NMR structure of $\alpha_{IIb}\beta_3$ TMD (PDB ID 2K9J) is colored in blue and indicates the analyzed distances (black dashed lines). White spheres indicate C_α atoms of the labeled amino acids. (**c**) Histogram of the mean relative occurrence of the hydrogen bond between $K716_{N\varepsilon}$ and $F992_O$ using a distance cutoff of 3.5 Å and an angle cutoff of 120°. Within the plot, a close-up view of the respective distance measured is shown (color code as in panel a). (**d**) Histogram of the mean relative occurrence of the salt bridge between $K716_{N\varepsilon}$ and the oxygens of phospholipids head groups of the lower lipid leaflet applying a distance cutoff of 4 Å. Within the plot, a close-up view of the respective distance measured is shown, with the phospholipid head groups depicted as spheres. (**a**–**d**) Error bars show the SEM (eq. 5) and stars indicate the statistical difference (see Methods section for definition).

	$\alpha_{IIb}\beta_3$ TMD			$\alpha_v\beta_3$ TMD			$\alpha_5\beta_1$ TMD		
Salt bridge	SimI	SimII	SimIII	SimI	SimII	SimIII	SimI	SimII	SimIII
R995-D723	47	92	35	57	8	46	14	66	38
	58 ± 6.7[b]			37 ± 14.8[b]			39 ± 15.0[b]		
R995-E726	47	50	2	70	29	18	24	78	24
	33 ± 15.5[b]			39 ± 18.8[b]			42 ± 18.0[b]		
R997-D723	23	95	23	84	52	7	—[c]	—[c]	—[c]
	47 ± 24.0[b]			48 ± 22.3[b]			—[c]		
R997-E726	10	39	2	10	31	51	—[c]	—[c]	—[c]
	17 ± 11.2[b]			31 ± 11.8[b]			—[c]		

Table 1. Frequency of occurrence of the up to four salt bridges in the membrane-proximal region for each TMD system[a]. [a]In %. [b]Mean values and SEM (eq. 6), calculated over three MD simulations. [c]Interactions that cannot be formed in the TMD of integrin $\alpha_5\beta_1$.

$\alpha_v\beta_3$ TMDs (~37%), and to a lower extent in the $\alpha_5\beta_1$ TMD (~25%) (Fig. 2c, Table S4). The differences between $\alpha_{IIb}\beta_3$ or $\alpha_v\beta_3$ TMDs with respect to $\alpha_5\beta_1$ TMD result in $p \approx 0.6$, respectively.

To evaluate the presence of electrostatic interactions between the K716 side chain and the head groups of lipids, first, we computed the minimal distance between N_ε of K716 and the nearest O atom of the phospholipid head

groups from the lower lipid leaflet ($d_{snorkeling}$). Then, we applied a 4 Å cutoff to $d_{snorkeling}$ and calculated the frequency of occurrence of a salt bridge. On average, the salt bridge is mainly formed in the $\alpha_{IIb}\beta_3$ TMD (~65%), followed by $\alpha_v\beta_3$ TMD (~38%), and to a lower extent in the $\alpha_5\beta_1$ TMD (~26%) (Fig. 2d, Table S5). The differences between $\alpha_{IIb}\beta_3$ TMD with respect to $\alpha_v\beta_3$ or $\alpha_5\beta_1$ TMDs result in $p \approx 0.08$ and ≈ 0.1, while the difference between $\alpha_v\beta_3$ and $\alpha_5\beta_1$ TMDs results in $p \approx 0.5$. To conclude, the K716 sidechain is engaged in either a hydrogen bond across the TMD or a salt bridge with phospholipid head groups in the $\alpha_{IIb}\beta_3$ TMD (~100%), followed by $\alpha_v\beta_3$ (~75%) and $\alpha_5\beta_1$ (~50%) TMDs, with the salt bridge being the more prevalent interaction in the case of $\alpha_{IIb}\beta_3$ TMD.

Configurational free energies of TM helix association. The above analyses strongly suggest that the TMDs of the integrin isoforms differ in their potential to associate. To corroborate these findings in an independent manner, we computed the configurational free energy (potential of mean force, PMF) of TM helix association using the distance between COMs of the sections of the α and β subunits embedded in the membrane as a reaction coordinate (referred to as $d_{COM\text{-}COM}$). The PMFs were computed using umbrella sampling[52] along a pathway from the bound subunits to subunits where any pair of atoms between the two subunits is at least 10 Å apart, and WHAM[53] post-processing. The PMF profiles were obtained employing 16 biased MD simulations of 200 ns length for reaction coordinate values of $d_{COM\text{-}COM} = 8$ Å to 20 Å, and four biased MD simulations of 70 ns length for reaction coordinate values of $d_{COM\text{-}COM} = 21$ Å to 24 Å. Together, this sums up to a total of ~ 3.5 μs simulation time. Approximately Gaussian-shaped frequency distributions were obtained for each reference point along the reaction coordinates, with all such distributions well overlapping (Fig. S4). These are prerequisites for the successful application of WHAM to extract a PMF from these distributions[53]. Repeating the computations of the PMFs for the range of $d_{COM\text{-}COM} = 8$ Å to 20 Å for parts of the simulation time demonstrates that, for all three systems, the PMFs are converged after at most 160 ns of simulation time per window (maximal difference between two PMFs: 0.2 kcal mol^{-1}) (Fig. S5). The same procedure was repeated for the PMFs from $d_{COM\text{-}COM} = 20$ Å to 24 Å (fully dissociated state), demonstrating that these PMFs are converged after at most 50 ns of simulation time per window (Fig. S5). For comparison, the PMF values at $d_{COM\text{-}COM} = 20$ Å were set to zero in all three cases (Fig. 3a).

The global minima ($d_{COM\text{-}COM} \approx 9$ Å) are in all three cases close to the initial distance (10 Å resp. 12.6 Å) calculated from the NMR structure of the $\alpha_{IIb}\beta_3$ TMD (PDB ID 2K9J) or the structure based on Cys cross-linking results, and the general shapes of the PMFs are comparable, with a rising free energy with increasing reaction coordinate values and rather flat PMFs beyond $d_{COM\text{-}COM} \approx 20$ Å. Furthermore, in going from the global minima to $d_{COM\text{-}COM} \approx 20$ Å, two local minima are passed (marked by roman numbers II and III in Fig. 3a). These minima are located at $d_{COM\text{-}COM} \approx 12$ to 13 Å and $d_{COM\text{-}COM} \approx 15$ Å in all three systems.

However, the PMFs also show pronounced differences. First, the global minima show values of −6.5, −3.8, and −2.1 kcal mol^{-1} for the $\alpha_{IIb}\beta_3$, $\alpha_v\beta_3$, and $\alpha_5\beta_1$ TMDs, respectively, demonstrating the largest tendency for the TM helices to associate in the case of $\alpha_{IIb}\beta_3$, and the lowest in the case of $\alpha_5\beta_1$. For computing association free energies ΔG from the PMFs (eqs 1–3), we, first, assessed to what extent the dissociated TMD helices of α_{IIb} and β_3 sample the accessible configuration space on the simulated time scales. This yielded values for $||\Omega||$, a factor describing the restriction of the configurational space of the monomers upon dimer formation (eq. 4), of 0.05 to 0.10 (Table 2). Compared to the value of the overall accessible space of $(2\pi)^2$, these values indicate that the dissociated TMD helices sample only a fraction of the overall accessible space. Hence, we followed a procedure by Johnston *et al.*[54] to compute dimerization and mole fraction dimerization constants K_a and K_X, respectively, (eqs 1,2) and from there ΔG (eq. 3) (Table 2). The results indicate that $\alpha_{IIb}\beta_3$ TMD is the most stable system ($\Delta G = -3.8$ kcal mol^{-1}), followed by $\alpha_v\beta_3$ and $\alpha_5\beta_1$ TMDs ($\Delta G = -0.8$ kcal mol^{-1} and 0.5 kcal mol^{-1}, respectively). Note that the exact value of the dimerization distance D (eq. 1; here evaluated between 8 and 12 Å) has a low impact on the results (see Table S6 for ΔG values evaluated between 8 and 14 Å), because the integrals reach plateaus after ~10 Å[55]. Second, the TM association requires to pass configurational free energy barriers that are similar for $\alpha_{IIb}\beta_3$ and $\alpha_5\beta_1$ TMDs (~1.5 kcal mol^{-1}, respectively), whereas a larger barrier occurs in the case of $\alpha_v\beta_3$ TMD (~3 kcal mol^{-1}).

To conclude, the PMFs of TM helix association and computed association free energies show overall similar shapes but reveal that the $\alpha_{IIb}\beta_3$ TMD has the strongest tendency to associate, and the PMF of the $\alpha_5\beta_1$ TMD shows the smallest configurational free energy changes.

Distinct order of TMD clasp formation and differences in the persistence of IMC and OMC with increasing helix-helix distance. To further investigate differences between the integrin isoforms in more detail, averaged d_{OMC} and d_{IMC} were computed on the reweighted ("unbiased") configurations from umbrella sampling (reweighting done according to ref.[56]) (Fig. S6) for free energy minima I – II, respectively (Fig. 3b,c; Table S7).

At the global minimum I, the d_{OMC}, averaged over windows 3–5, is very similar in the $\alpha_{IIb}\beta_3$ and $\alpha_v\beta_3$ TMDs (~7.3 Å, ~7.4 Å, SEM ≈ 0.09 Å), and smaller by ~0.8 Å than in the $\alpha_5\beta_1$ TMD (~8.1 Å, SEM ≈ 0.09 Å). The differences between $\alpha_{IIb}\beta_3$ or $\alpha_v\beta_3$ TMDs *versus* $\alpha_5\beta_1$ TMD are (highly) significant ($p < 0.0001$, and $p \approx 0.0003$). The d_{IMC} is smaller by ~0.9 Å in the $\alpha_{IIb}\beta_3$ TMD (~5.1 Å, SEM ≈ 0.08 Å) than in the $\alpha_v\beta_3$ and $\alpha_5\beta_1$ TMDs (~6.0 Å, SEM ≈0.3 Å and ≈ 0.6 Å, respectively). The difference between $\alpha_{IIb}\beta_3$ and $\alpha_v\beta_3$ TMDs is highly significant ($p < 0.0001$), while for that between $\alpha_{IIb}\beta_3$ and $\alpha_5\beta_1$ TMDs, $p \approx 0.06$ results. Hence, both the OMC and IMC are conserved, with the clasps being more compact in the $\alpha_{IIb}\beta_3$ TMD, followed by $\alpha_v\beta_3$ and $\alpha_5\beta_1$ TMDs.

At minimum II, the d_{OMC}, averaged over windows 8–9, is slightly smaller in the $\alpha_{IIb}\beta_3$TMD (~10.1 Å, SEM ≈ 0.03 Å) than in the $\alpha_v\beta_3$ TMD (~10.4 Å, SEM ≈ 0.09 Å), and smaller by ~0.8 Å than in the $\alpha_5\beta_1$ TMD (~10.9 Å, SEM ≈ 0.1 Å). The difference between $\alpha_{IIb}\beta_3$ and $\alpha_v\beta_3$ TMDs is significant ($p \approx 0.04$) and highly significant in the other cases ($p < 0.0001$). The d_{IMC} is smaller by ~0.6 Å in the $\alpha_{IIb}\beta_3$ TMD (~5.6 Å, SEM ≈ 0.08 Å) than in the $\alpha_v\beta_3$ TMD (~6.2 Å, SEM ≈ 0.4 Å), and by ~2.4 Å than in the $\alpha_5\beta_1$ TMD (~8.0 Å, SEM ≈ 0.4 Å). The difference between $\alpha_{IIb}\beta_3$ and $\alpha_v\beta_3$ TMDs is significant ($p \approx 0.03$ Å), and highly significant in the

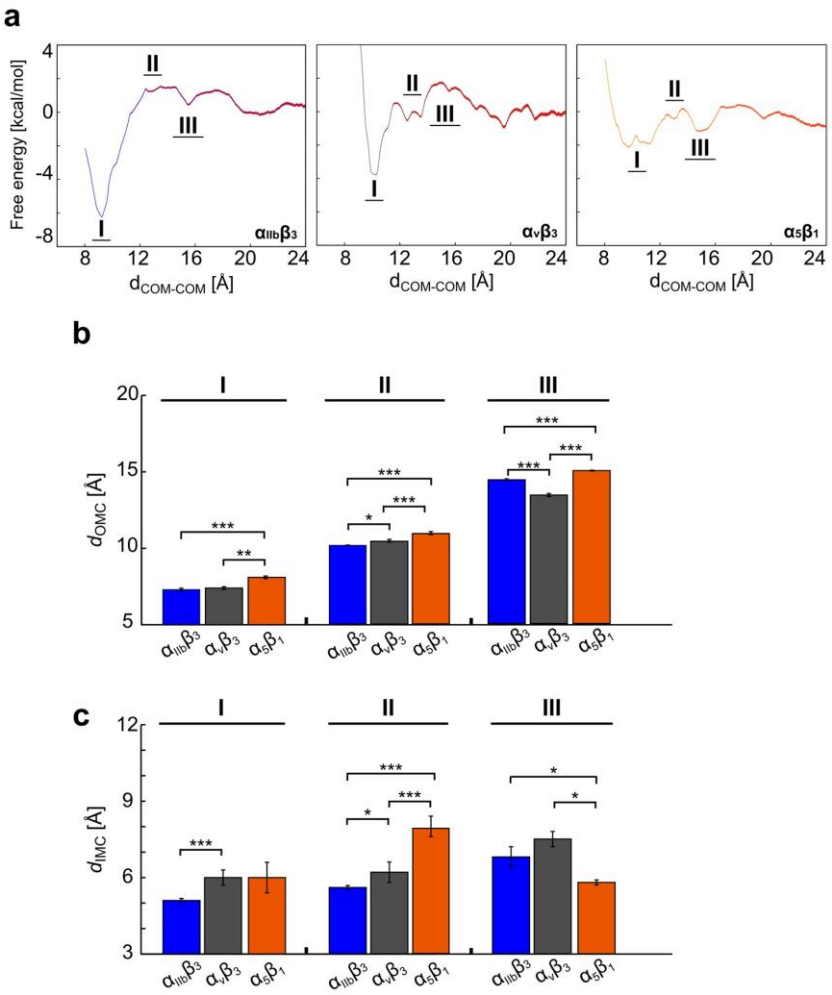

Figure 3. Potential of mean force of TM helix association of $\alpha_{IIb}\beta_3$, $\alpha_v\beta_3$, and $\alpha_5\beta_1$ TMDs and differences at the OMC/IMC interface with increasing $d_{COM\text{-}COM}$. (**a**) Configurational free energies as a function of the $d_{COM\text{-}COM}$ used as a reaction coordinate for $\alpha_{IIb}\beta_3$ (left panel), $\alpha_v\beta_3$ (middle panel), and $\alpha_5\beta_1$ (right panel) TMDs. Roman numbers indicate free energy minima. Statistical errors, calculated using bootstrap analysis, are displayed as red shaded curves added to the PMF profiles. The PMF values at $d_{COM\text{-}COM} = 20$ Å were set to zero. (**b**,**c**) Histograms of the averaged d_{OMC} (B) and d_{IMC} (C) across umbrella sampling windows linked to free energy minima I–III observed in panel (A) (see also Table S7), using reweighted ("unbiased") TMD configurations. Error bars denote the SEM (eq. 5) and stars indicate the statistical difference (see Methods section for definition).

System	$\alpha_{IIb}\beta_3$ TMD	$\alpha_v\beta_3$ TMD	$\alpha_5\beta_1$ TMD
$\|\|\Omega\|\|$[b]	0.07	0.05	0.1
K_d[c]	38009.8	280.9	27.7
K_X	543.0	4.0	0.4
ΔG[d]	−3.8	−0.8	0.5

Table 2. Thermodynamic quantities for each TMD system[a]. [a]The integral in eq. 1 was evaluated at $D = 12$ Å. [b]In radians. [c]In Å^2. [d]In kcal mol^{-1}.

other cases ($p < 0.0001$). Hence, the interface at the OMC is less compact than before and starts to disintegrate ($d_{OMC} > 10$ Å). In contrast, the IMC packing is conserved, similar to as before, but the interface is tighter in $\alpha_{IIb}\beta_3$ TMD than in $\alpha_v\beta_3$ and $\alpha_5\beta_1$ TMDs.

Finally, at minimum III, d_{OMC} and d_{IMC}, averaged over windows 11–12, reveal that the OMC packing is largely lost (distances > 13 Å), while the IMC packing is still conserved. The d_{IMC} is ~0.8 Å smaller in the $\alpha_{IIb}\beta_3$ TMD (~6.8 Å, SEM ≈ 0.4 Å) than in the $\alpha_v\beta_3$ TMD (~7.5 Å, SEM ≈ 0.3 Å), and ~1 Å larger than in the $\alpha_5\beta_1$ TMD (~5.8 Å, SEM ≈ 0.1 Å). The difference between $\alpha_{IIb}\beta_3$ and $\alpha_v\beta_3$ TMDs is not significant ($p \approx 0.2$), but both differences *versus* $\alpha_5\beta_1$ TMD are significant ($p \approx 0.005$).

To conclude, our results suggest for all investigated integrin isoforms that helix association in the TMDs proceeds first via IMC formation, and that OMC formation then reinforces the coiled-coil conformation. The reverse order is suggested to occur upon helix dissociation. However, pronounced differences among the three TMDs as to the conservation of OMC/IMC packing with increasing $d_{COM\text{-}COM}$ became obvious, with $\alpha_{IIb}\beta_3$ TMD showing the most persistent clasps.

Discussion

In this study, we have shown by molecular simulations at the atomistic level that the TMD of integrin $\alpha_{IIb}\beta_3$ is most stably associated compared to that of $\alpha_v\beta_3$ and $\alpha_5\beta_1$, and that this difference is related to differences in particular interactions across the TMDs, notably in the OMC. We furthermore identified an "OMC before IMC" order of clasp disintegration upon TMD dissociation as a uniform property of all three investigated TMDs. Our study was motivated by the considerable evidence that the TMD separate upon integrin activation[7,11,13,14,17,57–60] and so are expected to influence conformational properties of integrins, which, in turn, have been correlated to integrin adhesiveness and affinity[26,61–66]. Furthermore, while the overall structural organization and activation mechanism of integrins appears largely conserved[48,62,66–68], subunit-specific differences in the activation sensitivity had been reported[26,27,29]. Accordingly, here, we comparatively assessed the TMD of $\alpha_5\beta_1$, a physiologically relevant[69,70] member of the β_1 integrin subfamily that is considered basally active[26] and TMDs of $\alpha_{IIb}\beta_3$ and $\alpha_v\beta_3$, physiologically relevant[71,72] members of the β_3 integrin subfamily that is considered basally inactive[26], although a cell-specific influence on the activation sensitivity has been reported for integrin $\alpha_v\beta_3$[29].

That $\alpha_{IIb}\beta_3$ TMD is most stably associated compared to that of $\alpha_v\beta_3$ and $\alpha_5\beta_1$ has been demonstrated in two independent ways. First, we performed unbiased microsecond-long MD simulations at the atomistic level in explicit solvent and an explicit lipid bilayer on the three TMDs, likely the currently most accurate way to explore structure and dynamics of transmembrane proteins[73]. The length of our MD simulations surpasses comparable previous ones on integrin TMDs by at least one order of magnitude[51,74,75]. We performed triplicate MD simulations for each system, which allows probing for the influence of the starting conditions and determining the significance of the computed results by statistical testing and rigorous error estimation[46]. As to the latter, we paid close attention to only consider uncorrelated instances for SEM calculations (eqs 5 and 6). The assessment of convergence of internal motions between independent MD simulations revealed for motions of the TMDs described by the first three PCs that they are relatively well-converged on the timescale of the simulations. For the MD simulations, we used established parameterizations for the solvent[76], lipids[77], and proteins[78]; the latter, we had also applied successfully in other integrin simulations[79–82], although we note that more recent protein force fields have become available[83,84]. Yet, the impact of force field deficiencies on our results is expected to be small due to cancellation of errors when comparatively assessing the TMDs. While for $\alpha_{IIb}\beta_3$ TMD an experimental structure was available for system setup[15], structures generated by homology modeling were used for $\alpha_v\beta_3$ and $\alpha_5\beta_1$ TMDs. Still, with sequence identities of 40 to 65%, C_α-RMSD values to the native structure below 1 Å and, hence, close to experimental uncertainty can be expected for transmembrane regions[85]. The quality of the modeled starting structures is indirectly supported by the fact that for all three systems, very similar magnitudes of structural deviations along the MD trajectories were found (Fig. 1c). The simulated protein sequences contain a linker region at the N-terminal ends and up to six residues of the cytoplasmic domains at the C-terminal ends, in addition to the TM helices. For β_1 and β_3, the linker region is almost conserved (Fig. 1b), and the linker of α_{IIb} has been shown to be dynamically unstructured[45]. Together with crystallographic studies of inactive ectodomains that were unable to obtain structural information on these linkers, indicating their high flexibility[48,86,87], we thus do not expect these linker regions to influence the TMD association differentially. In contrast, for the cytoplasmic membrane-proximal region, an influence on maintaining integrin inactivity has been suggested[36] (see also below). Of particular relevance is the choice of lipid type, as it has been shown that annular anionic lipids can stabilize $\alpha_{IIb}\beta_3$ TMD[51]. Therefore, our lipid bilayer consisted of zwitterionic 1,2-dioleoyl-*sn*-glycero-3-phosphocholine (DOPC) lipids, which were shown to interfere much less with inter-TM helix interactions[51].

As a second, independent means to investigate the energetics of TMD association and because we cannot expect to observe a dissociation of the TMDs on the time scale of our MD simulations[44], we performed biased MD simulations at the atomistic level followed by PMF computations, using established protocols successfully applied previously by us[50,88,89] and $d_{COM\text{-}COM}$ as an intuitive reaction coordinate previously applied on similar systems[6,90]. To our knowledge, so far, the association energetics of integrin TMDs, by computational means, has only been investigated by coarse-grained MD simulations followed by PMF computations[6,90]. By repeating the PMF computations for parts of the biased simulations, we demonstrated that the PMFs are converged with respect to the overall simulation time per sampling window (Fig. S5). Still, even with sampling times of up to 200 ns per sampling window, pronounced helix tilting or even helix rotation around an axis perpendicular to the helix axis, once the helices are separated by a large enough distance, cannot be expected. Likewise, such sampling times may not be sufficient to yield sampled helix-helix configurations that are completely unbiased from the respective starting structures. While these potential issues may be expected to disfavor separated helix-helix configurations with respect to associated TMD, their impact on our results is expected to be small due to cancellation of errors when comparatively assessing the respective TMD. Comparing quantitative results from the PMFs (Fig. 3a) and subsequent association free energy calculations[54] (Table 2) to experimental data lends remarkable support to the quality of the setup, parameterization, and execution of our simulations: (I) For $\alpha_{IIb}\beta_3$ TMD, association free energies of −4.33 and −4.84 kcal mol^{-1} have been determined in 1-palmitoyl-2-oleoyl-*sn*-glycero-3-phosphocholine

(POPC) lipids by NMR spectroscopy and calorimetry[44,51], and our computed ΔG of -3.8 kcal mol^{-1} (Table 2) is within chemical accuracy of these results; (II) for $\alpha_5\beta_1$, to our knowledge, the energetics of TMD association has not been explicitly probed experimentally. However, from comparing conformational equilibria between the extended-closed and extended-open states for full-length integrin $\alpha_5\beta_1$ *versus* the $\alpha_5\beta_1$ ectodomain, one may infer that the associated and dissociated states of the TMDs and cytoplasmic domains are almost isoenergetic[26], which is in very good agreement with a computed ΔG of 0.5 kcal mol^{-1} (Table 2); (III) obtaining a barrier height pertinent to kinetics *via* a PMF has been debated[91]. Still, when inserting the configurational free energy barrier for $\alpha_{IIb}\beta_3$ TMD association of ~1.5 kcal mol^{-1} (Fig. 3a) as $\Delta G^{\ddagger}$ in the transition state theory equation $k = k^{\ddagger} \exp(-\Delta G^{\ddagger}/RT)$[92] and approximating $k^{\ddagger}$ with a collision frequency of a transmembrane protein of 10^5 to 10^6 s^{-1} [93], a rate k of $\sim 8 * 10^3$ to $\sim 8 * 10^4$ s^{-1} is obtained as a coarse upper bound[94], in good to fair agreement with an association rate of $\alpha_{IIb}\beta_3$ TMD in phospholipid bicelles of $4.5 * 10^3$ s^{-1} found by NMR spectroscopy[44]. As to probing the internal consistency of our results, the shallow contact minimum found in the PMF for $\alpha_5\beta_1$ TMD and the apparent lack of pronounced barriers towards the dissociated state suggest that in MD simulations that are long enough, the two helices should (start to) come apart. In fact, such a tendency is found as $d_{COM\text{-}COM}$ in the unbiased MD simulations of $\alpha_5\beta_1$ TMD is ~1 and 0.6 Å larger than for $\alpha_{IIb}\beta_3$ and $\alpha_V\beta_3$ TMDs (Fig. S7, Table S8). Likewise, internal consistency can be probed by analyzing structural parameters of configurations from unbiased MD simulations and reweighted ("unbiased") configurations from umbrella sampling simulations. This reveals qualitatively similar results for subtype-specific differences in the distances characterizing OMC formation (d_{OMC}; Fig. 2a *versus* Fig. 3b, part I), and likewise similar results for $\alpha_v\beta_3$ and $\alpha_5\beta_1$ TMDs concerning the distance characterizing IMC formation (d_{IMC}; Fig. 2b *versus* Fig. 3c, part I), although the results for $\alpha_{IIb}\beta_3$ deviate in this case. The latter discrepancy may be explained in that distances in Fig. 2b where directly computed from the (tightly associated) $\alpha_{IIb}\beta_3$ TMD configurations in the unbiased MD simulations, while three umbrella sampling windows were evaluated for distances in Fig. 3c.

The PMF and association free energy calculations clearly revealed that $\alpha_{IIb}\beta_3$ TMD is most stably associated, followed by $\alpha_v\beta_3$ TMD and $\alpha_5\beta_1$ TMD (Table 2). It had been previously suggested by experiment[13,39] and computations[49,95] that the two structural motifs OMC and IMC are responsible for the correct TMD packing but if, and how, sequence variations there (Fig. 1b), especially in the OMC, lead to differential TMD association has remained largely elusive. Our unbiased MD simulations reveal that the most stable association of $\alpha_{IIb}\beta_3$ TMD is paralleled by this TMD forming more contacts in general across the whole TMD interface (Fig. S3) as well as particularly in the OMC interface (Fig. 1d); also, this TMD shows the most compact OMC (Fig. 2a; Fig. 3b in part I). Although differences in the prevalence of single hydrogen bonds or salt bridges among the three TMDs were not significant, our unbiased MD simulations still suggest a trend, according to which the importance of the membrane-proximal region for TMD association is confirmed, particularly of the R995-D723 salt bridge[24,39,51], as this interaction is also most prevalent in $\alpha_{IIb}\beta_3$ TMD (>20%, Table 1). Our results may also provide an explanation as to why, in *in vivo* experiments on transgenic mice carrying a point mutation of the respective D723 of the β_1 subunit, a normal integrin function was found[32]: In $\alpha_5\beta_1$ TMD, the R995-E726 salt bridge is more prevalent than the R995-D723 one. Other questions relate to the role of β_3-K716 as a key determinant for the stability at the IMC interface[96] and whether the proposed stabilization arises from an engagement of K716 with the surroundings lipid molecules[96] or by forming a hydrogen bond with F992[17]. Our MD simulations revealed that K716 occurs most frequently in either a hydrogen bond across the TMD or a salt bridge with phospholipid head groups in $\alpha_{IIb}\beta_3$ TMD, followed by $\alpha_v\beta_3$ and $\alpha_5\beta_1$ TMDs, consistent with the notion that K716 is important for integrin function in $\alpha_{IIb}\beta_3$, but not in $\alpha_5\beta_1$[25].

Although more work would be required to establish unequivocally a link between differences in K716/phospholipid head group interactions and differences in TMD association free energies, we do not find it unlikely that this link exists. This link would then stress that (differences in) TMD association may be governed by additional factors besides sequence differences, including interactions to annular lipids, as previously demonstrated for the $\alpha_{IIb}\beta_3$ TMD[51], or membrane tension[97]. Along these lines, recent work on integrin $\alpha_5\beta_1$ suggested the hypothesis that the non-ligand binding leg domains and *N*-glycans may have previously unappreciated roles in regulating integrin conformations[26]. Hence, while considering a subsystem such as the TMD in this study has the benefit of yielding detailed answers under well-defined conditions, at the same time, it leads to the limitation that effects from other parts of the system are not accounted for.

To our knowledge, a novel aspect resulting from our study with respect to the question what governs integrin adhesiveness and affinity in relation to conformational changes is the finding that the two clasps disintegrate in the order "OMC before IMC" upon TMD dissociation. This finding leads to the relevant prediction that the closed state of integrins might not be single but rather comprising several microstates that vary in the extent of TMD association, e.g., with the TMD associated at both OMC *and* IMC, or with the TMD associated only at the IMC. A similar proposition was made for the extended state(s) of integrins based on the flexibility of integrin legs[26,67]. Our finding may also be related to, not yet fully understood, results on conformational free energies for intact integrin $\alpha_5\beta_1$ that revealed that the presence of the TMD and cytoplasmic domains favors considerably the bent-closed over the extended-closed conformation[26], when one considers that the bent-closed → extended-closed transition may already contain energetic contributions from a partial TMD dissociation in the OMC region. In that respect, computations as performed here may support valuable efforts of gaining affinity information for specific integrin conformational states[26] providing access to the energetic contributions of defined subsystems. Finally, we find it striking to note that the order of association free energies of the TMDs ($\alpha_{IIb}\beta_3 \ll \alpha_v\beta_3 < \alpha_5\beta_1$ (Table 2)) parallels reports on the basal activity of these integrins ($\alpha_{IIb}\beta_3 \ll \alpha_v\beta_3 < \alpha_5\beta_1$)[26,27]. While it is not possible to establish a direct link between these two series from the comparative simulation studies on TMDs alone, our finding suggests, to our knowledge for the first time, that the sequence composition of the TM helices can have a decisive effect on free energies associated with distinct conformational states of different integrins. A likewise suggestion has been made regarding the strength of interactions between leg domains for integrins $\alpha_{IIb}\beta_3$ and $\alpha_v\beta_3$[29]. Notably,

the magnitude of differences in association free energies across the investigated TMDs (~2.7 kcal mol^{-1}; Table 2) is clearly in the range of observed changes in conformational free energies upon activation of full-length integrin $\alpha_5\beta_1$ (~3.7 kcal mol^{-1})[26], suggesting that TMD differences can indeed significantly impact overall conformational integrin energetics.

In summary, $\alpha_{IIb}\beta_3$ TMD is most stably associated compared to that of $\alpha_v\beta_3$ and $\alpha_5\beta_1$, which is related to differences in particular interactions across the TMDs, notably in the OMC. The order of TMD association stability is paralleled by the basal activity of these integrins, which suggests that TMD differences can have a decisive effect on conformational free energies of integrin states. The "OMC before IMC" order of clasp disintegration upon TMD dissociation uniformly identified for all three investigated TMDs suggests that the closed state of integrins might not be single but rather comprising several microstates that vary in the extent of TMD association.

Methods

Generation of starting structures. The starting structure for MD simulations of the $\alpha_{IIb}\beta_3$ TMD was obtained from the coordinates of the NMR structure (PDB ID 2K9J) available in the RCSB Protein Data Bank[98]. The starting structures for MD simulations of the $\alpha_v\beta_3$ and $\alpha_5\beta_1$ TMDs were generated by homology modeling. The homology models were generated using MODELLER v9.9[99], and the NMR structure of the $\alpha_{IIb}\beta_3$ TMD was used as a template. In the case of $\alpha_v\beta_3$ integrin, only the α_v sequence was modeled based on an alignment with the α_{IIb} TMD with a sequence identity of 45%. In the case of the $\alpha_5\beta_1$ TMD, the α_5 and β_1 sequences are 40% and 65% identical to those of $\alpha_{IIb}\beta_3$ TMD, respectively. The quality of the models was assessed by the QMEANBrane scoring function available in QMEAN server[42,43]. A global QMEAN score of 0.60, 0.64, and 0.67 was computed for the $\alpha_{IIb}\beta_3$, $\alpha_v\beta_3$, and $\alpha_5\beta_1$ TMDs, respectively.

Setup of simulation systems. The membrane builder tool available on the CHARMM-GUI website[100] was used for embedding the TMDs in a pre-equilibrated bilayer of DOPC lipids[101] using the replacement method[102]. The PPM web server[103] was used to assess the correct orientation of the $\alpha_{IIb}\beta_3$ TMD relative to the hydrocarbon core of the lipid bilayer. The required rectangular simulation box was generated by defining the number of lipids (88 and 85 for the upper and lower leaflet, respectively) and setting a value of 17 Å for the water layer above and below the protein. The total system size is ~60,000 atoms, including TIP3P water molecules[76] and Cl^- counter ions.

Molecular dynamics simulations. All MD simulations were performed using the AMBER 14 suite of programs[47], the ff99SB force field for the proteins[78], the Lipid14 force field[77] for the lipids, and the TIP3P water model[76]. The particle mesh Ewald method[104] was used to treat long-range electrostatic interactions, and bond lengths involving bonds to hydrogen atoms were constrained using the SHAKE algorithm[105]. The time step for integrating Newton's equations of motion was 2 fs with a direct space, nonbonded cutoff of 8 Å. Initially, harmonic restraints with a force constant of 500 kcal mol^{-1} Å^{-2} were applied to all solute atoms during the first 250 steps of steepest descent and then reduced to 25.0 kcal mol^{-1} Å^{-2} for the second 2500 steps of conjugate gradient minimization and 10 kcal mol^{-1} Å^{-2} for the last 2500 steps of conjugate gradient minimization. MD simulations in the NVT (constant number of particles, volume, and temperature) ensemble were carried out for 50 ps, during which the system was heated from 100 to 300 K. Subsequent MD simulations in the NPT (constant number of particles, pressure, and temperature) ensemble were used for 150 ps to adjust the solvent density. In both steps, a force constant of 10 kcal mol^{-1} Å^{-2} was applied to all solute and lipid atoms. The production MD simulations of 9 μs length were performed with the GPU version of the program *pmemd*[106] in the tensionless NPT ensemble using the anisotropic Berendsen barostat[107] to control the pressure (coupling constant = 1 ps) and the Langevin thermostat[107] to control the temperature (coupling constant = 1 ps), as suggested in ref.[77].

Potential of mean force computations. Profiles of the free energy of association of $\alpha_{IIb}\beta_3$, $\alpha_v\beta_3$, and $\alpha_5\beta_1$ TMDs were constructed from umbrella sampling MD simulations[108,109] in combination with the WHAM method[53]. As reaction coordination, the distance between the COMs of the TM segments embedded in the membrane was considered (C_α atoms of residues P996-V1015 and D718-I747, for the α_{IIb} and β_3 subunits, respectively (equivalent ranges of residues were used for $\alpha_v\beta_3$ and $\alpha_5\beta_1$)). The initial distance computed from the NMR structure of the TMD of $\alpha_{IIb}\beta_3$ integrin is 10.0 Å. To generate starting structures for umbrella sampling, the initial distance was reduced to 8 Å and increased to 11 Å in 0.5 Å steps, and from 11 Å increased to 24 Å in 1 Å steps. Each TMD configuration was inserted in a pre-equilibrated bilayer of DOPC lipids as described above. This resulted in a total of 20 initial systems per TMD. Each of the 20 windows of the three integrin systems was subjected to umbrella sampling simulations, carried out in the NPT ensemble for 200 ns each for $d_{COM\text{-}COM}$ = 8 Å to 20 Å and 70 ns each for $d_{COM\text{-}COM}$ = 21 Å to 24 Å. This resulted in a total of ~3.5 μs of MD simulation time.

Within each umbrella sampling window, a harmonic potential with a force constant of 4 kcal mol^{-1} Å^{-2} was applied to restrain the conformations close to the reference point. Force constants of 20 kcal mol^{-1} Å^{-2} were also used to restrain conformations whose initial $d_{COM\text{-}COM}$ ranged from 8.0 Å to 10 Å to generate approximately Gaussian-shaped frequency distributions. Otherwise, the parameters described above were used for thermalization and production runs. Finally, to compute the errors at the reference points of the PMF profiles, the Monte Carlo bootstrapping analysis implemented in WHAM using 200 resampling trials was applied.

Estimation of association free energy. An association free energy was estimated from the obtained PMF following the membrane two-body derivation from Johnston *et al.*[54]. In brief, the PMF is integrated along the reaction coordinate to calculate an association constant (K_a), transformed to the mole fraction scale (K_x) taking into account the number of lipids N_L per surface area A, and this value is used to calculate the difference in free energy between dimer and monomers (ΔG), according to eqs 1–3

$$K_a = \frac{||\Omega||}{(2\pi)^2} \int_0^D re^{\frac{-w(r)}{k_B T}} dr \quad (1)$$

$$K_x = K_a \frac{N_L}{A} \quad (2)$$

$$\Delta G = -RT\ ln(K_x) \quad (3)$$

where r is the value of the reaction coordinate, $w(r)$ is the PMF at value r, D is the maximum distance at which the protein is still considered a dimer, k_B is the Boltzmann constant, and T is the temperature at which the simulations were performed. Additionally, a factor that considers the restriction of the configurational space of the monomers upon dimer formation is included in terms of the sampled angle between the two chains in the dimeric state (eq. 4)

$$||\Omega|| = [\max(\theta_a) - \min(\theta_a)] * [\max(\theta_b) - \min(\theta_b)] \quad (4)$$

and the accessible space for the monomers, $(2\pi)^2$. In eq. 4, the angle θ_a is defined as the angle formed between the vectors connecting the COM of helix 1 with the COM of helix 2 and with the COM of residues V971 to V973 of the latter helix; θ_b is defined analogously starting from the COM of helix 2 and using the COM of residues L698 to V700 in helix 1.

Analysis of trajectories. For the analysis of the trajectories, *ptraj*/*cpptraj*[110] of the AmberTools 14 suite of programs was applied. For the unbiased MD simulations, the first 200 ns were not considered for analysis. To evaluate the helix-helix interface (indicated as $d_{\text{COM-COM}}$), a maximal distance of 3.5 Å and a minimal angle of 120° were used as exclusion criteria to identify hydrogen bond formation, as was a maximal distance of 4 Å to identify salt bridge formation. To examine the OMC interface, the distance between the C_α atoms of G972/G976 (α_{IIb} subunit) and V700/I704 (β_3 subunit) was computed (indicated as d_{OMC}). To evaluate the IMC interface, the distance between the centers of mass of the phenyl rings of F992 or F993 (α_{IIb} subunit) and W715 (β_3 subunit) (indicated as d_{IMC1} and d_{IMC2}, respectively) was computed, and the smaller distance of the two was considered further as d_{IMC}. To evaluate the TMD association, we calculated the total number of native and non-native contacts formed between the two helices. A native contact was defined as a contact satisfying the distance cutoff of 7 Å in the first frame (used as reference frame), a non-native contact as a contact satisfying the distance cutoff of 7 Å without being already found in the reference frame. This definition is according to ref.[47]. The same set of analyses was also carried out to analyze the configurations sampled during umbrella sampling. For all the configurations t generated, we estimated a weight w^t according to eqs 7 and 8 from ref.[56]. The reweighting is performed over the entire ensemble of each system and, then, normalized by dividing each w^t by the sum of all w^t for each integrin system.

Statistical analysis. Results from three independent MD simulations are expressed as arithmetic means ± SEM calculated over the time. The overall SEM for each simulated system was calculated according to the law of error propagation (eq. 5):

$$\text{SEM}_{total} = \sqrt{\text{SEM}_1^2 + \text{SEM}_2^2 + \text{SEM}_3^2} \quad (5)$$

where the subscripts $i = \{1, 2, 3\}$ indicate the three trajectories. SEM_i was computed following ref.[111] (see particularly eqs 11–13 there) by, first, detecting the decorrelation time of an investigated variable along each MD simulation and, second, establishing the effective sample size from that time, which is then used to compute SEM_i. In the case of hydrogen bond, salt bridge, and contact analyses, SEM is calculated from the standard deviation (SD) of the three means of the three MD simulations according to eq. 6, assuming that the three MD simulations are statistically independent:

$$SEM = SD/\sqrt{3} \quad (6)$$

p values related to eq. 5 are calculated according to the Student's t-test for parametric testing, with $N_{eff} \equiv (T - t_o + 1)/g$, where N_{eff} is the total number of uncorrelated frames within the trajectories based on the statistical inefficiency g_{t0} and the simulation time range $[t_0, T]$ following ref.[111]; the same test is applied for p values related to eq. 6, with $N_{eff} = 3$. Differences between mean values are considered to be statistically significant if $p < 0.05$ and $p < 0.001$ (indicated as "*" and "**" in figures, respectively) and highly statistically significant if $p < 0.0001$ (indicated as "***" in figures). The statistical analysis was performed using the R software[112] and the pymbar module for MBAR[113].

Data availability. All data generated or analyzed during this study are included in this published article (and its Supplementary Information files).

References

1. Luo, B. H. & Springer, T. A. Integrin structures and conformational signaling. *Curr. Opin. Cell. Biol.* **18**, 579–586 (2006).
2. Ye, F., Kim, C. & Ginsberg, M. H. Reconstruction of integrin activation. *Blood* **119**, 26–33 (2012).
3. Hynes, R. O. Integrins: bidirectional, allosteric signaling machines. *Cell* **110**, 673–687 (2002).
4. Luo, B. H., Carman, C. V. & Springer, T. A. Structural basis of integrin regulation and signaling. *Annu. Rev. Immunol.* **25**, 619–647 (2007).

5. Calderwood, D. A. Integrin activation. *J. Cell. Sci.* **117**, 657–666 (2004).
6. Chng, C. P. & Tan, S. M. Leukocyte integrin alpha(L)beta(2) transmembrane association dynamics revealed by coarse-grained molecular dynamics simulations. *Proteins* **79**, 2203–2213 (2011).
7. Peterson, J. A., Visentin, G. P., Newman, P. J. & Aster, R. H. A recombinant soluble form of the integrin alpha(IIb)beta(3) (GPIIb-IIIa) assumes an active, ligand-binding conformation and is recognized by GPIIb-IIIa-specific monoclonal, allo-, auto-, and drug-dependent platelet antibodies. *Blood* **92**, 2053–2063 (1998).
8. Wegener, K. L. & Campbell, I. D. Transmembrane and cytoplasmic domains in integrin activation and protein-protein interactions (Review). *Mol. Membr. Biol.* **25**, 376–387 (2008).
9. Adair, B. D. & Yeager, M. Three-dimensional model of the human platelet integrin alpha(IIb)beta(3) based on electron cryomicroscopy and X-ray crystallography. *Proc. Natl. Acad. Sci. USA* **99**, 14059–14064 (2002).
10. Gottschalk, K. E. A coiled-coil structure of the alpha(IIb)beta(3) integrin transmembrane and cytoplasmic domains in its resting state. *Structure* **13**, 703–712 (2005).
11. Luo, B. H., Springer, T. A. & Takagi, J. A specific interface between integrin transmembrane helices and affinity for ligand. *PLOS Biol.* **2**, e153 (2004).
12. Li, W. *et al*. A push-pull mechanism for regulating integrin function. *Proc. Natl. Acad. Sci. USA* **102**, 1424–1429 (2005).
13. Luo, B. H., Carman, C. V., Takagi, J. & Springer, T. A. Disrupting integrin transmembrane domain heterodimerization increases ligand binding affinity, not valency or clustering. *Proc. Natl. Acad. Sci. USA* **102**, 3679–3684 (2005).
14. Partridge, A. W., Liu, S., Kim, S., Bowie, J. U. & Ginsberg, M. H. Transmembrane domain helix packing stabilizes integrin alpha(IIb)beta(3) in the low affinity state. *J. Biol. Chem.* **280**, 7294–7300 (2005).
15. Lau, T. L., Kim, C., Ginsberg, M. H. & Ulmer, T. S. The structure of the integrin alpha(IIb)beta(3) transmembrane complex explains integrin transmembrane signalling. *EMBO J.* **28**, 1351–1361 (2009).
16. Yang, J. *et al*. Structure of an integrin alpha(IIb)beta(3) transmembrane-cytoplasmic heterocomplex provides insight into integrin activation. *Proc. Natl. Acad. Sci. USA* **106**, 17729–17734 (2009).
17. Zhu, J. *et al*. The structure of a receptor with two associating transmembrane domains on the cell surface: integrin alpha(IIb) beta(3). *Mol. Cell. Biol.* **34**, 234–249 (2009).
18. Luo, B. H., Springer, T. A. & Takagi, J. Stabilizing the open conformation of the integrin headpiece with a glycan wedge increases affinity for ligand. *Proc. Natl. Acad. Sci. USA* **100**, 2403–2408 (2003).
19. Tng, E., Tan, S. M., Ranganathan, S., Cheng, M. & Law, S. K. The integrin alpha(L)beta(2) hybrid domain serves as a link for the propagation of activation signal from its stalk regions to the I-like domain. *J. Biol. Chem.* **279**, 54334–54339 (2004).
20. Hantgan, R. R., Paumi, C., Rocco, M. & Weisel, J. W. Effects of ligand-mimetic peptides Arg-Gly-Asp-X (X = Phe, Trp, Ser) on alpha(IIb)beta(3) integrin conformation and oligomerization. *Biochemistry* **38**, 14461–14474 (1999).
21. Plow, E. F., Haas, T. K., Zhang, L., Loftus, J. & Smith, J. W. Ligand binding to integrins. *J. Biol. Chem.* **275**, 21785–21788 (2000).
22. Takagi, J., Erickson, H. P. & Springer, T. A. C-terminal opening mimics 'inside-out' activation of integrin alpha(5)beta(1). *Nat. Struct. Biol.* **8**, 412–416 (2001).
23. Shattil, S. J., Kim, C. & Ginsberg, M. H. The final steps of integrin activation: the end game. *Nat. Rev. Mol. Cell. Biol.* **11**, 288–300 (2010).
24. Vinogradova, O. *et al*. A structural mechanism of integrin alpha(IIb)beta(3) "inside-out" activation as regulated by its cytoplasmic face. *Cell* **110**, 587–597 (2002).
25. Lu, Z. *et al*. Implications of the differing roles of the beta(1) and beta(3) transmembrane and cytosplasmic domains for integrin function. *eLife* **5**, e18633 (2016).
26. Li, J. *et al*. Conformational equilibria and intrinsic affinities define integrin activation. *EMBO J.* **36**, 629–645 (2017).
27. Bazzoni, G., Ma, L., Blue, M. L. & Hemler, M. E. Divalent cations and ligands induce conformational changes that are highly divergent among beta(1) integrins. *J. Biol. Chem.* **273**, 6670–6678 (1998).
28. Askari, J. A., Buckley, P. A., Mould, A. P. & Humphries, M. J. Linking integrin conformation to function. *J. Cell Sci.* **122**, 165–170 (2009).
29. Kamata, T., Handa, M., Sato, Y., Ikeda, Y. & Aiso, S. Membrane-proximal alpha/beta stalk interactions differentially regulate integrin activation. *J. Biol. Chem.* **280**, 24775–24783 (2005).
30. Weljie, A. M., Hwang, P. M. & Vogel, H. J. Solution structures of the cytoplasmic tail complex from platelet integrin alpha(IIb) and beta(3) subunits. *Proc. Natl. Acad. Sci. USA* **99**, 5878–5883 (2002).
31. O'Toole, T. E. *et al*. Integrin cytoplasmic domains mediate inside-out signal transduction. *J. Cell. Biol.* **124**, 1047–1059 (1994).
32. Czuchra, A., Meyer, H., Legate, K. R., Brakebusch, C. & Fassler, R. Genetic analysis of beta(1) integrin "activation motifs" in mice. *J. Cell. Biol.* **174**, 889–899 (2006).
33. Campbell, I. D. & Humphries, M. J. Integrin structure, activation, and interactions. *Cold Spring Harb. Perspect. Biol.* **3**, a004994 (2011).
34. Ma, Y. Q., Qin, J. & Plow, E. F. Platelet integrin alpha(IIb)beta(3): activation mechanisms. *J. Thromb. Haemost.* **5**, 1345–1352 (2007).
35. Schneider, D. & Engelman, D. M. Involvement of transmembrane domain interactions in signal transduction by alpha/beta integrins. *J. Biol. Chem.* **279**, 9840–9846 (2004).
36. Kim, C., Ye, F. & Ginsberg, M. H. Regulation of integrin activation. *Annu. Rev. Cell. Dev. Biol.* **27**, 321–345 (2011).
37. Hughes, P. E., O'Toole, T. E., Ylanne, J., Shattil, S. J. & Ginsberg, M. H. The conserved membrane-proximal region of an integrin cytoplasmic domain specifies ligand binding affinity. *J. Biol. Chem.* **270**, 12411–12417 (1995).
38. Strandberg, E. & Killian, J. A. Snorkeling of lysine side chains in transmembrane helices: how easy can it get? *FEBS Lett.* **544**, 69–73 (2003).
39. Hughes, P. E. *et al*. Breaking the integrin hinge. A defined structural constraint regulates integrin signaling. *J. Biol. Chem.* **271**, 6571–6574 (1996).
40. Haas, T. A. & Plow, E. F. Development of a structural model for the cytoplasmic domain of an integrin. *Protein Eng.* **10**, 1395–1405 (1997).
41. Vallar, L. *et al*. Divalent cations differentially regulate integrin alpha(IIb) cytoplasmic tail binding to beta(3) and to calcium- and integrin-binding protein. *J. Biol. Chem.* **274**, 17257–17266 (1999).
42. Studer, G., Biasini, M. & Schwede, T. Assessing the local structural quality of transmembrane protein models using statistical potentials (QMEANBrane). *Bioinformatics* **30**, I505–I511 (2014).
43. Benkert, P., Tosatto, S. C. E. & Schomburg, D. QMEAN: A comprehensive scoring function for model quality assessment. *Proteins: Struct., Funct., Bioinf.* **71**, 261–277 (2008).
44. Situ, A. J., Schmidt, T., Mazumder, P. & Ulmer, T. S. Characterization of membrane protein interactions by isothermal titration calorimetry. *J. Mol. Biol.* **426**, 3670–3680 (2014).
45. Schmidt, T. *et al*. A Conserved Ectodomain-Transmembrane Domain Linker Motif Tunes the Allosteric Regulation of Cell Surface Receptors. *J. Biol. Chem.* **291**, 17536–17546 (2016).
46. Galindo-Murillo, R., Roe, D. R. & Cheatham, T. E. 3rd Convergence and reproducibility in molecular dynamics simulations of the DNA duplex d(GCACGAACGAACGAACGC). *Biochim. Biophys. Acta* **1850**, 1041–1058 (2015).
47. Case, D. A. *et al*. The Amber biomolecular simulation programs. *J. Comp. Chem.* **26**, 1668–1688 (2005).
48. Zhu, J. *et al*. Structure of a complete integrin ectodomain in a physiologic resting state and activation and deactivation by applied forces. *Mol. Cell. Biol.* **32**, 849–861 (2008).

49. Berger, B. W. *et al*. Consensus motif for integrin transmembrane helix association. *Proc. Natl. Acad. Sci. USA* **107**, 703–708 (2010).
50. Ciupka, D. & Gohlke, H. On the potential alternate binding change mechanism in a dimeric structure of Pyruvate Phosphate Dikinase. *Sci. Rep.* **7**, 8020 (2017).
51. Schmidt, T. *et al*. Annular anionic lipids stabilize the integrin alpha(IIb)beta(3) transmembrane complex. *J. Biol. Chem.* **290**, 8283–8293 (2015).
52. Kastner, J. Umbrella sampling. *Wiley Interdiscip. Rev. Comput. Mol. Sci.* **1**, 932–942 (2011).
53. Kumar, S., Bouzida, D., Swendsen, R. H., Kollman, P. A. & Rosenberg, J. M. The Weighted Histogram Analysis Method for Free-Energy Calculations onBiomolecules .1. The Method. *J. Comp. Chem.* **13**, 1011–1021 (1992).
54. Johnston, J. M., Wang, H., Provasi, D. & Filizola, M. Assessing the Relative Stability of Dimer Interfaces in G Protein-Coupled Receptors. *PLOS Comp. Biol.* **8**, e1002649 (2012).
55. Hénin, J., Pohorille, A. & Chipot, C. Insights into the Recognition and Association of Transmembrane α-Helices. The Free Energy of α-Helix Dimerization in Glycophorin A. *J. Am. Chem. Soc.* **127**, 8478–8484 (2005).
56. Moradi, M., Enkavi, G. & Tajkhorshid, E. Atomic-level characterization of transport cycle thermodynamics in the glycerol-3-phosphate: phosphate antiporter. *Nat. Commun.* **6**, 8393, https://doi.org/10.1038/ncomms9393 (2015).
57. Kim, M., Carman, C. V. & Springer, T. A. Bidirectional transmembrane signaling by cytoplasmic domain separation in integrins. *Science* **301**, 1720–1725 (2003).
58. Yin, H. *et al*. Activation of platelet alpha(IIb)beta(3) by an exogenous peptide corresponding to the transmembrane domain of alpha(IIb). *J. Biol. Chem.* **281**, 36732–36741 (2006).
59. Dana, N., Fathallah, D. M. & Arnaout, M. A. Expression of a soluble and functional form of the human beta(2) integrin CD11b/CD18. *Proc. Natl. Acad. Sci. USA* **88**, 3106–3110 (1991).
60. Mehta, R. J. *et al*. Transmembrane-truncated alpha(V)beta(3) integrin retains high affinity for ligand binding: evidence for an 'inside-out' suppressor? *Biochem. J.* **330**(Pt 2), 861–869 (1998).
61. Takagi, J., Petre, B. M., Walz, T. & Springer, T. A. Global conformational rearrangements in integrin extracellular domains in outside-in and inside-out signaling. *Cell* **110**, 599–511 (2002).
62. Takagi, J., Strokovich, K., Springer, T. A. & Walz, T. Structure of integrin alpha(5)beta(1) in complex with fibronectin. *EMBO J.* **22**, 4607–4615 (2003).
63. Xiao, T., Takagi, J., Coller, B. S., Wang, J. H. & Springer, T. A. Structural basis for allostery in integrins and binding to fibrinogen-mimetic therapeutics. *Nature* **432**, 59–67 (2004).
64. Schurpf, T. & Springer, T. A. Regulation of integrin affinity on cell surfaces. *EMBO J.* **30**, 4712–4727 (2011).
65. Zhu, J., Zhu, J. & Springer, T. A. Complete integrin headpiece opening in eight steps. *J. Cell Biol.* **201**, 1053–1068 (2013).
66. Chen, X. *et al*. Requirement of open headpiece conformation for activation of leukocyte integrin alpha(X)beta(2). *Proc. Natl. Acad. Sci. USA* **107**, 14727–14732 (2010).
67. Takagi, J. & Springer, T. A. Integrin activation and structural rearrangement. *Immunol. Rev.* **186**, 141–163 (2002).
68. Su, Y. *et al*. Relating conformation to function in integrin alpha(5)beta(1). *Proc. Natl. Acad. Sci. USA* **113**, E3872–E3881 (2016).
69. Gohlke, H., Schmitz, B., Sommerfeld, A., Reinehr, R. & Häussinger, D. alpha(5)beta(1)-integrins are sensors for tauroursodeoxycholic acid in hepatocytes. *Hepatology* **57**, 1117–1129 (2013).
70. Schwarzbauer, J. E. & DeSimone, D. W. Fibronectins, their fibrillogenesis, and *in vivo* functions. *Cold Spring Harb. Perspect. Biol.* **3**, a005041 (2011).
71. Gottschalk, K. E., Adams, P. D., Brunger, A. T. & Kessler, H. Transmembrane signal transduction of the alpha(IIb)beta(3) integrin. *Protein Sci.* **11**, 1800–1812 (2002).
72. Müller, M. A. *et al*. Cytoplasmic salt bridge formation in integrin alpha(V)beta(3) stabilizes its inactive state affecting integrin-mediated cell biological effects. *Cell Signal.* **26**, 2493–2503 (2014).
73. Chavent, M., Duncan, A. L. & Sansom, M. S. Molecular dynamics simulations of membrane proteins and their interactions: from nanoscale to mesoscale. *Curr. Opin. Struct. Biol.* **40**, 8–16 (2016).
74. Kalli, A. C., Campbell, I. D. & Sansom, M. S. Multiscale simulations suggest a mechanism for integrin inside-out activation. *Proc. Natl. Acad. Sci. USA* **108**, 11890–11895 (2011).
75. Vararattanavech, A. *et al*. A transmembrane polar interaction is involved in the functional regulation of integrin alpha(L)beta(2). *J. Mol. Biol.* **398**, 569–583 (2010).
76. Jorgensen, W. L., Chandrasekhar, J., Madura, J. D., Impey, R. W. & Klein, M. L. Comparison of simple potential functions for simulating liquid water. *J. Chem. Phys.* **79**, 926–935 (1983).
77. Dickson, C. J. *et al*. Lipid14: The Amber Lipid Force Field. *J. Chem. Theory Comput.* **10**, 865–879 (2014).
78. Hornak, V. *et al*. Comparison of multiple Amber force fields and development of improved protein backbone parameters. *Proteins* **65**, 712–725 (2006).
79. Reinehr, R., Gohlke, H. & Sommerfeld, A. vom Dahl, S. & Häussinger, D. Activation of integrins by urea in perfused rat liver. *J. Biol. Chem.* **285**, 29348–29356 (2010).
80. Bopp, B. *et al*. Design and biological testing of peptidic dimerization inhibitors of human Hsp90 that target the C-terminal domain. *Biochim. Biophys. Acta* **1860**, 1043–1055 (2016).
81. Ciglia, E. *et al*. Resolving hot spots in the C-terminal dimerization domain that determine the stability of the molecular chaperone Hsp90. *PLOS one* **9**, e96031 (2014).
82. Metz, A. *et al*. Hot spots and transient pockets: predicting the determinants of small-molecule binding to a protein-protein interface. *J. Chem. Inf. Model* **52**, 120–133 (2012).
83. Perez, A., MacCallum, J. L., Brini, E., Simmerling, C. & Dill, K. A. Grid-based backbone correction to the ff12SB protein force field for implicit-solvent simulations. *J. Chem. Theory. Comput.* **11**, 4770–4779 (2015).
84. Maier, J. A. *et al*. ff14SB: Improving the Accuracy of Protein Side Chain and Backbone Parameters from ff99SB. *J. Chem. Theory Comput.* **11**, 3696–3713 (2015).
85. Forrest, L. R., Tang, C. L. & Honig, B. On the accuracy of homology modeling and sequence alignment methods applied to membrane proteins. *Biophys. J.* **91**, 508–517 (2006).
86. Xiong, J. P. *et al*. Crystal structure of the complete integrin alpha(V)beta(3) ectodomain plus an alpha/beta transmembrane fragment. *J. Cell. Biol.* **186**, 589–600 (2009).
87. Dong, X. *et al*. alpha(V)beta(3) integrin crystal structures and their functional implications. *Biochemistry* **51**, 8814–8828 (2012).
88. Minges, A. *et al*. Structural intermediates and directionality of the swiveling motion of Pyruvate Phosphate Dikinase. *Sci. Rep.* **7**, 45389 (2017).
89. Koller, A. N., Bozilovic, J., Engels, J. W. & Gohlke, H. Aromatic N versus aromatic F: bioisosterism discovered in RNA base pairing interactions leads to a novel class of universal base analogs. *Nucleic Acids Res.* **38**, 3133–3146 (2010).
90. Sengupta, D. & Marrink, S. J. Lipid-mediated interactions tune the association of glycophorin A helix and its disruptive mutants in membranes. *Phys. Chem. Chem. Phys.* **12**, 12987–12996 (2010).
91. Dellago, C., Bolhuis, P. G., Csajka, F. S. & Chandler, D. Transition path sampling and the calculation of rate constants. *J. Phys. Chem.* **108**, 1964–1977 (1998).
92. Eyring, H. The Activated Complex in Chemical Reactions. *J. Chem. Phys*. **3** (1935).
93. Poo, M. & Cone, R. A. Lateral diffusion of rhodopsin in the photoreceptor membrane. *Nature* **247**, 438–441 (1974).

94. Rhee, Y. M. & Pande, V. S. One-dimensional reaction coordinate and the corresponding potential of mean force from commitment probability distribution. *J. Phys. Chem. B* **109**, 6780–6786 (2005).
95. Kalli, A., Campbell, I. D. & Sansom, S. P. Multiscale simulations suggest a mechanism for integrin inside-out activation. *PNAS* **108**, 11890–11895 (2011).
96. Kim, C. *et al*. Basic amino-acid side chains regulate transmembrane integrin signalling. *Nature* **481**, 209–213 (2012).
97. Ferraris, G. M. *et al*. The interaction between uPAR and vitronectin triggers ligand-independent adhesion signalling by integrins. *EMBO J.* **33**, 2458–2472 (2014).
98. Bernstein, F. C., *et al*. The Protein Data Bank: A Computer-based Archival File For Macromolecular Structures. *J. Mol. Biol.* **112**, (1977).
99. Enswar, N. *et al*. Comparative Protein Structure Modeling using MODELLER. *Curr. Protoc. Bioinformatics* **15**, 5.6.1–5.6.30 (2006).
100. Jo, S., Kim, T., Lyer, V. G. & Lm, W. CHARMM-GUI: A Web-Based Graphical User Interface for CHARMM. *J. Comput. Chem.* **29**, 1860–1865 (2008).
101. Domański, J., Stansfeld, P., Sansom, M. S. P. & Beckstein, O. Lipidbook: A Public Repository for Force Field Parameters Used in Membrane Simulations. *J. Memb. Biol.* **236**, 255–258 (2010).
102. Jo, S., Kim, T. & Im, W. Automated Builder and Database of Protein/Membrane Complexes for Molecular Dynamics Simulations. *PLOS one* **2**, e880 (2007).
103. Lomize, M. A., Pogozheva, I. D., Joo, H., Mosberg, H. I. & Lomize, A. L. OPM database and PPM web server: resources for positioning of proteins in membranes. *Nucleic Acids Res.* **40**, D370–D376 (2012).
104. Cheatham, T. E., Miller, J. L., Fox, T., Darden, T. A. & Kollman, P. A. Molecular-Dynamics simulations on solvated biomolecular systems - the particle Mesh Ewald method leads to stable trajectories of DNA, RNA, and proteins. *J. Am. Chem. Soc.* **117**, 4193–4194 (1995).
105. Ryckaert, J. P., Ciccotti, G. & Berendsen, H. J. C. Numerical-Integration of Cartesian Equations of Motion of a System with Constraints - Molecular-Dynamics of N-Alkanes. *J. Comput. Phys.* **23**, 327–341 (1977).
106. Salomon-Ferrer, R., Gotz, A. W., Poole, D., Le Grand, S. & Walker, R. C. Routine microsecond molecular dynamics simulations with AMBER on GPUs. 2. Explicit solvent particle Mesh Ewald. *J. Chem. Theory Comput.* **9**, 3878–3888 (2013).
107. Berendsen, H. J. C., Postma, J. P. M., van Gunsteren, W. F., Dinola, A. & Haak, J. R. Molecular-Dynamics with Coupling to an External Bath. *J. Chem. Phys.* **81**, 3684–3690 (1984).
108. Torrie, G. M. & Valleau, J. P. Monte-Carlo Free-Energy Estimates Using Non-Boltzmann Sampling - Application to Subcritical Lennard-Jones Fluid. *Chem. Phys. Lett.* **28**, 578–581 (1974).
109. Torrie, G. M. & Valleau, J. P. Non-Physical Sampling Distributions in Monte-Carlo Free-Energy Estimation - Umbrella Sampling. *J. Comp. Phys.* **23**, 187–199 (1977).
110. Roe, D. R. & Cheatham, T. E. PTRAJ and CPPTRAJ: software for processing and analysis of molecular dynamics trajectory data. *J. Chem. Theory Comput.* **9**, 3084–3095 (2013).
111. Chodera, J. D. A Simple Method for Automated Equilibration Detection in Molecular Simulations. *J. Chem. Theory Comput.* **12**, 1799–1805 (2016).
112. Team, R. D. C. *R: a language and environment for statistical computing*, http://www.R-project.org (2010).
113. Shirts, M. R. & Chodera, J. D. Statistically optimal analysis of samples from multiple equilibrium states. *J. Chem. Phys.* **129**, 124105 (2008).

Acknowledgements
We are grateful for computational support and infrastructure provided by the "Zentrum für Informations- und Medientechnologie" (ZIM) at the Heinrich Heine University Düsseldorf and the computing time provided by the John von Neumann Institute for Computing (NIC) to H.G. on the supercomputer JURECA at Jülich Supercomputing Centre (JSC) (project IDs: 6710, 8348, 10307; user ID: HDD11). We are grateful to Stephan Schott Verdugo for the calculation of the thermodynamic quantities.

Author Contributions
H.G. designed research, G.P. performed research, G.P. and H.G. analyzed data and wrote the manuscript.

Additional Information
Supplementary information accompanies this paper at https://doi.org/10.1038/s41598-018-23778-5.

Competing Interests: The authors declare no competing interests.

Publisher's note: Springer Nature remains neutral with regard to jurisdictional claims in published maps and institutional affiliations.

Supporting Information

On the contributing role of the transmembrane domain for subunit-specific sensitivity of integrin activation

Giulia Pagani[1], Holger Gohlke[1,2*]

[1]Institute for Pharmaceutical and Medicinal Chemistry, Heinrich-Heine-Universität Düsseldorf, 40225 Düsseldorf, Germany

[2]John von Neumann Institute for Computing (NIC), Jülich Supercomputing Centre (JSC) & Institute for Complex Systems - Structural Biochemistry (ICS 6), Forschungszentrum Jülich GmbH, 52425 Jülich, Germany.

Table of Contents

Supplemental Tables

Table S1: OMC and IMC total number of contacts.

	Residue number α subunit	SimI[a]	SimII[a]	SimIII[a]	Mean ± SEM[b]
$\alpha_{IIb}\beta_3$ OMC	972	408	452	295	385 ± 5.19
	973	424	513	456	464 ± 3.88
	974	190	80	49	106 ± 4.97
	975	147	184	135	155 ± 2.92
	976	390	426	366	394 ± 3.17
	Total	1559[c]	1655[c]	1301[c]	**1505 ± 7.81**[d]
$\alpha_v\beta_3$ OMC	972	611	375	356	447 ± 6.88
	973	520	380	161	353 ± 7.77
	974	49	24	8	27 ± 2.62
	975	231	47	63	113 ± 5.83
	976	375	151	170	232 ± 6.43
	Total	1786[c]	977[c]	758[c]	**1174 ± 13.43**[d]
$\alpha_5\beta_1$ OMC	972	266	367	289	307 ± 4.20
	973	256	197	52	168 ± 5.91
	974	13	12	2	9 ± 1.42
	975	69	264	217	183 ± 5.82
	976	178	224	138	180 ± 3.79
	Total	782[c]	1064[c]	698[c]	**848 ± 7.99**[d]
$\alpha_{IIb}\beta_3$ IMC	992	731	583	45	453 ± 10.97
	993	932	1021	1011	988 ± 3.88
	Total	1663[c]	1604[c]	1056[c]	**1441 ± 10.56**[d]
$\alpha_v\beta_3$ IMC	992	586	662	751	666 ± 5.25
	993	1014	860	169	681 ± 12.25
	Total	1600[c]	1522[c]	920[c]	**1347 ± 11.14**[d]
$\alpha_5\beta_1$ IMC	992	640	641	37	439 ± 10.78
	993	840	972	962	925 ± 4.95
	Total	1480[c]	1613[c]	999[c]	**1364 ± 10.38**[d]

[a] Mean values calculated for each simulation per residue.
[b] Mean value and SEM (eq. 6 in the main text) calculated over three simulations per residue.
[c] Total number of contacts at the OMC/IMC calculated for each simulation.
[d] Mean value and SEM calculated over three simulations.

Table S2: RMSF of the $\alpha_{IIb}\beta_3$, $\alpha v\beta_3$, and $\alpha_5\beta_1$ integrin TMDs.

Residue number α-subunit	$\alpha_{IIb}\beta_3$[a]	$\alpha_v\beta_3$[a]	$\alpha_5\beta_1$[a]	Min value[b]
959	4.52	6.29	4.73	4.52
960	4.18	5.01	3.76	3.76
961	3.35	4.21	3.18	3.18
962	2.59	3.32	2.89	2.59
963	1.93	2.77	2.95	1.93
964	1.45	2.08	2.43	1.45
965	1.17	1.56	1.77	1.17
966	0.99	1.17	1.62	0.99
967	0.92	1.12	1.47	0.92
968	0.73	1.03	1.20	0.73
969	0.65	0.78	1.07	0.65
970	0.70	0.73	0.99	0.70
971	0.65	0.70	0.89	0.65
972	0.54	0.62	0.82	0.54
973	0.61	0.62	0.77	0.61
974	0.67	0.65	0.72	0.65
975	0.62	0.63	0.68	0.62
976	0.57	0.62	0.64	0.57
977	0.61	0.64	0.64	0.61
978	0.62	0.66	0.66	0.62
979	0.57	0.65	0.64	0.57
980	0.55	0.63	0.61	0.55
981	0.57	0.65	0.63	0.57
982	0.58	0.70	0.67	0.58
983	0.58	0.72	0.64	0.58
984	0.56	0.67	0.60	0.56
985	0.58	0.72	0.67	0.58
986	0.68	0.83	0.75	0.68
987	0.73	0.86	0.71	0.71
988	0.77	0.96	0.77	0.77
989	0.94	1.16	0.96	0.94
990	1.09	1.28	1.04	1.04
991	1.11	1.32	1.06	1.06
992	1.12	1.28	1.00	1.00
993	1.30	1.76	1.21	1.21
994	1.63	2.20	1.61	1.61
995	2.51	2.51	2.33	2.33
996	3.45	3.22	3.50	3.22
997	4.42	4.14	5.16	4.14
998	5.70	5.80	7.08	5.70
999	6.55	6.81	8.40	6.55

[a] Mean values, in Å, of the backbone atoms after a mass-weighted alignment onto the TM segment embedded in the membrane (residues P996-V1015 and D718-I747, for the α_{IIb}- and β_3-subunits, respectively) calculated over three MD simulations for $\alpha_{IIb}\beta_3$, $\alpha_v\beta_3$, and $\alpha_5\beta_1$ integrin.

[b] Minimal value for each row. Red color highlights when the minimal value corresponds to the value for $\alpha_{IIb}\beta_3$ integrin.

Table S2 continued.

Residue number β-subunit	$\alpha_{IIb}\beta_3$[a]	$\alpha_v\beta_3$[a]	$\alpha_5\beta_1$[a]	Min value[b]
684	13.17	13.77	11.09	11.09
685	12.41	13.01	10.26	10.26
686	10.30	11.23	8.76	8.76
687	8.31	9.64	7.34	7.34
688	6.31	8.19	5.59	5.59
689	4.70	6.18	4.28	4.28
690	3.20	5.13	3.23	3.20
691	2.00	3.66	2.51	2.00
692	1.50	2.15	2.09	1.50
693	0.93	1.42	1.58	0.93
694	0.85	1.08	1.30	0.85
695	0.87	0.99	1.26	0.87
696	0.72	0.88	1.15	0.72
697	0.55	0.70	0.87	0.55
698	0.61	0.66	0.83	0.61
699	0.62	0.71	0.83	0.62
700	0.53	0.64	0.79	0.53
701	0.53	0.62	0.76	0.53
703	0.67	0.78	0.80	0.67
704	0.63	0.76	0.70	0.63
705	0.62	0.71	0.70	0.62
706	0.67	0.70	0.75	0.67
707	0.68	0.68	0.78	0.68
708	0.63	0.68	0.74	0.63
709	0.61	0.70	0.70	0.61
710	0.61	0.64	0.70	0.61
711	0.64	0.62	0.74	0.62
712	0.63	0.79	0.79	0.63
713	0.69	0.87	0.85	0.69
714	0.81	0.88	0.89	0.81
715	0.85	1.01	0.91	0.85
716	1.02	1.21	1.09	1.02
717	1.39	1.35	1.27	1.27
718	1.63	1.59	1.43	1.43
719	1.87	1.90	1.72	1.72
720	2.43	2.20	2.25	2.20
721	3.12	2.45	2.61	2.45
722	3.19	2.72	2.70	2.70
723	3.26	3.34	2.94	2.94
724	4.03	3.76	3.55	3.55
725	4.75	4.46	3.64	3.64
726	5.49	5.35	3.67	3.67
727	6.57	6.73	4.31	4.31

[a] Mean values, in Å, of the backbone atoms after a mass-weighted alignment onto the TM segment embedded in the membrane (residues P996-V1015 and D718-I747, for the α_{IIb}- and β_3-subunits, respectively) calculated over three MD simulations for $\alpha_{IIb}\beta_3$, $\alpha_v\beta_3$, and $\alpha_5\beta_1$ integrin.

[b] Minimal value for each row. Red color highlights when the minimal value corresponds to the value for $\alpha_{IIb}\beta_3$ integrin.

Table S3: OMC and IMC distances.

	SimI[a]	SimII[a]	SimIII[a]	Mean± SEM[b]
$d_{OMC}\alpha_{IIb}\beta_3$	6.9 ± 0.01	6.9 ± 0.01	6.8 ± 0.02	6.8 ± 0.03
$d_{OMC}\alpha_v\beta_3$	7.2 ± 0.03	7.2 ± 0.05	7.1 ± 0.02	7.1 ± 0.06
$d_{OMC}\alpha_5\beta_1$	10.1 ± 0.3	7.6 ± 0.06	7.5 ± 0.02	8.4 ± 0.09
$d_{IMC}\alpha_{IIb}\beta_3$	7.5 ± 0.1	5.0 ± 0.2	7.1 ± 0.02	6.8 ± 0.5
$d_{IMC}\alpha_v\beta_3$	6.2 ± 0.3	6.7 ± 0.9	6.0 ± 0.1	6.3 ± 0.9
$d_{IMC}\alpha_5\beta_1$	6.0 ± 0.1	6.1 ± 0.1	5.7 ± 0.05	5.9 ± 0.2

[a] Mean values and SEM, in Å, calculated within each simulation.
[b] Mean value and SEM (eq. 5 in the main text), in Å, calculated over three simulations.

Table S4: Hydrogen bond between $K716_{N\varepsilon}$ and $F992_O$.

	SimI[a]	SimII[a]	SimIII[a]	Mean ± SEM[b]
$\alpha_{IIb}\beta_3$ TMD	74	40	0	38 ± 21.4
$\alpha_v\beta_3$ TMD	71	26	13	37 ± 17.6
$\alpha_5\beta_1$ TMD	4	61	11	25 ± 17.9

[a] Mean values, in %, calculated for each simulation.
[b] Mean value and SEM (eq. 6 in the main text), in %, calculated over three simulations.

Table S5: Salt bridge between $K716_{N\varepsilon}$ and the oxygens of phospholipid head groups.

	SimI[a]	SimII[a]	SimIII[a]	Mean ± SEM[b]
$\alpha_{IIb}\beta_3$ TMD	55	59	82	65 ± 8.4
$\alpha_v\beta_3$ TMD	21	45	49	38 ± 8.7
$\alpha_5\beta_1$ TMD	9	9	60	26 ± 17.0

[a] Mean values, in %, calculated for each simulation.
[b] Mean value and SEM (eq. 6 in the main text), in %, calculated over three simulations.

Table S6: Thermodynamic quantities for each TMD system.[a]

System	$\alpha_{IIb}\beta_3$ TMD	$\alpha_v\beta_3$ TMD	$\alpha_5\beta_1$ TMD
$\|\|\Omega\|\|$[a]	0.07	0.06	0.1
K_a[b]	140733.1	1360.9	75.2
K_X	2010.5	19.4	1.1
ΔG[c]	-4.5	-1.8	-0.04

[a] The integral in eq. 1 in the main text was evaluated at D = 14 Å.
[b] In radians.
[c] In Å^2.
[d] In kcal mol^{-1}.

Table S7: OMC and IMC distances across the umbrella sampling windows linked to free energy minima I – III.

Distance	Minima I			Mean ± SEM[b]
	w3[a]	w4[a]	w5[a]	
$d_{OMC\alpha IIb\beta 3}$	6.9 ± 0.01	7.5 ± 0.05	7.4 ± 0.07	7.3 ± 0.09
$d_{OMC\alpha v\beta 3}$	7.2 ± 0.05	7.5 ± 0.03	7.6 ± 0.07	7.4 ± 0.09
$d_{OMC\alpha 5\beta 1}$	7.3 ± 0.04	9.2 ± 0.05	7.6 ± 0.02	8.1 ± 0.09
$d_{IMC\alpha IIb\beta 3}$	4.2 ± 0.07	4.8 ± 0.03	6.2 ± 0.02	5.1 ± 0.08
$d_{IMC\alpha v\beta 3}$	4.3 ± 0.03	8.0 ± 0.3	5.6 ± 0.1	6.0 ± 0.3
$d_{IMC\alpha 5\beta 1}$	6.0 ± 0.5	6.8 ± 0.3	5.1 ± 0.01	6.0 ± 0.6

Distance	Minima II		Mean ± SEM[b]
	w8[a]	w9[a]	
$d_{OMC\alpha IIb\beta 3}$	10.9 ± 0.1	9.3 ± 0.08	10.1 ± 0.03
$d_{OMC\alpha v\beta 3}$	10.8 ± 0.07	9.9 ± 0.04	10.4 ± 0.09
$d_{OMC\alpha 5\beta 1}$	11.4 ± 0.1	10.4 ± 0.02	10.9 ± 0.1
$d_{IMC\alpha IIb\beta 3}$	6.1 ± 0.05	5.0 ± 0.07	5.6 ± 0.08
$d_{IMC\alpha v\beta 3}$	6.2 ± 0.1	6.2 ± 0.4	6.2 ± 0.4
$d_{IMC\alpha 5\beta 1}$	6.2 ± 0.2	9.7 ± 0.4	8.0 ± 0.4

Distance	Minima III		Mean ± SEM[b]
	w11[a]	w12[a]	
$d_{OMC\alpha IIb\beta 3}$	15.7 ± 0.05	13.1 ± 0.06	14.4 ± 0.08
$d_{OMC\alpha v\beta 3}$	13.7 ± 0.1	13.1 ± 0.1	13.4 ± 0.1
$d_{OMC\alpha 5\beta 1}$	13.4 ± 0.1	16.7 ± 0.2	15.0 ± 0.03
$d_{IMC\alpha IIb\beta 3}$	5.8 ± 0.3	7.9 ± 0.3	6.8 ± 0.4
$d_{IMC\alpha v\beta 3}$	8.0 ± 0.3	7.1 ± 0.08	7.5 ± 0.3
$d_{IMC\alpha 5\beta 1}$	6.1 ± 0.1	5.5 ± 0.05	5.8 ± 0.1

[a] Mean value and SEM, in Å, calculated within the respective umbrella sampling window.
[b] Mean value and SEM (eq. 5 in the main text), in Å, calculated over two resp. three umbrella sampling windows.

Table S8: $d_{COM\text{-}COM}$ distance computed from unbiased MD simulations of $\alpha_{IIb}\beta_3$, $\alpha_v\beta_3$, and $\alpha_5\beta_1$ integrin.

	SimI[a]	SimII[a]	SimIII[a]	Mean ± SEM[b]
$\alpha_{IIb}\beta_3$ TMD	9.2 ± 0.06	8.9 ± 0.07	10 ± 0.05	9.3 ± 0.1
$\alpha_v\beta_3$ TMD	9.5 ± 0.16	9.8 ± 0.23	9.5 ± 0.07	9.6 ± 0.3
$\alpha_5\beta_1$ TMD	9.4 ± 0.07	10.8 ± 0.27	10.4 ± 0.16	10.2 ± 0.3

[a] Mean values and SEM, in Å, calculated for each simulation.
[b] Mean value and SEM (eq. 5 in the main text), in Å, calculated over three simulations.

Supplemental Figures

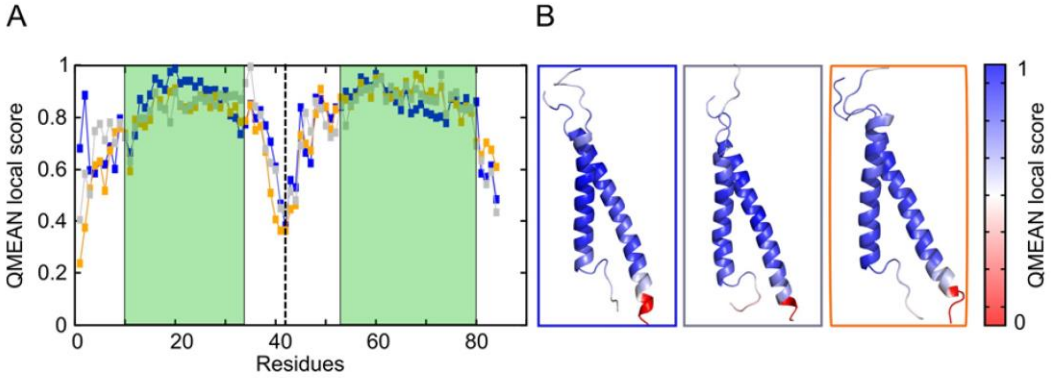

Fig S1: Assessment of the quality of TMD homology models.

The QMEANBrane version of the QMEAN scoring function implemented within the QMEAN server is used to evaluate the quality of homology models of TMDs of $\alpha_v\beta_3$ and $\alpha_5\beta_1$ integrin, respectively, in comparison to the NMR structure of $\alpha_{IIb}\beta_3$ (PDB ID: 2K9J) used as a template[1,2]. The local scores are provided in a range [0,1], with one being the optimal. (**A**) Local scores computed for the three structures (blue: $\alpha_{IIb}\beta_3$ TMD; gray: $\alpha_v\beta_3$ TMD; orange: $\alpha_5\beta_1$ TMD). Two green boxes are used to highlight the TM region (residues P996-V1015 and D718-I747 for the α_{IIb}- and β_3-subunits, respectively), and the black dashed line separates the α-subunit (left side) from the β-subunit (right side). (**B**) In each box (colored as in panel A), the QMEAN local scores are encoded in a color gradient from red to blue and mapped onto the integrin TMDs depicted in cartoon representation.

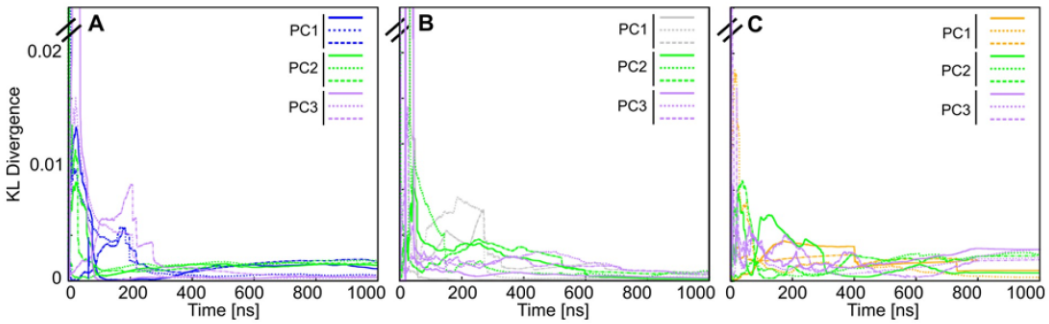

Fig S2: Convergence of internal motions in unbiased MD simulations.

Kullback-Leibler (KL) divergence[3] as a parameter to evaluate the convergence of the three independent MD simulations of (**A**) $\alpha_{IIb}\beta_3$ integrin TMD, (**B**) $\alpha_v\beta_3$ integrin TMD, and (**C**) $\alpha_5\beta_1$ integrin TMD. The KL divergence was computed for pair-wise comparisons of replicates of MD simulations in terms of histograms describing the projection of snapshots onto a given principal component (PC). The principal component analysis was performed on the residues embedded in the membrane (as shown in Fig. S1) after alignment onto their C_α atoms; color code of PC1 as in Fig. S1, PC2 colored in green and PC3 in purple in all plots.

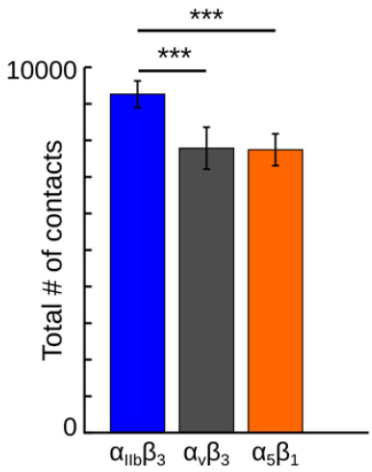

Fig S3: Total number of contacts calculated for $\alpha_{IIb}\beta_3$, $\alpha_v\beta_3$, and $\alpha_5\beta_1$ integrin.

Histograms of the total number of contacts ("native" and "non-native") between the α- and β-subunits averaged over three independent MD simulations for TMDs of $\alpha_{IIb}\beta_3$ (blue), $\alpha_v\beta_3$ (grey), and $\alpha_5\beta_1$ (orange) integrin, respectively. Error bars denote the SEM (eq. 6 in the main text). Stars denote a significant difference ($p < 0.0001$) between the TMDs of $\alpha_{IIb}\beta_3$ and $\alpha_v\beta_3$, and the TMDs of $\alpha_{IIb}\beta_3$ and $\alpha_5\beta_1$, respectively. A native contact was defined as a contact between two residues satisfying a distance cut-off of 7 Å in the first (reference) frame of a MD trajectory; a non-native contact is any contact whose distance satisfies the distance cut-off of 7 Å without being already found in the reference frame. This definition is according to ref.[4].

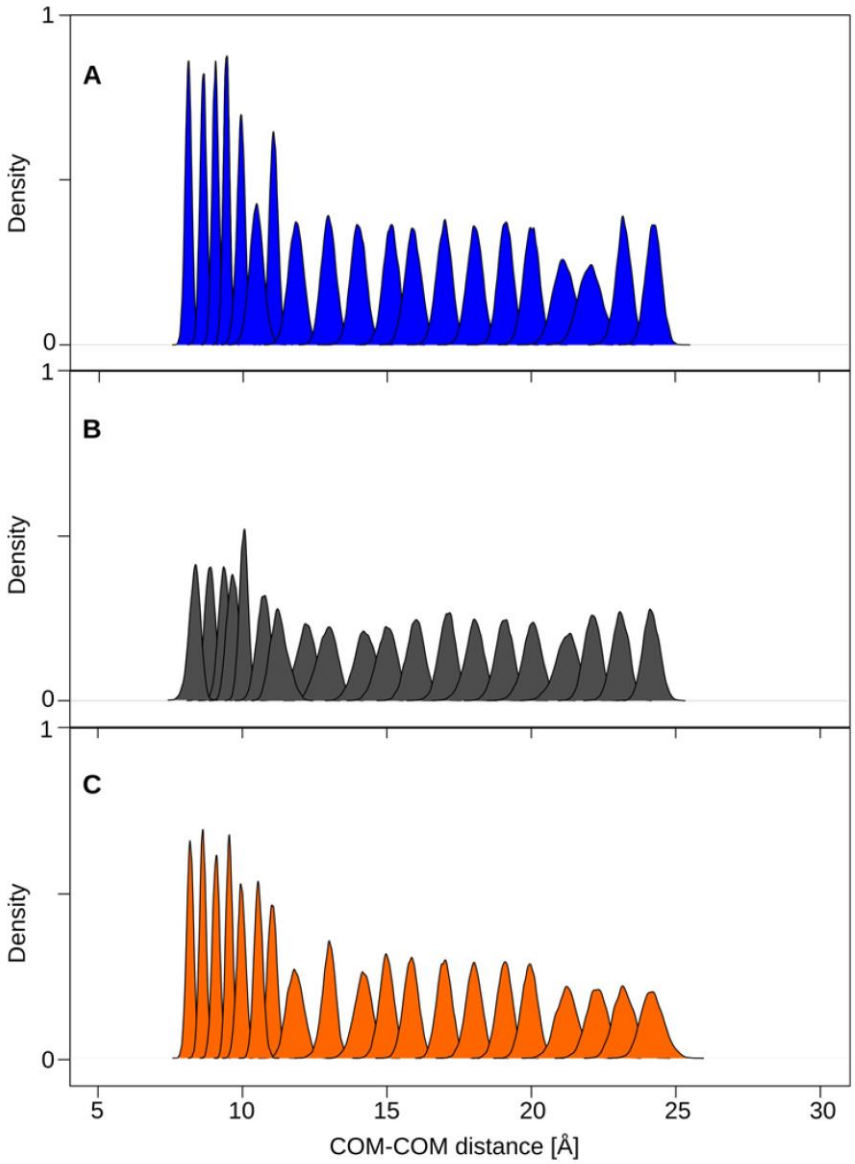

Fig S4: Overlap of umbrella sampling simulations of the association of TMDs of (A) $\alpha_{IIb}\beta_3$, (B) $\alpha_v\beta_3$, and (C) $\alpha_5\beta_1$ integrin.

Frequency distributions of values of the reaction coordinate obtained from umbrella sampling simulations.

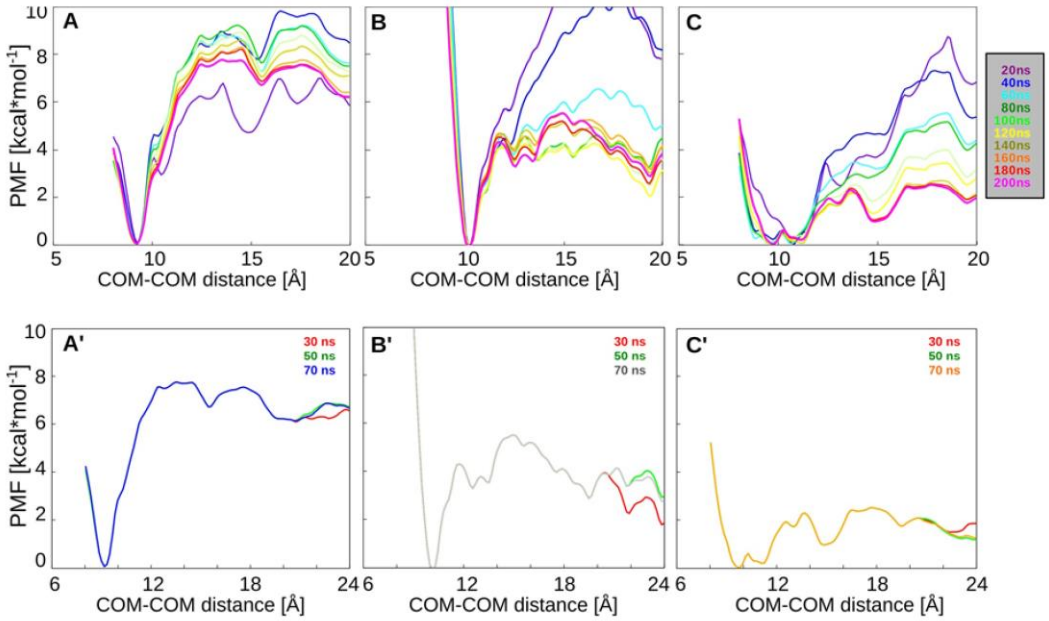

Fig S5: Convergence of the PMFs of the association of TMDs of (A, A') $\alpha_{IIb}\beta_3$, (B, B') $\alpha_v\beta_3$, and (C, C') $\alpha_5\beta_1$ integrin.

(**A-C**) Development over time of the PMF profiles computed for the association of the integrin's TMDs as indicated by the color scale at the right. In all cases, the PMF curves almost perfectly overlap after 160 ns of sampling time per umbrella sampling window. The reaction coordinate (distance between the centers of mass of the α- and β-subunits) ranges from 8 Å (fully associated state) to 20 Å (dissociated state). (**A'-C'**) Development over time of the PMF profiles computed for the full disassociation of the integrin's TMDs as indicated by the color scale inside each plot. In all cases, an almost perfect overlap is reached after 50 ns of sampling time per umbrella sampling window. The reaction coordinate considered ranges from 21 Å to 24 Å (fully dissociated state).

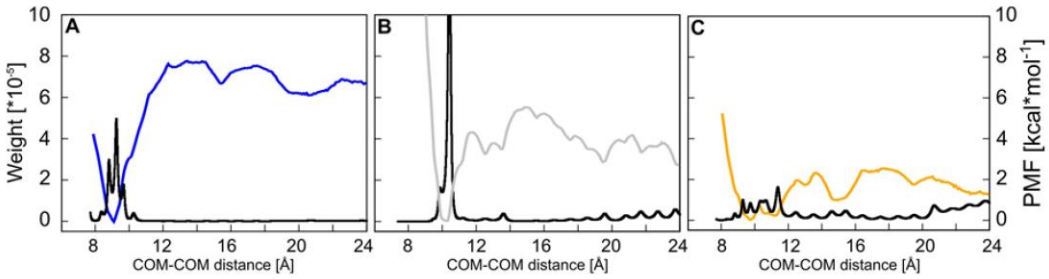

Fig S6: Reweighting of configurations obtained by umbrella sampling of the TMDs of (A) $\alpha_{IIb}\beta_3$, (B) $\alpha_v\beta_3$, and (C) $\alpha_5\beta_1$ integrin.

The curves colored black (left ordinate values) depict the weight w^t of a configuration t computed according to eqs. 7 and 8 from ref.[5], which is normalized by dividing it by the sum of all weights for each integrin system. Overlaid is the respective PMF profile (colored blue, grey, or orange; right ordinate values). The reweighting is performed considering the entire ensemble for each system between reaction coordinate values 8 to 24 Å.

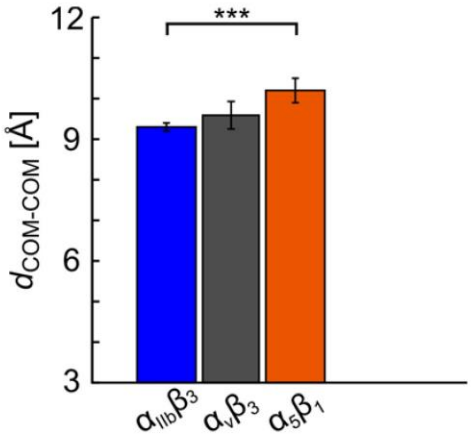

Fig S7: $d_{COM-COM}$ distance computed from unbiased MD simulations of $\alpha_{IIb}\beta_3$, $\alpha_v\beta_3$, and $\alpha_5\beta_1$ integrin.

Histograms of the distance $d_{COM-COM}$ (see main text for definition) averaged over three MD simulations. Values for $\alpha_{IIb}\beta_3$, $\alpha_v\beta_3$, and $\alpha_5\beta_1$ TMD are represented in blue, grey, and orange, respectively. Error bars denote the SEM (eq. 5 in the main text). Stars denote a significant difference ($p < 0.0001$) between the TMDs of $\alpha_{IIb}\beta_3$ and $\alpha_5\beta_1$.

Supplemental References

1 Lau, T. L., Kim, C., Ginsberg, M. H. & Ulmer, T. S. The structure of the integrin alpha(IIb)beta(3) transmembrane complex explains integrin transmembrane signalling. *EMBO J.* **28**, 1351-1361, (2009).

2 Studer, G., Biasini, M. & Schwede, T. Assessing the local structural quality of transmembrane protein models using statistical potentials (QMEANBrane). *Bioinformatics* **30**, I505-I511, (2014).

3 Galindo-Murillo, R., Roe, D. R. & Cheatham, T. E., 3rd. Convergence and reproducibility in molecular dynamics simulations of the DNA duplex d(GCACGAACGAACGAACGC). *Biochim. Biophys. Acta* **1850**, 1041-1058, (2015).

4 Case, D. A., et al. The Amber biomolecular simulation programs. *J. Comp. Chem.* **26**, 1668-1688, (2005).

5 Moradi, M., Enkavi, G. & Tajkhorshid, E. Atomic-level characterization of transport cycle thermodynamics in the glycerol-3-phosphate: phosphate antiporter. *Nat. Commun.* **6**, 8393; 10.1038/ncomms9393, (2015).

10 CURRICULUM VITAE

Personal Information

Name:	Giulia Pagani
Date of Birth:	30/12/1986 in Milan (Italy)

Education

11/2012- Present	PhD student and research assistant Group of Computational Pharmaceutical Chemistry and Molecular Bioinformatics at the Heinrich Heine University (Duesseldorf) Supervisor: Prof. Dr. Holger Gohlke
10/2009-07/2012	Master degree in Bioinformatics University of Milano-Bicocca
10/2005-07/2009	Bachelor degree in Pharmaceutical Biotechnology University of Milan
09/2000-06/2005	High School degree Liceo Classico "L. Berchet", Milan (Italy)

Work Experience and Internships

11/2012-Present	Teaching Assistant Heinrich Heine University (Duesseldorf) • Teaching and supervising Pharmacy Students within the "Inorganic chemistry" practical course
01/2006-06/2009	Part time Placement for Students University of Milan (Italy) • Collecting, saving and processing data • Collaboration for the use of IT equipment

Internship Abroad

10/2015-12/2015	Visiting PhD student CSRI-Indian Institute of Chemical Technology Ministry of Science & Technology, Government of India. Hyderabad (India) Supervisor: Dr. Sastry, G. Narahari

Advanced Training

Interdisciplinary Graduate and Research Academy (iGRAD), Duesseldorf:

- Good Scientific practice for doctoral researches
- Presenting Science I – comprehensive, competent and convincing
- Optimizing Writing Strategies for Publishing Research in English
- Career Planning in Business – How to shape your future

Modeling of Chemical and Biological (Re)Activity Winter School:

- Electronic structure theory

Additional Skills

Computational skills

Operating systems:	Linux, Microsoft Windows, Mac OS.
Programming languages:	Bash, Perl, Python (basic skills), HTML, R, SPSS
Molecular modeling:	AMBER molecular Simulations, Schroedinger Maestro, Modeller, Gaussian, VMD, Pymol

Language skills

Italian:	Native speaker
English:	Fluent in spoken and written
German:	Intermediate

Awards

08/2013-08/2016	Approved applications for computing resources on Supercomputer JUROPA and JURECA at JSC Juelich Supercomputing Centre (Juelich)

Publications

Donner, L., Fälker, K., Gremer, L., Klinker, S., Pagani, G., Ljungberg, L.U., Lothmann, K., Rizzi, F., Schaller, M., Gohlke, H., Willbold, D., Grenegard, M., Elvers, M.

Blood platelets contribute to the formation of amyloid deposits in cerebral vessels via integrin $\alpha_{IIb}\beta_3$ induced outside-in signaling and clusterin release. Sci. Signal. 2016, 9, RA52.

Pagani, G., Pereira, J. P. V., Stoldt, V. R., Beck, A., Scharf, R. E., Gohlke, H.
The human platelet antigen-1b variant of $\alpha_{IIb}\beta_3$ allosterically shifts the dynamic conformational equilibrium of the integrin toward the active state.
J. Biol. Chem. 2018, DOI: 10.1074/jbc.RA118.002149.

Pagani, G., Gohlke, H.
On the contributing role of the transmembrane domain for subunit-specific sensitivity of integrin activation.
Submitted 2018.

Poster presentation

Pagani G., Ventura Pereira J., Homeyer N., Stoldt V., Scharf R.E., Gohlke H.
THE PRO33 VARIANT OF PLATELET ALPHAIIB BETA3: allosteric changes resulting from a point mutation in the integrin ectodomain are associated with a prothrombotic receptor phenotype. ISTH 2015 Congress, Toronto, Canada, June 20 June 25, 2015.

11 REFERENCES

1. Durrant, J.D. and J.A. McCammon, *Molecular dynamics simulations and drug discovery.* BMC Biol., 2011. **9**: p. 71.
2. Mccammon, J.A., B.R. Gelin, and M. Karplus, *dynamics of folded proteins.* Nature, 1977. **267**(5612): p. 585-590.
3. Karplus, M. and J.A. McCammon, *Molecular dynamics simulations of biomolecules.* Nat. Struct. Biol., 2002. **9**(9): p. 646-52.
4. Dror, R.O., et al., *Exploring atomic resolution physiology on a femtosecond to millisecond timescale using molecular dynamics simulations.* J. Gen. Physiol., 2010. **135**(6): p. 555-62.
5. Borhani, D.W. and D.E. Shaw, *The future of molecular dynamics simulations in drug discovery.* J. Comput. Aided Mol. Des., 2012. **26**(1): p. 15-26.
6. Kim, C., F. Ye, and M.H. Ginsberg, *Regulation of integrin activation.* Annu. Rev. Cell. Dev. Biol., 2011. **27**: p. 321-45.
7. Hynes, R.O., *Integrins: a family of cell surface receptors.* Cell, 1987. **48**(4): p. 549-554.
8. Hynes, R.O., *Integrins: bidirectional, allosteric signaling machines.* Cell, 2002. **110**(6): p. 673-87.
9. Humphries, M.J., *Integrin structure.* Biochem. Soc. Trans., 2000. **28**(4): p. 311-339.
10. Bokel, C. and N.H. Brown, *Integrins in development: moving on, responding to, and sticking to the extracellular matrix.* Dev. Cell., 2002. **3**(3): p. 311-21.
11. Hynes, R.O., *The emergence of integrins: a personal and historical perspective.* Matrix Biol., 2004. **23**(6): p. 333-40.
12. Calderwood, D.A., *Integrin activation.* J. Cell. Sci., 2004. **117**(Pt 5): p. 657-666.
13. Campbell, I.D. and M.J. Humphries, *Integrin structure, activation, and interactions.* Cold Spring Harb. Perspect. Biol., 2011. **3**(3): p. a004994.
14. Giancotti, F.G. and E. Ruoslahti, *Integrin signaling.* Science, 1999. **285**(5430): p. 1028-1032.
15. Schwartz, M.A. and M.H. Ginsberg, *Networks and crosstalk: integrin signalling spreads.* Nat. Cell. Biol., 2002. **4**(4): p. E65-8.
16. Shattil, S.J., H. Kashiwagi, and N. Pampori, *Integrin signaling: the platelet paradigm.* Blood, 1998. **91**(8): p. 2645-57.
17. McDowall, A., et al., *A novel form of integrin dysfunction involving beta(1), beta(2), and beta(3) integrins.* J. Clin. Invest., 2003. **111**(1): p. 51-60.
18. Catricala, S., M. Torti, and G. Ricevuti, *Alzheimer disease and platelets: how's that relevant.* Immun. Ageing, 2012. **9**.
19. Lim, K.M., et al., *Inhibition of platelet aggregation by 1-methyl-4-phenyl pyridinium ion (MPP+) through ATP depletion: Evidence for the reduced platelet activities in Parkinson's disease.* Platelets, 2009. **20**(3): p. 163-70.
20. Asor, E. and D. Ben-Shachar, *Platelets: A possible glance into brain biological processes in schizophrenia.* World J. Psychiatry, 2012. **2**(6): p. 124-33.
21. Bledzka, K., S.S. Smyth, and E.F. Plow, *Integrin alpha(IIb)beta(3): from discovery to efficacious therapeutic target.* Circ. Res., 2013. **112**(8): p. 1189-200.
22. Srichai, M.B., Zent, R., , *Integrin structure and function*, in *Cell-Extracellular Matrix Interactions in Cancer*, R.Z.a.A. Pozzi, Editor. 2010.
23. Puklin-Faucher, E. and M.P. Sheetz, *The mechanical integrin cycle.* J. Cell Sci., 2009. **122**(2): p. 179-186.
24. Wolfenson, H., I. Lavelin, and B. Geiger, *Dynamic regulation of the structure and functions of integrin adhesions.* Dev. Cell., 2013. **24**(5): p. 447-58.
25. Xiong, J.P., et al., *Crystal structure of the extracellular segment of integrin alpha(v)beta(3)* Science, 2001. **294**(5541): p. 339-345.
26. Xiong, J.P., et al., *Crystal structure of the complete integrin alpha(V)beta(3) ectodomain plus an alpha/beta transmembrane fragment.* J. Cell. Biol., 2009. **186**(4): p. 589-600.
27. Donner, L., et al., *Platelets contribute to amyloid-beta aggregation in cerebral vessels through integrin alpha(IIb)beta(3)-induced outside-in signaling and clusterin release.* Sci. Signal., 2016. **9**(429): p. ra52.

28. Eng, E.T., et al., *Intact alpha(IIb)beta(3) integrin is extended after activation as measured by solution X-ray scattering and electron microscopy.* J. Biol. Chem., 2011. **286**(40): p. 35218-35226.
29. Bennett, J.S., *Structure and function of the platelet integrin alpha(IIb)beta(3).* J. Clin. Invest., 2005. **115**(12): p. 3363-9.
30. Bennett, J.S., B.W. Berger, and P.C. Billings, *The structure and function of platelet integrins.* J. Thromb. Haemost., 2009. **7 Suppl 1**: p. 200-5.
31. Tamkun, J.W., et al., *Structure of integrin, a glycoprotein involved in the transmembrane linkage between fibronectin and actin.* Cell, 1986. **46**(2): p. 271-282.
32. Springer, T.A. and M.L. Dustin, *Integrin inside-out signaling and the immunological synapse.* Curr. Opin. Cell. Biol., 2012. **24**(1): p. 107-15.
33. Schwartz, M.A., M.D. Schaller, and M.H. Ginsberg, *Integrins: emerging paradigms of signal transduction.* Annu. Rev. Cell Dev. Biol., 1995. **11**: p. 549-99.
34. Hynes, R.O., *Integrins - versatility, modulation, and signaling in cell-adhesion.* Cell, 1992. **69**(1): p. 11-25.
35. Johnson, M.S., et al., *Integrins during evolution: evolutionary trees and model organisms.* Biochim. Biophys. Acta, 2009. **1788**(4): p. 779-789.
36. Vinogradova, O., et al., *A structural mechanism of integrin alpha(IIb)beta(3) "inside-out" activation as regulated by its cytoplasmic face.* Cell, 2002. **110**(5): p. 587-97.
37. Plow, E.F., et al., *Ligand binding to integrins.* J. Biol. Chem., 2000. **275**(29): p. 21785-21788.
38. Müller, M.A., et al., *Cytoplasmic salt bridge formation in integrin alpha(V)beta(3) stabilizes its inactive state affecting integrin-mediated cell biological effects.* Cell Signal., 2014. **26**(11): p. 2493-2503.
39. Askari, J.A., et al., *Linking integrin conformation to function.* J. Cell Sci., 2009. **122**(Pt 2): p. 165-70.
40. Kim, M., C.V. Carman, and T.A. Springer, *Bidirectional transmembrane signaling by cytoplasmic domain separation in integrins.* Science, 2003. **301**(5640): p. 1720-1725.
41. Luo, B.H., T.A. Springer, and J. Takagi, *A specific interface between integrin transmembrane helices and affinity for ligand.* PLOS Biol., 2004. **2**(6): p. e153.
42. Hemler, M.E., *VLA proteins in the integrin family: structures, functions, and their role on leukocytes.* Annu. Rev. Immunol., 1990. **8**: p. 365-400.
43. Harburger, D.S. and D.A. Calderwood, *Integrin signalling at a glance.* J. Cell Sci., 2009. **122**(Pt 2): p. 159-63.
44. Arnaout, M.A., *Integrin structure: new twists and turns in dynamic cell adhesion.* Immunol. Rev., 2003. **186**(1): p. 125-140.
45. Takagi, J., et al., *Global conformational rearrangements in integrin extracellular domains in outside-in and inside-out signaling.* Cell, 2002. **110**(5): p. 599-11.
46. Arnaout, M.A., *Integrin structure: new twists and turns in dynamic cell adhesion.* Immunol. Rev., 2002. **186**: p. 125-40.
47. Kim, S.H., J. Turnbull, and S. Guimond, *Extracellular matrix and cell signalling: the dynamic cooperation of integrin, proteoglycan and growth factor receptor.* J. Endocrinol., 2011. **209**(2): p. 139-51.
48. Ginsberg, M.H., X. Du, and E.F. Plow, *Inside-out integrin signalling.* Curr. Opin. Cell Biol., 1992. **4**(5): p. 766-71.
49. Hughes, P.E. and M. Pfaff, *Integrin affinity modulation.* Trends Cell Biol., 1998. **8**(9): p. 359-64.
50. Das, M., et al., *Mechanisms of talin-dependent integrin signaling and crosstalk.* Biochim. Biophys, Acta-Biomem., 2014. **1838**(2): p. 579-588.
51. Hughes, A.L., *Evolution of the integrin alpha and beta protein families.* J. Mol. Evol., 2001. **52**(1): p. 63-72.
52. Burke, R.D., *Invertebrate integrins: structure, function, and evolution.* Int. Rev. Cytol., 1999. **191**: p. 257-84.
53. Santala, P. and J. Heino, *Regulation of integrin-type cell adhesion receptors by cytokines.* J. Biol. Chem., 1991. **266**(34): p. 23505-9.
54. Takada, Y., X. Ye, and S. Simon, *The integrins.* Genome Biol., 2007. **8**(5): p. 215.

55. Tarone, G., et al., *Integrin function and regulation in development.* Int. J. Dev. Biol., 2000. **44**(6): p. 725-731.
56. Barczyk, M., S. Carracedo, and D. Gullberg, *Integrins.* Cell Tissue Res., 2010. **339**(1): p. 269-280.
57. Humphries, J.D., A. Byron, and M.J. Humphries, *Integrin ligands at a glance.* J. Cell Sci., 2006. **119**(Pt 19): p. 3901-3.
58. Xiong, J.P., et al., *Integrins, cations and ligands: making the connection.* J. Thromb. Haemost., 2003. **1**(7): p. 1642-54.
59. Luo, B.H., C.V. Carman, and T.A. Springer, *Structural basis of integrin regulation and signaling.* Annu. Rev. Immunol., 2007. **25**: p. 619-47.
60. Xiong, J.P., et al., *Crystal structure of the extracellular segment of integrin alpha(v)beta(3) in complex with an Arg-Gly-Asp ligand.* Science, 2002. **296**(5565): p. 151-5.
61. Li, J. and T.A. Springer, *Integrin extension enables ultrasensitive regulation by cytoskeletal force.* Proc. Natl. Acad. Sci. U. S. A., 2017. **114**(18): p. 4685-4690.
62. Arnaout, M.A., B. Mahalingam, and J.P. Xiong, *Integrin structure, allostery, and bidirectional signaling.* Ann. Rev. Cell Dev. Biol., 2005. **21**: p. 381-410.
63. Nermut, M.V., et al., *Electron microscopy and structural model of human fibronectin receptor.* EMBO J., 1988. **7**(13): p. 4093-9.
64. Zhu, J., et al., *Structure of a complete integrin ectodomain in a physiologic resting state and activation and deactivation by applied forces.* Mol. Cell., 2008. **32**(6): p. 849-61.
65. Du, X., et al., *Long range propagation of conformational changes in integrin alpha(IIb)beta(3).* J. Biol. Chem., 1993. **268**(31): p. 23087-92.
66. Takagi, J., H.P. Erickson, and T.A. Springer, *C-terminal opening mimics 'inside-out' activation of integrin alpha(5)beta(1).* Nat. Struct. Biol., 2001. **8**(5): p. 412-416.
67. Arnaout, M.A., S.L. Goodman, and J.P. Xiong, *Structure and mechanics of integrin-based cell adhesion.* Curr. Opin. Cell. Biol., 2007. **19**(5): p. 495-507.
68. Luo, B.H., C.V. Carman, and T.A. Springer, *Structural basis of integrin regulation and signaling.* Annu. Rev. Immunol., 2007. **25**: p. 619-47.
69. Ma, Y.Q., J. Qin, and E.F. Plow, *Platelet integrin alpha(IIb)beta(3): activation mechanisms.* J. Thromb. Haemost., 2007. **5**(7): p. 1345-1352.
70. Xiao, T., et al., *Structural basis for allostery in integrins and binding to fibrinogen-mimetic therapeutics.* Nature, 2004. **432**(7013): p. 59-67.
71. Xie, C., et al., *Structure of an integrin with an alpha(I) domain, complement receptor type 4.* EMBO J. , 2010. **29**(3): p. 666-79.
72. Schurpf, T. and T.A. Springer, *Regulation of integrin affinity on cell surfaces.* EMBO J., 2011. **30**(23): p. 4712-27.
73. Litvinov, R.I., et al., *Functional and structural correlations of individual alphaIIbbeta3 molecules.* Blood, 2004. **104**(13): p. 3979-85.
74. Adair, B.D., et al., *Three-dimensional EM structure of the ectodomain of integrin alpha(V)beta(3) in a complex with fibronectin.* J. Cell. Biol., 2005. **168**(7): p. 1109-18.
75. Xiong, J.P., et al., *New insights into the structural basis of integrin activation.* Blood, 2003. **102**(4): p. 1155-1159.
76. Parise, L.V. and D.R. Phillips, *Platelet membrane glycoprotein IIb-IIIa complex incorporated into phospholipid vesicles. Preparation and morphology.* J. Biol. Chem., 1985. **260**(3): p. 1750-6.
77. Weisel, J.W., et al., *Examination of the platelet membrane glycoprotein IIb-IIIa complex and its interaction with fibrinogen and other ligands by electron microscopy.* J. Biol. Chem., 1992. **267**(23): p. 16637-43.
78. Erb, E.M., et al., *Integrin alpha(IIb)beta(3) reconstituted into lipid bilayers is nonclustered in its activated state but clusters after fibrinogen binding.* Biochemistry, 1997. **36**(24): p. 7395-402.
79. Nagae, M., et al., *Crystal structure of alpha(5)beta(1) integrin ectodomain: atomic details of the fibronectin receptor.* J. Cell Biol., 2012. **197**(1): p. 131-40.
80. Takagi, J., et al., *Structure of integrin alpha(5)beta(1) in complex with fibronectin.* EMBO J., 2003. **22**(18): p. 4607-15.

81. Chen, X., et al., *Requirement of open headpiece conformation for activation of leukocyte integrin alpha(X)beta(2).* Proc. Natl. Acad. Sci. U. S. A., 2010. **107**(33): p. 14727-32.
82. Zhu, J., J. Zhu, and T.A. Springer, *Complete integrin headpiece opening in eight steps.* J. Cell Biol., 2013. **201**(7): p. 1053-68.
83. Su, Y., et al., *Relating conformation to function in integrin alpha(5)beta(1).* Proc. Natl. Acad. Sci. U. S. A., 2016. **113**(27): p. E3872-E3881.
84. Li, J., et al., *Conformational equilibria and intrinsic affinities define integrin activation.* EMBO J., 2017: p. 629-645.
85. Springer, T.A., *Folding of the N-terminal, ligand-binding region of integrin alpha-subunits into a beta-propeller domain.* Proc. Natl. Acad. Sci. U. S. A., 1997. **94**(1): p. 65-72.
86. Springer, T.A., H. Jing, and J. Takagi, *A novel Ca2+ binding beta hairpin loop better resembles integrin sequence motifs than the EF hand.* Cell, 2000. **102**(3): p. 275-7.
87. Larson, R.S., et al., *Primary structure of the leukocyte function-associated molecule-1 alpha subunit: an integrin with an embedded domain defining a protein superfamily.* J. Cell. Biol., 1989. **108**(2): p. 703-12.
88. Mould, A.P., *Getting integrins into shape: recent insights into how integrin activity is regulated by conformational changes.* J. Cell Sci., 1996. **109**: p. 2613-8.
89. Takagi, J. and T.A. Springer, *Integrin activation and structural rearrangement.* Immunol. Rev., 2002. **186**: p. 141-63.
90. Lee, J.O., et al., *Crystal structure of the A domain from the alpha subunit of integrin CR3 (CD11b/CD18).* Cell, 1995. **80**(4): p. 631-8.
91. Lo Conte, L., C. Chothia, and J. Janin, *The atomic structure of protein-protein recognition sites.* J. Mol. Biol., 1999. **285**(5): p. 2177-98.
92. Bledzka, K., Pesho, M. M., Ma, Y. Q., Plow, E., *Integrin alpha(IIb)beta(3)*, in *PLATELETS*, A.D. Michelson, Editor. 2013, ELSEVIER.
93. Bork, P., et al., *Domains in plexins: links to integrins and transcription factors.* Trends Biochem. Sci., 1999. **24**(7): p. 261-263.
94. Xiong, J.P., et al., *A novel adaptation of the integrin PSI domain revealed from its crystal structure.* J. Biol. Chem., 2004. **279**(39): p. 40252-4.
95. Springer, T.A., J. Zhu, and T. Xiao, *Structural basis for distinctive recognition of fibrinogen gammaC peptide by the platelet integrin alpha(IIb)beta(3).* J. Cell. Biol., 2008. **182**(4): p. 791-800.
96. Shi, M.L., et al., *A structural hypothesis for the transition between bent and extended conformations of the leukocyte beta(2) integrins.* J. Biol. Chem., 2007. **282**(41): p. 30198-30206.
97. Zhu, J.H., et al., *Structure of a complete integrin ectodomain in a physiologic resting state and activation and deactivation by applied forces.* Mol. Cell., 2008. **32**(6): p. 849-861.
98. Beglova, N., et al., *Cysteine-rich module structure reveals a fulcrum for integrin rearrangement upon activation.* Nat. Struct. Biol., 2002. **9**(4): p. 282-7.
99. Downing, A.K., et al., *Solution structure of a pair of calcium-binding epidermal growth factor-like domains: implications for the Marfan syndrome and other genetic disorders.* Cell, 1996. **85**(4): p. 597-605.
100. Campbell, I.D. and M.J. Humphries, *Integrin Structure, Activation, and Interactions.* Cold Spring Harbor. Persp. Biol., 2011. **3**(3).
101. Adair, B.D. and M. Yeager, *Three-dimensional model of the human platelet integrin alpha(IIb)beta(3) based on electron cryomicroscopy and X-ray crystallography.* Proc. Natl. Acad. Sci. U. S. A., 2002. **99**(22): p. 14059-64.
102. Lau, T.L., V. Dua, and T.S. Ulmer, *Structure of the integrin alpha(IIb) transmembrane segment.* J. Biol. Chem., 2008. **283**(23): p. 16162-8.
103. Lau, T.L., et al., *Structure of the integrin beta(3) transmembrane segment in phospholipid bicelles and detergent micelles.* Biochemistry, 2008. **47**(13): p. 4008-16.
104. Lau, T.L., et al., *The structure of the integrin alpha(IIb)beta(3) transmembrane complex explains integrin transmembrane signalling.* EMBO J., 2009. **28**(9): p. 1351-61.
105. Ulmer, T.S., *Structural basis of transmembrane domain interactions in integrin signaling.* Cell Adh. Migr., 2010. **4**(2): p. 243-248.

106. Wegener, K.L. and I.D. Campbell, *Transmembrane and cytoplasmic domains in integrin activation and protein-protein interactions (Review).* Mol. Membr. Biol., 2008. **25**(5): p. 376-387.
107. Yang, J., et al., *Structure of an integrin alpha(IIb)beta(3) transmembrane-cytoplasmic heterocomplex provides insight into integrin activation.* Proc. Natl. Acad. Sci. U. S. A., 2009. **106**(42): p. 17729-17734.
108. Zhu, J., et al., *The structure of a receptor with two associating transmembrane domains on the cell surface: integrin alpha(IIb)beta(3).* Mol. Cell., 2009. **34**(2): p. 234-249.
109. Li, R., et al., *Activation of integrin alpha(IIb)beta(3) by modulation of transmembrane helix associations.* Science, 2003. **300**(5620): p. 795-798.
110. Parthasarathy, K., et al., *Transmembrane helices that form two opposite homodimeric interactions: an asparagine scan study of alpha(M) and beta(2) integrins.* Protein Sci., 2008. **17**(5): p. 930-8.
111. Luo, B.H., J. Takagi, and T.A. Springer, *Locking the beta(3) integrin I-like domain into high and low affinity conformations with disulfides.* J. Biol. Chem., 2004. **279**(11): p. 10215-21.
112. Partridge, A.W., et al., *Transmembrane domain helix packing stabilizes integrin alpha(IIb)beta(3) in the low affinity state.* J. Biol. Chem., 2005. **280**(8): p. 7294-300.
113. Kalli, A.C., I.D. Campbell, and M.S. Sansom, *Multiscale simulations suggest a mechanism for integrin inside-out activation.* Proc. Natl. Acad. Sci. U. S. A., 2011. **108**(29): p. 11890-5.
114. Gottschalk, K.E., *A coiled-coil structure of the alpha(IIb)beta(3) integrin transmembrane and cytoplasmic domains in its resting state.* Structure, 2005. **13**(5): p. 703-12.
115. Metcalf, D.G., et al., *Multiple approaches converge on the structure of the integrin alphaIIb/beta3 transmembrane heterodimer.* J. Mol. Biol., 2009. **392**(4): p. 1087-101.
116. Wang, W. and B.H. Luo, *Structural basis of integrin transmembrane activation.* J. Cell Biochem., 2010. **109**(3): p. 447-52.
117. Lau, T.L., et al., *The structure of the integrin αIIbβ3 transmembrane complex explains integrin transmembrane signalling.* EMBO J., 2009. **28**(9): p. 1351-61.
118. Schneider, D. and D.M. Engelman, *Involvement of transmembrane domain interactions in signal transduction by alpha/beta integrins.* J. Biol. Chem., 2004. **279**(11): p. 9840-9846.
119. Luo, B.H., et al., *Disrupting integrin transmembrane domain heterodimerization increases ligand binding affinity, not valency or clustering.* Proc. Natl. Acad. Sci. U. S. A., 2005. **102**(10): p. 3679-84.
120. Leung-Hagesteijn, C.Y., et al., *Cell attachment to extracellular matrix substrates is inhibited upon downregulation of expression of calreticulin, an intracellular integrin alpha-subunit-binding protein.* J. Cell Sci., 1994. **107 (Pt 3)**: p. 589-600.
121. Hughes, P.E., et al., *Breaking the integrin hinge. A defined structural constraint regulates integrin signaling.* J. Biol. Chem., 1996. **271**(12): p. 6571-6574.
122. O'Toole, T.E., et al., *Integrin cytoplasmic domains mediate inside-out signal transduction.* J. Cell. Biol., 1994. **124**(6): p. 1047-59.
123. Hughes, P.E., et al., *The conserved membrane-proximal region of an integrin cytoplasmic domain specifies ligand binding affinity.* J. Biol. Chem., 1995. **270**(21): p. 12411-7.
124. Weljie, A.M., P.M. Hwang, and H.J. Vogel, *Solution structures of the cytoplasmic tail complex from platelet integrin alpha(IIb) and beta(3) subunits.* Proc. Natl. Acad. Sci. U.S. A., 2002. **99**(9): p. 5878-5883.
125. Haas, T.A. and E.F. Plow, *Development of a structural model for the cytoplasmic domain of an integrin.* Protein Eng., 1997. **10**(12): p. 1395-405.
126. Vallar, L., et al., *Divalent cations differentially regulate integrin alpha(IIb) cytoplasmic tail binding to beta(3) and to calcium- and integrin-binding protein.* J. Biol. Chem., 1999. **274**(24): p. 17257-66.
127. Srichai MB, Z.R., *Integrin Structure and Function.* Cell-Extracellular Matrix Interactions in Cancer 2010: p. chapter 2.
128. Metcalf, D.G., et al., *NMR analysis of the alpha(IIb)beta(3) cytoplasmic interaction suggests a mechanism for integrin regulation.* Proc. Natl. Acad. Sci. U. S. A., 2010. **107**(52): p. 22481-22486.

129. Wegener, K.L., et al., *Structural basis of integrin activation by talin.* Cell, 2007. **128**(1): p. 171-82.
130. Anthis, N.J., et al., *The structure of an integrin/talin complex reveals the basis of inside-out signal transduction.* EMBO J., 2009. **28**(22): p. 3623-32.
131. Moser, M., et al., *The tail of integrins, talin, and kindlins.* Science, 2009. **324**(5929): p. 895-899.
132. Plow, E.F., et al., *Ligand binding to integrins.* J. Biol. Chem., 2000. **275**(29): p. 21785-8.
133. Michishita, M., V. Videm, and M.A. Arnaout, *A novel divalent cation-binding site in the A domain of the beta(2) integrin CR3 (CD11b/CD18) is essential for ligand binding.* Cell, 1993. **72**(6): p. 857-67.
134. Dickeson, S.K., J.J. Walsh, and S.A. Santoro, *Contributions of the I and EF hand domains to the divalent cation-dependent collagen binding activity of the alpha(2)beta(1) integrin.* J. Biol. Chem., 1997. **272**(12): p. 7661-7668.
135. Stanley, P., et al., *Integrin LFA-1 alpha subunit contains an ICAM-1 binding site in domains V and VI.* EMBO J., 1994. **13**(8): p. 1790-8.
136. Qu, A. and D.J. Leahy, *Crystal structure of the I-domain from the CD11a/CD18 (LFA-1, alpha(l)beta(2)) integrin.* Proc. Natl. Acad. Sci. U. S. A., 1995. **92**(22): p. 10277-81.
137. Emsley, J., et al., *Crystal structure of the I domain from integrin alpha(2)beta(1).* J. Biol. Chem., 1997. **272**(45): p. 28512-7.
138. Emsley, J., et al., *Structural basis of collagen recognition by integrin alpha(2)beta(1).* Cell, 2000. **101**(1): p. 47-56.
139. Nolte, M., et al., *Crystal structure of the alpha(1)beta(1) integrin I-domain: insights into integrin I-domain function.* FEBS Lett., 1999. **452**(3): p. 379-85.
140. Lee, J.O., et al., *Two conformations of the integrin A-domain (I-domain): a pathway for activation?* Structure, 1995. **3**(12): p. 1333-40.
141. Lam, S.C., et al., *Isolation and characterization of a platelet membrane protein related to the vitronectin receptor.* J. Biol. Chem., 1989. **264**(7): p. 3742-9.
142. Loftus, J.C., et al., *The amino-terminal one-third of alpha IIb defines the ligand recognition specificity of integrin alpha(IIb)beta(3).* J. Biol. Chem., 1996. **271**(4): p. 2033-9.
143. Honda, S., et al., *A two-amino acid insertion in the Cys146- Cys167 loop of the alpha(IIb) subunit is associated with a variant of Glanzmann thrombasthenia. Critical role of Asp163 in ligand binding.* J. Clin. Invest., 1998. **102**(6): p. 1183-92.
144. Kamata, T., et al., *Critical residues of integrin alpha(IIb) subunit for binding of alpha(IIb)beta(3) (glycoprotein IIb-IIIa) to fibrinogen and ligand-mimetic antibodies (PAC-1, OP-G2, and LJ-CP3).* J. Biol. Chem., 1996. **271**(31): p. 18610-5.
145. Arnaout, M.A., *Integrin structure: new twists and turns in dynamic cell adhesion. (vol 186, pg 125, 2002).* Immun. Rev., 2003. **193**(1): p. 146-146.
146. Xiong, J.P., et al., *Integrins, cations and ligands: making the connection.* J. Thromb. Haemost., 2003. **1**(7): p. 1642-1654.
147. Ruoslahti, E. and M.D. Pierschbacher, *New perspectives in cell adhesion: RGD and integrins.* Science, 1987. **238**(4826): p. 491-7.
148. Ruoslahti, E., *RGD and other recognition sequences for integrins.* Annu. Rev. Cell Dev. Biol., 1996. **12**: p. 697-715.
149. Ruoslahti, E., *Integrins.* J. Clin. Invest., 1991. **87**(1): p. 1-5.
150. Calvete, J.J., *Structures of integrin domains and concerted conformational changes in the bidirectional signaling mechanism of alpha(IIb)beta(3).* Exp. Biol. Med., 2004. **229**(8): p. 732-44.
151. Puklin-Faucher, E., et al., *How the headpiece hinge angle is opened: New insights into the dynamics of integrin activation.* J. Cell Biol., 2006. **175**: p. 349-360.
152. Raborn, J., W. Wang, and B.H. Luo, *Regulation of integrin alpha(IIb)beta(3) ligand binding and signaling by the metal ion binding sites in the beta(I) domain.* Biochemistry, 2011. **50**(12): p. 2084-91.
153. Shimaoka, M., J. Takagi, and T.A. Springer, *Conformational regulation of integrin structure and function.* Annu. Rev. Biophys. Biomol. Struct., 2002. **31**: p. 485-516.

154. Cai, T.Q. and S.D. Wright, *Energetics of leukocyte integrin activation.* J. Biol. Chem., 1995. **270**(24): p. 14358-65.
155. Cai, T.Q., et al., *Reversible inactivation of purified leukocyte integrin CR3 (CD11b/CD18, alpha(m)beta(2)) by removal of divalent cations from a cryptic site.* Cell Adhes. Commun., 1995. **3**(5): p. 399-406.
156. Hantgan, R.R., et al., *Effects of ligand-mimetic peptides Arg-Gly-Asp-X (X = Phe, Trp, Ser) on alpha(IIb)beta(3) integrin conformation and oligomerization.* Biochemistry, 1999. **38**(44): p. 14461-74.
157. Li, J. and T.A. Springer, *Energy landscape differences among integrins establish the framework for understanding activation.* J. Cell. Biol., 2018. **217**(1): p. 397-412.
158. Nishida, N., et al., *Activation of leukocyte beta(2) integrins by conversion from bent to extended conformations.* Immunity, 2006. **25**(4): p. 583-94.
159. Schurpf, T., et al., *The RGD finger of Del-1 is a unique structural feature critical for integrin binding.* FASEB J., 2012. **26**(8): p. 3412-20.
160. Calzada, M.J., M.V. Alvarez, and J. Gonzalez-Rodriguez, *Agonist-specific structural rearrangements of integrin alpha IIbbeta 3. Confirmation of the bent conformation in platelets at rest and after activation.* J. Biol. Chem., 2002. **277**(42): p. 39899-908.
161. Chigaev, A., et al., *FRET detection of cellular alpha(4)-integrin conformational activation.* Biophys J., 2003. **85**(6): p. 3951-62.
162. Chigaev, A., et al., *Regulation of cell adhesion by affinity and conformational unbending of alpha(4)beta(1) integrin.* J. Immunol., 2007. **178**(11): p. 6828-39.
163. Mould, A.P., *Getting integrins into shape: Recent insights into how integrin activity is regulated by conformational changes.* J. Cell Sci., 1996. **109**: p. 2613-2618.
164. Luo, B.H. and T.A. Springer, *Integrin structures and conformational signaling.* Curr. Opin. Cell. Biol., 2006. **18**(5): p. 579-86.
165. Frelinger, A.L., 3rd, et al., *Selective inhibition of integrin function by antibodies specific for ligand-occupied receptor conformers.* J. Biol. Chem., 1990. **265**(11): p. 6346-52.
166. Beglova, N., et al., *Cysteine-rich module structure reveals a fulcrum for integrin rearrangement upon activation.* Nat. Struct. Biol., 2002. **9**(4): p. 282-7.
167. Mould, A.P. and M.J. Humphries, *Regulation of integrin function through conformational complexity: not simply a knee-jerk reaction?* Curr. Opin. Cell Biol., 2004. **16**(5): p. 544-51.
168. Lefort, C.T., et al., *Outside-in signal transmission by conformational changes in integrin Mac-1.* J. Immunol., 2009. **183**(10): p. 6460-8.
169. Rocco, M., et al., *Integrin conformational regulation: uncoupling extension/tail separation from changes in the head region by a multiresolution approach.* Structure, 2008. **16**(6): p. 954-64.
170. Luo, B.H., T.A. Springer, and J. Takagi, *Stabilizing the open conformation of the integrin headpiece with a glycan wedge increases affinity for ligand.* Proc. Natl. Acad. Sci. U. S. A., 2003. **100**(5): p. 2403-8.
171. Mould, A.P., et al., *Conformational changes in the integrin beta A domain provide a mechanism for signal transduction via hybrid domain movement.* J. Biol. Chem., 2003. **278**(19): p. 17028-35.
172. Puklin-Faucher, E. and V. Vogel, *Integrin activation dynamics between the RGD-binding site and the headpiece hinge* J. Biol. Chem., 2009. **284**: p. 36557-36568.
173. Luo, B.H., et al., *Allosteric beta(1) integrin antibodies that stabilize the low affinity state by preventing the swing-out of the hybrid domain.* J. Biol. Chem., 2004. **279**(26): p. 27466-71.
174. Puklin-Faucher, E., et al., *How the headpiece hinge angle is opened: new insights into the dynamics of integrin activation.* J. Cell Biol., 2006. **175**(2): p. 349-360.
175. Gohlke, H., et al., *alpha(5)beta(1)-integrins are sensors for tauroursodeoxycholic acid in hepatocytes.* Hepatology, 2013. **57**(3): p. 1117-1129.
176. Xiong, J.P., et al., *An isoleucine-based allosteric switch controls affinity and shape shifting in integrin CD11b A-domain.* J. Biol. Chem., 2000. **275**(49): p. 38762-7.
177. Huth, J.R., et al., *NMR and mutagenesis evidence for an I domain allosteric site that regulates lymphocyte function-associated antigen 1 ligand binding.* Proc. Natl. Acad. Sci. U. S. A., 2000. **97**(10): p. 5231-6.

178. Kallen, J., et al., *Structural basis for LFA-1 inhibition upon lovastatin binding to the CD11a I-domain.* J. Mol. Biol., 1999. **292**(1): p. 1-9.
179. Honda, S., et al., *Topography ofligand-induced binding-sites, including a novel cation sensitive epitope (Ap5) at the amino-terminus, of the human integrin beta(3) subunit.* J. Biol. Chem., 1995. **270**(20): p. 11947-11954.
180. Xiong, J.P., et al., *A novel adaptation of the integrin PSI domain revealed from its crystal structure.* J Biol.l Chem., 2004. **279**(39): p. 40252-40254.
181. Shi, M.L., et al., *A structural hypothesis for the transition between bent and extended conformations of the leukocyte beta(2) integrins.* J. Biol. Chem., 2007. **282**(41): p. 30198-30206.
182. Dana, N., D.M. Fathallah, and M.A. Arnaout, *Expression of a soluble and functional form of the human beta(2) integrin CD11b/CD18.* Proc. Natl. Acad. Sci. U. S. A., 1991. **88**(8): p. 3106-10.
183. Peterson, J.A., et al., *A recombinant soluble form of the integrin alpha(IIb)beta(3) (GPIIb-IIIa) assumes an active, ligand-binding conformation and is recognized by GPIIb-IIIa-specific monoclonal, allo-, auto-, and drug-dependent platelet antibodies.* Blood, 1998. **92**(6): p. 2053-63.
184. Mehta, R.J., et al., *Transmembrane-truncated alpha(v)beta(3) integrin retains high affinity for ligand binding: evidence for an 'inside-out' suppressor?* Biochem. J., 1998. **330 (Pt 2)**: p. 861-9.
185. Gottschalk, K.E., et al., *Transmembrane signal transduction of the alpha(IIb)beta(3) integrin.* Protein Sci., 2002. **11**(7): p. 1800-12.
186. Bledzka, K., S.S. Smyth, and E.F. Plow, *Integrin alpha(IIb)beta(3) from discovery to efficacious therapeutic target.* Circulation Res., 2013. **112**(8): p. 1189-1200.
187. Lawler, J. and R.O. Hynes, *An integrin receptor on normal and thrombasthenic platelets that binds thrombospondin.* Blood, 1989. **74**(6): p. 2022-7.
188. Bennett, J.S., *Structure and function of the platelet integrin alpha(IIb)beta(3).* J. Clin. Invest., 2005. **115**(12): p. 3363-9.
189. Oki, T., et al., *Evidence that integrin alpha(IIb)beta(3)-dependent interaction of mast cells with fibrinogen exacerbates chronic inflammation.* J. Biol. Chem., 2009. **284**(45): p. 31463-72.
190. Oki, T., et al., *Integrin alphaIIbbeta3 induces the adhesion and activation of mast cells through interaction with fibrinogen.* J. Immunol., 2006. **176**(1): p. 52-60.
191. Trikha, M., et al., *Human prostate carcinoma cells express functional alphaIIb(beta)3 integrin.* Cancer Res., 1996. **56**(21): p. 5071-8.
192. Uzan, G., et al., *Tissue-specific expression of the platelet GPIIb gene.* J. Biol. Chem., 1991. **266**(14): p. 8932-9.
193. Beer, A.J. and M. Schwaiger, *Imaging of integrin alpha(V)beta(3) expression.* Cancer Metastasis Rev., 2008. **27**(4): p. 631-44.
194. Sheldrake, H.M. and L.H. Patterson, *Function and antagonism of beta(3) integrins in the development of cancer therapy.* Curr. Cancer Drug Targets, 2009. **9**(4): p. 519-40.
195. Cheresh, D.A., *Structural and biologic properties of integrin-mediated cell adhesion.* Clin. Lab. Med., 1992. **12**(2): p. 217-36.
196. Bray, P.F., *Integrin polymorphisms as risk factors for thrombosis.* J. Thromb. Haemost., 1999. **82**(2): p. 337-344.
197. Phillips, D.R., et al., *The platelet membrane glycoprotein IIb-IIIa complex.* Blood, 1988. **71**(4): p. 831-43.
198. Ma, Y.Q., J. Qin, and E.F. Plow, *Platelet integrin alpha(IIb)beta(3): activation mechanisms.* J. Thromb. Haemost., 2007. **5**(7): p. 1345-1352.
199. Bennett, J.S., *The molecular biology of platelet membrane proteins.* Semin. Hematol., 1990. **27**(2): p. 186-204.
200. Plow, E.F. and T. Byzova, *The biology of glycoprotein IIb-IIIa.* Coron. Artery Dis., 1999. **10**(8): p. 547-51.
201. Marguerie, G.A., E.F. Plow, and T.S. Edgington, *Human platelets possess an inducible and saturable receptor specific for fibrinogen.* J. Biol. Chem., 1979. **254**(12): p. 5357-63.

202. Plow, E.F., et al., *Related binding mechanisms for fibrinogen, fibronectin, von Willebrand factor, and thrombospondin on thrombin-stimulated human platelets.* Blood, 1985. **66**(3): p. 724-7.
203. Payrastre, B., et al., *The integrin alpha(IIb)beta(3) in human platelet signal transduction.* Biochem. Pharmacol., 2000. **60**(8): p. 1069-74.
204. Brakebusch, C., et al., *Genetic analysis of beta1 integrin function: confirmed, new and revised roles for a crucial family of cell adhesion molecules.* J. Cell Sci., 1997. **110 (Pt 23)**: p. 2895-904.
205. Cukierman, E., et al., *Taking cell-matrix adhesions to the third dimension.* Science, 2001. **294**(5547): p. 1708-12.
206. Hynes, R.O. and K.M. Yamada, *Fibronectins: multifunctional modular glycoproteins.* J. Cell Biol., 1982. **95**(2 Pt 1): p. 369-77.
207. Pierschbacher, M.D. and E. Ruoslahti, *Cell attachment activity of fibronectin can be duplicated by small synthetic fragments of the molecule.* Nature, 1984. **309**(5963): p. 30-3.
208. George, E.L., et al., *Defects in mesoderm, neural tube and vascular development in mouse embryos lacking fibronectin.* Development, 1993. **119**(4): p. 1079-91.
209. Yang, J.T., H. Rayburn, and R.O. Hynes, *Embryonic mesodermal defects in alpha 5 integrin-deficient mice.* Development, 1993. **119**(4): p. 1093-105.
210. Goh, K.L., J.T. Yang, and R.O. Hynes, *Mesodermal defects and cranial neural crest apoptosis in alpha(5) integrin-null embryos.* Development, 1997. **124**(21): p. 4309-19.
211. Adams, P.C., et al., *Role of platelets in atherogenesis: relevance to coronary arterial restenosis after angioplasty.* Cardiovasc. Clin., 1987. **18**(1): p. 49-71.
212. Nurden, A.T., *Platelets, inflammation and tissue regeneration.* J. Thromb. Haemost., 2011. **105 Suppl 1**: p. S13-33.
213. Gawaz, M., H. Langer, and A.E. May, *Platelets in inflammation and atherogenesis.* J. Clin. Invest., 2005. **115**(12): p. 3378-84.
214. Ruggeri, Z.M., *Platelets in atherothrombosis.* Nat. Med., 2002. **8**(11): p. 1227-34.
215. Ross, R., *Rous-Whipple Award Lecture. Atherosclerosis: a defense mechanism gone awry.* Am. J. Pathol., 1993. **143**(4): p. 987-1002.
216. Laudanna, C., et al., *Rapid leukocyte integrin activation by chemokines.* Immunol. Rev., 2002. **186**: p. 37-46.
217. Hogg, N., et al., *Mechanisms contributing to the activity of integrins on leukocytes.* Immunol. Rev., 2002. **186**: p. 164-71.
218. Serpell, L.C., *Alzheimer's amyloid fibrils: structure and assembly.* Biochim. Biophys. Acta 2000. **1502**(1): p. 16-30.
219. Selkoe, D.J., *The Molecular Pathology of Alzheimers-Disease.* Neuron., 1991. **6**(4): p. 487-498.
220. Lorenzo, A. and B.A. Yankner, *Beta-Amyloid Neurotoxicity Requires Fibril Formation and Is Inhibited by Congo Red.* Proc. Natl. Acad. Sci. U. S. A., 1994. **91**(25): p. 12243-12247.
221. Langer, H.F., et al., *Capture of endothelial progenitor cells by a bispecific protein/monoclonal antibody molecule induces reendothelialization of vascular lesions.* J. Mol. Med., 2010. **88**(7): p. 687-99.
222. Jang, H., et al., *New structures help the modeling of toxic amyloidbeta ion channels.* Trends Biochem. Sci., 2008. **33**(2): p. 91-100.
223. Rambaran, R.N. and L.C. Serpell, *Amyloid fibrils Abnormal protein assembly.* Prion, 2008. **2**(3): p. 112-117.
224. Murphy, M.P. and H. LeVine, *Alzheimer's Disease and the Amyloid-beta Peptide.* J. Alzheimers Disease, 2010. **19**(1): p. 311-323.
225. Donner, L., et al., *Platelets contribute to amyloid-beta aggregation in cerebral vessels through integrin alpha(IIb)beta(3)-induced outside-in signaling and clusterin release.* Science Signal., 2016. **9**(429).
226. Deshpande, A., et al., *Different conformations of amyloid beta induce neurotoxicity by distinct mechanisms in human cortical neurons.* J. Neurosci., 2006. **26**(22): p. 6011-8.
227. Thal, D.R., et al., *Cerebral amyloid angiopathy and its relationship to Alzheimer's disease.* Acta Neuropathologica, 2008. **115**(6): p. 599-609.

228. Tian, J., J. Shi, and D.M.A. Mann, *Cerebral amyloid angiopathy and dementia.* Panminerva Medica, 2004. **46**(4): p. 253-264.
229. Luchsinger, J.A., et al., *Aggregation of vascular risk factors and risk of incident Alzheimer disease.* Neurology, 2005. **65**(4): p. 545-51.
230. Bush, A.I., et al., *The amyloid precursor protein of Alzheimer's disease is released by human platelets.* J. Biol. Chem., 1990. **265**(26): p. 15977-83.
231. Roher, A.E., et al., *Amyloid beta peptides in human plasma and tissues and their significance for Alzheimer's disease.* Alzheimers Dement, 2009. **5**(1): p. 18-29.
232. Deane, R. and B.V. Zlokovic, *Role of the blood-brain barrier in the pathogenesis of Alzheimer's disease.* Curr. Alzheimer Res., 2007. **4**(2): p. 191-7.
233. Ruoslahti, E. and M.D. Pierschbacher, *New perspectives in cell-adhesion - Rgd and integrins.* Science, 1987. **238**(4826): p. 491-497.
234. Ghiso, J., et al., *A 109-amino-acid C-terminal fragment of alzheimers-disease amyloid precursor protein contains a sequence, -rhds-, that promotes cell-adhesion.* Biochem. J., 1992. **288**: p. 1053-1059.
235. McFadyen, J. and K. Peter, *Forget about thrombosis: Platelets and Alzheimer's disease, yet another sticky situation.* Science Signal., 2016. **9**(429).
236. Gregg, D. and P.J. Goldschmidt-Clermont, *Cardiology patient page. Platelets and cardiovascular disease.* Circulation, 2003. **108**(13): p. e88-90.
237. Newman, P.J., R.S. Derbes, and R.H. Aster, *The human platelet alloantigens, PlA1 and PlA2, are associated with a leucine33/proline33 amino acid polymorphism in membrane glycoprotein IIIa, and are distinguishable by DNA typing.* J. Clin. Invest., 1989. **83**(5): p. 1778-81.
238. El Khattouti, A., Stoldt, R.V., Scharf, R.E., *The HPA-1b (Pro33) isoform of platelet integrin alpha(IIb)beta(3) is a prothrombotic variant: characterization by fluorescence resonance energy transfer.* Blood, 2010. **116**(21): p. 2028.
239. Weiss, E.J., et al., *A polymorphism of a platelet glycoprotein receptor as an inherited risk factor for coronary thrombosis.* N. Engl. J. Med., 1996. **334**(17): p. 1090-1094.
240. Zotz, R.B., et al., *Association of polymorphisms of platelet membrane integrins alpha(IIb)beta(3) (HPA-1b/Pl) and alpha(2)beta(1) (alpha807TT) with premature myocardial infarction.* J. Thromb. Haemost., 2005. **3**(7): p. 1522-9.
241. Zotz, R.B., et al., *Polymorphism of platelet membrane glycoprotein IIIa: Human platelet antigen 1b (HPA-1b/PIA2) is an inherited risk factor for premature myocardial infarction in coronary artery disease.* J. Thromb. Haemost., 1998. **79**(4): p. 731-735.
242. Corral, J., et al., *HPA-1 genotype in arterial thrombosis--role of HPA-1b polymorphism in platelet function.* Blood Coagul. Fibrinolysis, 1997. **8**(5): p. 284-90.
243. Stoldt, V.R., et al., *Evaluation of platelet thrombus formation under flow.* Blood, 2005. **106**(11): p. 70B-71B.
244. Guzzo, A.V., *The influence of amino-acid sequence on protein structure.* Biophys J., 1965. **5**(6): p. 809-22.
245. Zang, Q. and T.A. Springer, *Amino acid residues in the PSI domain and cysteine-rich repeats of the integrin beta(2) subunit that restrain activation of the integrin alpha(x)beta(2).* J. Biol. Chem., 2001. **276**(10): p. 6922-9.
246. Bazzoni, G., et al., *Divalent cations and ligands induce conformational changes that are highly divergent among beta(1) integrins.* J. Biol. Chem., 1998. **273**(12): p. 6670-8.
247. Kamata, T., et al., *Membrane-proximal alpha/beta stalk interactions differentially regulate integrin activation.* J. Biol. Chem., 2005. **280**(26): p. 24775-24783.
248. Schmidt, T., et al., *Annular anionic lipids stabilize the integrin alpha(IIb)beta(3) transmembrane complex.* J. Biol. Chem., 2015. **290**(13): p. 8283-93.
249. Adcock, S.A. and J.A. McCammon, *Molecular dynamics: survey of methods for simulating the activity of proteins.* Chem. Rev., 2006. **106**(5): p. 1589-615.
250. Stansfeld, P.J. and M.S. Sansom, *Molecular simulation approaches to membrane proteins.* Structure, 2011. **19**(11): p. 1562-72.
251. Grossfield, A., S.E. Feller, and M.C. Pitman, *Convergence of molecular dynamics simulations of membrane proteins.* Proteins, 2007. **67**(1): p. 31-40.

252. Sanbonmatsu, K.Y. and C.S. Tung, *High performance computing in biology: multimillion atom simulations of nanoscale systems.* J. Struct. Biol., 2007. **157**(3): p. 470-80.
253. Villa, E., et al., *Ribosome-induced changes in elongation factor Tu conformation control GTP hydrolysis.* Proc. Natl. Acad. Sci. U. S. A., 2009. **106**(4): p. 1063-8.
254. Zink, M. and H. Grubmuller, *Mechanical properties of the icosahedral shell of southern bean mosaic virus: a molecular dynamics study.* Biophys. J., 2009. **96**(4): p. 1350-63.
255. Freddolino, P.L., et al., *Molecular dynamics simulations of the complete satellite tobacco mosaic virus.* Structure, 2006. **14**(3): p. 437-49.
256. Shaw, D.E., *Anton: A specialized machine for millisecond-scale molecular dynamics simulations of proteins.* Abstracts of Papers of the American Chemical Society, 2009. **238**.
257. Provasi, D., et al., *Talin-driven inside-out activation mechanism of platelet alpha(IIb)beta(3) integrin probed by multimicrosecond, all-atom molecular dynamics simulations.* Proteins: Struct., Funct., Bioinf., 2014. **82**(12): p. 3231-3240.
258. Grossfield, A., et al., *Internal hydration increases during activation of the G-protein-coupled receptor rhodopsin.* J. Mol. Biol., 2008. **381**(2): p. 478-86.
259. Dror, R.O., et al., *Identification of two distinct inactive conformations of the beta2-adrenergic receptor reconciles structural and biochemical observations.* Proc. Natl. Acad. Sci. U. S. A., 2009. **106**(12): p. 4689-94.
260. Reinehr, R., et al., *Activation of integrins by urea in perfused rat liver.* J. Biol. Chem., 2010. **285**(38): p. 29348-29356.
261. Marrink, S.J. and D.P. Tieleman, *Perspective on the Martini model.* Chem. Soc. Rev., 2013. **42**(16): p. 6801-22.
262. Schulten, K., *Manipulating proteins by steered molecular dynamics.* J. Mol. Graph. Mod., 1998. **16**: p. 286.
263. Chavent, M., A.L. Duncan, and M.S. Sansom, *Molecular dynamics simulations of membrane proteins and their interactions: from nanoscale to mesoscale.* Curr. Opin. Struct. Biol., 2016. **40**: p. 8-16.
264. Kalli, A., Campbell, I.D., Sansom, S.P., *Multiscale simulations suggest a mechanism for integrin inside-out activation.* PNAS, 2011. **108**: p. 11890–11895.
265. Kalli, A.C., et al., *The structure of the talin/integrin complex at a lipid bilayer: an NMR and MD simulation study.* Structure, 2010. **18**(10): p. 1280-8.
266. Chen, W., et al., *Molecular dynamics simulations of forced unbending of integrin alpha(v)beta(3).* PLOS Comput. Biol., 2011. **7**(2): p. e1001086.
267. Mori, T., et al., *Molecular dynamics simulations of biological membranes and membrane proteins using enhanced conformational sampling algorithms.* Biochim. Biophys. Acta, 2016. **1858**(7 Pt B): p. 1635-51.
268. Lee, E.H., et al., *Discovery Through the Computational Microscope.* Structure, 2009. **17**(10): p. 1295-1306.
269. Sawle, L. and K. Ghosh, *Convergence of Molecular Dynamics Simulation of Protein Native States: Feasibility vs Self-Consistency Dilemma.* J. Chem. Theory Comput., 2016. **12**(2): p. 861-9.
270. Cheatham, T.E., et al., *Molecular-Dynamics simulations on solvated biomolecular systems - the particle Mesh Ewald method leads to stable trajectories of DNA, RNA, and proteins.* J. Am. Chem. Soc., 1995. **117**(14): p. 4193-4194.
271. Galindo-Murillo, R., D.R. Roe, and T.E. Cheatham, 3rd, *Convergence and reproducibility in molecular dynamics simulations of the DNA duplex d(GCACGAACGAACGAACGC).* Biochim. Biophys. Acta, 2015. **1850**(5): p. 1041-58.
272. Kullback, S. and R.A. Leibler, *On Information and Sufficiency.* Annals of Mathematical Statistics, 1951. **22**(1): p. 142-143.
273. Amadei, A., A.B.M. Linssen, and H.J.C. Berendsen, *Essential dynamics of proteins.* Proteins-Structure Function and Genetics, 1993. **17**(4): p. 412-425.
274. Chodera, J.D., *A simple method for automated equilibration detection in molecular simulations.* J. Chem. Theory Comput., 2016. **12**(4): p. 1799-1805.
275. Shirts, M.R. and J.D. Chodera, *Statistically optimal analysis of samples from multiple equilibrium states.* J. Chem. Phys., 2008. **129**(12): p. 124105.

276. Anandakrishnan, R., et al., *Speed of conformational change: comparing explicit and implicit solvent molecular dynamics simulations.* Biophys. J., 2015. **108**(5): p. 1153-64.
277. Onufriev, A., *Continuum electrostatics solvent modeling with the generalized Born model* in *Modeling solvent environments* Wiley, Editor. 2010. p. 127-165.
278. Schlick, T., *Molecular modeling and simulation*, in *An interdisciplinary guide*, Wiley, Editor. 2002.
279. Cramer, C.J. and D.G. Truhlar, *Implicit solvation models: equilibria,structure, spectra, and synamics.* Chem. Rev., 1999. **99**(8): p. 2161-2200.
280. Tsui, V., Case, D., *Molecular dynamics simulations of nucleic acids with a generalized born solvation mode.* J. Am. Chem. Soc., 2000. **122**: p. 2489-2498.
281. Amaro, R.E., et al., *Characterizing loop dynamics and ligand recognition in human- and avian-type influenza neuraminidases via generalized born molecular dynamics and end-point free energy calculations.* J. Am. Chem. Soc., 2009. **131**(13): p. 4702-9.
282. Feig, M., *Kinetics from implicit solvent simulations of biomolecules as a function of viscosity.* J. Chem. Theory. Comput., 2007. **3**(5): p. 1734-48.
283. Zagrovic, B. and V. Pande, *Solvent viscosity dependence of the folding rate of a small protein: distributed computing study.* J. Comput. Chem., 2003. **24**(12): p. 1432-6.
284. Amaro, R.E., et al., *Mechanism of 150-cavity formation in influenza neuraminidase.* Nat. Commun., 2011. **2**: p. 388.
285. Jorgensen, W.L., et al., *Comparison of simple potential functions for simulating liquid water.* J. Chem. Phys., 1983. **79**: p. 926-935.
286. Rosenbaum, D.M., S.G. Rasmussen, and B.K. Kobilka, *The structure and function of G-protein-coupled receptors.* Nature, 2009. **459**(7245): p. 356-63.
287. Shenoy, S.K. and R.J. Lefkowitz, *beta-arrestin-mediated receptor trafficking and signal transduction.* Trends Pharmacol. Sci., 2011. **32**(9): p. 521-33.
288. Head, B.P., H.H. Patel, and P.A. Insel, *Interaction of membrane/lipid rafts with the cytoskeleton: impact on signaling and function: membrane/lipid rafts, mediators of cytoskeletal arrangement and cell signaling.* Biochim. Biophys. Acta, 2014. **1838**(2): p. 532-45.
289. MacCallum, J.L., W.F.D. Bennett, and D.P. Tieleman, *Distribution of amino acids in a lipid bilayer from computer simulations.* Biophys. J., 2008. **94**(9): p. 3393-3404.
290. Kandt C, A.W., Tieleman DP, *Setting up and running molecular dynamics simulations of membrane proteins.* Methods, 2006. **41**: p. 457-488.
291. Woolf, T.B. and B. Roux, *Molecular dynamics simulation of the gramicidin channel in a phospholipid-bilayer.* PNAS, 1994. **91**(24): p. 11631-11635.
292. Marrink, S.J. and H.J.C. Berendsen, *Simulation of water transport through a lipid-membrane.* J. Phys. Chem., 1994. **98**(15): p. 4155-4168.
293. Feller, S.E., R.M. Venable, and R.W. Pastor, *Computer simulation of a DPPC phospholipid bilayer: Structural changes as a function of molecular surface area.* Langmuir, 1997. **13**(24): p. 6555-6561.
294. Moore, P.B., C.F. Lopez, and M.L. Klein, *Dynamical properties of a hydrated lipid bilayer from a multinanosecond molecular dynamics simulation.* Biophys. J., 2001. **81**(5): p. 2484-2494.
295. Dickson, C.J., et al., *GAFFlipid: a General Amber Force Field for the accurate molecular dynamics simulation of phospholipid.* Soft Matter, 2012. **8**: p. 9617-9627.
296. Skievik AA, M.B., Walker RC, Teigen K, *LIPID11: a molecular framework for lipid simulation using Amber.* J. Phys. Chem., 2012. **116**: p. 11124-11136.
297. Rosso, L. and I.R. Gould, *Structure and dynamics of phospholipid bilayers using recently developed general all-atom force fields.* J. Comput. Chem., 2008. **29**(1): p. 24-37.
298. Woolf, T.B. and B. Roux, *Structure, energetics, and dynamics of lipid-protein interactions: A molecular dynamics study of the gramicidin A channel in a DMPC bilayer.* Proteins-Structure Function and Genetics, 1996. **24**(1): p. 92-114.
299. Shen, L.Y., D. Bassolino, and T. Stouch, *Transmembrane helix structure, dynamics, and interactions: multi-nanosecond molecular dynamics simulations.* Biophys. J., 1997. **73**(1): p. 3-20.

300. Tieleman, D.P. and H.J.C. Berendsen, *A molecular dynamics study of the pores formed by Escherichia coli OmpF porin in a fully hydrated palmitoyloleoylphosphatidylcholine bilayer.* Biophys. J., 1998. **74**(6): p. 2786-2801.
301. Petrache, H.I., et al., *Modulation of glycophorin A transmembrane helix interactions by lipid bilayers: Molecular dynamics calculations.* J. Mol. Biol., 2000. **302**(3): p. 727-746.
302. Jo, S., Kim, T., Im, W., *Automated builder and database of protein/membrane complexes for molecular dynamics simulations.* PLOS ONE, 2007. **2**(9): p. e880.
303. Lomize, A.L., et al., *Positioning of proteins in membranes: A computational approach.* Protein Science, 2006. **15**(6): p. 1318-1333.
304. Lee, A.G., *Lipid-protein interactions in biological membranes: a structural perspective.* Biochim. Biophys. Acta-Biomem., 2003. **1612**(1): p. 1-40.
305. Lomize, M.A., et al., *OPM database and PPM web server: resources for positioning of proteins in membranes.* Nucleic Acids Res., 2012. **40**(D1): p. D370-D376.
306. Dickey, A.a.F., R., *Molecular modelig of biomembranes: a how-to approach*, in *Biomedical applications of Biophysics*, T. Jue, Editor., Springer Science+Business Media.
307. Tieleman, D.P., S.J. Marrink, and H.J. Berendsen, *A computer perspective of membranes: molecular dynamics studies of lipid bilayer systems.* Biochim. Biophys. Acta, 1997. **1331**(3): p. 235-70.
308. Lyubartsev, A.P. and A.L. Rabinovich, *Force Field Development for Lipid Membrane Simulations.* Biochim. Biophys. Acta, 2016. **1858**(10): p. 2483-2497.
309. Berendsen, H.J.C., et al., *Molecular-Dynamics with Coupling to an External Bath.* J. Chem. Phys., 1984. **81**(8): p. 3684-3690.
310. Dickson, C.J., et al., *Lipid14: The Amber Lipid Force Field.* J. Chem. Theory Comput., 2014. **10**(2): p. 865-879.
311. Sugita, Y., Okamoto, Y., *Replica-exchange molecular dynamics method for protein folding.* Chem. Phys. Lett., 1999(314): p. 141-151.
312. Kastner, J., *Umbrella sampling.* Wiley Interdiscip. Rev. Comput. Mol. Sci., 2011. **1**(6): p. 932-942.
313. Patey, G.N., Valeau, J.P., *A monte carlo method for obtaining the interionic potential of mean force in ionic solution.* J. Chem. Phys., 1975. **63**(2334): p. 2334-2339.
314. Torrie, G.M. and J.P. Valleau, *Monte-Carlo Free-Energy Estimates Using Non-Boltzmann Sampling - Application to Subcritical Lennard-Jones Fluid.* Chem. Phys. Lett., 1974. **28**(4): p. 578-581.
315. Kumar, S., et al., *The weighted histogramanalysis method for free-energy calculations on biomolecules .1. the method.* J. Comp. Chem., 1992. **13**(8): p. 1011-1021.
316. Mulders, T., et al., *Free energy as the potential of mean constraint force.* J. Chem. Phys., 1996. **104**(12): p. 4869-4870.
317. Dickinson, C.D., et al., *Crystal structure of the tenth type III cell adhesion module of human fibronectin.* J. Mol. Biol., 1994. **236**(4): p. 1079-92.
318. Shattil, S.J., C. Kim, and M.H. Ginsberg, *The final steps of integrin activation: the end game.* Nat. Rev. Mol. Cell. Biol., 2010. **11**(4): p. 288-300.
319. Shen, M.Y., et al., *Amyloid beta peptide-activated signal pathways in human platelets.* European J. Pharma., 2008. **588**(2-3): p. 259-266.
320. Gowert, N.S., et al., *Blood Platelets in the Progression of Alzheimer's Disease.* Plos One, 2014. **9**(2).
321. Rosenberg, R.N., et al., *Altered amyloid protein processing in platelets of patients with Alzheimer disease.* Arch. Neurol., 1997. **54**(2): p. 139-44.
322. Baskin, F., et al., *Platelet APP isoform ratios correlate with declining cognition in AD.* Neurology, 2000. **54**(10): p. 1907-9.
323. Kunicki, T.J. and P.J. Newman, *The molecular immunology of human platelet proteins.* Blood, 1992. **80**(6): p. 1386-1404.
324. Scharf, R.E., Hasse, M., Reiff E., Gyenes, M., Stoldt, V.R., *CD40 ligand (CD40L) increases thrombus stability and outside-in signaling through integrin alpha(IIb)beta(3).* J. Thromb. Haemost. , 2009. **7 Suppl 2**: p. 920-929.
325. Ginsberg, M.H., *Integrin activation.* BMB Rep., 2014. **47**(12): p. 655-9.

326. Pfleger, C., et al., *Constraint Network Analysis (CNA): a python software package for efficiently linking biomacromolecular structure, flexibility, (thermo-)stability, and function.* J. Chem. Inf. Mod., 2013. **53**(4): p. 1007-1015.
327. Lau, T.L., et al., *The structure of the integrin alphaIIbbeta3 transmembrane complex explains integrin transmembrane signalling.* EMBO J., 2009. **28**(9): p. 1351-61.
328. Benkert, P., S.C.E. Tosatto, and D. Schomburg, *QMEAN: A comprehensive scoring function for model quality assessment.* Proteins: Struct., Funct., Bioinf., 2008. **71**(1): p. 261-277.
329. Studer, G., M. Biasini, and T. Schwede, *Assessing the local structural quality of transmembrane protein models using statistical potentials (QMEANBrane).* Bioinformatics, 2014. **30**(17): p. I505-I511.
330. Schmidt, T., et al., *A conserved ectodomain-transmembrane domain linker motif tunes the allosteric regulation of Cell surface receptors.* J. Biol. Chem., 2016. **291**(34): p. 17536-46.
331. Zotz, R.B., et al., *Prospective analysis after coronary-artery bypass grafting: platelet GP IIIa polymorphism (HPA-1b/PIA2) is a risk factor for bypass occlusion, myocardial infarction, and death.* J. Thromb. Haemost., 2000. **83**(3): p. 404-7.
332. Loncar, R., et al., *HPA-1 polymorphism of alpha(IIb)beta(3) modulates platelet adhesion onto immobilized fibrinogen in an in-vitro flow system.* Thromb. J., 2007: p. 10.1186/1477-9560-5-2.